APPLIED COMPUTATIONAL ELECTROMAGNETICS SOCIETY JOURNAL

Special Issue on CEM and Multiphysics Simulation for Electromagnetic Materials, Structures and Devices

Lead Guest Editor:
Long Li, Xidian University, China

Guest Editors:
Wei E. I. Sha, Zhijiang University, China
Xiuyin Zhang, South China University of Technology, China
Sheng Sun, University of Electronic and Technology of China, China
Zhihao Jiang, Southeast University, China
Maokun Li, Tsinghua University, China
Dazhi Ding, Nanjing University of Science & Technology, China
Qi Wu, Beihang University, China
Kuang Zhang, Harbin Institute of Technology, China
Lei Zhao, China University of Mining and Technology, China
Yingsong Li, Harbin Engineering University, China
Yan Shi, Xidian University, China

July 2019
Vol. 34 No. 7
ISSN 1054-4887

The ACES Journal is abstracted in INSPEC, in Engineering Index, DTIC, Science Citation Index Expanded, the Research Alert, and to Current Contents/Engineering, Computing & Technology.

The illustrations on the front cover have been obtained from the research groups at the Department of Electrical Engineering, The University of Mississippi.

THE APPLIED COMPUTATIONAL ELECTROMAGNETICS SOCIETY JOURNAL

Vol. 34 No. 7 July 2019

SPECIAL ISSUE ON CEM AND MULTIPHYSICS SIMULATION FOR ELECTROMAGNETIC MATERIALS, STRUCTURES AND DEVICES

A Succinct Explicit Local Time-Stepping Method for Helmholtz Wave Equation Based Discontinuous Galerkin Time Domain Method for 3-D Multiscale Electromagnetic Modeling
Peng Wang and Yan Shi 1002

Improvement of Microwave Metamaterial Aperture Imager with Genetic Algorithm
Shuncheng Tian and Long Li 1009

The 3D Fractional Modeling of Electromagnetic Sub-Diffusion Based on FDTD
Xuejiao Zhao, Yao Jiang, and Yanju Ji 1015

The Direction Switching Control of Electromagnetic Waves Based on All-dielectric Metamaterials
Yanan Hua, Kejian Chen, Yanjun Fu, and Xiaofan Zhang 1020

A Dual-band WLAN Antenna with Reactive Loading
Yinfeng Xia, Wei Xue, Yingsong Li, and Lei Zhao 1026

A Transmitarray Antenna with Double Conformal Rings as the Cell Elements
Keyu Yan, Xiuzhu Lv, Zhihua Han, and Yongliang Zhang 1032

A Low-Profile Dual-Polarized Crossed Dipole Antenna on AMC Surface
Rui He, Ze-Hong Yan, and Yan-Bo Meng 1038

Low-Cost Miniaturized NFC Antenna Design for Mobile Phone
Weijia Li, Difei Liang, Liang Chen, Li Zhang, and Longjiang Deng 1043

A Low Frequency Ultra-Wideband Electrically Small Monopole Antenna for HF/VHF Application
Yinfeng Xia, Wei Xue, Yingsong Li, Wanlu Shi, Beiming Li 1050

A Novel Frequency Reconfigurable Polarization Converter Based on Active Metasurface
Guangyao Liu, Jiaqi Han, Xiaohe Gao, Haixia Liu, and Long Li 1058

A Novel Multi-Functional Electronically Tuned Polarization Converter Based on Reconfigurable Reflective Metasurface
Jiaqi Han, Guangyao Liu, Yajie Mu, Haixia Liu, and Long Li 1064

The Temperature Compensation for TE011 Mode Resonator with Bimetal Material
Qiuyi Wu, Jiangbo Zhang, Yimin Yang, Xiaowei Shi 1070

Transient Electro-Thermal Analysis of a Common Source Amplifier Circuit with a Physics-based MOSFET Model
Tao Pan, Dazhi Ding, Hanxiang Li, and Xiaolin Cheng 1076

Analysis of the Charge Collection Mechanism of the Diamond Based on a Multi-physics Method
Yong Li, Haiyan Xie, Linyue Liu, and Jianfu Zhang 1082

Geometrical Dependence in Fixtures for 2D Multipole Micromagnets Magnetization Pattering
Miriam Martinez-Muñoz, Efren Diez-Jimenez, Gabriel Villalba Alumbreros, Marcin Michalowski, and Alberto Lastra-Sedano 1092

The Influence of Thermal Deformation on the AMB-rotor System of HTR-PM Helium Circulator
Jinpeng Yu, Guowei Du, Hong Wang, Zhe Sun, and Lei Zhao 1102

A Succinct Explicit Local Time-Stepping Method for Helmholtz Wave Equation Based Discontinuous Galerkin Time Domain Method for 3-D Multiscale Electromagnetic Modeling

Peng Wang and Yan Shi

School of Electronic Engineering
Xidian University, Xi'an, 710071, China
15029038715@163.com and shiyan@mail.xidian.edu.cn

Abstract ─ A succinct explicit local time-stepping (LTS) method for Helmholtz wave equation based discontinue Galerkin time domain method has been developed to analyze 3-D multiscale electromagnetic problems. In the proposed LTS scheme, a simple linear interpolation procedure is implemented to calculate the fields in the subdomain with the larger mesh size at the time steps corresponding to its neighboring subdomains with the smaller mesh size, and thus the proposed method can be easily generalized to the situation of the multiple subdomains with arbitrary time step ratio. With the proposed LTS method, the computational efficiency can be improved for the analysis of the multiscale problems. Several numerical examples including dielectric loaded resonance cavity, microstrip filter, and Vivaldi antenna are given to illustrate good performance of the proposed succinct explicit LTS method.

Index Terms ─ Arbitrary integral time step ratio, discontinue Galerkin time domain, local time-stepping (LTS), multiple subdomains, vector wave equation.

I. INTRODUCTION

In recent years, the discontinuous Galerkin time-domain (DGTD) methods have been rapidly developed for transient simulation of electromagnetic problems [1-5]. Compared with the conventional finite difference time domain (FDTD) method [6], the DGTD method can model the complex structures easily and obtain higher-order solution accuracy. With the use of numerical fluxes defined on the interface between two adjacent elements and explicit time integration method [1-5], the DGTD methods can lead to block-diagonal mass matrices with the block size equal to the number of degrees of freedom per element, thus leading to a highly efficient parallel solution scheme.

The conventional DGTD method is based on the Maxwell equations, which needs to solve the electric field **E** and the magnetic field **H** simultaneously. On the other hand, due to the use of the numerical flux, the conventional DGTD method results in more degrees of freedom, which consumes more computational resources. Recently, an interior penalty discontinuous Galerkin time domain (IPDG-WE) method has been developed to solve the complicate EM problems. Built on the Helmholtz wave equation, the IPDG-WE method [7, 8] only needs to solve one field variable, which can achieve significant reduction in computational time and memory usage. Moreover, with the introduction of the interior penalty fluxes, the IPDG-WE method can achieve optimal convergence rate of $O(h^{p+1})$ and meanwhile be free from the numerical dissipation, which the conventional DGTD method suffers from [7, 8].

The real-life electromagnetic problems generally involve various complex objects with multiscale geometries. When modelling this kind of the objects, the sizes of the discretization meshes are significantly different. With either the DGTD or the IPDG-WE methods for the analysis of the multiscale problems, the time step must be chosen according to the smallest grid size in the computational domain due to the CFL stability of the explicit time integration scheme, thus resulting in a high computational cost. To overcome this stability restriction, the implicit time integration methods [9] and marching-on-in degree-based approaches [10-12] have been developed. However, these methods suffer from the larger memory consumption. Except implicit-like time integration methods, some explicit local time-stepping (LTS) schemes [13-17] have been proposed. By implementing the different time steps in the elements with the larger and smaller sizes, respectively, the computational efficiency can be improved. However, most of the local LTS schemes are based on the DGTD method [13-16]. Recently, Diaz and Grote [17] theoretically studies the LTS methods for second-order scale wave equations. No reports have been given about the LTS method for the second order Helmholtz wave equation based discontinuous Galerkin time domain method to model the practical 3D electromagnetic (EM) problems.

Submitted On: December 31, 2018
Accepted On: May 7, 2019

In this paper, we propose a succinct explicit LTS method combining the central difference time marching scheme in the IPDG method to model the practical 3D multiscale EM problems. With a simple linear interpolation scheme, the proposed LTS method needs no additional memory usages and introduces slightly computational overhead at the subdomain interfaces. Hence the proposed approach is very suitable to the multiple subdomains with arbitrary geometry ratio. Some practical 3D EM problems are presented to illustrate the efficiency and potential of the proposed LTS method.

II. FORMULATIONS

In this section, the IPDG method is first introduced. Then the succinct explicit LTS scheme is developed.

A. IPDG method

Let Ω be a computational domain which is discretized by N nonoverlapping tetrahedrons and terminated by boundary Γ_b, including perfect electric conductor (PEC) surface Γ_{PEC}, perfect magnetic conductor (PMC) surface Γ_{PMC} and first-order absorbing boundary condition (ABC) surface Γ_{ABC}. So we have $\Gamma_b = \Gamma_{PEC} \cup \Gamma_{PMC} \cup \Gamma_{ABC}$. We denote $\Gamma = \partial\Omega$ as all the faces in Ω and $\Gamma = \Gamma_i \cup \Gamma_b$, in which Γ_i is defined as the interior faces.

To avoid the late-time drifting problem, the IPDG method starts from a modified Helmholtz wave equation, i.e.,

$$\nabla\times\left(\mu^{-1}\nabla\times\tilde{\mathbf{E}}\right)+\varepsilon\frac{\partial^2\tilde{\mathbf{E}}}{\partial t^2}+\sigma\frac{\partial\tilde{\mathbf{E}}}{\partial t}=-\frac{\partial\mathbf{J}_S}{\partial t}, \tag{1}$$

where $\tilde{\mathbf{E}}=\partial_t^{-1}\mathbf{E}$. Here ε and μ are the permittivity and permeability, respectively. The hierarchical vector basis functions $\mathbf{N}_{k,j}(\mathbf{r})$ [18] are used to expand $\tilde{\mathbf{E}}$ in (1) as:

$$\tilde{\mathbf{E}}=\sum_{j=0}^{N_E}e_j(t)\mathbf{N}_j(\mathbf{r}), \tag{2}$$

in which $e_j(t)$ is the time dependent expansion coefficient and N_E is the number of the vector basis functions. Applying the Galerkin's spatial testing procedure with $\mathbf{N}_i$ into (1), we can have:

$$\begin{aligned}&\int_\Omega\varepsilon\frac{\partial^2\tilde{\mathbf{E}}}{\partial t^2}\cdot\mathbf{N}_i d\mathbf{r}+\int_\Omega\sigma\frac{\partial\tilde{\mathbf{E}}}{\partial t}\cdot\mathbf{N}_i d\mathbf{r}+\\&\int_\Omega\nabla\times\left(\mu^{-1}\nabla\times\tilde{\mathbf{E}}\right)\cdot\mathbf{N}_i d\mathbf{r}=-\int_\Omega\frac{\partial\mathbf{J}_S}{\partial t}\cdot\mathbf{N}_i d\mathbf{r}.\end{aligned} \tag{3}$$

By using the vector calculus identities and Gauss's theorem to the term $\nabla\times\left(\mu^{-1}\nabla\times\tilde{\mathbf{E}}\right)$ in (3) and introducing numerical fluxes, we obtain a weak form as:

$$\begin{aligned}&\int_\Omega\varepsilon\frac{\partial^2\tilde{\mathbf{E}}}{\partial t^2}\cdot\mathbf{N}_i d\mathbf{r}+\int_\Omega\sigma\frac{\partial\tilde{\mathbf{E}}}{\partial t}\cdot\mathbf{N}_i d\mathbf{r}\\&+\int_\Omega\mu^{-1}\tilde{\mathbf{E}}\cdot\nabla\times\left(\nabla\times\mathbf{N}_i\right)d\mathbf{r}+\sum_{\Omega_K\in\Omega}\int_{\partial\Omega_K}\mathbf{n}\times\left(\mu^{-1}\tilde{\mathbf{E}}\right)^*\cdot\nabla\times\mathbf{N}_i dS\\&+\sum_{\Omega_K\in\Omega}\int_{\partial\Omega_K}\mathbf{n}\times\left(\mu^{-1}\nabla\times\tilde{\mathbf{E}}\right)^*\cdot\mathbf{N}_i dS=-\int_\Omega\frac{\partial\mathbf{J}_S}{\partial t}\cdot\mathbf{N}_i d\mathbf{r},\end{aligned} \tag{4}$$

in which superscript * denotes the numerical flux. Further, (4) is rewritten as a strong from, i.e.,

$$\begin{aligned}&\int_\Omega\varepsilon\frac{\partial^2\tilde{\mathbf{E}}}{\partial t^2}\cdot\mathbf{N}_i d\mathbf{r}+\int_\Omega\sigma\frac{\partial\tilde{\mathbf{E}}}{\partial t}\cdot\mathbf{N}_i d\mathbf{r}+\int_\Omega\mu^{-1}\nabla\times\tilde{\mathbf{E}}\cdot\nabla\times\mathbf{N}_i d\mathbf{r}+\\&\sum_{\Omega_K\in\Omega}\int_{\partial\Omega_K}\mathbf{n}\times\left(\tilde{\mathbf{E}}^*-\tilde{\mathbf{E}}\right)\cdot\mu^{-1}\nabla\times\mathbf{N}_i dS+\\&\sum_{\Omega_K\in\Omega}\int_{\partial\Omega_K}\mathbf{n}\times\left(\mu^{-1}\nabla\times\tilde{\mathbf{E}}\right)^*\cdot\mathbf{N}_i dS=-\int_\Omega\frac{\partial\mathbf{J}_S}{\partial t}\cdot\mathbf{N}_i d\mathbf{r}.\end{aligned} \tag{5}$$

The numerical fluxes are vital to the accuracy and stability of the IPDG method. The well-defined numerical fluxes can be obtained as [7, 8]:

$$\begin{aligned}\tilde{\mathbf{E}}^*&=\begin{cases}\left\{\tilde{\mathbf{E}}\right\} & f\subset\Gamma_i\\ 0 & f\subset\Gamma_{PEC}\\ \tilde{\mathbf{E}} & f\subset\Gamma_{PMC}\\ \tilde{\mathbf{E}} & f\subset\Gamma_{ABC}\end{cases},\\\left(\mu^{-1}\nabla\times\tilde{\mathbf{E}}\right)^*&=\begin{cases}\left\{\mu^{-1}\nabla\times\tilde{\mathbf{E}}\right\}-\tau_f\left[\!\left[\tilde{\mathbf{E}}\right]\!\right]_T & f\subset\Gamma_i\\ \mu^{-1}\nabla\times\tilde{\mathbf{E}}-\tau_f\tilde{\mathbf{E}} & f\subset\Gamma_{PEC}\\ 0 & f\subset\Gamma_{PMC}\\ -Y_s\mathbf{n}\times\mathbf{n}\times\partial\tilde{\mathbf{E}}/\partial t & f\subset\Gamma_{ABC}\end{cases},\end{aligned} \tag{6}$$

in which τ_f is an interior penalty parameter defined on the interface. The tangential jump $[\![\cdot]\!]_T$ and average $\{\cdot\}$ across an interface are expressed as,

$$\left[\!\left[\mathbf{u}\right]\!\right]_T=\begin{cases}\mathbf{n}^-\times\mathbf{u}^-+\mathbf{n}^+\times\mathbf{u}^+ & f\subset\Gamma_i\\ \mathbf{n}^-\times\mathbf{u}^- & f\subset\Gamma_b\end{cases}, \tag{7}$$

and,

$$\left\{\mathbf{u}\right\}=\begin{cases}\dfrac{\mathbf{u}^-+\mathbf{u}^+}{2} & f\subset\Gamma_i\\ \mathbf{u} & f\subset\Gamma_b\end{cases}. \tag{8}$$

Here the superscripts "-" and "+" denote the local element and the adjacent element corresponding to the face f, respectively.

By inserting (6) into (5), the semi-discrete system in each element yields:

$$\begin{aligned}&\left[\mathbf{M}_k\right]\left(\frac{\partial^2\tilde{\mathbf{e}}_k}{\partial t^2}\right)+\left[\mathbf{R}_k\right]\left(\frac{\partial\tilde{\mathbf{e}}_k}{\partial t}\right)+\left[\mathbf{S}_k^{mm}\right]\tilde{\mathbf{e}}_k\\&+\sum_f\left[\mathbf{S}_k^{mn,f}\right]\tilde{\mathbf{e}}_{k,f}=-\frac{\partial\tilde{\mathbf{j}}_k}{\partial t},\end{aligned} \tag{9}$$

in which $\tilde{\mathbf{e}}_k=[\tilde{e}_{k,1},\tilde{e}_{k,2},.....,\tilde{e}_{k,N_k}]_T$ denotes the vector of the expansion coefficients of the electric fields in the kth element, $\tilde{\mathbf{e}}_{k,f}$ denotes the coefficient vector in the elements adjacent to the kth element, and N_k is the number of the unknowns of the kth element. Here definitions of the matrices $\left[\mathbf{M}_k\right]$, $\left[\mathbf{R}_k\right]$, $\left[\mathbf{S}_k^{mm}\right]$ and $\left[\mathbf{S}_k^{mn,f}\right]$ can be found in [5].

Employing the central difference method to discretize

the time derivatives in (9) and sampling the electric fields at integer time steps $n\Delta t$ ($n = 0, 1, \ldots, N_t$), we can obtain the full-discrete system as

$$\begin{aligned}&\left(\left[\mathbf{M}_k\right]+\frac{\Delta t}{2}\left[\mathbf{R}_k\right]\right)\tilde{\mathbf{e}}_k^{n+1}=\\&\left(2\left[\mathbf{M}_k\right]+\Delta t^2\left[\mathbf{S}_k^{mm}\right]\right)\tilde{\mathbf{e}}_k^{n}-\Delta t^2\sum_f\left[\mathbf{S}_k^{mn,f}\right]\tilde{\mathbf{e}}_{k,f}^{n}\\&+\left(\frac{\Delta t}{2}\left[\mathbf{R}_k\right]-2\left[\mathbf{M}_k\right]\right)\tilde{\mathbf{e}}_k^{n-1}-\frac{\Delta t}{2}\left(\mathbf{j}_k^{n}-\mathbf{j}_k^{n-1}\right).\end{aligned}\tag{10}$$

B. Succinct explicit LTS method

In order to develop a multi-domain explicit LTS approach for the solution of the multiscale problem, we first consider the computational domain discretized by nonuniform meshes which can be categorized into two subdomains, as illustrated in Fig. 1. In each subdomain, the time step is chosen based on the minimal geometric sizes of the meshes according to CFL stability condition. Assume that ratio of the time steps in the two subdomains is p. Specifically, the time-steps in subdomains 1 and 2 are chosen as Δt_1 and $\Delta t_2=p\Delta t_1$, respectively. Let p an arbitrary positive integral number greater than 1 in this paper.

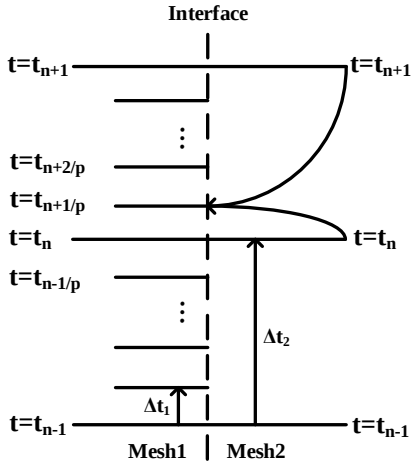

Fig. 1. The interface between two domains with the different meshes.

Consider that the subdomain 2 with the larger mesh size marches on from t_n to t_{n+1} in a time increment of Δt_2, while the subdomain 1 with the smaller mesh size successively marches on from t_n to t_{n+1} in a time increment of Δt_1. According to (10), we can know that the fields at the time step t_{n+1} in the elements of the subdomain 2 can be solved in the conventional way. On the other hand, the fields in the elements of the subdomain 1 except the elements adjacent to the interface between two subdomains are also updated in the traditional way. However, the fields at time step $t_{n+k/p}$ (k=2,3,⋯,p) in the elements on the interface of the subdomain 1 are solved in a modified way. In order to update the fields in an element of the subdomain 1 at time step $t_{n+k/p}$ (k=1,2,⋯,p-1), the fields of the subdomain 2 at the corresponding time step must be known. Here a linear interpolation approximation method is implemented to solve the fields in the subdomain 2 at the time step $t_{n+k/p}$ according to those at the time steps of t_n and t_{n+1}, i.e.,

$$\tilde{\mathbf{e}}^{n+k/p}=\left(1-\frac{k}{p}\right)\tilde{\mathbf{e}}^{n}+\left(\frac{k}{p}\right)\tilde{\mathbf{e}}^{n+1}.\tag{11}$$

Substituting (11) into (10), the fields in the element of the subdomain 1 at the time step $t_{n+(q+1)/p}$ can be solved as:

$$\begin{aligned}&\left(\left[\mathbf{M}_k\right]+\frac{\Delta t_1}{2}\left[\mathbf{R}_k\right]\right)\tilde{\mathbf{e}}_k^{n+(q+1)/p}\\&=\left(2\left[\mathbf{M}_k\right]+\Delta t_1^{\,2}\left[\mathbf{S}_k^{mm}\right]\right)\tilde{\mathbf{e}}_k^{n+q/p}-\Delta t_1^{\,2}\sum_{f\notin\text{interface}}\left[\mathbf{S}_k^{mn,f}\right]\tilde{\mathbf{e}}_{k,f}^{n+q/p}\\&-\Delta t_1^{\,2}\sum_{f\in\text{interface}}\left[\mathbf{S}_k^{mn,f}\right]\left(\left(1-\frac{q}{p}\right)\tilde{\mathbf{e}}_{k,f}^{n}+\left(\frac{q}{p}\right)\tilde{\mathbf{e}}_{k,f}^{n+1}\right)\\&+\left(\frac{\Delta t_1}{2}\left[\mathbf{R}_k\right]-2\left[\mathbf{M}_k\right]\right)\tilde{\mathbf{e}}_k^{n+(q-1)/p}-\frac{\Delta t_1}{2}\left(\mathbf{j}_k^{n+q/p}-\mathbf{j}_k^{n+(q-1)/p}\right).\end{aligned}\tag{12}$$

Comparing (12) and (10), we can find that in the proposed LTS-based scheme, no extra memory is required due to the use of the linear interpolation.

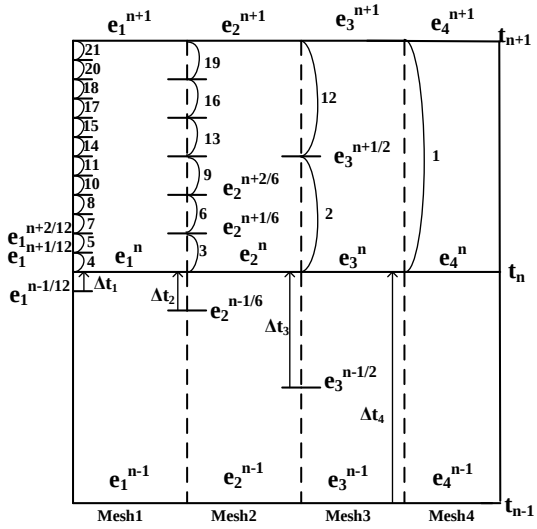

Fig. 2. The proposed LTS scheme for four subdomains with different meshes.

The proposed method can be easily generalized to the case of the multiple subdomains. Without the loss of generality, assume that there are four subdomains. The ratios of the mesh sizes in the four subdomains are 1: 2: 6: 12, as shown in Fig. 2. Therefore, the relationship of the time steps in the four subdomains becomes $\Delta t_4=2\Delta t_3=6\Delta t_2=12\Delta t_1$, where Δt_s (s=1,2,3,4) denotes the time step of the s-th subdomain.

Assume that all elements march on from the time step

t_n. The fields in the elements of the subdomain with the larger mesh size are first updated to its next time step, and then those with the smaller mesh size are stepped into the corresponding next time step successively. In this scenario, the linear interpolation method (11) can be implemented to solve the fields in the element of the subdomain with the larger mesh size at the time step corresponding to those of the subdomain with the smaller mesh size. And then (12) can be used to solve the fields in the elements of the subdomain with the smaller mesh size. It is worthwhile pointing out that the proposed LTS scheme can be applicable into the situation in which those elements adjacent to the certain element belong to more than two subdomains. Besides, in the proposed LTS method the arbitrary integral time step ratio between different subdomains can be valid.

In order to obtain a good speed up for the proposed LTS approach, a reasonably grouping strategy should be used. For a multiscale problem, the tetrahedrons with the different sizes are used to discretize the computational domain. All the tetrahedrons are first classified into different levels, i.e., Level=Int($10h/h_{\max}$), where h denotes the minimum edge length of each tetrahedron, h_{max} is the largest one among h, and Int (x) is a function to map a real number x to the largest integer not greater than x. Next, the tetrahedrons belonging to the neighboring levels are grouped into a subdomain according to the following criterions:

1. The number of the tetrahedrons which are adjacent to the interface between two subdomains is as small as possible;
2. The number of the tetrahedrons in the subdomain corresponding to the larger level is as many as possible;
3. The ratio of the time step between two neighboring subdomains is as large as possible.

It is worthwhile pointing out that we should use the above three criterions in a trade-off way to obtain a good speedup of the LTS method.

III. NUMERICAL RESULTS AND ANALYSIS

A. Dielectric ring in a resonant PEC cavity

As the first numerical example, a resonant PEC cavity with a dielectric ring shown in Fig. 3 is studied to demonstrate the accuracy and conservative energy property of the proposed method. The relative permittivity of the resonant ring is 2.06. The geometrical sizes of the computational region and the resonant ring are given in Fig. 3. The origin of coordinates is chosen as the center of the computational domain, and the center point of the resonant ring is set as (-45.25 mm, 0 mm, -21.5 mm). A dipole source is located at (-105 mm, -20 mm, 11.25 mm) and the observation point is chosen as (155 mm, 20 mm, 11.25 mm).

The computational region is meshed into some tetrahedrons with the average side length of λ/10 at 3 GHz, while the dielectric ring is discretized by using the refinement meshes with the average side length of λ/30 in order to get an accurate result. Therefore, there are 15,739 disjoint tetrahedrons in total and 3,463 tetrahedrons in the refinement region. In this example, all tetrahedrons are divided into ten different levels and are grouped into two subdomains. Ratio of the numbers of the discretized elements in two subdomains is shown as shown in Table 2. According to the CFL stability, the time steps of the two subdomains are chosen as 0.4×10^{-12} s and 1.6×10^{-12} s, respectively. A dipole source along the z-axis is used to generate a transient modulated Gaussian wave with a frequency band covering from 0.5 GHz to 5 GHz. Here the mixed 2nd order vector bases are adopted.

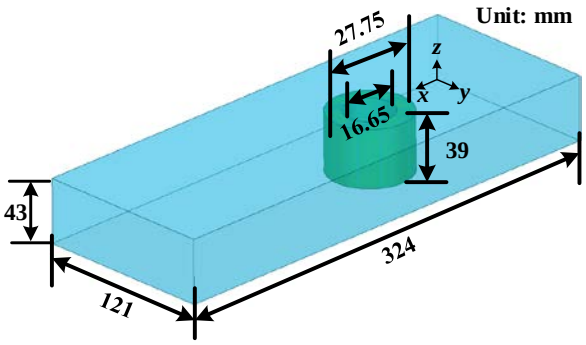

Fig. 3. Geometry of the resonant ring cavity.

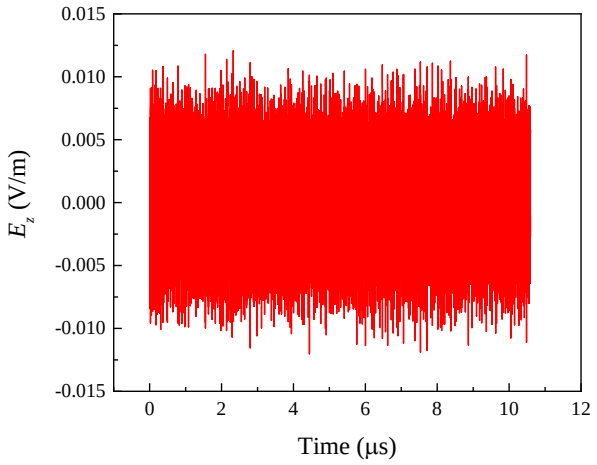

Fig. 4. Transient E_z component at the observation point.

The transient field E_z at the observation point is solved by the proposed method and plotted in Fig. 4. It can be seen from Fig. 4 that there is no numerical dissipation of the solution during a long simulation period more than 10 μs, and thus the proposed LTS-

based IPDG-WE method has energy conservation characteristic.

As shown in Table 1, the first eight resonance frequencies are extracted from the obtained time domain signals and compared with the results solved by the global time stepping (GTS) scheme and the high accuracy FDTD method [19]. The results by proposed LTS method agrees well with those by the GTS scheme and the in the reference. The computation performances of the LTS method and the GTS method are compared in Table 2. According to Table 2, the proposed LTS method can achieve 2.26 times speedup without the increase of the memory usage.

Table 1: The first eight resonant frequencies of the resonant PEC cavity, unit (GHz)

Scheme	FDTD	GTS	LTS
1st mode	1.2605	1.2503	1.2521
2nd mode	1.5076	1.5062	1.5061
3rd mode	1.8341	1.8303	1.8310
4th mode	2.1607	2.1564	2.1582
5th mode	2.5513	2.5431	2.5451
6th mode	2.6123	2.6092	2.6103
7th mode	2.8229	2.8213	2.8231
8th mode	3.0243	3.0202	3.0225

B. Microstrip filter

In the second example, a microstrip filter is analyzed by using the proposed method, as shown in Fig. 5. The relative permittivity of the substrate is 10.4 and the thickness is 1.27 mm. Two lumped ports are used in this example. The computational region terminated by the ABC boundary is set as 64 mm × 89.61 mm × 41.27 mm. The average size of the meshes in the whole region is chosen as $\lambda/10$ at 3 GHz and the regions corresponding to the narrow microstrip line are discretized by using the meshes with a higher spatial resolution. Hence, we have 52,948 tetrahedrons in total. The tetrahedrons are classified into ten different levels and then are grouped into 5 subdomains. Ratio of the mesh numbers in the 5 subdomains is 0.20:0.10:0.53:0.14:0.003, and therefore the time steps of the 5 subdomains are 0.28×10^{-13} s, 0.56×10^{-13} s, 1.12×10^{-13} s, 2.24×10^{-13} s and 4.48×10^{-13} s, respectively. The mixed 2nd order edge basis is used in this example. The S-parameters are calculated by the proposed LTS method and compared with the results by the GTS and FEM methods, as shown in Fig. 6. Good agreement between each other can be observed. Table 2 demonstrates comparison of the computational performance between the LTS and the GTS methods. The LTS method consumes less CPU time with the same memory usage.

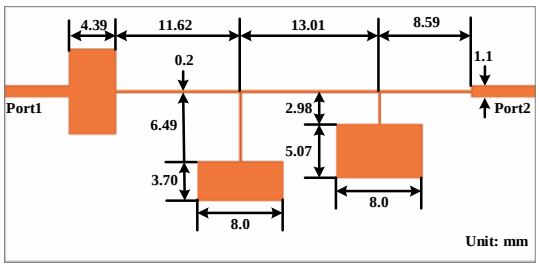

Fig. 5. Geometry of a microstrip filter.

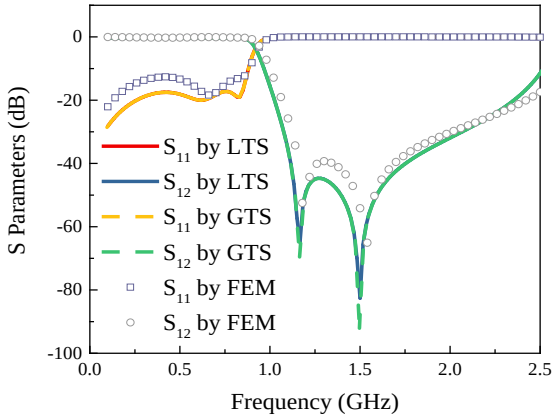

Fig. 6. S-parameters of the microstrip filter.

C. Vivaldi antenna

In the final example, a Vivaldi antenna is considered. The Vivaldi antenna is shown in Fig. 7, whose tapered slot is patterned with PEC ground plane on the top of the dielectric substrate. The relative permittivity of the substrate is 3.38 and the thickness is 1.524 mm. The geometrical parameters of the Vivaldi antenna are as follows: w_1 = 80 mm, w_2 = 0.5 mm, l_1 = 14.5 mm, l_2 = 12.9 mm, l_3 =12.6 mm, l_4 = 70 mm, l_5 = 3.2 mm, r =12 mm. The curves of the tapered slot are built by an exponential function of $e^{0.044x}$. One end of the slot is open to air and the other is ended with a circular slot. On the bottom of the substrate, there is a shorted 50 Ω microstrip feed line. A lumped port is used to excite the Vivaldi antenna.

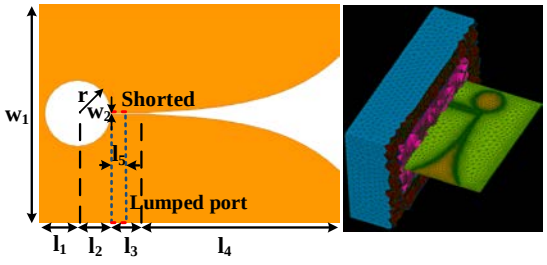

Fig. 7. Geometry and mesh of the Vivaldi antenna.

The computational domain is terminated by a perfectly matched layer (PML) which acts like an anechoic chamber absorbing all radiated energy. The whole region is meshed using a tetrahedral mesh with an approximate size length of 5 mm (λ/10 at 6 GHz), while the tapered slot is discretized by the meshes with the side length of 0.5 mm to guarantee the solution accuracy. The total number of the elements is 176895. Here 4 subdomains are used according to the side length of the tetrahedron, as shown in Table 2. The time step sizes of the 4 subdomains are set as 0.2×10^{-13} s, 0.8×10^{-13} s, 1.6×10^{-13} s and 3.2×10^{-13} s, respectively. Mixed 2nd order vector bases are utilized to expand the unknown fields. The S-parameter calculated by the proposed LTS method has a good agreement with those by the GTS and the FEM methods, as shown in Fig. 8. The performance comparison between the LTS and the GTS methods has been given in Table 2. A 6 times speedup is obtained by using the LTS-based method.

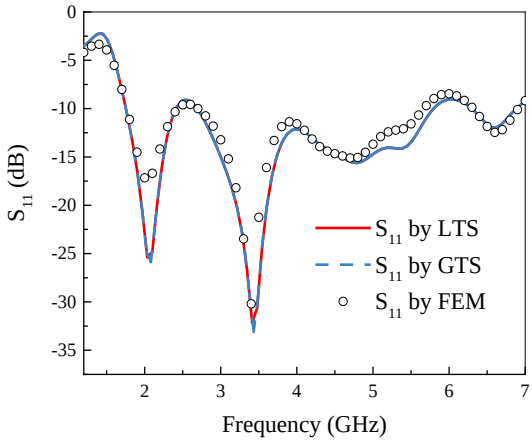

Fig. 8. S11 of the Vivaldi antenna.

Table 2: Performance comparison of LTS method and GTS method in the numerical examples

Examples	Method	Ratio of the Numbers of Elements in the Different Subdomains	Ratio of Time Steps in the Different Subdomains	Memory (MB)	Speedup Ratio
A	LTS	0.22: 0.78	1: 4	711	2.26
	GTS	------	------	711	
B	LTS	0.20: 0.10: 0.53: 0.14: 0.003	1: 2: 4: 8: 16	2332	2.23
	GTS	------	------	2332	
C	LTS	0.12: 0.26: 0.52: 0.10	1: 4: 8: 16	9988	6.00
	GTS	------	------	9988	

VI. CONCLUSION

In this paper, a succinct explicit LTS scheme for IPDG-WE method is presented to model 3-D multiscale electromagnetic problem. With a simple linear interpolation scheme, the proposed LTS method can be easily implemented in the situation of the multiple subdomains with arbitrary integral time step ratio. Good energy conservative property is achieved. Some numerical examples are given to illustrate good accuracy and speedup ratio without the increase of the memory usage for the solution of 3-D multiscale electromagnetic problems.

ACKNOWLEDGMENT

This work was supported by National Natural Science Foundation of China (No. 61771359), Natural Science Basic Research Plan in Shaanxi Province under Grant 2018JM6006, and Fundamental Research Funds for the Central Universities (No. JBF180202).

REFERENCES

[1] J. S. Hesthaven and T. Warburton, *Nodal Discontinuous Galerkin Methods: Algorithms, Analysis, and Applications*.Springer, New York, 2008.

[2] P. Wang, Y. Shi, C. Y. Tian, and L. Li, "Analysis of Graphene-based devices using wave equation-based discontinuous Galerkin time domain method," *IEEE Antennas and Wireless Propagation Letters*, vol. 17, no. 12, pp. 2169-2173, 2018.

[3] S. Dosopoulos and J. F. Lee, "Interior penalty discontinuous Galerkin finite element method for the time-dependent first order Maxwell's equations," *IEEE Transactions on Antennas and Propagation*, vol. 58, no. 12, pp. 4085-4090, 2010.

[4] C. Y. Tian, Y. Shi, and C. H. Liang, "A low-storage discontinuous Galerkin time-domain method," *IEEE Microwave and Wireless Component Letters*, vol. 27, no. 1, pp. 1-3, 2017.

[5] X. L. Li and J. M. Jin, "A comparative study of three finite element based explicit numerical schemes for solving Maxwell's equations," *IEEE Transactions on Antennas and Propagation*, vol. 60, no. 3, pp. 1450-1457, 2012.

[6] A. Taflove and S. C. Hagness. *Computational Electrodynamics: The Finite-Difference Time-Domain Method*. 3rd edition, Artech House, Boston, 2005.

[7] C. Y. Tian, Y. Shi, and C. H. Chan, "Interior

penalty discontinuous Galerkin time domain method based on wave equation for 3D electromagnetic modeling," *IEEE Transactions on Antennas and Propagation*, vol. 65, no. 12, pp. 7174-7184, 2017.

[8] C. Y. Tian, Y. Shi, and C. H. Chan, "An improved vector wave equation-based discontinuous Galerkin time domain method and its hybridization with Maxwell's equation-based discontinuous Galerkin time domain method," *IEEE Transactions on Antennas and Propagation*, vol. 66, no. 11, pp. 6170-6178, 2018.

[9] J. F. Chen and Q. H. Liu, "Discontinuous Galerkin time-domain methods for multiscale electromagnetic simulations: A review," *Proceedings of IEEE*, vol. 101, no. 2, pp. 242-254, 2013.

[10] Y. Shi, C. Y. Tian, and C. H. Liang, "Discontinuous Galerkin time domain method based on marching-on-in-degree scheme," *IEEE Antennas and Wireless Propagation Letters*, vol. 16, pp. 250-253, 2016.

[11] C. Y. Tian, Y. Shi, Z. Q. Liu, and C. H. Liang, "A Laguerre-based time-domain discontinuous Galerkin finite element-boundary integral method," *Microwave and Optical Technology Letters*, vol. 58, no. 11, pp. 2774-2780, 2016.

[12] Y. Shi, C. Y. Tian, Z. Q. Liu, and C. H. Liang, "A new Laguerre-based discontinuous Galerkin time-domain method," *Microwave and Optical Technology Letters*, vol. 59, no. 7, pp. 1499-1503, 2017.

[13] V. Dolean, H. Fahs, and L. Fezoui, "Locally implicit discontinuous Galerkin method for time domain electromagnetics," *Journal of Computational Physics*, vol. 229, no. 2, pp. 512-526, 2009.

[14] S. Piperno, "Symplectic local time-stepping in non-dissipative DGTD methods applied to wave propagation problems," *ESAIM: Mathematical Modelling and Numerical Analysis*, vol. 40, no. 5, pp. 815-841, 2006.

[15] A. Taube, M. Dumbser, C. D. Munz, and R. Schneider, "A high-order discontinuous Galerkin method with time-accurate local time stepping for the Maxwell equations," *International Journal of Numerical Modelling: Electronic Networks, Devices and Fields*, vol. 22, no. 1, pp. 77-103, 2009.

[16] E. Montseny, S. Pernet, X. Ferriéres, and G. Cohen, "Dissipative terms and local time-stepping improvements in a spatial high order discontinuous Galerkin scheme for the time-domain Maxwell's equations," *Journal of Computational Physics*, vol. 227, no. 14, pp. 6795-6820, 2008.

[17] J. Diaz and M. J. Grote, "Energy conserving explicit local time stepping for second-order wave equations," *SIAM Journal on Scientific Computing*, vol. 31, no. 3, pp. 1985-2014, 2009.

[18] J. P. Webb, "Hierarchal vector basis functions of arbitrary order for triangular and tetrahedral finite elements," *IEEE Transactions on Antennas and Propagation*, vol. 47, no. 8, pp. 1244-1253, 1999.

[19] S. D. Gedney and J. A. Roden, "Numerical stability of nonorthogonal FDTD methods," *IEEE Transactions on Antennas and Propagation*, vol. 48, no. 2, pp. 231-239, 2000.

Peng Wang received the B.E. degree in Electronic Science and Technology from the School of Electric Power, North China University of Water Resources and Electric Power, Henan, China, in 2015. He is currently working towards the Ph.D. degree in Electromagnetics and Microwave Technology at Xidian University, Xi'an, China. His research interest convers computational electromagnetics, IH heating technology, electromagnetic compatibility.

Yan Shi received the B.Eng. and Ph.D. degrees in Electromagnetic Fields and Microwave Technology from Xidian University, Xi'an, China, in 2001 and 2005, respectively.

Shi joined the School of Electronic Engineering, Xidian University, in 2005 and was promoted to Full Professor in 2011. From July 2007 to July 2008, he worked at City University of Hong Kong, Hong Kong, China, as a Senior Research Associate. From September 2009 to September 2010, he was a Visiting Postdoctoral Research Associate with the University of Illinois at Urbana-Champaign. From June 2017 to July 2017, he was a Visiting Professor at State Key Laboratory of Millimeter Wave of City University of Hong Kong, Hong Kong, China. He has authors or coauthored over 100 papers in referred journal, a book chapter, and a book. His research interests cover computational electromagnetics, metamaterial, antenna, and electromagnetic compatibility.

Shi received Program for New Century Excellent Talents in University awarded by Ministry of Education of China in 2011, New Scientific and Technological Star of Shaanxi Province awarded by Education Department of Shaanxi Provincial Government in 2013, First Prize of Awards for Scientific Research Results of High Education of Shaanxi Province awarded by Education Department of Shaanxi Provincial Government in 2013, and Second Prize of Awards of Science and Technology awarded by Shaanxi Province Government in 2015. Shi is a Senior Member of IEEE and the Chinese Institute of Electronics (CIE).

Improvement of Microwave Metamaterial Aperture Imager with Genetic Algorithm

Shuncheng Tian and Long Li

Key Laboratory of High Speed Circuit Design and EMC of Ministry of Education
School of Electronic Engineering
Xidian University, Xi'an, 710071, China
sctian@xidian.edu.cn, lilong@mail.xidian.edu.cn

Abstract ─ The genetic algorithm is used to improve the imaging capability of the microwave metamaterial aperture imager operating at Ku-band. The microwave metamaterial aperture imager is made up of the complementary electric-LC elements and Jerusalem cross structures elements. Besides, the genetic algorithm is applied to optimize the array of the elements, which can reduce the average mutual coherence of the patterns of the microwave metamaterial aperture imager at different frequencies. Then, the patterns of the microwave metamaterial aperture imager is used for the image reconstruction experiments. From the image reconstruction results, it can be seen that the quality of the recovered image is improved. The performance of the microwave metamaterial aperture imager using the genetic algorithm is crucially enhanced and extensive simulations verify the effectiveness of the proposed improvement approaches.

Index Terms ─ Complementary electric-LC element, imager, genetic algorithm, metamaterial, quality-factor.

I. INTRODUCTION

The traditional imaging system is mainly based on the Nyquist sampling theorem. However, for this type of the imaging system, if we want to get a higher resolution image, we have to increase the sampling rate. As a result, a large amount of redundant data will be discarded in the process of data compression. Microwave metamaterial aperture imager (MMAI) is a novel imager system, which can generate forward looking image without using mechanical scanning or antenna arrays. The first MMAI system was proposed in [1]. The MMAI used a one-dimensional metamaterial aperture with an extremely wide frequency band to generate enough radiation fields to illuminate the target, and two-dimensional sparse targets in the scene can be reconstructed with an optimized compressed sensing (CS) algorithm as shown in Fig. 1. x and y represent the $N\times1$ original image signal and the $M\times1$ measurement image signal, respectively. A is the $M\times N$ measurement matrix, where $M<<N$. In [2], a 2D metamaterial aperture was verified to realize 3D imaging, and it was shown that by increasing the quality factor (Q-factor) of the metamaterial element, the image performance of MMAI could be improved. The potential of multisensor fusion by integrating an infrared structured-light and optical image sensor to accelerate the microwave was illustrated in [3]. In [4-5], different reconstruction algorithms were investigated, and the imaging performance could also be improved. In [6], a coherent computational imaging system was proposed which can utilize a sparse detector array of planar, frequency-diverse, metasurface antennas designed to operate over the W-band frequency range. In [7], a new approach for short-range wireless localization based on meta-aperture and compressed sensing (CS) was proposed. In [8], a reconfigurable, dynamic beam steering holographic metasurface aperture to synthesize a microwave camera at K-band frequencies was present.

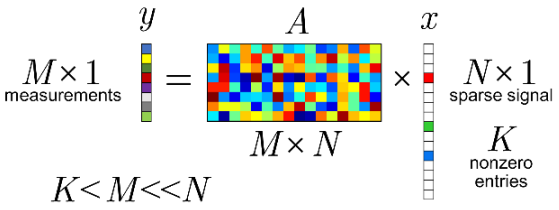

Fig. 1. Mathematical model of the CS algorithm.

For these methods above, the critical point is to ensure the non-correlative property between different measurement modes. From Fig. 2, it can been seen that the imaging performance is based on the radiation fields of the metamaterial aperture and the CS reconstruction algorithms. The information of the object can be obtained through repeating samples under different measurement modes. The performance of MMAI is mainly determined by the radiation field modes which provide enough measurements for the target. The common methods to increase the system radiation modes are to select the high Q-factor metamaterial resonant element and to design

Submitted On: December 1, 2018
Accepted On: July 10, 2019

MMAI in an extremely wide frequency bandwidth.

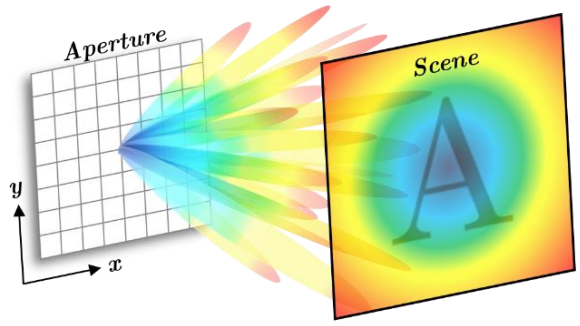

Fig. 2. Microwave metamaterial aperture imager system.

In the design of the metamaterial aperture, the non-correlative property converted to be the irrelevance of aperture's radiation characteristics under different frequencies changed in the work band to achieve much more measurements. The main contribution of this paper is the development of the higher frequency *Q*-factor CELC element and the random generation of the MMAI with the genetic algorithm. Specifically, Section II gives a brief introduction on the principles of MMAI. In Section III, a higher frequency *Q*-factor CELC element is analyzed. Section IV is devoted to the genetic algorithm on the design of the MMAI. Imaging experimental simulation results are given and discussed in Section V to demonstrate the effectiveness of the proposed design improvements on the MMAI. Finally, Section VI summarizes this work.

II. PRINCIPLE OF MMAI

In this section, the mathematical model of MMAI is briefly introduced. For the metamaterial aperture as an imaging system, a forward model must be implemented that describes how objects in the scene scatter the incident field, such that the collections by the receiver can be inverted and the scene will be retrieved. Though more sophisticated models can be developed, for our purposes the first born approximation provides a sufficient description. In this approximation, the field scattered from the target $\mathbf{E}_s$, is simply related to the incident field $\mathbf{E}_s$:

$$\mathbf{E}_s = \mathbf{E}_t f(\mathbf{r}), \tag{1}$$

where $f(r)$ is the target reflectivity at *r*. The scattered field propagating into the receiving probe antenna complies with the following proportionality:

$$y = \int \mathbf{E}_t(\mathbf{r})\mathbf{E}_s(\mathbf{r}) f(\mathbf{r}) d\mathbf{r}, \tag{2}$$

where *y* is the measurement of the scattered field collected by the receiving probe antenna. Considering the inherent frequency-diverse feature of complex radiation field, we can simplify (2) to:

$$y(\omega) = \int \mathbf{H}(\omega, \mathbf{r}) f(\mathbf{r}) d\mathbf{r}, \tag{3}$$

where $y(\omega)$ denotes the measurement of receiving probe at a certain driving frequency ω, $\mathbf{H}(\omega, \mathbf{r})$ is the measurement matrix, and the relationship between $\mathbf{E}_t(\mathbf{r})$ and $\mathbf{E}_s(\mathbf{r})$ can be calculated by:

$$\mathbf{H}(\omega, \mathbf{r}) = \mathbf{E}_t(\mathbf{r})\mathbf{E}_s(\mathbf{r}), \tag{4}$$

where $\mathbf{E}_t(\mathbf{r})$ and $\mathbf{E}_s(\mathbf{r})$ denote the fields from the transmitting metamaterial aperture and the receiving probe antenna projected to the point *r*, respectively. When the target information is reconstructed, its exact location is unknown. As a result, the scene is discretized into *N* voxels. If the frequency sweep is sampled at *M* frequency points, (3) becomes a finite dimension matrix equation as follows:

$$g_M = H_{M\times N} f_N, \tag{5}$$

where g_M is the received measurement matrix under a sequence of radiation field illumination varying with frequency, and f_N denotes the unknown reflectivities matrix of scene targets, and $H_{M\times N}$ is the measurement matrix whose k^{th} row elements corresponds to the complex field pattern at the driving frequency ω_k. Since the discretized pixels *N* is normally much larger than the number of measurement modes *M*, the linear equation in (5) can be extremely underdetermined, and it is difficult to solve (5) by the direct matrix inversion, thus the sophisticated CS technique is chose to estimate f_N with a promising solution.

III. COMPLEMENTARY ELECTRIC-LC (CELC) ELEMENT

For microwave metamaterial aperture imager system, the key is to increase the *Q*-factor of the metamaterial unit. That is to say, the unit must possess different center operating frequency and much narrower bandwidth in the operating frequency band of the metamaterial aperture. As pointed out by Hunt et al. [2], an increase in the *Q*-factor of the element for the metamaterial aperture causes the average mutual coherence μ to decrease, which indicates less correlation between measurements represents better orthogonality of the far-field patterns. Here the frequency *Q*-factor is defined as:

$$Q = f/BW, \tag{6}$$

where *f* and *BW* represent the center operating frequency and the frequency range in which the radiation efficiency decreases by half, respectively. If we want to recover images more accurately, the metamaterial aperture needs to work under more measurement modes in the limited operating frequency band. In other words, the *BW* of the metamaterial aperture unit needs to be much narrower and the frequency *Q*-factor will be even higher. In order to improve the frequency *Q*-factor, we select the following three methods in our work: 1) Use the asymmetric rectangular ring slot to instead the square ring slot because

the asymmetric structure can provide improvement on the frequency *Q*-factor; 2) Enlarge the period of the complementary electric-LC (CELC) element *P* while keep the size of the slot fixed, to raise the frequency *Q*-factor.

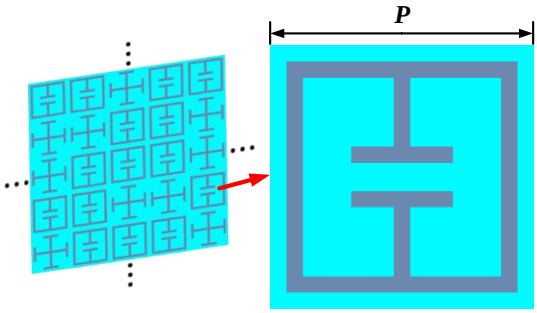

Fig. 3. Complementary electric-LC element.

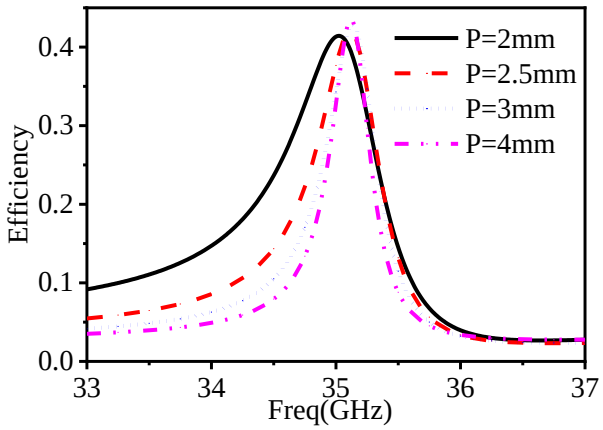

Fig. 4. Efficiency with different *P*.

Table 1: *Q*-factor of the CELC element with different *P*

***P* (*mm*)**	***Q*-factor**	***P* (*mm*)**	***Q*-factor**
2	37	3	70
2.5	58	4	86

By above ways, we could maximize the frequency diversity in the finite operating frequency band. In this paper, the improved the CELC element is proposed in Fig. 3. The CELC elements and Jerusalem cross structures elements with the proportion of 0.8 and 0.2, respectively. The higher *Q*-factor metamaterial cell is etched on the substrate upper plate and the bottom is the metal ground. Rogers 4350 is used with the dielectric constant of 3.66 and the thickness is 0.508*mm*. The proposed element is simulated with the infinite periodic boundary condition in HFSS. From Fig. 4, the *BW* of the metamaterial aperture unit can be narrowed by enlarging the period *P*. Meanwhile, if the dielectric constant is higher and the thickness is thinner, the *Q*-factor can also be enlarged. Because of the much smaller bandwidth, the number of measurement modes will be more in the same bandwidth, which makes it possible that more information can be obtained with the more different radiation features. As listed in Table 1, when *P*=4*mm*, the *Q*-factor is about 86, which means that the *Q*-factor of the novel CELC element can be improved by enlarging the period of the CELC unit.

As the operating frequency changes, the far-field radiation pattern of the MMAI changes. As pointed out by [9-10], when the bandwidth of the element becomes smaller, the average mutual coherence becomes much lower. As a result, the proposed higher *Q*-factor CELC element may realize to decrease the average mutual coherence μ to improve the imaging effect of the MMAI.

IV. THE GENETIC ALGORITHM ON THE DESIGN OF THE MMAI

Object within the scene scatters the incident fields and produce a backscattered field. In a transceiver configuration, the backscattered fields are detected by a single, low-gain waveguide probe with the same frequency. The low-gain waveguide probe ensures all the backscattered radiation field from object is collected as shown in Fig. 2. The MMAI system must obtain the detection ability in all the field of view (FOV) because the object may appear at any position in the scene. If the MMAI is made up of the CELC elements and Jerusalem cross structures elements randomly, which may lead to the result that the far field patterns of MMAI is not uniform distribution. As a result, the electromagnetic signals of the incident field cannot detect the object if the object is in the weak signals range in the FOV.

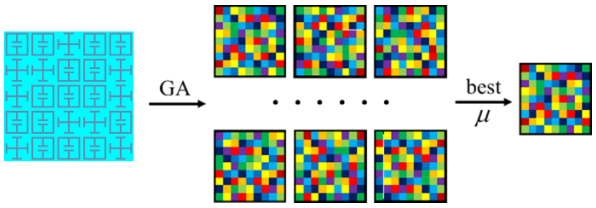

Fig. 5. Process of the genetic algorithm on the design of the MMAI.

In this section, the genetic algorithm (GA) is selected to assist to design the MMAI as shown in Fig. 5. The design process with the genetic algorithm can be summarize as follows:

1) Select the higher *Q*-factor CELC element with different sizes based on the element model base, determine the element amount and proportion of the higher *Q*-factor CELC element and Jerusalem Cross Unit; Initializatie the first population of the MMAI with different distributions and the cross mutation probability, take these MMAIs into the HFSS to simulate for the far field characteristics;

2) Take the simulation results of these MMAI into MATLAB to build the measurement matrix and compute the average mutual coherence μ; compare the average mutual coherence μ of different MMAIs and select some better MMAI with the lower μ as the new population;

3) Produce the novel MMAIs with the cross mutation operation based on the new population; repeat the simulation, computation μ, selection, production new population until the average mutual coherence not decrease.

Table 2: Average mutual coherence of different MMAIs

MMAI	Iteration Time		
	1	2	3
1	0.30704	0.29790	0.29945
2	0.31504	0.29819	0.29955
3	0.29964	0.30298	0.29589
4	0.29893	0.30088	0.29852
5	0.30562	0.29893	0.29790
6	0.30452	0.29964	0.29819
7	0.30024	0.30024	0.29893
8	0.31250	0.30452	0.29964
MMAI	**Iteration Time**		
	4	**5**	**6**
1	0.29790	0.29589	0.29589
2	0.29589	0.29589	0.29589
3	0.29819	0.29790	0.29589
4	0.29852	0.29790	0.29589
5	0.29589	0.29589	0.29589
6	0.29790	0.29589	0.29589
7	0.29819	0.29790	0.29589
8	0.29852	0.29790	0.29589

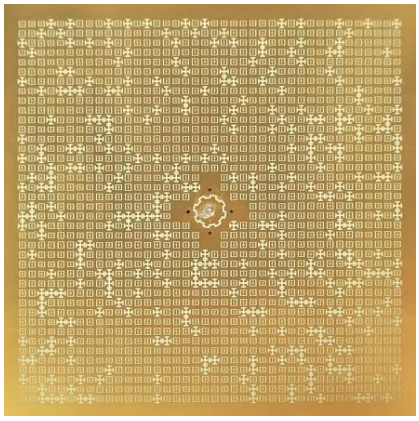

Fig. 6. Microwave metamaterial aperture.

With the properties of high Q-factor and frequency agility characteristic, the far-field pattern is different at different frequency because only a few elements mainly work at it particular frequency in the operating band. With the feature, the MMAI can be used in the imaging system. Finally, the measurement matrix A is set up by the use of the far-field patterns at different frequencies. The operating frequency range of the MMAI is set from 33GHz to 37GHz. In our work, eight MMAIs with different element distributions are selected as the initial population and optimized with the genetic algorithm. From the results in Table 2, when the iteration time reaches 6, the average mutual coherence of these MMAIs decreases to 0.29589, which verifies the effectiveness of the optimization on the MMAI design with the genetic algorithm.

V. IMAGE RECONSTRUCTION EXPERIMENTS

The MMAI is made up of 80% higher Q-factor metamaterial elements and 20% Jerusalem Cross elements as shown in Fig. 6. The far field patterns of the MMAI at 33GHz, 35GHz and 37GHz are described in Fig. 7, Fig. 8 and Fig. 9, respectively.

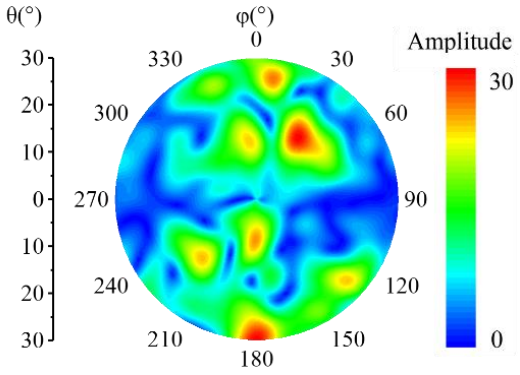

Fig. 7. Far field radiation patterns at 33GHz.

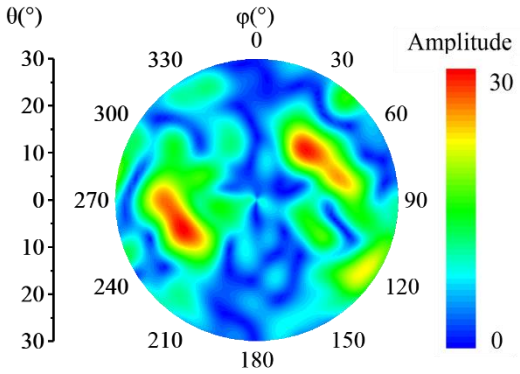

Fig. 8. Far field radiation patterns at 35GHz.

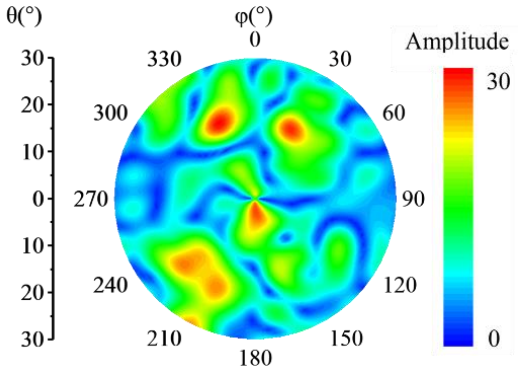

Fig. 9. Far field radiation patterns at 37GHz.

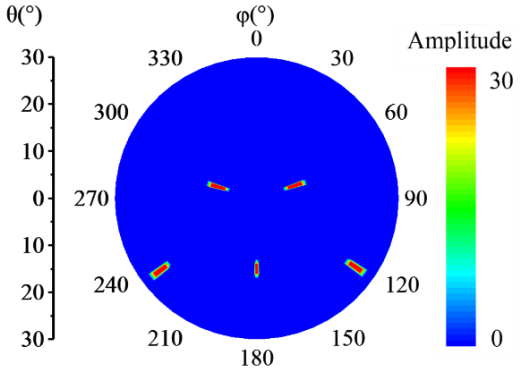

Fig. 10. The original image with five points.

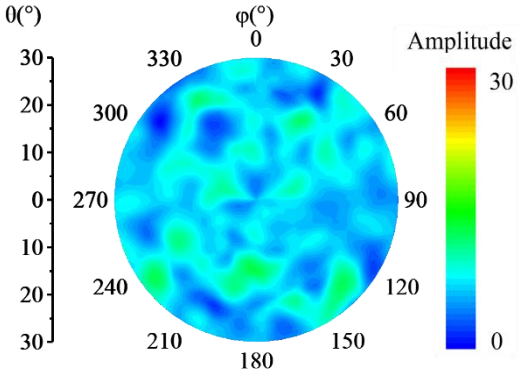

Fig. 11. Image reconstruction with the original MMAI.

The far field patterns can be used to build the measurement matrix to verify the feasibility of the MMAI. The optimized MMAI is used for the image reconstruction experimental simulations in Matlab. The goal of reconstruction is to estimate the set of target fractional scattering coefficients using the simulated measurement matrix. For the metamaterial-based frequency-diverse MMAI of consideration here, the number of available measurement modes can be significantly smaller than the number of voxels to be estimated according to compressed sensing theory.

To accomplish this goal, we discretize the scene into N voxels. Given the appropriate parameter for the reconstruction, it is in our interest to compare the image reconstruction effects with the measurement matrix of different average mutual coherences. The original image, in Fig. 10, is segmented into 31×361 blocks. The five red blocks is set as the object and the blue blocks is the background. Then, the restored image x can be calculated by $y=Ax$. x and y represent the $N\times1$ original image signal and the $M\times1$ received image signal, respectively. These image reconstruction experiments are done on a PC with Intel Xeon CPU E3-1230. Figure 11 and Fig. 12 give the image reconstruction of a simple target with two MMAIs with the average mutual coherence μ=0.35104 and μ=0.29589, respectively. Interestingly, the image reconstructed with the MMAI of the lower average mutual coherence has better quality than the higher μ MMAI. Through imaging experiments, the correctness and feasibility of the approaches proposed in this paper have been verified.

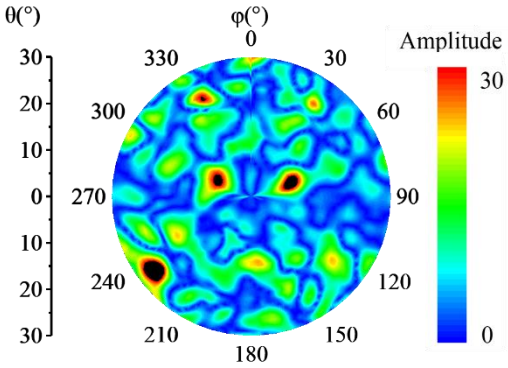

Fig. 12. Image reconstruction with the improved MMAI.

VI. CONCLUSION

An imaging system using dynamic MMAI has great potential in various applications. In particular, MMAI can overcome the complications of using complex hardware systems or moving parts. As such, a higher Q-factor metamaterial element is proposed to be applied in the imaging system, which holds a good frequency agility property. The bandwidth of it is much narrower than the common metamaterial element. Besides, by using the genetic algorithm, a lot of MMAIs is designed and simulated to produce the best one. The far field radiation patterns at different frequencies are used to construct suitable deterministic measurement matrix and improve the accuracy of image reconstruction. Then, the image reconstruction simulations are done to verify the correctness of the proposed approaches. The combination of a dynamic MMAI with reconstruction algorithm can lead to an imaging system that is efficient

and simple on the hardware and software levels. This exciting prospect opens the door to new opportunities in various research areas such as high-resolution, real-time, volumetric imaging.

ACKNOWLEDGMENT

This work is supported by National Natural Science Foundation of China under Contract No. 51477126, and supported by Technology Explorer and Innovation Research Project, and Fundamental Research Funds for the Central Universities (K5051202051 and SPSZ021409).

REFERENCES

[1] J. Hunt, T. Driscoll, A. Mrozack, G. Lipworth, M. Reynolds, D. Brady, and D. R. Smith, "Metamaterial apertures for computational imaging," *Science*, vol. 339, no. 6117, pp. 310-313, Jan. 2012.

[2] G. Lipworth, A. Mrozack, J. Hunt, D. L. Marks, T. Driscoll, D. Brady, and D. R. Smith, "Metamaterial apertures for coherent computational imaging on the physical layer," *Journal of the Optical Society of America A*, vol. 30, no. 8, pp. 1603-1612, Aug. 2013.

[3] J. Hunt, J. Gollub, T. Driscoll, G. Lipworth, A. Mrozack, M. Reynolds, D. J. Brady, and D. R. Smith, "Metamaterial microwave holographic imaging system," *Journal of the Optical Society of America A*, vol. 31, no. 10, pp. 2109-2119, Oct. 2014.

[4] O. Yurduseven1, M. F. Imani, H. Odabasi, J. Gollub, G. Lipworth, A. Rose, and D. R. Smith, "Resolution of the frequency diverse metamaterial aperture imager," *Progress In Electromagnetics Research*, vol. 150, pp. 97-107, Jan. 2015.

[5] G. Lipworth, A. Rose, O. Yurduseven, V. R. Gowda, M. F. Imani, and H. Odabasi, "Comprehensive simulation platform for a metamaterial imaging system," *Applied Optics*, vol. 54, no. 31, pp. 9343-53, Nov. 2015.

[6] T. Zvolensky, J. N. Gollub, D. L. Marks, and D. R. Smith, "Design and analysis of a w-band metasurface-based computational imaging system," *IEEE Access*, vol. 5, pp. 9911-9918, May 2017.

[7] T. Zhou, H. Li, D. Ye, J. Huangfu, S. Qiao, Y. Sun, W. Zhu, C. Li, and L. Ran, "Short-range wireless localization based on meta-aperture assisted compressed sensing," *IEEE Transactions on Microwave Theory and Techniques*, vol. 65, no. 7, pp. 2516-2524, Jan. 2017.

[8] O. Yurduseven, D. L. Marks, T. Fromenteze, and D. R. Smith, "Dynamically reconfigurable holographic metasurface aperture for a mills-cross monochromatic microwave camera," *Optics Express*, vol. 26, no. 5, pp. 5281-5291, Mar. 2018.

[9] N. Kou, L. Li, and S. Tian "Measurement matrix analysis and radiation improvement of metamaterial aperture antenna for coherent computational imaging," *Applied Science*, vol. 7, no. 9, p. 933, Sep. 2017.

[10] Z. Wu, Z. Lei, H. Liu, and N. Kou, "Range decoupling algorithm for accelerating metamaterial apertures-based computational imaging," *IEEE Sensors Journal*, vol. 18, no. 9, pp. 3619-3631, Mar. 2018.

Shuncheng Tian was born in Tianjin, China, in 1990. He received the B.E. degree from Xidian University, Xi'an, China, in 2013. He is currently pursuing the Ph.D. degree in Electromagnetic Fields and Microwave Technology at Xidian University, Xi'an, China.

His research interests include reflectarray analysis, frequency-selective surface analysis and design, automated neural network model generation algorithm, and electromagnetic field simulation and optimization.

Long Li (M'06–SM'11) was born in Guizhou Province, China. He received the B.E. and Ph.D. degrees in Electromagnetic Fields and Microwave Technology from Xidian University, Xi'an, China, in 1998 and 2005, respectively.

He was a Senior Research Associate with City University of Hong Kong, in 2006. He received the Japan Society for Promotion of Science (JSPS) Postdoctoral Fellowship and visited Tohoku University, Sendai, Japan, as a JSPS Fellow from November 2006 to November 2008. He was a Senior Visiting Scholar with the Pennsylvania State University, State College, PA, USA, from December 2013 to July 2014. He is currently a Professor with the School of Electronic Engineering, Xidian University. He is also the Director of Key Lab of High Speed Circuit Design and EMC, Ministry of Education, China. His research interests include metamaterials, electromagnetic compatibility, novel antennas, OAM, and wireless power transfer and harvesting technology.

Li was the recipient of the Nomination Award of National Excellent Doctoral Dissertation of China in 2007. He was also the recipient of the Program for New Century Excellent Talents in the University of the Ministry of Education of China in 2010, the First Prize of Awards for Scientific Research Results offered by Shaanxi Provincial Department of Education, China, in 2013, the IEEE APS Raj Mittra Travel Grant Senior Researcher Award in 2015, and the Shaanxi Youth Science and Technology Award in 2016.

The 3D Fractional Modeling of Electromagnetic Sub-Diffusion Based on FDTD

Xuejiao Zhao [1], Yao Jiang [1], and Yanju Ji [1,2*]

[1] College of Instrumentation and Electrical Engineering
Jilin University, Changchun, Jilin, China
zhaoxj16@mails.jlu.edu.cn, 447077967@qq.com

[2] Key Laboratory of Earth Information Detection Instrumentation
Ministry of Education, Jilin University, Changchun, Jilin, China
jiyj@jlu.edu.cn

Abstract ─ The anomalous diffusion has been discovered in many natural motions, it is defined as a phenomenon that does not conform to FICK's diffusion law. One of the anomalous diffusions is the electromagnetic sub-diffusion, which indicated the power law decay rate is slower than normal -2/5. In this paper, we modeled electromagnetic sub-diffusion based on 3D finite-different time-domain (FDTD) method. Through the introduction of roughness parameter in the definition of conductivity and the discretization of fractional integrations, the electromagnetic sub-diffusion can be efficiently modeled. The improved method is verified by homogeneous half-space models and anomalous models with 3D bodies, the results show that it can model 3D electromagnetic sub-diffusion with high precisions and has a good performance in the recognitions of anomalous bodies.

Index Terms ─ Electromagnetic sub-diffusion, finite-different time-domain method, fractional calculus.

I. INTRODUCTION

In the modeling of electromagnetic propagation, the electrical conductivity of the ground is usually imagined to be uniformly and constant [1-4]. However, the ground conductivity usually presents heterogeneity and nonlinearity which results in anomalous diffusion occurred in the measured data [5-7]. One of the anomalous diffusions is called sub-diffusion [8]. It manifests as the measured data decays slower especially in late time. In this case, the measured data can't be explained accurately based on the classical electromagnetic theory, which has hindered the application of electromagnetic method in the mineral resource's exploration and other fields in a way. The previous researches have indicated that the fractional diffusion equation can provide the theoretical basis for the electromagnetic sub-diffusion which only need to introduce roughness parameter in the expression of electrical conductivity [9-10]. Accordingly, the fractional calculous should be solved in time domain which makes the discretization of the electromagnetic fields difficult. With the development of fractional derivative calculation in mathematics, lots of fractional order finite difference algorithms are developed [11-13], which provides a possibility for the electromagnetic sub-diffusion modeling in time domain.

In this paper, we introduce roughness parameter in the expression of electrical conductivity in frequency domain, and discrete fractional items after the frequency-time transformation. Accordingly, the iterative equations of electromagnetic fields are derived based on a FDTD method. At last the improved method is verified by different models, the results indicated that it can model electromagnetic sub-diffusion well and provide basis for a future study on the electromagnetic anomalous induction in time domain.

II. METHOD

After introduced the roughness parameter β ($0 < \beta < 1$), the electoral conductivity σ_β can be expressed as [9, 10]:

$$\sigma_\beta(\omega) = \sigma_0 + k\sigma_0 (i\omega)^{-\beta}. \tag{1}$$

The Ampere's law without sources in frequency domain:

$$\nabla \times H(\omega) = \sigma_\beta(\omega) E(\omega) + j\omega\varepsilon E(\omega), \tag{2}$$

can be transformed into time domain:

$$\nabla \times H(t) = \sigma_\beta(t) * E(t) + \varepsilon \frac{\partial E(t)}{\partial t}. \tag{3}$$

The convolution item in equation (3) can be expressed as:

$$\begin{aligned} \sigma_\beta(t) * E(t) &= \sigma_0 E(t) + k\sigma_0 {}_0D_t^{-\beta} E(t) \\ &= \sigma_0 E(t) + \frac{k\sigma_0}{\Gamma(\beta)} \int_0^t (t-\tau)^{\beta-1} E(\tau) d\tau \end{aligned}, \tag{4}$$

Submitted On: February 21, 2019
Accepted On: March 24, 2019

where $\Gamma(\beta)$ indicates the Gamma function:

$$\Gamma(z)=\int_0^{\infty} e^{-t}t^{z-1}dt, \qquad \mathrm{Re}(z)>0. \tag{5}$$

Discretized (4) can get:

$$\begin{aligned}&\int_0^{t_n}(t_n-\tau)^{\beta-1}E(\tau)d\tau=\int_0^{\Delta t_1}(t_n-\tau)^{\beta-1}E(\tau)d\tau+\\&\int_{\Delta t_1}^{\Delta t_1+\Delta t_2}(t_n-\tau)^{\beta-1}E(\tau)d\tau+\int_{\Delta t_1+\Delta t_2}^{\Delta t_1+\Delta t_2+\Delta t_3}(t_n-\tau)^{\beta-1}E(\tau)d\tau+\\&\ldots\ldots+\int_{t_n-\Delta t_n}^{t_n}(t_n-\tau)^{\beta-1}E(\tau)d\tau\\&=\frac{1}{\beta}\left(\begin{array}{l}\frac{E_0+E_1}{2}\left((t_n)^{\beta}-(t_n-t_1)^{\beta}\right)+\frac{E_1+E_2}{2}\left((t_n-t_1)^{\beta}-(t_n-t_2)^{\beta}\right)\\+\ldots\ldots+\frac{E_{n-1}+E_n}{2}\left((t_n-t_{n-1})^{\beta}-(t_n-t_n)^{\beta}\right)\end{array}\right)\end{aligned} \tag{6}$$

Inserting (6) into (3), and after discretion based on FDTD [14-17], we can get the iterative formulation of electric field:

$$\begin{aligned}&E_x^{n+1}(i+\tfrac{1}{2},j,k)=\frac{-\sigma_0\Delta t_n+2\varepsilon}{\sigma_0\Delta t_n+2\varepsilon}E_x^{n+1}(i+\tfrac{1}{2},j,k)+\\&\frac{2\Delta t_n}{(\sigma_0\Delta t_n+2\varepsilon)\Delta y(i,j,k)}(H_z^{n+1/2}(i+\tfrac{1}{2},j+\tfrac{1}{2},k)-H_z^{n+1/2}(i+\tfrac{1}{2},j-\tfrac{1}{2},k))-\\&\frac{2\Delta t_n}{(\sigma_0\Delta t_n+2\varepsilon)\Delta z(i,j,k)}(H_y^{n+1/2}(i+\tfrac{1}{2},j,k+\tfrac{1}{2})-H_y^{n+1/2}(i+\tfrac{1}{2},j,k-\tfrac{1}{2}))-\\&\frac{2k\sigma_0\Delta t}{(\sigma_0\Delta t_n+2\varepsilon)\beta\Gamma(\beta)\Delta z(i,j,k)}B_x^{n+1/2}(i+\tfrac{1}{2},j,k)\end{aligned} \tag{7}$$

where

$$\begin{aligned}&B_x^{n+1/2}(i+\tfrac{1}{2},j,k)=\\&\frac{E_0+E_1}{2}\left((t_{n+1/2}-t_0)^{\beta}-(t_{n+1/2}-t_1)^{\beta}\right)+\frac{E_1+E_2}{2}\left((t_{n+1/2}-t_1)^{\beta}-(t_{n+1/2}-t_2)^{\beta}\right)+\ldots\ldots\\&+\frac{E_{n-1}+E_n}{2}\left((t_{n+1/2}-t_{n-1})^{\beta}-(t_{n+1/2}-t_n)^{\beta}\right)+E_n\left((t_{n+1/2}-t_n)^{\beta}-(t_{n+1/2}-t_{n+1/2})^{\beta}\right)\end{aligned} \tag{8}$$

For the magnetic fields, we chose equation (9) as the control equation of H_x and H_y and equation (10) as the control equation of H_z,

$$\nabla\times E=-\mu\frac{\partial H}{\partial t}, \tag{9}$$

$$\nabla\cdot H=0. \tag{10}$$

Equation (9) and (10) can be expressed in components as equation (11-13):

$$\frac{\partial E_z}{\partial y}-\frac{\partial E_y}{\partial z}=\mu\frac{\partial H_x}{\partial t}, \tag{11}$$

$$\frac{\partial E_x}{\partial z}-\frac{\partial E_z}{\partial x}=\mu\frac{\partial H_y}{\partial t}, \tag{12}$$

$$\frac{\partial H_z}{\partial z}=-\frac{\partial H_x}{\partial x}-\frac{\partial H_y}{\partial y}. \tag{13}$$

The discrete form of equation (11, 13) is performed by a FDTD method [9-11] as:

$$\begin{aligned}&H_x^{n+1/2}(i+1,j+\frac{1}{2},k\frac{1}{2})=H_x^{n-1/2}(i+1,j+\frac{1}{2},k\frac{1}{2})+\\&\frac{\Delta t_{n-1}+\Delta t_n}{2\mu}\left[\frac{E_y^n\left(i,j+\frac{1}{2},k+1\right)-E_y^n\left(i,j+\frac{1}{2},k\right)}{\Delta z(i,j,\mathrm{k})}-\right.\\&\left.\frac{E_z^n\left(i,j+1,k+\frac{1}{2}\right)-E_z^n\left(i,j,k+\frac{1}{2}\right)}{\Delta y(i,j,\mathrm{k})}\right]\end{aligned} \tag{14}$$

$$\begin{aligned}&H_z^{n+1/2}(i+\frac{1}{2},j+\frac{1}{2},k)=H_z^{n+\frac{1}{2}}(i+\frac{1}{2},j+\frac{1}{2},k+1)+\Delta z(i,j,1)\times\\&\left[\frac{H_x^{n+1/2}\left(i+1,j+\frac{1}{2},k+\frac{1}{2}\right)-H_x^{n+1/2}\left(i,j+\frac{1}{2},k+\frac{1}{2}\right)}{\Delta x(i,j,1)}+\right.\\&\left.\frac{H_y^{n+1/2}\left(i+1,j+\frac{1}{2},k+\frac{1}{2}\right)-H_y^{n+1/2}\left(i+\frac{1}{2},j,k+\frac{1}{2}\right)}{\Delta y(i,j,1)}\right]\end{aligned} \tag{15}$$

III. EXAMPLES

To test the effectiveness of the improved method, homogeneous half-space models and anomalous models with 3D bodies are designed. All models have 117×117×58 grids. The grid is non-uniform with a smallest spacing of 10 m and a largest spacing of 120 m. The transmitting coil is located at the center of the model with a 120 m height, the radius is 7.5 m. The transmitting current is 30 A. The receiving coil is 130 m away from the transmitting coil with a height of 60 m. The electrical conductivity is set as 10 S/m and k=1. In Fig. 1, the responses with different roughness parameters are compared.

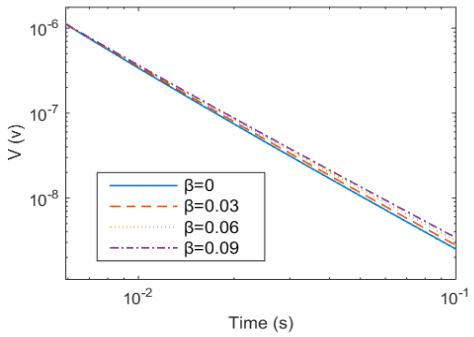

Fig. 1. The induced voltage with different roughness parameters.

The roughness parameter is set as 0, 0.03, 0.06 and 0.09. From Fig. 1 we can find that the induced voltage decay slowly as the increase of β which have indicated the improved method can model electromagnetic sub-diffusion efficiently. To verify the precision of the FDTD method, the FDTD solutions are compared with the numerical solutions calculated by integral method [18] in Fig. 2. The roughness parameters are chosen as 0.2 and 0.9. Figure 2 (a) shows the comparison of the two solutions and the relative errors responsibly when β=0.2. We can find the two solutions coincide well with a max relative error of 2.6%. Figure 2 (b) shows the comparison and the relative errors responsibly when β=0.9. The relative errors are less than 1.6% in 10 ms. The electromagnetic responses in the air with different roughness parameters are shown in Fig. 3.

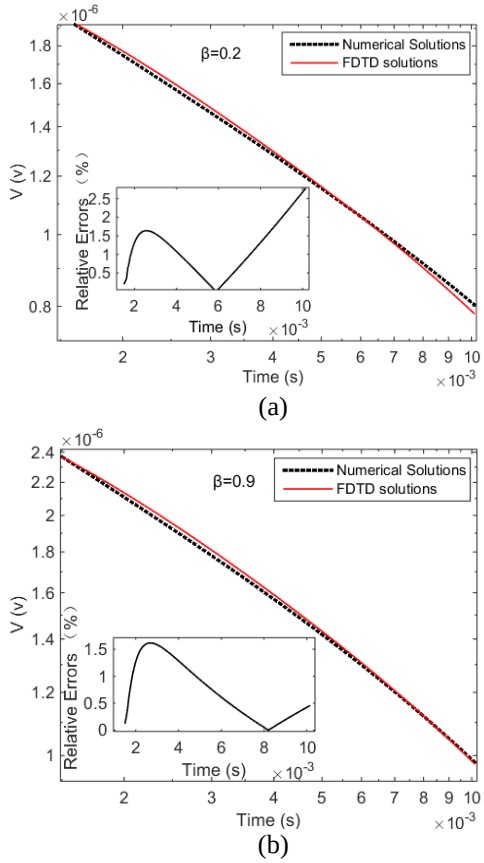

Fig. 2. The comparison of FDTD solutions and numerical solutions and the relative errors when: (a) β=0.2 and (b) β=0.9.

According to the definition of the generalized electrical conductivity, the conductivity varies with time, so the roughness parameter doesn't affect the diffusion pattern of electromagnetic wave. Accordingly, the responses decay slowly with the increase of roughness parameter.

The anomalous model is designed as Fig. 4. The roughness parameter is 0.7. The depth of the 3D body is 100 m, the size of the body is 410 m×410 m×450 m and is set in the center of x-y plane. The conductivity of the body is 100 S/m and the conductivity of the background is 5 S/m. The slices of electromagnetic responses of 1.5 ms and 5 ms are shown in Fig. 5. From these slices we can find that the responses can reflect the information of the 3D body well, which has verified the effectiveness of the improved method well again.

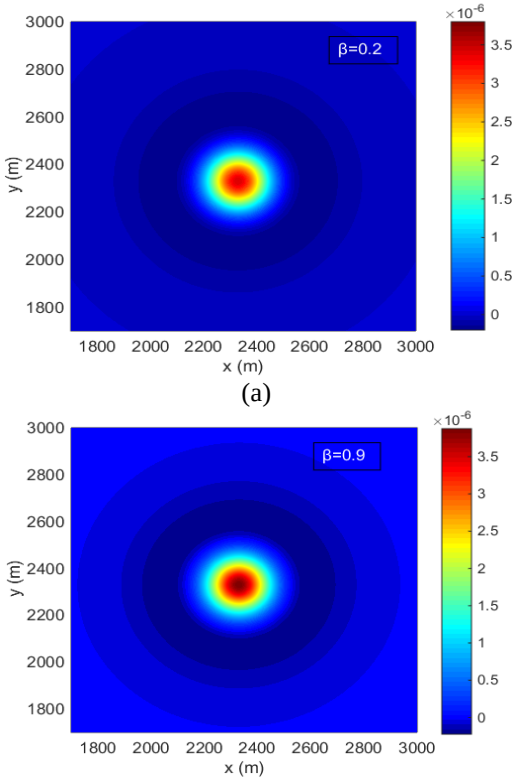

Fig. 3. The electromagnetic responses in the air with different roughness parameters: (a) β=0.2 and (b) β=0.9.

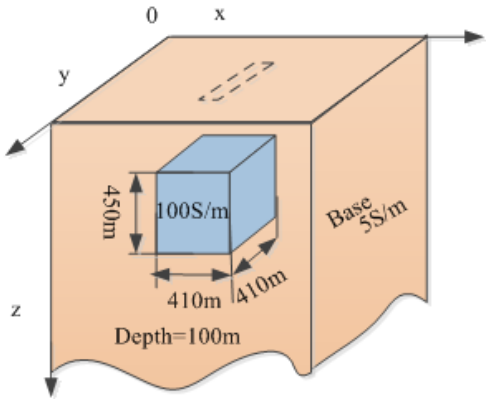

Fig. 4. Anomalous model with single 3D body.

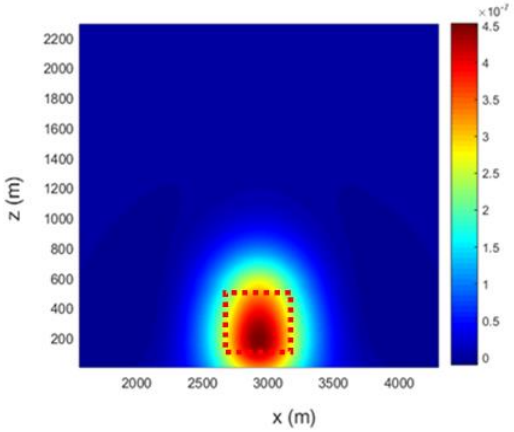

(a)

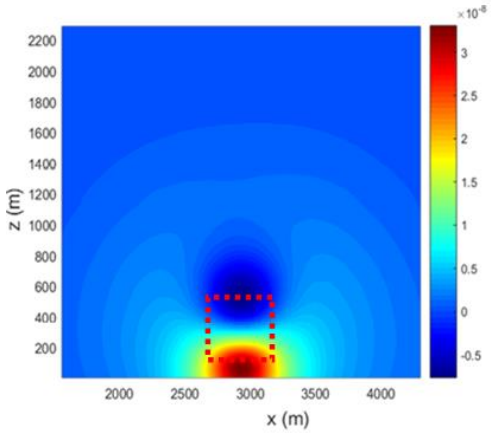

(b)

Fig. 5. The slices of electromagnetic responses at the time of: (a) 1.5 ms and (b) 5 ms.

IV. CONCLUSIONS

We have introduced roughness parameter in the expression of electrical conductivity. After the discretization of the fractional item we got the iterative formulation of electric field based on FDTD. The modeling results validated the effectiveness of the improved method in the modeling of electromagnetic sub-diffusion. As the discretization of the fractional item involved electric fields of every time-step, large memory needed consequently. For high-resistance models, as more time-steps divided, the method may be limited by the computer's storage. How to reduce the memory consumption is the focus of our following research.

ACKNOWLEDGMENT

This study was supported by the National Natural Science Foundation of China (41674109). The authors also thank the members of the project committee for their help.

REFERENCES

[1] Y. Shao and S. Wang, "Truncation error analysis of a pre-asymptotic higher-order finite difference scheme for Maxwell's equations," *ACES Journal*, vol. 30, no. 2, 2015.

[2] B. Mukherjee, "Numerical solution in FDTD for absorbing boundary condition over dielectric surfaces," *J. Adv. Res. Sci. Comput., IASR* 4.1: 13-23, 2012.

[3] B. Mukherjee and D. K. Vishwakarma, "Application of finite difference time domain to calculate the transmission coefficient of an electromagnetic wave impinging perpendicularly on a dielectric interface with modified MUR-I ABC," *Defence Science Journal*, vol. 62.4, pp. 228-235, 2012.

[4] Y. Ji and X. Zhao, "Reduction of electromagnetic reflections in 3D airborne transient electromagnetic modeling: Application of the CFS-PML in source-free media," *International Journal of Antennas and Propagation*, 2018.

[5] M. E. Everett, "Transient electromagnetic response of a loop source over a rough geological medium," *Geophysical Journal International*, vol. 177, pp. 421-429, May 2009.

[6] C. J. Weiss and M. E. Everett. "Anomalous diffusion of electromagnetic eddy currents in geological formations," *Journal of Geophysical Research*, vol. 112, B08102, 2007.

[7] A. Guellab and W. Qun, "High-order staggered finite difference time domain method for dispersive Debye medium," *ACES Journal*, vol. 33, no. 4, 2018.

[8] G. Gao, H. Sun, and Z. Sun, "Stability and convergence of finite difference schemes for a class of time-fractional sub-diffusion equations based on certain super convergence," *Journal of Computational Physics*, vol. 280, pp. 510-528, 2015.

[9] J. Ge, M. E. Everett, and C. J. Weiss, "Fractional diffusion analysis of the electromagnetic field in fractured media-Part I: 2D approach," *Geophysics*, vol. 77, no.4, pp.213-218, 2012.

[10] J. Ge, M. E. Everett, and C. J. Weiss, "Fractional diffusion analysis of the electromagnetic field in fractured media-Part 2: 3D approach," *Geophysics*, vol. 80, no. 3, pp. 175-185, 2015.

[11] A. A. Alikhanov, "A new difference scheme for the time fractional diffusion equation," *Journal of Computational Physics*, vol. 280, pp. 424-438, 2015.

[12] M. Dehghan, M. Safarpoor, and M. Abbaszadeh, "Two high-order numerical algorithms for solving the multi-term time fractional diffusion-wave equations," *Journal of Computational and Applied*

Mathematics, vol. 290, pp. 174-195, 2015.

[13] X. Zhao, Z. Sun, and G. E. Karniadakis, "Second-order approximations for variable order fractional derivatives: Algorithms and applications," *J. Computat. Phys.*, vol. 293, pp. 184-200, 2015.

[14] M. Dong, A. Zhang, J. Chen, S. Zhang, and Y. He, "The fourth-order one-step leapfrog HIE-FDTD method," *ACES Journal*, vol. 31, no. 12, 2016.

[15] T. Wang, "FDTD simulation of EM wave propagation in 3-D media," *Geophysics*, vol. 61, no. 1, pp. 110-120, 1996.

[16] T. Wang and G. W. Hohmann, "A finite-difference, time-domain solution for 3-dimensional electromagnetic modeling," *Geophysics*, vol. 58, no. 6, pp. 797-809, 1993.

[17] K. S. Yee, "Numerical solution of initial boundary value problems involving Maxwell's equations in isotropic media," *IEEE Transactions on Antennas & Propagation*, vol. 14, no. 3, pp. 302-307, 1966.

[18] D. Guptasarma, "Computation of the time-domain response of a polarizable ground," *Geophysics*, vol. 47, no. 11, pp. 1574-1576, 1982.

The Direction Switching Control of Electromagnetic Waves Based on All-dielectric Metamaterials

Yanan Hua, Kejian Chen*, Yanjun Fu, and Xiaofan Zhang

Shanghai Key Lab of Modern Optical System
Engineering Research Center of Optical Instrument and System, Ministry of Education
University of Shanghai for Science and Technology, 516Jungong Road, Shanghai 200093, China
*ee.kjchen@gmail.com

Abstract ─ Electromagnetic waves control is becoming more and more urgent for important applications in communication and military fields. Studies have shown that it is possible to achieve reflection and refraction control of electromagnetic waves by introducing phase gradient. Wavefront control of electromagnetic waves can be achieved with metamaterials devices. However, metamaterials devices have to be diversified and enhance their capabilities to catch up the rapidly expanding demand on dynamic control currently. In this paper, we design a dynamic-modulated all-dielectric microwave control device to reconstruct the phase profile by filling different dielectric constants of media into it. As a result, the deflection direction of the electromagnetic waves, including whether the deflection occurs or not, can be controlled by this device flexibly. The device with such dynamic modulation function has potential application in the design and development of other functional devices or system, such as switches, beam shaping and imaging systems.

Index Terms ─ All-dielectric metamaterials, beam shaping, dynamic switching.

I. INTRODUCTION

With the development of science and technology, research on electromagnetic waves control has become more and more significant. There are broad research and application prospects for the wavefront control of electromagnetic waves in imaging, stealth technology, communication technology, electromagnetically induced transparency [1-7], and so on. In recent years, the complete control of the phase, amplitude, and polarization direction of the refracted or reflected electromagnetic waves are studied extensively [8-10]. The amplitude and phase of the electromagnetic waves can be flexibly modulated by the different metamaterial structures and the distribution of the metamaterial unit cells [11-13]. Metamaterials are widely applied to functional electromagnetic waves devices because of their singular characteristics and have made great progress in practical applications in the field of microwaves. 3D all-dielectric metamaterials devices have attracted lots of interests since the development of 3D printing technology has been maturing [14-17]. Wavefront control devices fabricated by all-dielectric materials have attracted widespread attention for its advantages of low absorption and less expensive, compared with those based on the metal material. A series of electromagnetic waves control devices that used as beam steering devices or lens have been designed [18-20]. Dynamic metamaterials devices are more versatile and flexible compared with normal metamaterials devices to fulfill the demands in the imaging systems, communication systems [21-22]. Part or all areas are filled with dynamically changing materials in metamaterials devices that can enable the devices to be reconfigurable or adjustable, which will be suitable for more demanding applications. Compared to natural materials, all-dielectric metamaterials can achieve arbitrary effective dielectric constants by designing structure or mixing different dielectric constant natural materials in a set of proposed ratios to fulfill the requirements of the control the electromagnetic waves [2,23].

Based on generalized Snell's law, dynamic wavefront control can be achieved by reconstructing the phase profile of metamaterials. In this paper, an all-dielectric microwave control device has been designed to realize dynamic wavefront control. Any phase between 0 to 2π can be achieved by the proposed metamaterial unit cells, which enables the dynamic control of electromagnetic waves that has potential applications in microwave beam shaping and imaging.

II. DESIGN AND SIMULATION OF UNIT CELL STRUCTURE

Reflection and refraction occur when electromagnetic waves are incident on the interface of the medium [8, 24]. It is known from generalized Snell's law that modulation of electromagnetic waves can be achieved

Submitted On: January 23, 2019
Accepted On: May 12, 2019

by introducing a gradient phase at the interface. The generalized refractive law formula is as follows:

$$\sin(\theta_t)\, n_t - \sin(\theta_i)\, n_i = \frac{\lambda_0}{2\pi}\frac{d\Phi}{dx}, \quad (1)$$

Where θ_i , θ_t are the incident and refractive angle, n_i and n_t are the refractive indexes of the two media, respectively, $d\Phi$ is the phase gradient of the two intersections formed by the two optical paths and the interface, dx is the distance between the two intersections, λ_0 is the wavelength of light in vacuum.

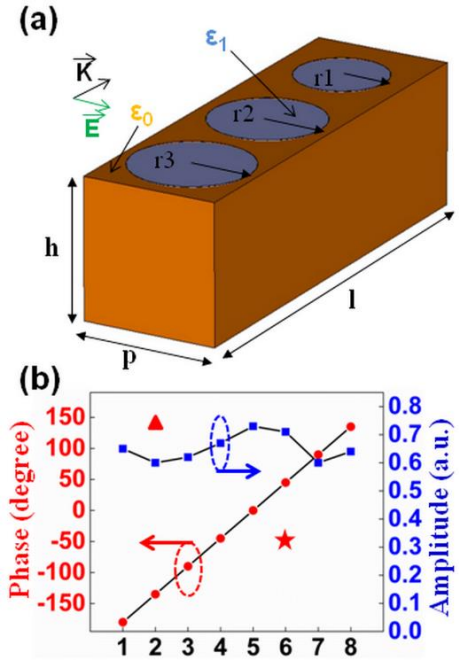

Fig. 1. (a) Schematic diagram of the unit cell (TCCH). (b) Calculated phase shift and amplitude from eight unit cells at 21 GHz. When ε_1=1, the square and circle represent the amplitude and phase of the eight basic unit cells respectively. When ε_1=2.25, the phase of Unit_2 is switched from -135° to 135° marked as triangle (▲). When ε_1=1.44, the phase of Unit_6 is switched from 45° to -45° marked as pentagram (★).

In order to obtain the phase that can achieve wavefront control, a new subwavelength metamaterials which consists of three combined circular holes (TCCH) is proposed in this paper, as shown in Fig. 1 (a). Three circular holes are designed on the top of the structure to be filled with different media. The material of the structure is nylon (its dielectric constant ε= 3.6 and loss tangent δ = 0.026) and the medium in the circular holes is air (ε_1= 1). According to the relationship between velocity of light c, wavelength λ and frequency v, which is shown as the formula (2):

$$\lambda = \frac{c}{v}, \quad (2)$$

To design subwavelength metamaterials, the period of metamaterial structure has been set less than a wavelength, and its dimensions are as follows: the length, width and height are respectively l=25 mm, p=8 mm, h=8 mm, r1, r2, r3 represent the radius of three circular holes respectively. In this paper, we use the commercial software CST to study the relationship between radius and phase of metamaterials. The phase is determined by the volume ratios of the two different media in the unit structure, so a complete 0 to 2π phase change can be realized by changing the radius r of the circular holes, and the transmission intensity remains relatively stable. The radius of the three circular holes are not set equal to obtain a relatively large phase change as much as possible. Such an asymmetric structural design can reduce the influence of the reflection phase to achieve a large angle deflection of electromagnetic waves [25]. Then eight unit cells are obtained as shown in Table 1. The phase amplitude of eight unit cells is uniform and the step size is π/4, as shown in Fig. 1 (b). Last but not least, the TCCH is flexible and can be made by 3D printing simply.

Table 1: Geometric parameters of the eight TCCH unit cells at 21 GHz (ε_1= ε_{air}= 1)

Unit	1	2	3	4	5	6	7	8
Phase (degree)	-180	-135	-90	-45	0	45	90	135
r1 (mm)	1.9	1.86	2.18	2.22	2.66	3.47	0.4	1
r2 (mm)	1.5	1.5	2	3	3.3	3.2	0.4	1.5
r3 (mm)	2	3	3.5	3.5	3.5	3.5	0.8	1.5

Metamaterials are effective EM media with arbitrary dielectric constants, and the effective dielectric constant determines the phase. For dynamitic control, it is necessary to introduce phase transition based on the existing structure to realize the reconfigurable and adjustable functions of the device. The relationship of the effective dielectric constant ε, the dielectric constant of different materials ε_a, ε_b, and their volume filling rate V is shown as the following formula [2]:

$$\varepsilon = \varepsilon_a * V + \varepsilon_b * (1 - V), \quad (3)$$

As mentioned above, two different methods can be adopted to reconstruct the phase as we desired. One is to mix materials with different dielectric constants at a specific ratio to obtain a specific dielectric constant, the other is to print structures at different filling rates through 3D printing technology. For instance, when the medium (ε_1=2.25) is filled into the circular holes of unit with initial phase -135°, a new phase 135° can be obtained as shown in Fig. 1 (b). Similarly, while the medium (ε_1=1.44) is filled into the circular holes of the unit with initial phase 45°, a new phase -45° can be obtained. The transmission amplitude remains relatively

stable during this process. Therefore, the purpose of reconfiguring phase can be achieved by filling media of different dielectric constants into circular holes.

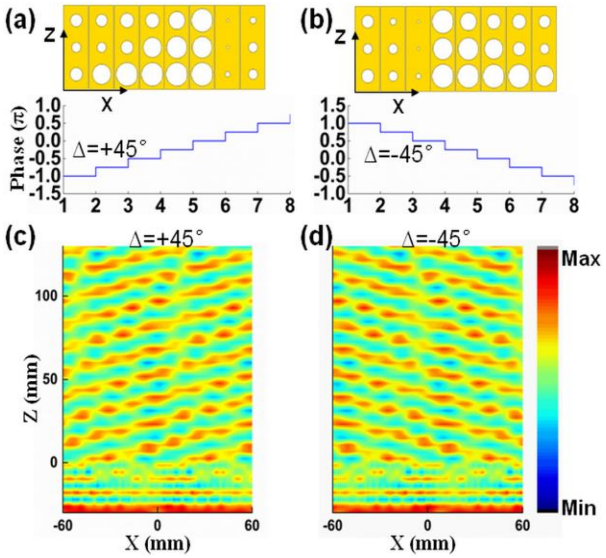

Fig. 2. Eight unit cells with different geometric parameters provide increased phase gradient (a), or provide decreased phase gradient (b). Electric field distribution in the XOZ plane according to a phase gradient of +45° (c) and -45° (d) at 21 GHz.

So as to prove the above generalized law of refraction, a set of arrays based on a combined circular structure is designed. For example, we construct two arrays of cell devices with a phase gradient of 45° (or -45°) in a one-dimensional array, the incident wave is deflected into two different directions, respectively. Here, the eight basic structures we chose were made of nylon and air. Under the incident of electromagnetic waves in the x-polarization direction, the electric field distribution of the device in the XOZ plane is as shown in Fig. 2. The simulation results demonstrate that the control of deflection of electromagnetic waves can be achieved by such devices based on TCCH structures properly.

III. SWITCHABLE CONTROL OF ELECTROMAGNETIC WAVES

In order to achieve dynamic control, such metamaterials devices are improved by inducing phase transition on the unit structures. What has been proved that when the media are filled into the cell structure, the phase can be reconstructed without changing the size of the cell structure [26]. Here, two basic units (Unit_2 and Unit_6) in Table 1 with phase -135° and 45° are selected to reconstruct their phases. As mentioned above, new phases (135° and -45°) can be obtained by filling media with different dielectric constants into the circular holes of Unit_2 (phase -135°) and Unit_6 (phase 45°), respectively. Based on the above conclusions, four coded particles "1", "2", "3", "4" are used to stand for the phases of the transmitted waves of -135°, 135°, -45°, and 45°. In particular, the phase 135° and -45° are reconstructed from the phase -135° and 45°, respectively. To mimic periodic boundary conditions, each of the code phases is on behalf of a super subunit consisting of 3*3 identical basic unit phases, which minimizes EM coupling between devices with different geometric parameters [13, 27]. Four sequences are designed with two basic coded particles. They are S1 (1144), S2 (2134), S3 (1243), S4 (without phase gradient) which are composed of 36*36 particles. In the simulation, the boundary in the X, Y and Z directions is set to the open space boundary condition. Then the X-direction polarized wave is incident along the Z perpendicular to the designed device surface. We observe that when the device is arranged according to the basic sequence S1, the 3D far-field scatter plot shows that the normal incident wave is split into two symmetrically distributed beams along the Z-axis, as shown in Fig. 3. It can be seen that two main lobes are symmetrically distributed on both sides of the Z-axis. For the purpose of better visualizing this phenomenon, the two-dimensional scattering pattern in the polar coordinate system and the electric field distribution are given as well. It should be noted that the incident direction of the 3D far-field scatter plot (Fig. 3 (c)) is opposite to that of the electric field distribution diagram (Fig. 3 (d)).

Modulating the phase by filling the media into the super subunits of the first and third columns of S1, we can get the sequence S2 (2134), the phases from left to right are 135°, -135°, -45°, and 45°, respectively. The 3D far-field scatter plot shows that the beam which has just been split into two symmetric distributions along the Z-axis is now suppressed on one side. This phenomenon is also observed in the two-dimensional scattering mode in the polar coordinate system. The electric field distribution is able to clearly observe the deflection of electromagnetic waves. Similarly, modulating the phase by filling the media into the super subunits of the second and fourth columns of S1, we can get the sequence S3 (1243), the phases from left to right are -135°, 135°, 45°, and -45°, respectively. We can observe the opposite phenomenon in S2. But when all the super subunits are filled with the media which have the same dielectric constant as substrate, the sequence S4 can be obtained. Then the phase gradient and the deflection of the electromagnetic waves disappear and the device is equivalent to a transparent window. These four functional devices selected for demonstration are based on the evolution of the two basic unit phases. Therefore, different gradient phase sequences can be constructed based on a set of basic sequences by filling different media into the super subunit structure, so as to control

the deflection direction of electromagnetic waves dynamically.

The method used in this paper for the design of devices is as same as those in the papers which is already proved effective by experiments [20,25,27-29], so the devices we designed in this paper can also be functional through specific fabrication methods, for example 3D printing.

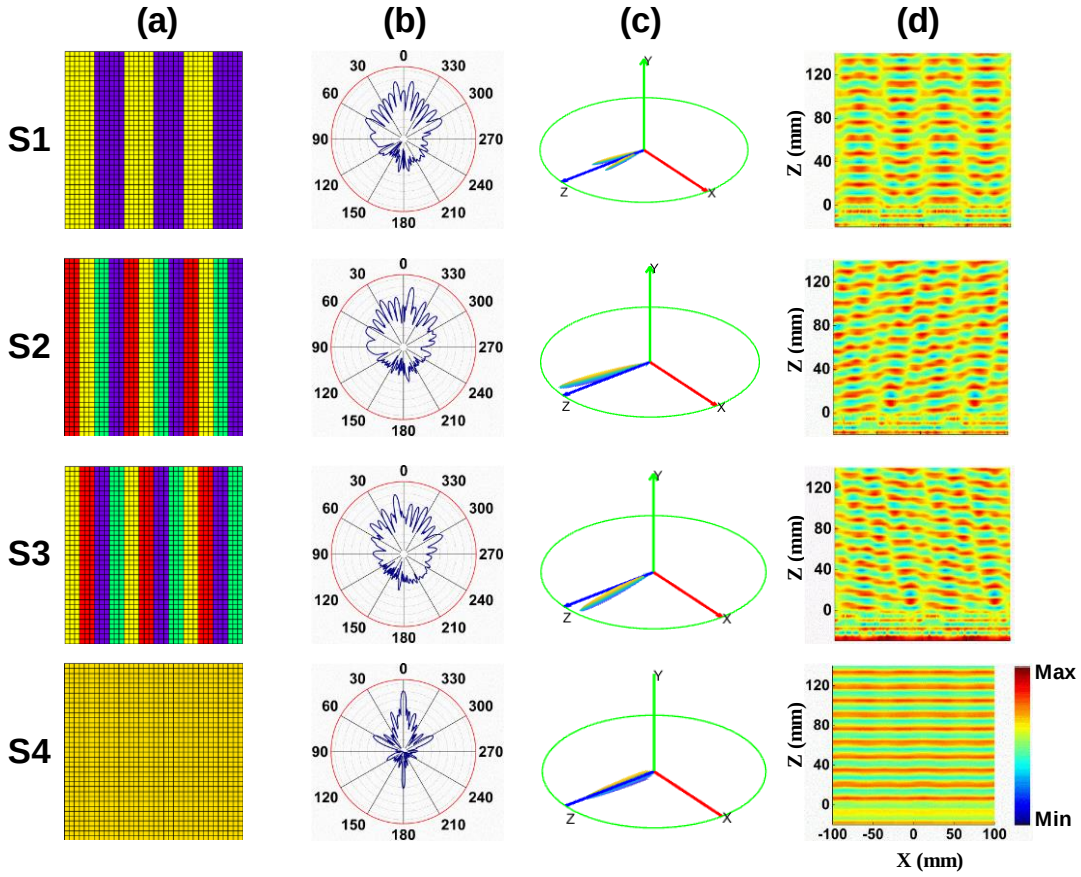

Fig. 3. Geometries of the four sequences and corresponding 2D circular coordinate scattering modes, 3D scattering patterns, and electric field phase distribution of the XOZ plane that are numerically simulated by CST. From top to bottom, S1, S2, S3, and S4 respectively. (a) Schematic representation of four sequences. (b) The 2D circular coordinate scattering modes of four sequences indicating different transmission angles clearly (in logarithmic coordinates). (c) The 3D far-field scattering patterns of four sequences (in linear coordinates). (d) Electric field distribution in the XOZ plane of four sequences.

IV. CONCLUSION

In conclusion, an all-dielectric functional device has been designed which enables dynamic wavefront control. The phase of unit cells can be reconstructed by filling different media into circular holes. Four different filling modes are demonstrated to prove that the proposed device can control the deflection direction of the electromagnetic waves, flexibly. Therefore, the all-dielectric metamaterials devices proposed in this paper are low-cost and can be easily printed by 3D printing. The method of dynamic modulation can be freely applied to many devices in the fields for imaging, communications and signal modulation.

ACKNOWLEDGMENT

This work was supported by the National Natural Science Foundation of China (No. 61205095), the Shanghai Young College Teacher Develop funding schemes (No. slg11006). The authors gratefully acknowledge Prof. T. J. Cui and Dr. S. Liu from Southeast University for the discussion on simulation method.

REFERENCES

[1] Q. Zhou, P. Liu, D. Yu, L. Bian, and C. Liu, "Field-controlled switchable frequency selective surface with broadband absorption characteristic," *Iet*

Microwaves Antennas & Propagation, 2018.

[2] L. Yin, J. Doyhamboure-Fouquet, X. Tian, and D. Li, "Design and characterization of radar absorbing structure based on gradient-refractive-index metamaterials," *Composites Part B: Engineering*, pp. 178-187, 2018.

[3] C. M. Watts, X. Liu, and W. J. Padilla, "Metamaterial electromagnetic wave absorbers," *Advanced Materials*, pp. OP98-OP120, 2012.

[4] J. A. Dockrey, M. J. Lockyear, S. J. Berry, S. A. R. Horsley, J. R. Sambles, and A. P. Hibbins, "Thin metamaterial Luneburg lens for surface waves," *Physical Review B Condensed Matter*, pp. 951-957, 2013.

[5] J. Zhou, J. Wang, K. Guo, F. Shen, Q. Zhou, Y. Zhiping, and Z. Guo, "High-efficiency terahertz polarization devices based on the dielectric metasurface," *Superlattices and Microstructures*, pp. 75-81, 2018.

[6] K. Chen, Y. Wang, J. Liu, Y. Bai, T. Bu, B. Cai, Y. Zhu, and S. Zhuang, "Polarization dependent dual-band EIT-like effect and its application in THz range," *Optics Communications*, pp. 69-73, 2016.

[7] Y. Bai, K. Chen, H. Liu, T. Bu, B. Cai, X. Jian, and Y. Zhu, "Optically controllable terahertz modulator based on electromagnetically-induced-transparency-like effect," *Optics Communications*, pp. 83-89, 2015.

[8] N. Yu, P. Genevet, M. A. Kats, F. Aieta, J. P. Tetienne, F. Capasso, and Z. Gaburro, "Light propagation with phase discontinuities: Generalized laws of reflection and refraction," *Science*, pp. 333-337, 2011.

[9] L. Liu, X. Zhang, M. Kenney, X. Su, and N. Xu, "Broadband metasurfaces with simultaneous control of phase and amplitude," *Advanced Materials*, pp. 5031-5036, 2014.

[10] D. Jia, Y. Tian, W. Ma, X. Gong, J. Yu, G. Zhao, and X. Yu, "Transmissive terahertz metalens with full phase control based on a dielectric metasurface," *Optics Letters*, pp. 4494-4497, 2017.

[11] Q. Zhang, M. Li, T. Liao, and X. Cui, "Design of beam deflector, splitters, wave plates and metalens using photonic elements with dielectric metasurface," *Optics Communications*, pp. 93-100, 2018.

[12] Z. Guo, L. Zhu, F. Shen, H. Zhou, and R. Gao, "Dielectric metasurface based high-efficiency polarization splitters," *Rsc. Advances*, pp. 9872-9879, 2017.

[13] X. Bie, X. Jing, Z. Hong, and C. Li, "Flexible control of transmitting terahertz beams based on multilayer encoding metasurfaces," *Applied Optics*, 2018.

[14] W. X. Jiang, S. Ge, T. Han, S. Zhang, M. Q. Mehmood, C. W. Qiu, and T. J. Cui, "Shaping 3D path of electromagnetic waves using gradient-refractive-index metamaterials," *Adv. Sci*., 2016.

[15] Y. Xie, S. Ye, C. Reyes, P. Sithikong, B. I. Popa, B. J. Wiley, and S. A. Cummer, "Microwave metamaterials made by fused deposition 3D printing of a highly conductive copper-based filament," *Applied Physics Letters*, pp. 788-792, 2017.

[16] H. Yi, S. W. Qu, K. Ng, C. Chan, and X. Bai, "3D printed millimeter-wave and terahertz lenses with fixed and frequency scanned beam," *IEEE Transactions on Antennas & Propagation*, pp. 442-449, 2016.

[17] H. F. Ma and T. J. Cui, "Three-dimensional broadband and broad-angle transformation-optics lens," *Nature Communications*, 2010.

[18] T. Ding, J. Yi, H. Li, H. Zhang, and S. N. Burokur, "3D field-shaping lens using all-dielectric gradient refractive index materials," *Scientific Reports*, 2017.

[19] J. Yi, S. N. Burokur, G. P. Piau, and A. D. Lustrac, "3D printed broadband transformation optics based all-dielectric microwave lenses," *Journal of Optics*, 2016.

[20] J. Yi, S. N. Burokur, G. Piau, and A. D. Lustrac, "Coherent beam control with an all-dielectric transformation optics based lens," *Sci. Rep*., 2016.

[21] C. Li, J. Wu, S. Jiang, R. Su, C. Zhang, C. Jiang, G. Zhou, B. Jin, L. Kang, and W. Xu, "Electrical dynamic modulation of THz radiation based on superconducting metamaterials," *Applied Physics Letters*, 2017.

[22] J. M. Manceau, N. H. Shen, M. Kafesaki, C. M. Soukoulis, and S. Tzortzakis, "Dynamic response of metamaterials in the terahertz regime: Blueshift tunability and broadband phase modulation," *Applied Physics Letters*, 2010.

[23] E. E. Narimanov and A. V. Kildishev, "Optical black hole: Broadband omnidirectional light absorber," *Applied Physics Letters*, pp. 041106-041103, 2009.

[24] K. Tan, C. Liang, and X. Shi, "Optic eikonal, Fermat's principle and the least action principle," *Science in China Series G: Physics, Mechanics and Astronomy*, pp. 1826-1834, 2008.

[25] J. Li, C. Shen, A. Díazrubio, S. A. Tretyakov, and S. A. Cummer, "Systematic design and experimental demonstration of bianisotropic metasurfaces for scattering-free manipulation of acoustic wavefronts," *Nature Communications*, 2018.

[26] P. C. Wu, W. Zhu, Z. X. Shen, P. H. J. Chong, W. Ser, D. P. Tsai, and A.-Q. Liu, "Broadband wide-angle multifunctional polarization converter via liquid-metal-based metasurface," *Advanced Optical Materials*, 2017.

[27] S. Liu, T. J. Cui, Z. Lei, X. Quan, W. Qiu, W.

Xiang, Q. G. Jian, X. T. Wen, Q. Q. Mei, and G. H. Jia, "Convolution operations on coding metasurface to reach flexible and continuous controls of terahertz beams," *Advanced Science*, 2016.

[28] M. Wei, Q. Xu, Q. Wang, et al., "Broadband non-polarizing terahertz beam splitters with variable split ratio," *Applied Physics Letters*, vol. 111, no. 7, p. 071101, 2017.

[29] C. Pfeiffer, N. K. Emani, A. M. Shaltout, et al., "Efficient light bending with isotropic metamaterial huygens' surfaces," *Nano Letters*, vol. 14, no. 5, pp. 2491-2497, 2014.

Yanan Hua received the B.S. degree in Optical Information Science and Technology from Nanjing University of Information Science and Technology (NUIST), Nanjing, China, in 2012. In 2016, she began her M.S. degree in University of Shanghai for Science and Technology (USST). Her research interests include Electromagnetic metamaterials, and 3D printing technology.

Kejian Chen is an Associate Professor at University of Shanghai for Science and Technology (USST). He received his B.S. and MPhil. degrees from Zhejiang University, in 2001 and 2004. After completing his Ph.D. in Electronic Engineering in 2009 at The Chinese University of Hong Kong, he worked in Shougang Concord Technology Holdings Limited and the was involved in research efforts at USST from 2011. His research interests include metamaterials; 3D/4D printing and sensors; semiconductor optoelectronic devices, as well as terahertz technologies.

Yanjun Fu received the B.S. degree from Nanjing University of Posts and Telecommunications (NJUPT) in 2017. Since 2017, she became a postgraduate in University of Shanghai for Science and Technology (USST). Her research interests include 4D printing, and shape memory materials.

Xiaofan Zhang began her B.S. degree in University of Shanghai for Science and Technology (USST) in 2013. After graduating from the Department of Electro-Optical Engineering, she went on to study for M.S. degree there. Her research interests include metamaterials absorption, and optical fiber transmission.

A Dual-band WLAN Antenna with Reactive Loading

Yinfeng Xia [1], Wei Xue [1], Yingsong Li [1,2,*], and Lei Zhao [3]

[1] College of Information and Communication Engineering
Harbin Engineering University, Harbin, Heilongjiang 150001, China
*liyingsong@ieee.org

[2] Key Laboratory of Microwave Remote Sensing, National Space Science Center
Chinese Academy of Sciences, Beijing 100190, China

[3] School of Information and Control Engineering
China University of Mining and Technology, Xuzhou 221116, China

Abstract ─ Dual-band antenna is very essential for multiple band communication systems like wireless local area network (WLAN) with lower and upper operating bands. In this paper, a dual-band antenna is proposed and analyzed for the WLAN applications. The proposed antenna fed by coplanar waveguide (CPW) consists of an L-shaped, reversed L-shaped strips and two inverted U-shaped loadings that are to implement the reactive characteristics. The reactive loadings can adjust the bandwidth and performance of the dual-frequency WLAN antenna that is verified by the simulation and measurement, respectively. The results demonstrate that the -10dB impedance bandwidth of the proposed dual-band antenna can cover the two WLAN frequency bands from 2.4 GHz to 2.484 GHz and from 5.15 GHz to 5.35 GHz, respectively. Moreover, the proposed antenna has omnidirectional radiation patterns at the two operating bands.

Index Terms ─ Dual-band, reactive loading, WLAN.

I. INTRODUCTION

With the increasing contribution and growing of wireless communication technology, more and more communication systems are created for various purpose. To meet these requirements, the modern communication systems are constructed to support more than one frequency band such as mobile communication and the wireless local area network (WLAN) communication systems. Thus, single-band antenna cannot be able to satisfy the requirement of the modern wireless communication system with more than one operating band. As a straightforward approach to solve these problems, dual-band antenna has been widely developed and considered for different purpose application for various terminals, which can reduce the cost of design and enhance the performance of the entire communication system [1].

A dual-band wireless communication system like WLAN has attracted more and more attention for researchers to study due to its high date transmission rate in short and mobility areas [2, 3]. Furthermore, the WLAN system has been used for a long time, which operates at two frequency band to meet the application according to the IEEE 802.11 a/b/g/n/ac standards. Thus, it is vital for us to design a dual-band WLAN antenna.

So far, many dual-band WLAN antennas have been proposed. Generally, the previous designed dual-band WLAN antennas are realized by carving slots or adding the parasitic branches to achieve dual-band characteristics. In [4-11], dual-band slots antennas are reported and investigated. In [12-19], the dual-band antennas are designed using parasitic branches. However, some of these antennas are large or other antennas are complex in structure. In [20], a compact asymmetric coplanar strip-fed dual-band antenna for 2.4/5.8 GHz WLAN applications is proposed and measured. Two loaded capacitance terminations are utilized to reduce the size of the antenna. But the structure of the proposed antenna is too complex, and the gain is very low.

In this paper, a dual-band antenna with reactive loading for WLAN applications is proposed and investigated by using simulation and measurement. The proposed antenna fed by coplanar waveguide (CPW) is composed of an L-shaped, reversed L-shaped strips and two inverted U-shaped branches. Two inverted U-shaped branches are loaded to the L-shaped, reversed L-shaped strips to form the coupling capacitors to reduce the size of the WLAN antenna. The coupling capacitor depends on the gap between the inverted U-shaped branches and the L-shaped or the reversed L-shaped strip. By adjusting the gap and the length of the U-shaped branches, the operating band can be flexibly controlled. The results present that the dual-band antenna can operate at 2.43

Submitted On: January 28, 2019
Accepted On: April 12, 2019

GHz with the bandwidth from 2.36 GHz to 2.5 GHz and 5.25 GHz with the bandwidth from 5.15 GHz to 5.35 GHz, which can cover the WLAN frequency bands. Moreover, the proposed antenna has omnidirectional radiation patterns at the two operating bands with simple and adjustable structure.

II. DESIGN OF THE PROPOSED DUAL-BAND WLAN ANTENNA

The geometry of the proposed antenna is described in Fig. 1, which is printed on a dielectric substrate with a relative permittivity of 4.4, a loss tangent of 0.02 and a thickness of h=1.6 mm. The designed dual-band WLAN antenna is fed by the CPW. The width of the feeding line and the gap between the feeding line and the ground can be calculated by the tool of coplanar waveguide calculation. From the calculation, the width s and the gap w are obtained and designed to be 1.4 mm and 0.3 mm, respectively.

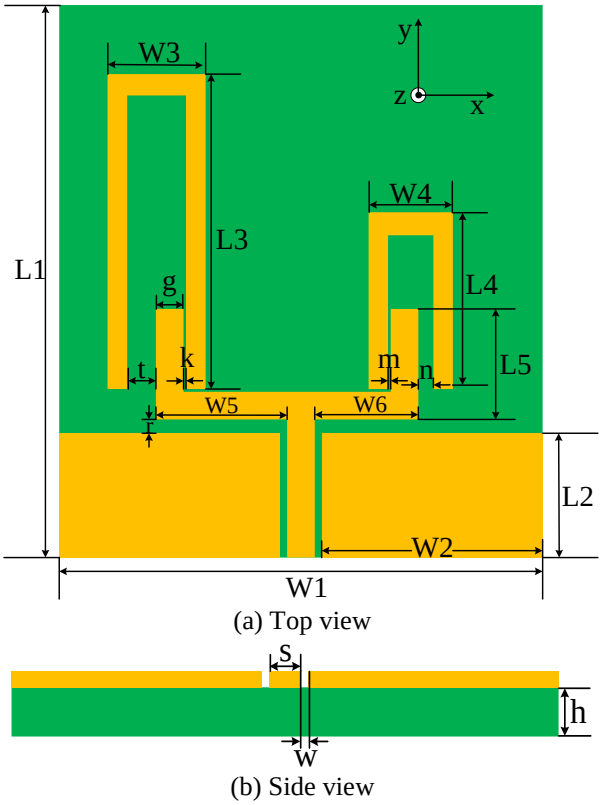

Fig. 1 Geometry structure of the proposed antenna.

To get the good impedance matching, the length L2 of the ground plane and the width of the L-shaped or the reversed L-shaped branch can be properly adjusted. In addition, the parameter r is also providing an important effect on the designed antenna. Thus, the performance can be adjusted by controlling the dimensions of the antenna for the lower and upper WLAN bands.

To better understand the principle of the designed dual-band antenna operating at the two WLAN bands, the equivalent circuit for each inverted U-shaped reactive loadings are given in the Fig. 2.

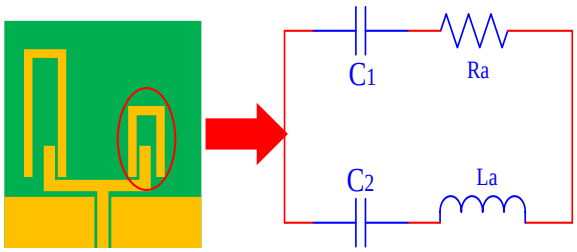

Fig. 2. Equivalent circuit of inverted U-shaped reactive loading.

The equivalent circuit of each inverted U-shaped reactive loading consists of two capacitors C1 and C2, an inductor La and a resistor Ra. Therefore, the resonance center frequency f can be calculated by considering the equivalent circuit, which is presented in formula (1) and (2):

$$2\pi f L_a = \frac{1}{2\pi f C_1} + \frac{1}{2\pi f C_2}, \quad (1)$$

where

$$f = \frac{1}{2\pi}\sqrt{\frac{1}{L_a}\left(\frac{1}{C_1}+\frac{1}{C_2}\right)}. \quad (2)$$

Thus, each frequency band of the designed antenna can be obtained by adjusting the La, C1 and C2. The values of C1 and C2 are depended on the coupling between the L-shaped or reversed L-shaped strip and the reactive loadings, namely the parameters L5, t, k, m, n. The value of La is obtained by the length of the strips and of the U-shaped loadings. In this design, the gaps between the (inverted) L-shaped strip and the loading can be regarded as equivalent capacitors, while the total effective length of the (inverted) L-shaped strip and the loading can be regarded as equivalent inductor. The dimensions of the devised antenna are obtained using the HFSS and are given in Table 1.

Table 1: Dimensions of the dual-band WLAN antenna (Unit: mm)

Parameters	W1	W2	W3	W4	W5	W6
Values	26	12	5.05	4.26	5.4	4.9
Parameters	r	g	m	n	t	k
Values	0.6	1.4	0.16	0.7	1.5	0.15
Parameters	L1	L2	L3	L4	L5	
Values	30	8	16.34	7.54	5	

Finally, the designed dual-band antenna can operate at the interested frequency bands by the optimization of

these dimensions, where the optimized dimensions are listed in the Table 1.

III. ANALYSISES AND EXPERIMENTAL RESULTS

The proposed dual-band WLAN antenna is analyzed based on the HFSS. To verify the analysis effectiveness, the designed dual-band WLAN antenna is fabricated and measured. The fabricated dual-band WLAN antenna is given in Fig. 3. The comparison of the simulated and measured reflection coefficients (S11s) is demonstrated in Fig. 4, where the measured S11 is obtained by using the Keysight PNA-X Microwave Network Analyzer N5244A.

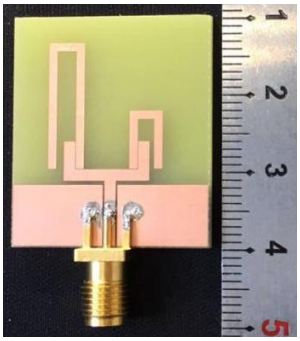

Fig. 3. Photograph of the fabricated dual-band WLAN antenna.

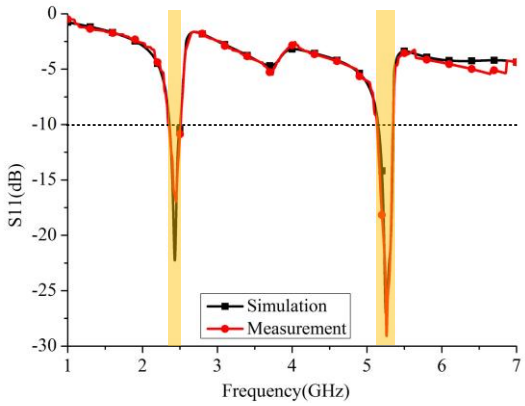

Fig. 4. S11 of the proposed dual-band antenna.

From Fig. 4, we can see that the dual-band antenna can operate well at the desired two frequency bands for WLAN applications. The lower band operates at 2.43 GHz with a -10dB impedance bandwidth of 140 MHz ranging from 2.36 GHz to 2.5 GHz to cover 2.4 GHz WLAN, and the upper band operates at 5.25 GHz with -10dB impedance bandwidth of 200 MHz ranging from 5.15 GHz to 5.35 GHz for serving for 5.25 GHz WLAN. The measurement result agrees well with the simulated S11, which helps to verify the effectiveness of the simulations. The discrepancies may be caused by the stability of the FR4 substrate, fabrication error and the soldering in the experiments. The 3D radiation patterns of the proposed dual-band antenna are presented in Fig. 5, while the measured radiation patterns of the proposed dual-band antenna are shown in Fig. 6. It can be found the designed antenna has omnidirectional radiation patterns at 2.43 GHz and 5.25 GHz.

For better understanding, the principle behind the designed dual-band antenna, the current distribution at 2.43 GHz and 5.25 GHz is given in Fig. 7. At 2.43 GHz, the current distribution focuses on the CPW signal feeding line, ground plane and the left U-shaped reactive loading, while the current distribution on the right reactive loading is very small. When the designed antenna operates at 5.25 GHz, the current distributed on the CPW structure and the right U-shaped reactive loading. From the current distributions, we can also see that the current distributions at the lower and upper bands are from different reactive loading, which is also depending on the resonance length of the two current paths.

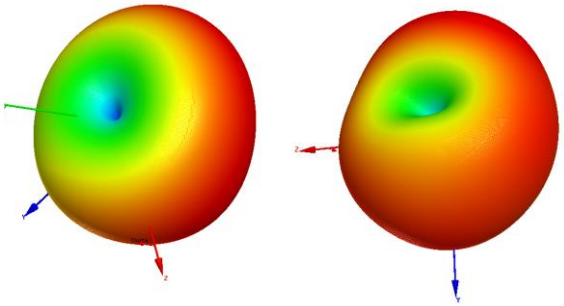

(a) 2.43 GHz (b) 5.25 GHz

Fig. 5. The simulated 3D radiation patterns of the proposed dual-band antenna.

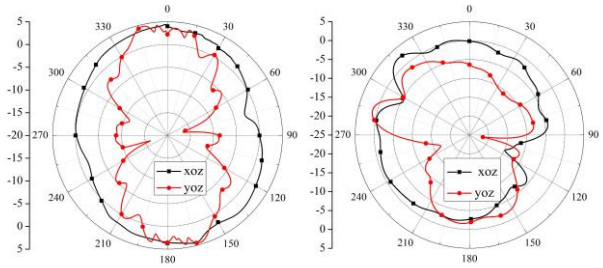

(a) 2.43 GHz (b) 5.25 GHz

Fig. 6. The measurement radiation patterns of the proposed dual-band antenna.

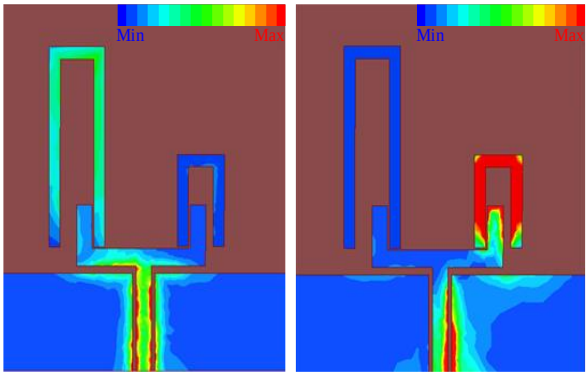

(a) 2.43 GHz (b) 5.25 GHz

Fig. 7. The current distribution of the proposed dual-band antenna.

To investigate the effects of the dimensions, the two key parameters L3 and L4 are selected to discuss their center controlling for the two frequency bands. Figure 8 demonstrates the effect of L3 on the impedance bandwidth of the proposed dual-band WLAN antenna. It is found that the center resonance frequency at lower band shifts to low frequency when we increase L3, while the resonance frequency of upper band is almost unchanged. Figure 9 shows the effect of L4 on the S11 of the proposed dual-band antenna. It can be concluded that the resonance frequency of upper band moves towards to low frequency with the increasing L4, while the resonance frequency at lower band is almost fixed.

In fact, it is easy to explain the effect of L3 and L4 on the center resonance frequency of the proposed dual-band antenna by using the formula (2). When the length of L3 and L4 are adjusted, the inductor La will be changed, while the capacitors C1 and C2 are unchanged because of the weak coupling. Hence, the center resonance frequency can be controlled by choosing the length of L3 and L4.

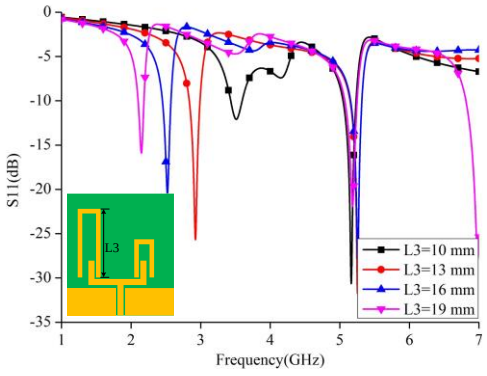

Fig. 8. Effect of L3 on the impedance of the proposed dual-band antenna.

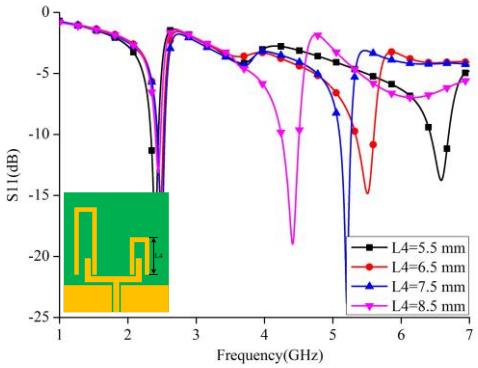

Fig. 9. Effect of L4 on the impedance of the proposed dual-band antenna.

The gain and the radiation efficiency are also essential for an antenna, which have been measured and presented in Table 2. The gain and the radiation efficiency measured are 4.95 dBi, 66% and 2.73 dBi, 72% at 2.43 GHz and 5.25 GHz respectively as shown in the Table 2. In order to know the advantage of the proposed dual-band antenna, we compare the proposed dual-band WLAN antenna and the previously reported dual-band WLAN antennas. The comparison for the resonance frequencies, size and gains of these antenna is presented in Table 3. From the above discussions, we can see that the proposed antenna can cover the lower WLAN band and 5.25 GHz WLAN band.

Table 2: The performance of the designed dual-band antenna

Size (mm^2)	26×30	
Resonant Frequency (GHz)	2.43	5.25
Bandwidth (MHz)	140	200
Gain (dBi)	4.95	2.73
Efficiency	66%	72%

Table 3: Comparison of the proposed antenna and the early reported antennas

	Resonant Frequency (GHz)	Size (mm^2)	Gain (dBi)
[5]	2.4 and 5.56	40×40	1.5 and 4
[21]	2.4 and 5.2	30×50	1.9 and 4.3
[22]	2.4 and 5.2	64.5×75	1.6 and 2.1
[23]	2.45 and 5.24	48×16	2.39 and 1.77
[24]	2.4 and 5.2	45×35	2.24 and 3.87
This work	2.43 and 5.25	26×30	4.95 and 2.73

From Table 3, we found that the proposed antenna has the smallest size, two resonance frequencies, good gains, making the developed antenna suitable for WLAN

applications. In addition, the proposed antenna has a radiation efficiency of 66% and 72% at the lower and upper bands.

IV. CONCLUSION

In this paper, a dual-band WLAN antenna is proposed, and its performance is analyzed and discussed in detail. The antenna operates at 2.43 GHz with a bandwidth of 140 MHz and 5.25 GHz with bandwidth of 200 MHz, which can cover WLAN band. The proposed antenna is simulated, optimized, fabricated and measured, the proposed antenna has two resonance frequencies, good omnidirectional radiation patterns and gains. Additionally, the proposed antenna has a compact size which can be integrated into a terminal device. In the future, the antenna can be easily developed to be a reconfigurable antenna. Moreover, we will design dual-band MIMO antenna to reduce the coupling between the closely set antenna elements [25-35].

ACKNOWLEDGMENTS

This work was partially supported by the National Key Research and Development Program of China (2016YFE111100), Key Research and Development Program of Heilongjiang (GX17A016), the Science and Technology innovative Talents Foundation of Harbin (2016RAXXJ044), the Natural Science Foundation of Beijing (4182077), China Postdoctoral Science Foundation (2017M620918) and the Fundamental Research Funds for the Central University (HEUCFG201829).

REFERENCES

[1] G. Augustin, S. Shynu, P. Mohanan, C. Aanandan and K. Vasudevan, "Compact dual-band antenna for wireless access point," *Electronics Letters*, vol. 42, no. 9, pp. 502-503, 2006.

[2] Y. Lin and P. Chi, "Taper bent folded monopole for dual-band wireless local area network (WLAN) systems," *IEEE Antennas and Wireless Propagation Letters*, vol. 4, no. 1, pp. 355-357, 2005.

[3] A. Basaran and Y. Erdemil, "A dual-band split-ring monopole antenna for WLAN applications," *Microwave Optical Technology Letters*, vol. 51, no. 11, pp. 2685-2688, 2009.

[4] C. Su, H. Chen, and F. Chang, "Dual-band slot antenna for 2.4/5.2 GHz WLAN operation," *Microwave Optical Technology Letters*, vol. 35, no. 4, pp. 306-308, 2002.

[5] T. Kim and D. Park, "Compact dual-band antenna with double L-slits for WLAN operations," *IEEE Antennas and Wireless Propagation Letters*, vol. 4, no. 1, pp. 249-252, 2005.

[6] N. Karmakar and M. Bialkowski, "Compact dual-band slot-antenna for WLAN applications," *Microwave Optical Technology Letters*, vol. 49, no. 5, pp. 1203-1204, 2010.

[7] C. Liu, T. Jiang, and Y. Li, "A compact wide slot antenna with dual band-notch characteristic for ultra-wideband applications," *Journal of Microwaves Optoelectronics and Electromagnetic Applications*, vol. 10, no. 1, pp. 55-64, 2011.

[8] Y. Zimu, H. Zhang, L. M. Zhang, and A. Wang, "A U-shaped slot antenna for WLAN and WiMAX applications," *IEEE 7th Asia-Pacific International Symposium on Electromagnetic Compatibility (APEMC)*, Shenzhen, China, 2016.

[9] S. Nandib and A. Mohan, "A compact dual-band MIMO slot antenna for WLAN applications," *IEEE Antennas and Wireless Propagation Letters*, vol. 16, pp. 2457-2460, 2017.

[10] W. Li, B. Liu, and H. Zhao, "The U-shaped structure in dual-band circularly polarized slot antenna design," *IEEE Antennas and Wireless Propagation Letters*, vol. 13, pp. 447-450, 2014.

[11] H. Wu, J. Zhang, L. Yan, L. Han, R. Yang, and W. Zhang, "Differential dual-band antenna-in-package with T-shaped slots," *IEEE Antenna and Wireless Propagation Letters*, vol. 11, pp. 1446-1449, 2012.

[12] F. Shi, T. Jiang, and Y. Li, "A fork-like dual-band antenna with an inverted U-shaped parasitic element for WLAN and WIMAX Applications," *2017 Progress in Electromagnetics Research Symposium*, Singapore, 2017.

[13] W. Liu and C. Hsu, "Dual-band CPW-fed Y-shaped monopole antenna for PCS/WLAN application," *Electronics Letters*, vol. 41, no. 7, pp. 390-391, 2005.

[14] C. Huang and P. Chiu, "Dual-band monopole antenna with shorted parasitic element," *Electronics Letters*, vol. 41, no. 21, pp. 1154-1155, 2005.

[15] S. Chang, Y. Li, X. Yang, and M. Li, "A dual and wide band antenna for WLAN/WiMAX/UWB applications," *2011 International Conference on Consumer Electronics, Communications and Networks (CECNet)*, Xianning, China, 2011.

[16] A. Roseline and K. Malathi, "Compact dual-band patch antenna using spiral shaped electromagnetic bandgap structures for high speed wireless networks," *International Journal of Electronics and Communications*, vol. 66, no. 12, pp. 963-968, 2012.

[17] Y. Li, W. Li, and R. Mittra, "A compact ACS-fed dual-band meandered monopole antenna for WLAN and WiMAX applications," *Microwave and Optical Technology Letters*, vol. 55, no. 10, pp. 2370-2373, 2013.

[18] C. Sim, C. Chen, X. Zhang, Y. Lee, and C. Chiang, "Very small-size uniplanar printed monopole antenna for dual-band WLAN laptop computer applications," *IEEE Transactions on Antenna and*

Propagation, vol. 65, no. 6, pp. 2916-2922, 2017.

[19] C. Jung and F. Flaviis, "A dual-band antenna for WLAN applications by double rectangular patch with 4-bridges," *IEEE Antennas and Propagation Society International Symposium*, Monterey, California, USA, 2004.

[20] Y. Li, W. Li, and Q. Ye, "A compact asymmetric coplanar strip-fed dual-band antenna for 2.4 GHz/ 5.8 GHz WLAN applications," *Microwave and Optical Technology Letters*, vol. 55, no. 9, pp. 2066-2070, 2013.

[21] C. Huang and E. Yu, "A slot-monopole antenna for dual-Band WLAN applications," *IEEE Antennas and Wireless Propagation Letters*, vol. 10, no. 5, pp. 500-502, 2011.

[22] Y. Kuo and K. Wong, "Printed double-T monopole antenna for 2.4/5.2 GHz dual-band WLAN operation," *IEEE Transactions on Antenna and Propagation*, vol. 51, no. 9, pp. 2187-2192, 2003.

[23] J. Rattapon, J. Keawkuman, and N. Intarawiset, "Design of dual-band CPS-fed dipole antenna for 2.4/5.2 GHz WLAN operation," *2017 IEEE MTT-S International Conference on Microwaves for Intelligent Mobility (ICMIM)*, Nagoya, Japan, 2017.

[24] A. Rathore, R. Nilavalan, H. AbuTarboush, and T. Peter, "Compact dual-band (2.4/5.2GHz) monopole antenna for WLAN applications," *2010 International Workshop on Antenna Technology*, Lisbon, Portugal, 2010.

[25] B. Pan and T. Cui, "Broadband decoupling network for dual-band microstrip patch antennas," *IEEE Transactions on Antenna and Propagation*, vol. 65, no. 10, pp. 5595-5598, 2017.

[26] F. Liu, A. Chen, and L. Zhao, "Dual-band antenna decoupling design with stepped impedance loaded dual-band dummy element," *2018 IEEE International Symposium on Antennas and Propagation and USNC/URSI National Radio Science Meeting*, Boston, USA, 2018.

[27] S. Luo and Y. Li, "A dual-band antenna array with mutual coupling reduction using 3D metamaterial structures," *2018 International Symposium on Antennas and Propagation*, Busan, Korea, 2018.

[28] L. Zhao and K. Wu, "A dual-band coupled resonator decoupling network for two coupled antennas," *IEEE Transactions on Antennas and Propagation*, vol. 63, no. 7, pp. 2843-2850, 2015.

[29] S. Luo, Y. Li, Y. Xia, G. Guo, L. Sun, and L. Zhao, "Mutual coupling reduction of a dual-band antenna array using dual-frequency metamaterial structure," *Applied Computational Electromagnetics Society Journal*, Accepted.

[30] K. Yu, Y. Li, and X. Liu, "Mutual coupling reduction of a MIMO antenna array using 3-D novel metamaterial structures," *Applied Computational Electromagnetics Society Journal*, vol. 33, no. 7, pp. 758-763, 2018.

[31] S. Luo, Y. Li, and W. Shi, "A dual-frequency antenna array with mutual coupling reduction via metamaterial structures," *2018 IEEE International Symposium on Antennas and Propagation and USNC/URSI National Radio Science Meeting*, Boston, USA, 2018.

[32] Y. Li, W. Li, and W. Yu, "A multi-band/UWB MIMO/diversity antenna with an enhance isolation using radial stub loaded resonator," *Applied Computational Electromagnetics Society Journal*, vol. 28, pp. 8-20, 2013.

[33] T. Jiang, T. Jiao, and Y. Li, "A low mutual coupling MIMO antenna using periodic multi-layered electromagnetic band gap structures," *Applied Computational Electromagnetics Society Journal*, vol. 33, no. 3, 2018.

[34] L. Zhao, F. Liu, X. Shen, G. Jing, Y. Cai, and Y. Li, "A high-pass antenna interference cancellation chip for mutual coupling reduction of antennas in contiguous frequency bands," *IEEE Access*, vol. 6, pp. 38097-38105, 2018.

[35] S. Luo, Y. Li, Y. Xia, G. Yang, L. Sun, and L. Zhao, "Mutual coupling reduction of a dual-band antenna array using dual-frequency metamaterial structure," *Applied Computational Electromagnetics Society Journal*, Accepted.

A Transmitarray Antenna with Double Conformal Rings as the Cell Elements

Keyu Yan [1], Xiuzhu Lv [1], Zhihua Han [1], and Yongliang Zhang[*1,2]

[1] College of Electronic Information Engineering
Inner Mongolia University, Hohhot, 010021, China
847312052@qq.com, 864144727@qq.com, 972834368@qq.com

[2] College of Transportation
Inner Mongolia University, Hohhot, 010021, China
namar@imu.edu.cn

Abstract ─ In this paper, we mainly study the electromagnetic transmission characteristics of transmission array antennas and transmission units. Based on array antenna theory and geometric theory, we construct a transmission array antenna for a double conformal rings (DCR). It works in a 10GHz two-layer transmission array. A double resonant conformal rings are used as the unit element. By changing the physical dimensions of the double conformal unit, phase coverage of up to 600° can be achieved. And the 1d B gain bandwidth is has by 7% compared to the previous transmission array. The simulated and measured peak gain is 27.59 dB and 25.91dB, respectively.

Index Terms ─ Compensation phase, double conformal rings, transmitarray antenna.

I. INTRODUCTION

The use of micro strip transmitarrays (TAs) and reflectarrays (RAs) is essential in long-range communication systems because of their high-gain radiations, narrow beam widths, simple configurations, and easy fabrication.

A four-layer transmitarray operating at 30 GHz is designed using a dual-resonant double square rings as the unit cell element. The two resonances of the double rings are used to increase the per-layer phase variation while maintaining a wide transmission magnitude bandwidth of the unit cell [1]. A novel antenna system that combines the functionalities of TAs and RAs is proposed. The antenna system consists of a specially designed bifunctional meta-lens and a self-made Vivaldi antenna (feed source). The meta-lens can focus the y-polarized incident wave at the transmission side and focus the x-polarized wave at the reflection side with the same focal length. By launching the meta-lens with differently polarized Vivaldi antennas, and it was able to obtain a TA and RA [2]. Based on the electrical characteristics of grapheme and using graphene-based 4-layer transmitarray unit cells, a 1024-element transmitarray antenna at 260GHz is designed. Simulation results show that these millimeter-wave antennas using graphene patches show good radiation performance. And die whole transmitarray plane and reflectarray plane are both transparent [3]. The impact of the phase compensation method on transmitarray (TA) performance is studied here in terms of directivity, gain, aperture efficiency, and beam scanning capability. The numerical results show that TTD compensation allows increasing the TA bandwidth and reducing beam squint as compared to constant phase-shift compensation [4]. The matching condition and the theoretical results are discussed, and the theory shows that an element with non-identical layers can realize similar phase range as the identical-layer design but with a much lower profile [5]. There is introduce two kinds of rectangular slots in the design to control the magnitude and phase range of transmission coefficients in the two designed frequency bands through changing the slot length [6].

In this letter, a broadband planar transmitarray antennas based on DCR structure is proposed. This element has a wide transmission band with only two metallic layers, which is 2 and 3 layers less than the TAs proposed in [10] and [11], respectively. The total thickness of substrate layers is only 3 mm ($0.1\lambda_0$), which is 30% and 23% thinner than the TAs proposed in [8] and [9], which makes the structure very compact at 10GHz. Therefore, a large array of this cell is low-profile and easy to fabricate. Also, the provided phase shift by the physical dimensions of this element is continuous and up to 600°.

The rest of the letter is organized as follows. In Section II, we introduce the design of a DRCL structure unit cell. In Sections III and IV, the simulation and measured results of the TA composed of the proposed cell are discussed, respectively. Finally, the results show the proposed TA with only two metallic layers can achieve a higer gain performance, and conclusions are

Submitted On: November 30, 2018
Accepted On: January 26, 2019

drawn in Section V.

II. UNIT CELL DESIGN AND SIMULATION

To collimate the incident wave from the feed horn, a transmitarray uses the antenna elements on its surface to re-phase the incoming spherical wave and then retransmit the signal as a plane wave. The amount of phase adjustment needed at each antenna element depends on the phase delay an incident ray has accumulated travelling between the feed horn and the transmitarray surface. Figure 1 (b) denotesas r_f the vector to the ith element from the feed's phase center, and r_i as the position vector to the ith element from the transmitarray centre; k_0 is the propagation constant, and $\hat{u}_0$ is thedirection of the transmitted main beam.

From [7], he necessary phase compensation value φ_c at each element is given by (1):

$$\varphi_c = -k_0(r_f + r_i\hat{u}_0) + 2n\pi, n = 1,2,3,\cdots. \quad (1)$$

This chapter proposes a new broadband planar transmission array unit structure, namely a DCR structure, as shown in Figs. 1 and 2, which has a large phase coverage and good polarization and angular stability. The cell structure diagram are given in Fig. 1. The lower layer of the dielectric substrate is a metal ground, and the upper layer etches a double conformal metal rings, and the circumference of the rings are about half the wavelength of the free space. The thickness of the dielectric substrate is generally much smaller than the wavelength, usually less than 0. 1λ (λ is the wavelength in the medium). By selecting an appropriate cell structure and size, the antenna cell period can be effectively reduced. The unit model is simulated using the master slave boundary conditions, and the simulation model is shown in Fig. 2.

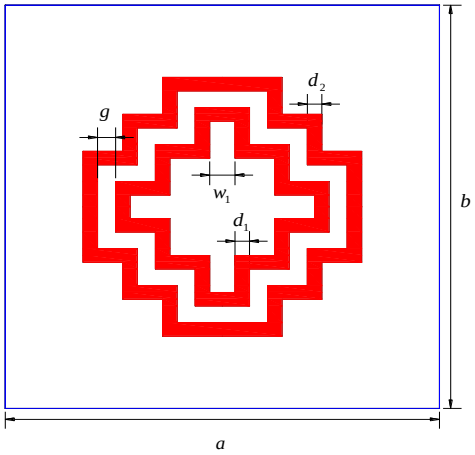

Fig. 1. DCR element the parameters of cell element d_1=d_2=0.4mm, a=b=12mm, g=0.5mm, w_1=0.7mm.

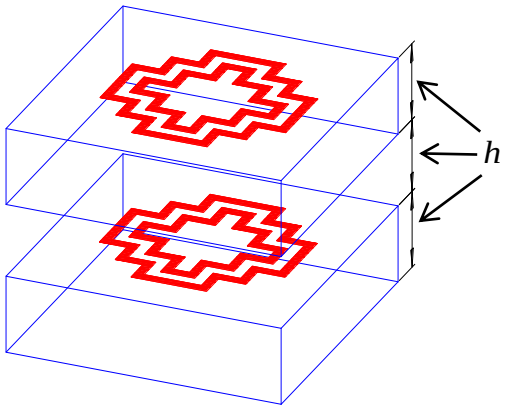

Fig. 2. DCR element's three-dimensional structure, h=3mm.

In order to improve the linearity of the phase curve, the transmission array unit must be optimized. The transmission phase curves of a single inner rings, a single outer rings and the DCR unit are shown in Fig. 3. As can be seen from Fig. 3, the phase shift curves of a single inner rings and a single outer rings are approximately 300° and are both smaller than the phase shift range of the DCR proposed herein. The main reason for the large phase coverage of the DCR unit is that the unit has dual resonance characteristics, as shown in Fig. 4, When the unit length is L=7.7mm. From the characteristic relationship between the transmission curve and the frequency, the double resonance frequencies appear at 4.4 GHz and 13.5 GHz, respectively.

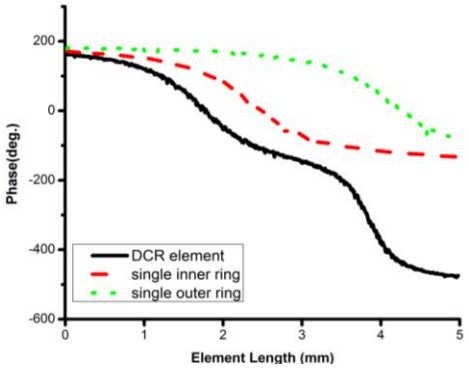

Fig. 3. Phase characteristics of the unit transmission coefficients.

Figure 5 shows the amplitude distribution of the scattered electric field on the surface of the element. The aperture efficiency of the unit can be better observed, and the electric field distribution on the cell aperture is relatively uniform, which also explains the high gain array phenomenon.

In order to effectively analyze and design the transmission array, it is important to accurately analyze the phase shift characteristics of the transmission unit when TE (Transverse Electric, TE) and TM (Transverse Magnetic, TM) polarized waves are incident. Since each unit is about half the length of the medium, each unit is in a resonant state when electromagnetic waves emitted by the feed source are incident on a transmissive surface composed of a large number of cells.

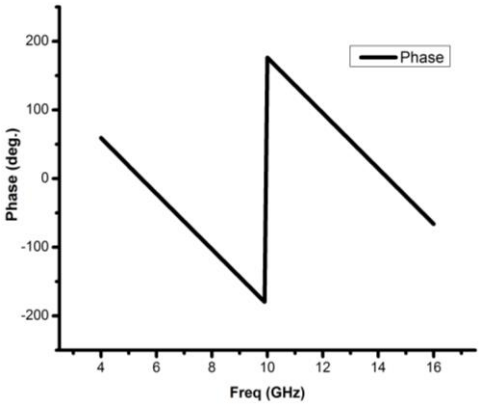

Fig. 4. Resonance characteristics of the unit transmission coefficients.

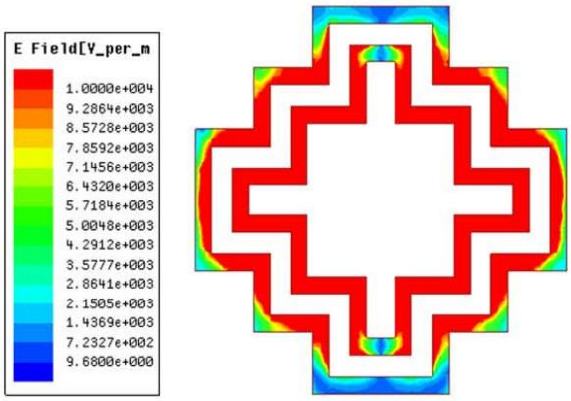

Fig. 5. Scattering E-field magnitude distribution on the DCR element in the normal incidence at 10 GHz.

In order to simplify the analysis and design, and also to increase the polarization stability of the unit structure, a symmetrical structure is adopted in the *x* direction and the *y* direction, and the unit period is a=b=12 mm. The double conformal rings element proposed in this chapter has more degrees of freedom, such as the inner rings line width d_1, the outer rings line width seedling d_2, the inner rings and the outer rings spacing g, and the inner rings line spacing w_1. So many degrees of freedom are an important reason for the degree of linearity of the curve to improve the phase shift.

III. TA CONFIGURATION

The simulation array model is shown in Fig. 6. The array consists of two layers with a substrate thickness of 3 mm, which is 35% and 25% thinner than the TAs proposed in [8] and [9], with a 3 mm gap between the two layers, and each layer consists of 30x30 cells. It should be noted that for each unit, the arm length in the *x* direction and the arm length in the *y* direction are the same, so the unit is symmetrical in the *x* and *y* directions. The plate was selected as F4BMX-2, the thickness of the substrate was sheet, the dielectric constant was 2.2, and the loss tangent at the center frequency of 10 GHz was 0.001. In order to obtain the desired phase shift curve, in the process of designing the transmission array, each unit size or rotation angle in the array must be adjusted. This compensated phase shift curve can be obtained by full-wave simulation of infinite period boundary conditions.

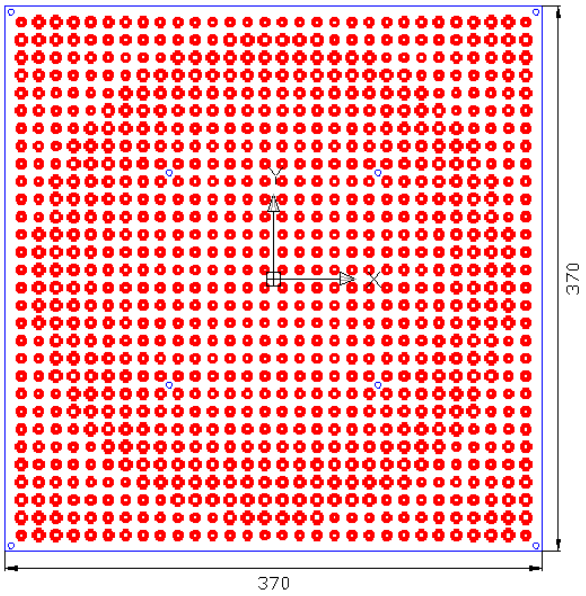

Fig. 6. 30x30 DCR transmission array simulation model.

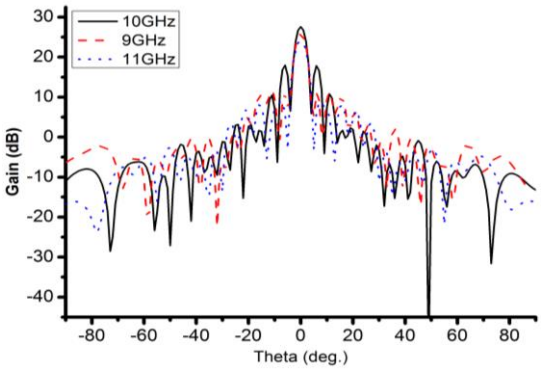

Fig. 7. The simulated transmitarray radiation gains at 9 GHz, 10 GHz, and 11 GHz.

In the design of this chapter, in order to reduce the unit size and the coupling between the units, we use the unit size of the more linear region in the phase length curve as much as possible. Figure 7 shows the simulation pattern of the three frequencies of 9 GHz, 10 GHz and 11 GHz in the *xoy* flat. There is a certain offset in the direction of the main beam throughout the operating band. The main reason for generating the main beam offset is that each cell has a certain phase difference at different frequency points. The peak gain of the simulation at a center frequency of 10 GHz is 27.59 dB. To demonstrate its gain bandwidth, Fig. 8 shows the relationship of gain as a function of frequency. The 1dB relative bandwidth of the center operating frequency of 10 GHz is 7%, and the absolute operating bandwidth is from 9.3 GHz to 11.3 GHz.

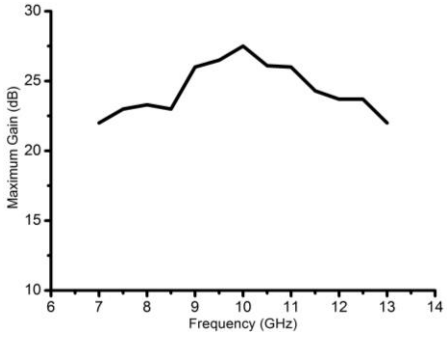

Fig. 8. The maximum gain versus frequency within the operational frequency band.

IV. MEASURED RESULTS AND DISCUSSION

Based on the above simulation and design, the transmitarray with 30x30 elements was fabricated and measured. The processing array is shown in Fig. 9, the array and cell prototype of this sample correspond to Fig. 6. The measured system is shown in Fig. 10. TA represents the fabricated array. Tx and Rx represent the transmitting horn and the receiving horn, respectively, and during the measurement that the polarizations of RX and TX horn antennas are vertical the same as TM polarization. The measurement of the radiation pattern was performed in an anechoic chamber at Xidian University, China. The distance from TX to TA is 0.45 m and from RX to TA 3m.The height of TX to the ground is 1.5 m. The heights of RX and TA to the ground are 3 m.

Figure 11 shows the normalized radiation pattern of the measurements. It can be seen that there is a certain decrease in the main beam gain of other frequency points in the main beam direction of the operating frequency band of 10 GHz with respect to the center frequency. The peak gain of the measurement at a center frequency of 10 GHz is 25.91dB. It is generally consistent with the simulation. Figure 12 shows the comparison of the normalized radiation pattern for the center frequency 10 GHz simulation and measurement. Although there is a deviation in the direction of the main beam, the overall agreement is good. The processing error and the instability of the plate during the experiment are the main causes of measurement deviation.

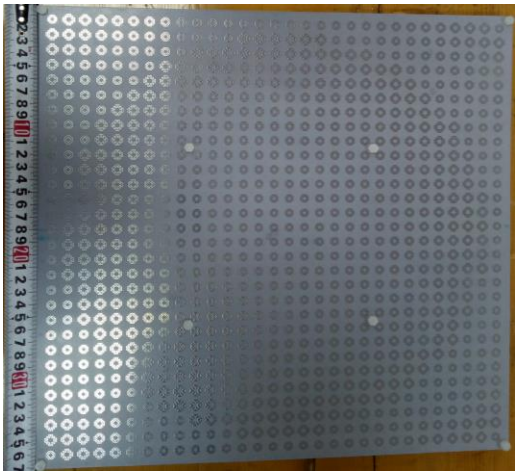

Fig. 9. Fabricated array antenna with 30x30 elements.

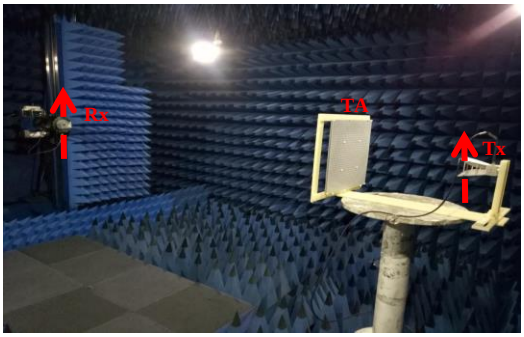

Fig. 10. Measurement system at Xidian University.

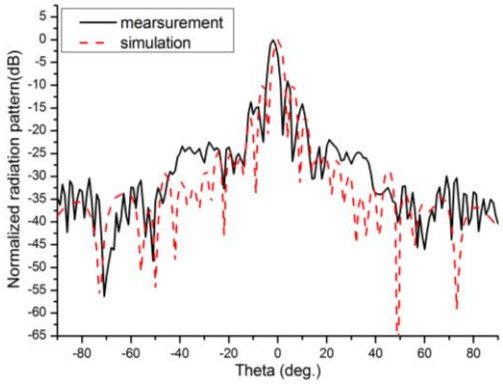

Fig. 11. Measured normalized radiation patterns of the transmitarray with 30x30 DCR elements.

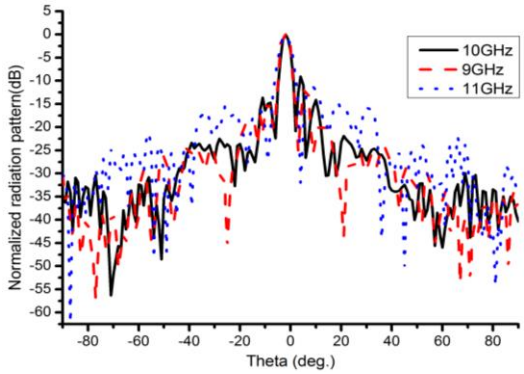

Fig. 12. Comparison between the simulated and measured results of the normalized radiation pattern at 10 GHz.

V. CONCLUSION

This work gives the design process and design ideas of a planar transmission array based on a DCR. This DCR unit has more degrees of freedom and can greatly improve the linearity of the phase curve. By changing the cell length of the DCR, not only can the phase shift range of up to 600° be obtained, but also the linearity is good. The 30x30 dual resonant rings unit double layer array was designed, processed and measured. The measured results show that the transmission array unit proposed in this chapter has 1dB bandwidth reaches 7%. The simulated and measured peak gain is 27.59 dB and 25.91 dB, respectively.

ACKNOWLEDGMENT

This work was supported by the National Natural Science Foundation of China (NSFC) under Project No. 61761032.

REFERENCES

[1] C. G. M. Ryan, M. R. Chaharmir, J. Shaker, J. R. Bray, Y. M. M. Antar, and A. Ittipiboon, "A wideband transmitarray using dual-resonant double square rings," *IEEE Transactions on Antennas and Propagation*, vol. 58, no. 5, pp. 1486-1493, May 2010.

[2] T. Cai, G.-M. Wang, X.-L. Fu, J.-G. Liang, and Y.-Q. Zhuang, "High-efficiency metasurface with polarization-dependent transmission and reflection properties for both reflectarray and transmitarray," *IEEE Transactions on Antennas and Propagation*, vol. 66, no. 6, pp. 3219-3224, June 2018.

[3] X.-Y. Xia, "Millimeter-Wave Reflectarray and Transmitarray Antennas," *Southeast University*, 2016.

[4] F. Diaby, A. Clemente, L. Di Palma, L. Dussopt, and R. Sauleau, "Impact of phase compensation method on transmitarray performance," *11th European Conference on Antennas and Propagation*, 2017.

[5] J. Luo, F. Yang, S. V. Hum, S. Xu, and M. Li, "Study of a low-profile transmitarray element using 3 non-identical layers," *IEEE MTT-S International Wireless Symposium*, pp. 1-3, May 2018.

[6] R. Y. Wu, Y. B. Li, W. Wu, C. B. Shi, and T. J. Cui, "High-gain dual-band transmitarray," *IEEE Transactions on Antennas and Propagation*, vol. 65, no. 7, July 2017.

[7] Y. Li and L. Li, "Broadband microstrip beam deflector based on dual-resonance conformal loops array," *IEEE Transactions on Antennas and Propagation*, vol. 62, no. 6, June 2014.

[8] R. H. Phillion and M. Okoniewski, "Lenses for circular polarization using planar arrays of rotated passive elements," *IEEE Trans. Antennas Propag.*, vol. 59, no. 4, pp. 1217-1227, Apr. 2011.

[9] M. Euler and V. F. Fusco, "Frequency selective surface using nested split ring slot elements as a lens with mechanically reconfigurable beam steering capability," *IEEE Trans. Antennas Propag.*, vol. 58, no. 10, pp. 3417-3421, Oct. 2010.

[10] G. Liu, "High Efficiency Transmitarray Antenna Research," *University of Chinese Academy of Sciences*, pp. 64-67, May 2016.

[11] S. H. R. Tuloti, P. Rezaei, and F. T. Hamedani, "High-efficient wideband transmitarray antenna," *IEEE Antennas and Wireless Propagation Letters*, vol. 17, no. 5, pp. 817-820, May 2018.

Keyu Yan received bachelor degree in Automation from Dalian Minzu University, Dalian, China, in 2016. From 2017, he purse his Master degree in Inner Mongolia University. His research interests transmission array antennas and frequency selective surface.

Xiuzhu Lv received bachelor degree in Automation from Inner Mongolia University of Science and Technology, Baotou, China, in 2018. From 2018, she pursued her Master degree in Inner Mongolia University. Her research interests transmission array antennas and frequency selective surface.

Zhihua Han received bachelor degree in Automation from the Beihua University, Jilin, China, in 2016. From 2018, he pursued his Master degree in Inner Mongolia University. His research interests transmission array antennas and frequency selective surface.

Yongliang Zhang received bachelor and doctor degree from the Xidian University, Xian, China, in 2009 and 2014 respectively. From 2014, he joined Inner Mongolia University. His research interests transmission array antennas and frequency selective surface.

A Low-Profile Dual-Polarized Crossed Dipole Antenna on AMC Surface

Rui He, Ze-Hong Yan, and Yan-Bo Meng

National Key Laboratory of Antennas and Microwave Technology
Xidian University, Xi'an, China
576770279@qq.com, zhyan@mail.xidian.edu.cn

Abstract ─ A low-profile dual-polarized crossed dipole antenna on artificial magnetic conductor (AMC) surface is presented in this paper. The antenna consists of two orthogonal dipoles, a periodic arrangement of artificial magnetic conductors and a ground floor. The antenna has a section height of only 13mm ($0.13\lambda_0$, λ_0 is the wavelength in free space at 3 GHz). With utilizing the 6×6 unit cell of square patch based AMC, the antenna can achieve a wide band. To verify this design, a prototype of this antenna is designed, fabricated and measured. Measured results exhibit that bandwidth from 2.9 GHz to 3.32 GHz (S11< -10dB) for one port and from 2.995 GHz to 3.47 GHz (S22< -10dB) for another port are obtained, respectively. Meanwhile, the isolation between two ports is less than -30 dB, and stable radiation patterns are realized in operating frequency band.

Index Terms ─ AMC (artificial magnetic conductor), crossed dipole antenna, low-profile.

I. INTRODUCTION

In recent years, artificial magnetic conductors (AMC) have become an important research tendency in the field of metamaterials. Metamaterials have extremely valuable electromagnetic properties that do not exist in nature, breaking the physical limits of traditional materials or structures, opening up a new research space for the development of classical electromagnetic theory. Currently widely studied metamaterials include LHM (Left-handed materials), EBG (Electromagnetic band gap) and AMC (Artificial magnetic conductor). Among them, AMC structures feature in-phase reflection in designed frequency band.

The artificial magnetic conductor (AMC) structure was proposed by an American scholar Sievenpiper when studying the mushroom-type EBG structure [1]. It can exhibit the in-phase reflection characteristics of a perfect magnetic conductor (PMC) to a plane wave in a specific frequency range. Thus it has wide application in high performance antenna, radar target stealth, microwave transmission and many other aspects. The structural characteristics of AMC are similar to the reflection characteristics of an ideal magnetic conductor. For the incident plane wave which is perpendicular to the surface, the AMC has the effect of same phase reflection. That is to say, reflected wave and incident wave have no phase change. It is well known that a perfect electric conductor (PEC) has a reflection phase of 180° for a normally incident plane wave, while a perfect magnetic conductor (PMC), which does not exist in nature, has a reflection phase of 0° [2]. This is the opposite scenario if an AMC is placed instead of PEC due to its reflection of electromagnetic wave with zero phase shift [3]. Therefore, the AMC structure is used as the reflection surface of the antenna, and the distance between the antenna and the reflection surface is effectively reduced to realize the low-profile characteristics [4].

Traditionally, the dual-polarized crossed dipole antenna equipped with a metal reflector has a high profile. In order to miniaturize the antenna, the reduction of the profile has become a research trend [5].

In this paper, a low-profile dual-polarized crossed dipole with an AMC surface is studied. The dual-polarized antenna can simultaneously transmit and receive two orthogonally polarized electromagnetic waves. The presented antenna can operate in a band ranging from 2.9 GHz to 3.32 GHz (S11< -10dB), 2.995 GHz to 3.47 GHz (S22< -10dB) with a height of $0.13\lambda_0$ (λ_0 represents the wavelength in free space at 3 GHz). A 6×6 unit cell of square patch based AMC is loaded to the antenna to make it compact. Also, the better radiation performance is realized. Through simulation and measured results, the designed antenna can basically meet the industry standard of mobile communication base station antenna and can be applied to dual-polarized base station antenna.

II. ANTENNA DESIGN

The proposed dual-polarized crossed dipole antenna with an AMC reflector is shown in Fig. 1. The 3-D configuration includes two perpendicularly crossed-dipoles, an AMC surface, and a ground plane.

A. Dual-polarized crossed dipole

The two dipoles utilized in this paper have the same structure. For a single printed dipole antenna, it is printed on one side of the FR4 substrate with a relative dielectric

Submitted On: November 30, 2018
Accepted On: April 9, 2019

permittivity of 4.4, a loss tangent of 0.02, and a thickness of 0.5mm. While, the feeding line and the balanced balun are printed on the other side of the substrate. The detailed structure of a single dipole antenna is demonstrated in the Fig. 2. Figure 2 (a) shows the side view of the proposed antenna, and Fig. 2 (b) shows the feeding structure.

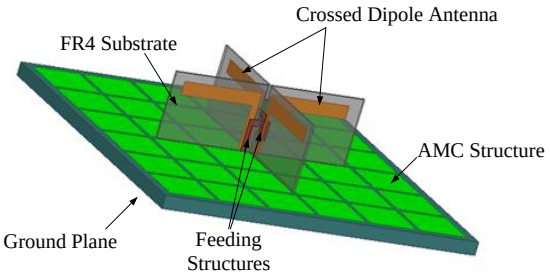

Fig. 1. 3D-view of the proposed antenna.

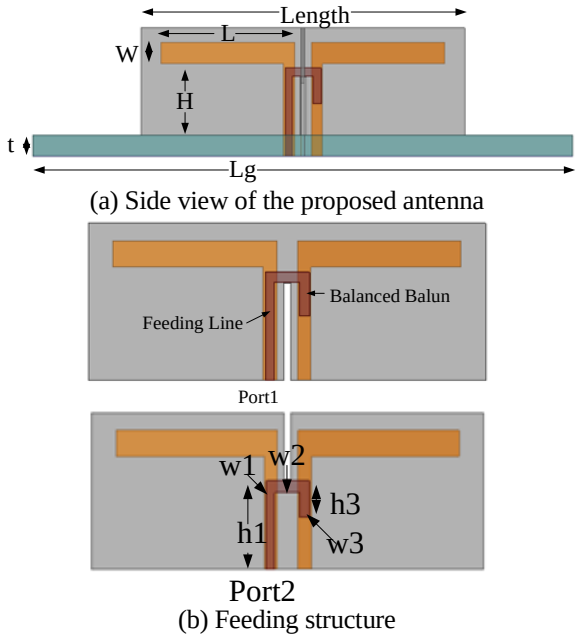

(a) Side view of the proposed antenna

(b) Feeding structure

Fig. 2. Configuration of the proposed antenna.

B. AMC principle

As a periodic artificial electromagnetic material, AMC has the in-phase reflection characteristics of plane waves. The basic structure of the AMC unit consists of a substrate with dielectric loss, a metal patch over the substrate, and a metal floor. When the electromagnetic wave incident perpendicularly, its impedance can be regarded as the capacitive patch array, the loss medium and the perceptual metal floor three parallel, as shown in Fig. 3. L1 and C are the inductance and capacitance between the AMC units, R includes the dielectric loss of the substrate and the ohmic loss of the metal, and L2 is the inductance between the metal patch and the floor. The admittance and reactance expressions of the circuit are as follows:

$$Y = \frac{1}{j\omega L_1 + 1/\ j\omega C} + \frac{1}{R} + \frac{1}{j\omega L_2}, \quad (1)$$

$$Z = \frac{1}{Y} = \frac{j\omega R L_2 (1-\omega^2 L_1 C)}{R(1-\omega^2 L_1 C - \omega^2 L_2 C) + j\omega L_2 (1-\omega^2 L_1 C)}. \quad (2)$$

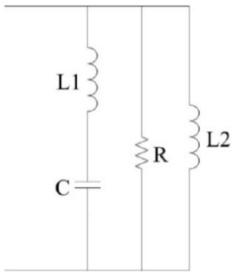

Fig. 3. AMC equivalent circuit.

C. Proposed AMC design

The geometry of proposed planar AMC unit cell is depicted in Fig. 4. It consists of a square patch on the same FR4 substrate which mentioned before, but with the thickness of 3mm. The unit cell is 11mm×11mm and the gap between two patches is 1mm, shown in Fig. 5 (a). Because the dipoles are placed vertically, the cell spacing should be considered when designing the cell structure to ensure that the antenna can be placed.

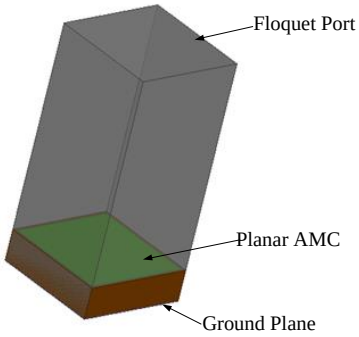

Fig. 4. Geometry of the AMC.

III. SIMULATION AND RESULTS

A. Analysis of the AMC unit cell

The AMC surface can be constructed by periodic unit cells, which is composed of metallic ground and dielectric substrate. It is known to be useful for improving antenna radiation performance and achieving low-profile design. AMC reflector is designed by means of reflection phase characterization [6].The resonance frequency of AMC surface corresponds to the 0° of the reflection coefficient phase, and the operating bandwidth is defined by the phase between +90° and -90° [7]. Figure 5 shows the AMC unit cell configuration and the corresponding reflection phase.

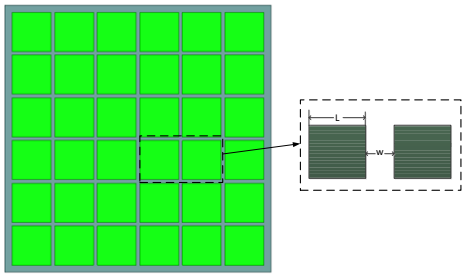

(a) AMC unit cell (L=11mm, w=1mm, height of FR4 is 3mm)

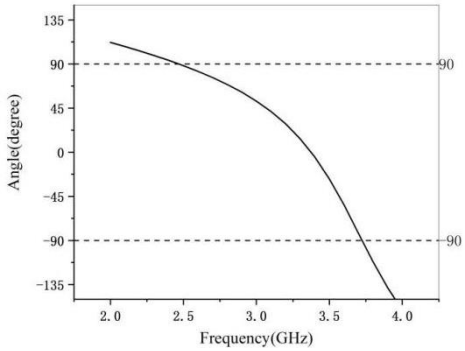

(b) Reflection phase

Fig. 5. AMC unit cell and reflection phase.

Figure 6 shows the simulated reflection phases of different size of square patches. Figure 6 (a) shows the reflection phases when the edge length of AMC unit L varies from 5mm to 15mm with all other dimensions fixed as in Fig. 5. As L increases, the reflection phase bandwidth increases and the frequency increases. Figure 6 (b) shows the reflection phases when the size of the gap between two patches w varies from 0.6mm to 5mm while other parameters remain unchanged. As w increases, the reflection phase bandwidth also increases and the frequency increases. In short, the operating band of present AMC unit cell can be basically independently controlled by the main physical parameters. So we choose the size of L is 11mm, and w is 1mm. The zero phase reflection band of the AMC ground plane is from 2.48 GHz to 3.72 GHz, shown in Fig. 5 (b).

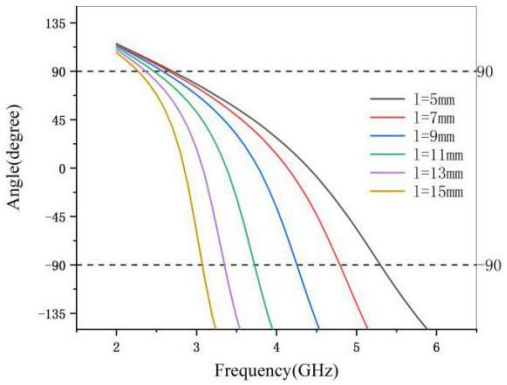

(a)

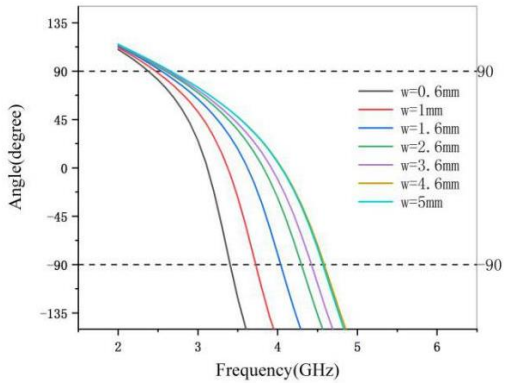

(b)

Fig. 6. Reflection phases of different size of square patches.

B. Results and discussions of the proposed antenna

For comparison, the antennas without AMC surface and with perfect electric conductor (PEC) reflector are also simulated. The PEC reflector has a size of 80×80mm^2 under the dual-polarized crossed dipole with a distance of about 25mm (one quarter of wavelength). The AMC is arranged in 6×6 units, the height of the substrate is 3mm, the size of the FR4 substrate is also 80×80mm^2 and the height of the antenna is 10mm from the substrate, shown in Fig. 7. We obtained the measurement results by processing the physical objects and testing. Figure 8 shows the performance of different antennas.

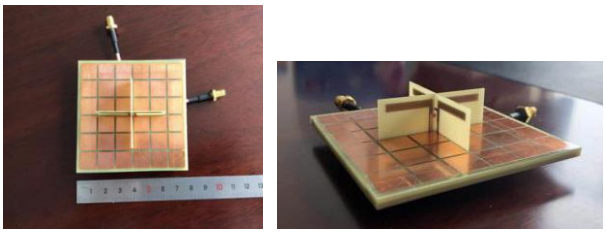

Fig. 7. Prototypes of the proposed antenna.

The ANSYS HFSS which is based on the finite element method (FEM) [8] is employed to simulate the antenna system. Simulated reflection coefficients of dual-polarized crossed dipole with and without AMC surface are shown in Fig. 8 (a). The bandwidth for S_{11}< -10 dB is from 2.85 GHz to 3.22 GHz, and for S_{22}< -10 dB is from 2.92 GHz to 3.35 GHz. The antenna's bandwidth is slightly narrowed due to the AMC's influence on impedance matching. The physical measured results of the processed antenna are also roughly the same as the simulation results, but the frequency offset is due to the error in the antenna processing accuracy. The height of the dual-polarized antenna with PEC as the reflecting surface is 25mm, and the height of the dual-polarized antenna with loaded AMC to the grounding plate is only 13mm. As the antenna height decreases, the size of the

feeding lines and baluns needs to be adjusted, and their low height may also affect the performance of the antenna. As shown in the Fig. 8 (b), the isolation between two ports of dual-polarized crossed dipole with AMC surface simulated by HFSS can all reduce to -30 dB, which can meet the needs of the application. But in the measurement, the isolation increases because the measured environment is not completely ideal and processing error. When using electromagnetic simulation software, the antenna model feed port we set is ideal. In the actual processing, the coaxial cable is used to feed, and the distance between the two ports is very small, so we use insulating tape to isolate the two ports.

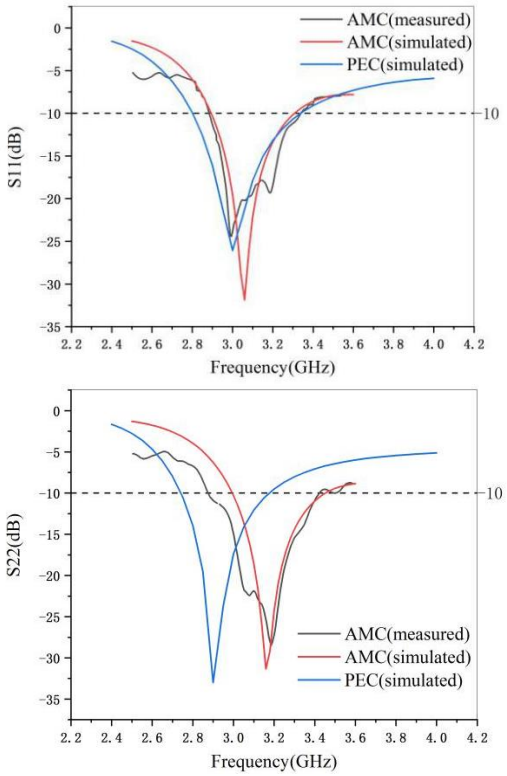

(a) Simulated/measured reflection coefficients of dual-polarized crossed dipole with/ without AMC surface

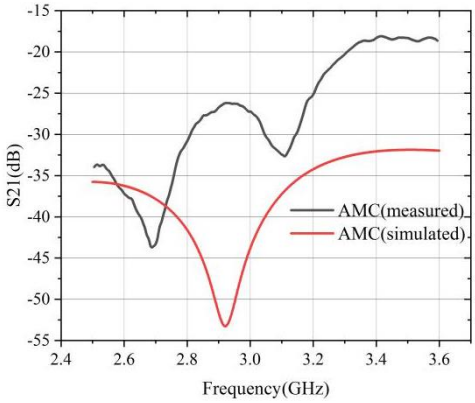

(b) Isolation between two ports of dual-polarized crossed dipole with AMC surface

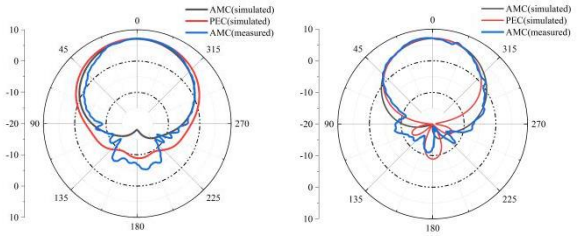

phi=0° phi=90°

(c) Radiation patterns of dual-polarized crossed dipole with/without AMC surface (port1 excitation) and measurement at 3.1GHz

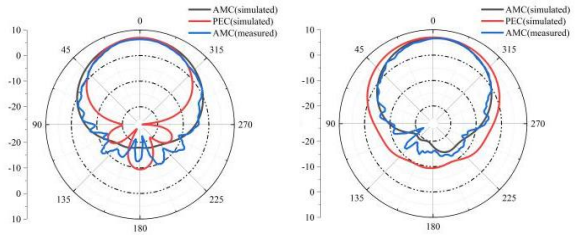

phi=0° phi=90°

(d) Radiation patterns of dual-polarized crossed dipole with/without AMC surface (port2 excitation) and measurement at 3.2 GHz

Fig. 8. Comparisons between the antenna with and without AMC surface (simulated/measured).

The Fig. 8 (c) shows the proposed antenna loading of AMC/PEC, and the measured results of the proposed antenna for port 1 at 3.1 GHz. The Fig. 8 (d) is the radiation pattern of antenna with and without AMC and the measurement for port2 at frequency 3.2GHz. A HB antenna rapid measurement system is used to measure the radiation patterns and gain. It can be noticed that the back radiation strength is reduced enormously with the AMC ground plane in the simulated results. In the working frequency band, the designed antenna has a stable radiation pattern with a front-to-back ratio of 24 dB, while the antenna of PEC reflector is 15dB. However, in the measurement, the back-lobe gain of the antenna is increased due to the incomplete idealization of the measured environment. Finally, the proposed antenna is reduced in profile, and AMC has a certain inhibitory effect on surface waves.

IV. CONCLUSION

In this paper, a dual-polarized crossed dipole antenna loaded with artificial magnetic conductors is designed. The in-phase reflection characteristics of AMC are used instead of metal plates to achieve directional radiation and reduce the profile height of the antenna. Through simulation analysis, the bandwidth for S_{11}< -10 dB is from 2.9 GHz to 3.32 GHz, and for S_{22}< -10 dB is from 2.995 GHz to 3.47GHz. Besides, the isolation between ports is less than -30 dB, and the radiation pattern is

stable, which has wide application value in the design of modern communication base stations.

REFERENCES

[1] D. Sievenpiper, L. J. Zhang, R. F. J. Broas, et al., "High-impedance electromagnetic surfaces with a forbidden frequency band," *IEEE Transactions on Microwave Theory and Techniques*, vol. 47, no. 11, pp. 2059-2074, 1999.

[2] H. R. Khaleeel, H. M. Al Rizzo, D. G. Rucker, and Y. Al-Naiemy, "Flexible printed monopole antennas for WLAN applications," *IEEE APSURSI International Symposium on Antennas and Propagation*, Spokane, WA, July 2011.

[3] H. R. Khaleel, H. M. Al-Rizzo, and D. G. Rucker, "An AMC based antenna for telemedicine applications," *ACES Journal*, vol. 27, no. 1, Jan. 2012.

[4] F. Yang and Y. Rahmat-Samii, "Reflection phase characteristics of the EBG ground plane for low profile wire antennas," *IEEE Trans. Antennas Propag*., vol. 51, pt. 1, pp. 2691-2703, Oct. 2003.

[5] Y. He, Z. Pan, X. Cheng, Y. He, J. Qiao, and M. M. Tentzeris, "A novel dual-band, dual-polarized, miniaturized and low-profile base station antenna," *IEEE Trans. Antennas Propag*., vol. 63, no. 12, pp. 5399-5408.

[6] A. Alemaryeen and S. Noghanian, "AMC integrated textile monopole antenna for wearable applications," *ACES Journal*, vol. 31, no. 6, June 2016.

[7] G. Li, H. Zhai, L. Li, C. Liang, R. Yu, and S. Liu, "AMC-loaded wideband base station antenna for indoor access point in MIMO system," *IEEE Trans. Antennas Propag*., vol. 63, no. 2, pp. 525-533, Feb. 2015.

Ansoft's HFSS, www.ansoft.com

Low-Cost Miniaturized NFC Antenna Design for Mobile Phone

Weijia Li [1,2], Difei Liang [1,2], Liang Chen [1,2], Li Zhang [1,2], and Longjiang Deng [1,2]

[1] National Engineering Research Center of Electromagnetic Radiation Control Materials
University of Electronic Science and Technology of China, Chengdu, 611731, China
LWJ2014@std.uestc.edu.cn, dfliang@uestc.edu.cn, chenliang@uestc.edu.cn, lzhang129@uestc.edu.cn, denglj@uestc.edu.cn

[2] Key Laboratory of Multi-spectral Absorbing Materials and Structures of Ministry of Education
University of Electronic Science and Technology of China, Chengdu, 611731, China

Abstract ─ A low-cost and miniaturized NFC antenna design for mobile phone is proposed. Among all the phone antennas, NFC antenna is the biggest one, thus leading to higher manufacturing costs and adverse conditions for device integration. It is well known that four radiation sides are used in the traditional NFC antennas However, this letter presents a novel single side radiation slender NFC antenna structure, which well solves the adjacent sides reverse current interference through magnetic substrate selectivity laying in the traditional slender NFC antenna. This proposed structure can not only save magnetic substrate materials, but also significantly increase the radiation capacity through asymmetric structure design, and ultimately lead to a 38% increase in the communication performance. Simulation and experiment results verify that this simple design can significantly reduce the cost, suggesting a good prospect in practical use.

Index Terms ─ Magnetic substrate, miniaturization, NFC antenna.

I. INTRODUCTION

NFC system operating at 13.56 MHz allows devices to communicate in a short distance (around 30 mm) through inductive coupling [1]. Owing to a high security level, NFC technology has been used in many fields, such as payment field, public transport field, access control field, etc [2-5]. Consequently, NFC functional modules have been integrated into mobile phones [6,7]. Among all the phone antennas, NFC antenna is the biggest one (usually 35mm × 35mm) [8], which need to be assembled with magnetic substrate to decrease metal environmental disturbance. This makes the cost of NFC antenna 3 to 5 times more expensive than that of other phone antennas. Furthermore, with the continuous improvement of the systems integration of mobile phones, such a large NFC antenna structure is not suitable for device integration. Based on above reasons, NFC antennas with miniaturization and low cost have been the focus of research in this field [9,10]. Slender type NFC antenna structure help reduce antenna dimension. Nevertheless, reverse carry currents of the adjacent sides will decrease space magnetic field, leading to poor antenna radiation performance. Hence, the magnetic field interference of the adjacent sides must be solved. Early researchers point out that wrap one side of slender NFC antenna with magnetic material can effectively decrease the magnetic field interference of adjacent sides, thus achieving good radiation performance [11]. Moreover, Murata company patent indicates that magnetic substrate through slender type NFC antennas would make antenna adjacent sides lie on different sides of magnetic substrate, which results in signal isolation on two adjacent sides. This method well solved NFC antenna miniaturization and radiation problem as well [12].

Previous researches proved that the designs of slender NFC antenna structure and magnetic substrate were beneficial to antenna miniaturization. In this case however, only single side of slender NFC antenna is utilized for radiation, resulting in a well radiation performance. Herein, this paper proposes a novel slender NFC antenna, in which antenna structure and magnetic substrate are combinational designed. The key to realize the miniaturization of slender NFC antennas lies in magnetic field radiation. In order to achieve the purpose of single side radiation, what made it different is that magnetic substrate only lay behind the one side of slender NFC antenna for radiation, and the opposite side lay on the metal environment. It is well known that NFC antennas usually affix to metal environment (in the main-board/battery of mobile phone in actual applications). The side on the magnetic substrate could emit magnetic field to the space. However, eddy current will offset most magnetic field of the side on the metal environment. In this way, it effectively decreases the interference of two adjacent sides, and thus forms well radiation field.

Submitted On: November 13, 2018
Accepted On: June 10, 2019

In order to further improve the antenna radiation performance, the effect of line width and magnetic substrate area and permeability on the radiation characteristics of antennas are studied. The results indicate that the asymmetric antenna structure can obviously improve radiation performance of the antenna.

II. ANTENNA DESIGN

A. Radiation line width optimization

Different from the traditional NFC antenna, only single side is used for radiation of the slender NFC antenna. Therefore, the distribution width of the antenna magnetic field is related to the total linewidth of the radiation side, as shown in Fig. 1 (b). According to the NFC Forum standard [13], the measurement diameter of the 000 plane is 10 mm, as shown in Fig. 1 (a). Hence, the total linewidth of radiation side should be closed to 10 mm, which lie in the range of the magnetic field distribution. NFC antenna is formed by several turns of planar spiral line, if radiation side total linewidth and turn number are fixed, then how to set each turn width will become an important factor that influence the antenna space magnetic field distribution.

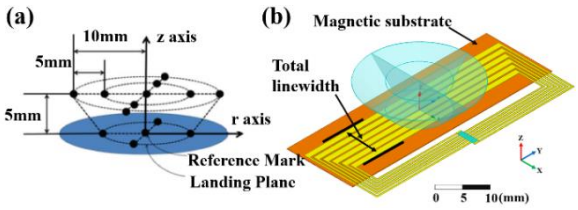

Fig. 1. NFC Forum standard testing zone: (a) test area and (b) slender NFC antenna structure with single side radiation.

The magnetic induction intensity of the long straight-line current in space can be expressed as equation (1) [14]. The magnetic field generated by the radiation side of slender NFC antenna is theoretically equivalent to the superposition of magnetic fields in space by multiple long straight-line currents. The different line width of antenna can be considered as different evenness currents in different lines. Assuming there are two parallel current lines, the distance between each line is L originally, and then each line splits into multiple lines. This model can be expressed as the magnetic field distribution variation with the current density or line width. The expression of spatial magnetic field can be written in equation (2), where L represents line distance, and N represents split number. Figure 2 shows the curve of the magnetic field intensity versus line split number at the height of symmetry center 30mm, where L is set to 10mm, and total current I is set to 1 A. It can be found that, the more uniform the current is distributed, the wider the magnetic field is distributed. Hence, as for the slender type NFC antenna, wide wire width is better for radiation performance under the same total linewidth and turn number:

$$\vec{B}=\vec{e_\phi}\frac{\mu_0 I}{2\pi r}=\frac{y\mu_0 I}{2\pi\left(x^2+y^2\right)}\cdot\vec{e_x}+\frac{x\mu_0 I}{2\pi\left(x^2+y^2\right)}\cdot\vec{e_y}, \quad (1)$$

$$\vec{B}=\sum_{n=-N}^{2N}\left(y\mu_0 I\Big/4\pi N\left(\left(x-\frac{L}{2N}\cdot n\right)^2+y^2\right)\cdot\vec{e_x}+\left(x-\frac{L}{2N}\cdot n\right)\mu_0 I\Big/4\pi N\left(\left(x-\frac{L}{2N}\cdot n\right)^2+y^2\right)\cdot\vec{e_y}\right) \quad (2)$$

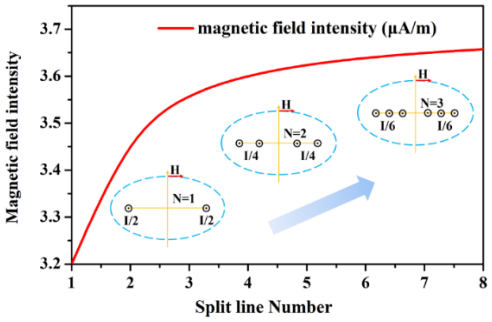

Fig. 2. The curve of the magnetic field intensity versus line split number.

B. Magnetic substrate area optimization

Another key factor that affects the performance of NFC antennas is the magnetic substrate. NFC antenna is always integrated on battery or mainboard of the smartphone, so the magnetic substrate is assembled to shield the impact of metal environment in the phone. Generally, NFC antenna is the same size as the designed magnetic substrate, which is placed between the antenna and metal environment. If magnetic substrate area is larger than that of NFC antenna, whose performance gets better. However, the traditional NFC antenna is large enough to have good performance, leading to less attention to magnetic substrate structure. As for the slender NFC antenna, magnetic substrate width is wider than the total linewidth, which results in obvious improvement in radiation performance. Hence, it is needed to balance the size and performance of the magnetic substrate.

In order to set the width of magnetic substrate we have a hypothesis that a long straight-line current flow above the magnetic substrate, whose permeability is high enough. In this case, both of substrate thickness and metal environment have no influence on the magnetic field of antenna (actually, the permeability of the ferrite magnetic substrate is very high indeed). Applying mirror principle, the single current generates double the magnetic field intensity in the semi-infinite space [15]. Equation (3) can be formed from the integration of Equation (1), the distribution of magnetic flux around the line current can be obtained according to Equation (3),

where a represents line current radius, b represents magnetic substrate width. Figure 3 is the curve of magnetic flux versus magnetic substrate width, where a is 0.1mm, and total current I is 1 A. It is can be found that, the growth rate of magnetic flux e decreases with the substrate width, which results in a decrease in the space magnetic field. As shown in Fig. 3, the 80% area integral is set to be the dividing point, and then a suitable width can be found as a reasonable distance of the magnetic substrate to exceed the radiation side of the antenna:

$$\Phi=\int_a^b \overrightarrow{e_y}\frac{\mu_0 I}{2\pi x}dx=\frac{\mu_0 I}{\pi}\ln\frac{b}{a}. \quad (3)$$

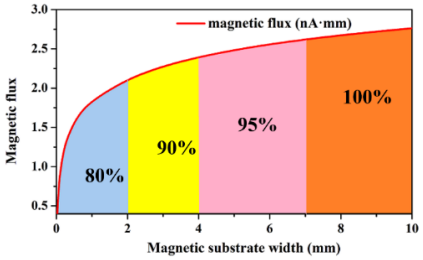

Fig. 3. The curve of magnetic flux versus magnetic substrate width.

C. Magnetic substrate permeability optimization

The magnetic permeability of the antenna substrate also has a great influence on the radiation performance of the NFC antenna. When the NFC antenna structure is fixed, the radiation performance can be reflected from the side of the antenna inductance. In this paper, the magnetic substrate thickness is 0.15mm for the designed NFC antenna. Figure 4 shows the simulation curve of NFC antenna inductance versus magnetic substrate permeability. It can be seen that the change rate of antenna inductance is less than 10% when the permeability exceeds 100. Which is due to the saturated magnetic field passing through the magnetic substrate. This result further conforms Hurley's computational theory [15]. Therefore, the permeability of the magnetic substrates is set to 150, which is also a common parameter of magnetic substrates in the current engineering applications.

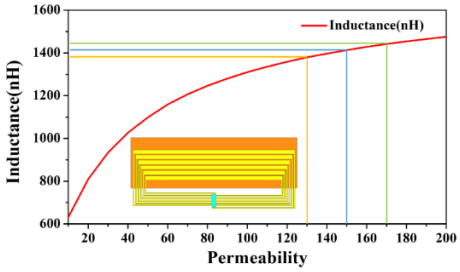

Fig. 4. The curve of NFC antenna inductance versus magnetic substrate permeability.

D. Antenna structure

In order to verify the design ideas above-mentioned, three types NFC antenna are built to illustrate the structural and radiation characteristics. As shown in Fig. 5, they are named, normal slender NFC antenna, single radiation (symmetry) slender NFC antenna and single radiation (asymmetric) slender NFC antenna, respectively. The orange square represents magnetic substrate with thickness of 0.015mm, permeability of 150 at 13.56MHz, and magnetic loss tangent of 0.02 at 13.56MHz. For normal slender NFC antenna, the overall dimension is 40mm×14mm×0.035mm, and there are 4 turns with width of 0.5mm and line spacing of 0.3mm. For single radiation (symmetry) slender NFC antenna, the dimension is 40mm×14mm×0.035mm, and there are 6 turns, with width of 0.5mm and line spacing of 0.3mm. It should be noted that the magnetic substrate lays under one side. As for single radiation (asymmetry) slender NFC antenna, it has a unique structure with outside dimension of 40mm×14mm×0.035mm. The top wires are design as radiation part with a width of 1mm for each turn, wider than that of the traditional antenna. The width of the magnetic substrate is larger than total-linewidth (2mm) in each side. The line width of leftover sides is 0.3mm and turn spacing is 0.3mm, thinner than those of the traditional antenna, and the leftover sides lay on the metal surface. Antenna inductance means the ability to generate magnetic field, so all these antennas approach the approximative inductance value (around 1400nH).

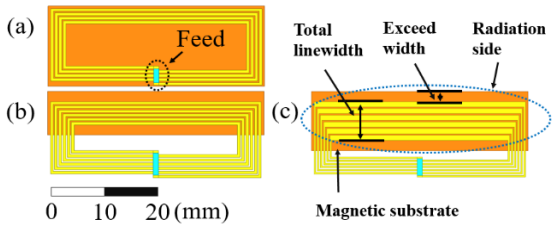

Fig. 5. Structure schematic diagrams for three types of NFC antenna: (a) normal slender NFC antenna, (b) single radiation (symmetry) slender NFC antenna, and (c) single radiation (asymmetric) slender NFC antenna.

Three types of NFC antennas are placed on the metal surface, which simulates the metal environment of mobile phones. Each antenna is excited by the same current source. Figure 6 illustrates the magnetic field distribution on XZ plane, which is the symmetry plane of these NFC antennas. Owing to the different radiation mechanism, normal slender NFC antenna forms a symmetrical field distribution, and single radiation slender NFC antenna forms an asymmetric field distribution. Adjacent sides of slender NFC antenna carry invert current, which generates invert space magnetic field and counteracts each other. In order to acquire better radiation performance, one of the adjacent sides must have no

emission to the space. Although only one side of symmetry antenna emit space magnetic field, a better space field distribution performance is acquired than that of normal one. In order to further improve the radiation capacity of single radiation slender NFC antenna, the wider line and magnetic substrate is adopted for radiation wires, then forms a single radiation (asymmetry) slender NFC antenna structure. Simulation results prove that the space magnetic field strength of single radiation (asymmetry) slender NFC antenna has been further improved.

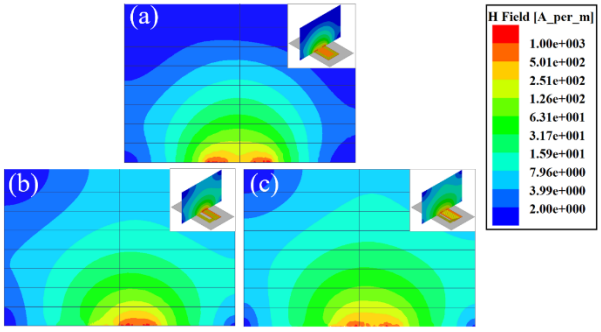

Fig. 6. Magnetic field distribution of three types of NFC antennas: (a) normal slender NFC antenna, (b) single radiation (symmetry) slender NFC antenna, and (c) single radiation (asymmetric) slender NFC antenna.

Vector magnetic field distribution on XZ plane of three types of NFC antenna are shown in Fig. 7. Vector magnetic field around radiation wires appears in form of irregular circles, but only Z-axis component of vector magnetic field can be received by opposed receive antenna. Therefore, when the position where Z-axis component of vector magnetic field tends to zero is identified as the dividing point, the maximum radiation direction of the antenna can be clearly determined. Take the height of 15mm as reference, and the direction angle θ of the NFC antenna can be calculated easily, as shown in Fig. 7. Direction angle θ of single radiation NFC antenna is around 82°, but the normal slender type NFC antenna is only 58°. This means that the reverse currents of adjacent sides of normal slender NFC antenna not only make magnetic field counteract each other, but also make radiation direction to the side position, which is more detrimental to antenna communication. For the single side radiation NFC antennas, the definition of radiation direction helps to point the maximum communication direction.

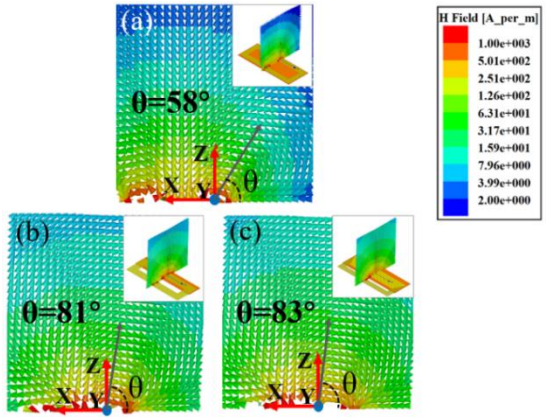

Fig. 7. Vector magnetic field distribution of three types of NFC antenna: (a) normal slender NFC antenna, (b) single radiation (symmetry) slender NFC antenna, and (c) single radiation (asymmetric) slender NFC antenna.

Then, along the direction of maximum radiation, simulation the Z direction magnetic flux (Φ) of the receiving plane in different height. In addition, the dimension of receiving plane is 40mm×30mm, similar with that of traffic card, which convenient to compare with actual card reading measurement later. As shown in Fig. 8, through simulation Φ data, antenna field emission & communication capabilities can be evaluated. The simulation result illustrates that single radiation (asymmetric) slender NFC antenna achieves better emission performance. As shown in Fig. 8, Φ strength of 0.008 Wb (empirical parameter) is acted as reference, and then the communication distance for three types of NFC antenna are 18mm, 21.5mm, 25mm respectively. The result shows that the proposed NFC antenna has a marked improvement in communication distance compared with normal slender NFC antenna.

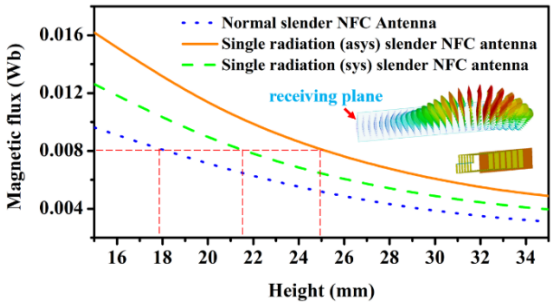

Fig. 8. Simulated magnetic flux (Φ) of the reference receiving plane in different heights.

Figure 9 shows the simulated magnetic field distribution of two typical slender NFC antennas, which are mentioned in the introduction and the proposed NFC structure in this paper. The three types of NFC antennas are basically the same size and have the same inductance. From the magnetic field distribution, it can be seen that under the same inductance value, the radiation intensity of wrap type NFC antenna is slightly lower than that of the other two antennas, because part of the magnetic field is bound to the inside of the magnetic substrate and can not radiate into space, as shown in Fig. 9 (a). Murata company patent slender NFC antenna exhibits good magnetic field radiation ability, and the space radiation field is almost the same as the proposed NFC antenna in this paper. However, its magnetic substrate area is 30% larger than than that of the proposed NFC antenna structurer, as shown in Fig. 9 (b).

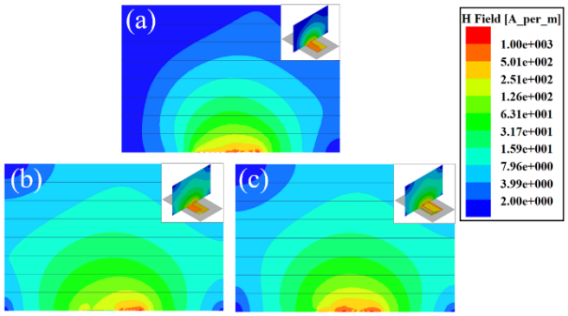

Fig. 9. Magnetic field distribution of two typical slender NFC antenna structures and the proposed NFC structure in this paper: (a) wrap type slender NFC antenna, (b) Murata company patent slender NFC antenna, and (c) single radiation (asymmetric) slender NFC antenna.

Above simulation results prove that, by combining NFC antenna structure and magnetic substrate distribution design, single radiation (asymmetric) slender NFC antenna exhibits a good radiation performance. The following experiments will verify the actual communication performance of this proposed NFC antenna.

III. MEASURED RESULTS

In order to verify the simulation results, three types of NFC antenna are fabricated on PCB board, as shown in Fig. 10. These NFC antennas are equipped with magnetic substrate and laid on the metal surface. The port characteristic of these three types NFC antenna are shown in Table 1. These NFC antennas get approximative volume of inductance, which are similar with simulation results. Owing to more wire turns and metal environment, single radiation slender NFC antennas have higher resistance compared with normal NFC antenna (resistance usually below 5Ω@13.56MHz), leading to lower antenna Q factor and disadvantage to communication. According to the classical π-type matching network of NFC system [16], these three types of NFC antennas are matched to 50Ω, and prepare to the radiation signal strength measurement.

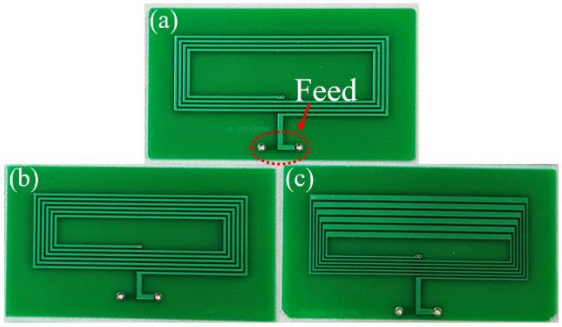

Fig. 10. Three types of fabricated NFC antennas: (a) normal slender NFC antenna, (b) single radiation (symmetry) slender NFC antenna, and (c) single radiation (asymmetric) slender NFC antenna.

Table 1: Port characteristic of three types NFC antennas

NFC Antenna Type	Resistance Ω@13.56MHz	Inductance μH@13.56MHz
Normal slender NFC antenna	3.2	1.51
Single radiation (symmetry) slender NFC antenna	9.5	1.45
Single radiation (asymmetric) slender NFC antenna	9.3	1.4

NFC antennas and receiving sensor are connected to signal generator and oscilloscope, respectively. AC voltage of the signal generator is set to 5V. 4 turns spiral wires are used to forms receive sensor, whose dimension is the same as the traffic card, as shown in Fig. 11. Based on the Faraday law, sensor voltage could change the magnetic flux volume, and then the sensor measurement data and simulation data can be unified. The measurement and simulation results are shown in Fig. 12. Comparison results indicate that measurement results are generally consistent with simulation ones. Because of higher inductance of the fabricated normal slender NFC antenna, measured magnetic flux data of normal slender NFC antenna is higher than the corresponding simulation result. However, the measurement result shows that a lower Q factor of single radiation (asymmetric) slender NFC antenna does not significantly affect the antenna's radiation capability, and the proposed NFC antenna structure exhibits a good magnetic field radiation performance.

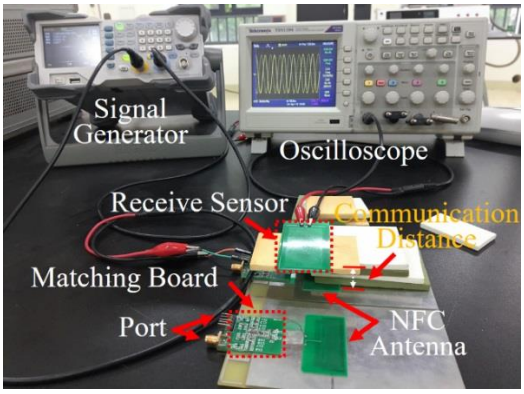

Fig. 11. Aerial view of magnetic flux (Φ) measurement.

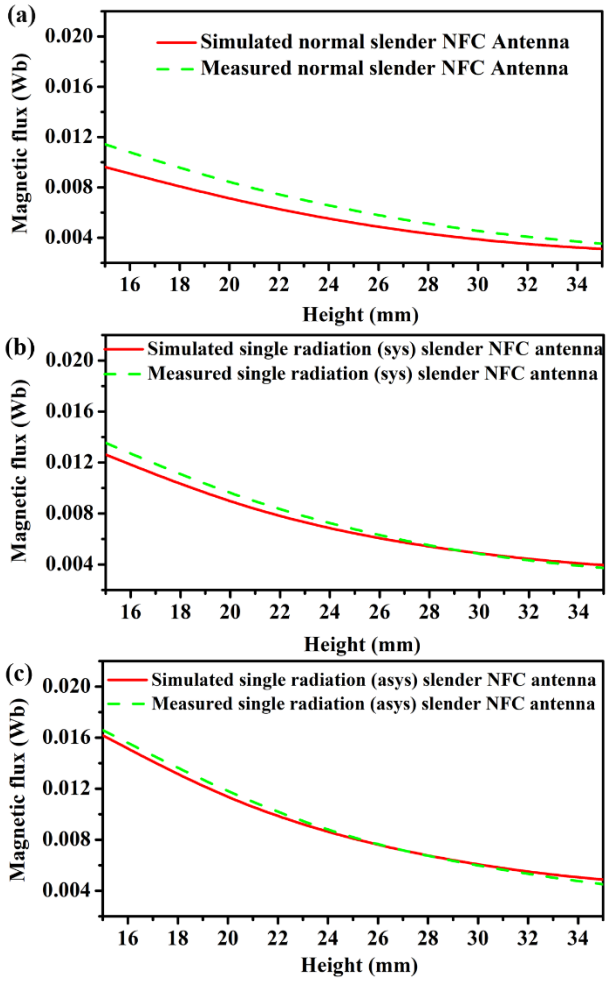

Fig. 12. Measured magnetic flux (Φ) of the reference receiving plane in different heights: (a) normal slender NFC antenna, (b) single radiation (symmetry) slender NFC antenna, and (c) single radiation (asymmetric) slender NFC antenna.

In order to verify the actual communication performance, these antennas are connected to the real smart phone circuit, as shown in Fig. 13. This experimental smart phone is equipped with NXP Company PN548 NFC controller chip, which is widely used in smart phone. All these NFC antennas are connected to the smart phone successively to measure the communication distance with Tag-4 standard NFC card. The measurement results are listed in Table 2. Communication distance of single radiation (asymmetric) slender NFC antenna reaches 25mm, which is a large communication distance for Tag-4 standard NFC card. The measurement results are consistent with the simulation results.

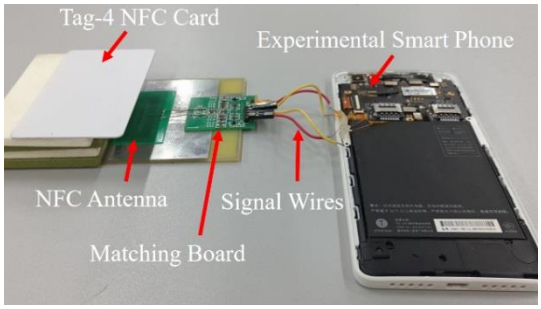

Fig. 13. Aerial view of actual communication distance measurement with Tag-4 NFC card.

Table 2: Communication distance of three type NFC antenna with TAG-4 NFC card

NFC Antenna Type	Communication Distance (mm)
Normal slender NFC antenna	18
Single radiation (symmetry) slender NFC antenna	22
Single radiation (asymmetric) slender NFC antenna	25

IV.CONCLUSION

NFC antenna is applied to the space magnetic field radiation, and a novel slender structure is proposed in this paper. By analyzing the mechanism of NFC antenna radiation, wider lines with magnetic substrate are utilized in the proposed NFC antenna for radiation, and thinner line with metal surface is useful for miniaturization. These two characteristics ultimately lead to the formation of asymmetric slender NFC antenna structure. The mutual interference of adjacent sides of slender NFC antenna has been reduced, resulting in the significant increase of the radiation capacity for NFC antenna. These design methods greatly reduce the NFC antenna size and magnetic substrate consumption, thereby reducing the cost of production. The proposed NFC antenna obtains a good performance of communication distance, simulation and experiment results verify that this proposed design is simple, effective and cost effective, suggesting a good prospect in practical use.

ACKNOWLEDGMENT

This work is supported by Department of Science and Technology of SiChuan Province under Grant Number 2017JY0348.

REFERENCES

[1] V. Coskun, B. Ozdenizci, and K. Ok, "The survey on near field communication," *Sensors (Basel)*, vol. 15, no. 6, pp. 13348-405, 2015.

[2] T. W. C. Brown and T. Diakos, "On the design of NFC antennas for contactless payment applications," *in European Conference on Antennas and Propagation*, Rome, Italy, pp. 44-47, 2011.

[3] O. Sajid and M. Haddara, "NFC mobile payments: are we ready for them?," *in Sai Computing Conference*, London, UK, pp. 960-967, 2016.

[4] U. D. Alan and D. Birant, "Server-based intelligent public transportation system with NFC," *IEEE Intelligent Transportation Systems Magazine*, vol. 10, no. 1, pp. 36-40, 2018.

[5] T. Bauernfeind, et al., "PEEC-based multi-objective synthesis of NFC antennas in the presence of conductive structures," *International Applied Computational Electromagnetics Society Symposium (ACES) IEEE*, vol. 34, no. 2, pp. 339-341, 2018.

[6] J. Fischer, "NFC in cell phones: The new paradigm for an interactive world [Near-Field Communications]," *IEEE Communications Magazine*, vol. 47, no. 6, pp. 22-28, 2009.

[7] P. Baumgartner, et al., "Synthesis of NFC antenna structure under multi-card condition," *Applied Computational Electromagnetics Society Journal*, vol. 33, no. 10, pp. 1161-1163, 2018.

[8] D. Paret, *Antenna Designs for NFC Devices*. John Wiley & Sons, Inc., pp. 82-88, 2016.

[9] H. Saghlatoon, R. M. Boroujeni, M. M. Honari, and P. Mousavi, "Low-cost inkjet printed passive booster for increasing the magnetic coupling in proximity of metal object for NFC systems," *IEEE Microwave & Wireless Components Letters*, vol. 26, no. 12, pp. 996-998, 2016.

[10] B. Lee, B. Kim, F. J. Harackiewicz, B. Mun, and H. Lee, "NFC antenna design for low-permeability ferromagnetic material," *IEEE Antennas & Wireless Propagation Letters*, vol. 13, no. 1, pp. 59-62, 2014.

[11] M. A. Chung and C. F. Yang, "Miniaturized NFC antenna design for a talet PC with a narrow border and metal back-cover," *IEEE Antennas & Wireless Propagation Letters*, vol. 15, pp. 1470-1474, 2015.

[12] A. P. Zhao and H. Chen, "Small size NFC antenna with high performance," *2016 IEEE International Symposium on Antennas and Propagation (APSURSI)*, Fajardo, Puerto Rico, pp. 1469-1470, 2016.

[13] NFC Analog Specification ANALOG 1.0 NFCForum-TSAnalog-1.0, *NFC Forum Standard*, 2012-07-11. http://www.nfc-forum.org/specs/

[14] D. K. Cheng, *Field and Wave Electromagnetics*. Addison-Wesley, 1983.

[15] W.G. Hurley and M.C. Duffy, "Calculation of self-and mutual impedances in planar sandwich inductors," *IEEE Transactions on Magnetics*, vol. 33, no. 3, pp. 2282-2290, 1997.

[16] N. Semiconductors, Eindhoven, and T. Netherlands, "AN 11363 PN547_C2 Antenna design guide," vol. Appl. Note 2.4, 2013.

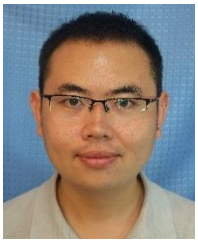

Weijia Li was born in Hebei, China, in 1986. He received the M.S. degree in Electronic Science and Technology from the University of Electronic Science and Technology of China, Chengdu, China, in 2013, and is currently working toward the Ph.D. degree at the University of Electronic Science and Technology of China.

His recently research activities have focused on the NFC antenna design and their applications in antenna test, magnetic material application, and wave absorber.

Difei Liang received the M.S. degree in Electronic Materials and Components from the University of Electronic Science and Technology of China (UESTC), Chengdu, China, in 2009.

He has worked as a Full Professor with the National Engineering Research Center of Electromagnetic Radiation Control Materials, UESTC. His research interests include magnetic material and devices, functional macromolecule, and electromagnetic absorbing structure.

A Low Frequency Ultra-Wideband Electrically Small Monopole Antenna for HF/VHF Application

Yinfeng Xia [1], Wei Xue [1], Yingsong Li [1,2,*], Wanlu Shi [1], Beiming Li [1]

[1] College of Information and Communication Engineering
Harbin Engineering University, Harbin, Heilongjiang 150001, China
*liyingsong@ieee.org

[2] Key Laboratory of Microwave Remote Sensing, National Space Science Center
Chinese Academy of Sciences, Beijing 100190, China

Abstract ─ In this paper, a low frequency ultra-wideband electrically small monopole antenna (ESMA) with a non-foster circuit (NFC) loading for HF/VHF application is proposed. The devised ESMA has a very small height of 30 cm at 18 MHz, whose performance is severely limited due to the electrically small size characterized by large reactance and small radiation resistance. To conquer the limitation of the passive matching method, a NFC is developed and properly designed to cancel out the large reactance of ESMA and broaden the bandwidth. In this paper, the design principle is presented in detail for devising an ESMA system. At last, circuit and electromagnetism co-simulation is constructed to make the results more accurate and convinced. The simulated and measured results indicate that a -10 dB fractional bandwidth of 169% ranging from 18 MHz to 218 MHz is obtained for the designed ESMA matched by the NFC.

Keywords ─ Electrically small monopole antenna, non-foster circuit, ultra-bandwidth.

I. INTRODUCTION

High frequency (HF) band (3-30 MHz) and very high frequency (VHF) band (30-300 MHz) are very popular for radio frequency communications due to their long wavelength, which is appropriate for long-range wireless communications including long-range military communication, frequency modulation (FM) broadcasting, amateur radio, and so on. As an intrinsic and essential component in wireless communication systems, antennas usually exist with the form of large size and perform narrow bandwidth for HF/VHF band applications, which are not always feasible choice. Hence, electrically small antennas (ESAs) are developed for HF and VHF applications owing to their advantage of small electrically size. However, the previously designed ESAs have high-Q impedances characterized by large reactance and small radiation resistance [1-3], which make them difficult to match together. Generally, the passive matching method is the first choice to match the ESAs. Nevertheless, these ESAs matched by the passive matching networks usually lead to a narrow operation band [4].

As is known to us, the non-foster element means the Foster reactance theorem is violated. For example, the element can be designed to provide a negative capacitor or inductor characteristic. In this regard, the non-foster element enables to cancel the high-Q impedance in ESA designs, which of course, can broaden its bandwidth. The first NFC, constructed via negative impedance converters (NICs), was devised and tested by Linviill in 1953 [5]. After that, many NFCs have been utilized to match ESAs. However, most of them are developed based on simulation analyses with ideal models [6-13]. Several early reports have verified the performance of NFC matched ESAs by experimental investigations [14-17]. Theoretically, ESAs matched by NFC can get a very wide frequency band. However, so far, only a few references have reported the achievement of wideband ESAs matched using NFCs [18-20]. Unfortunately, most of them are operated over 30 MHz, while lower frequency band is lack of consideration.

In this paper, a 30-cm ESMA is designed for HF/VHF bands. To enhance its bandwidth, a conventional passive network is utilized to match the ESMA, which leads to a narrow bandwidth. To overcome the limitation of the passive matching method, a floating NFC is developed based on the concept in [21], where the stability of the floating NFC is analyzed and demonstrated. The design procedure of the NFC matched ESMA is given in this paper. To increase the experimental accuracy, the layout of the designed NFC has been analyzed in HFSS and a co-simulation between circuits and electromagnetic is accomplished. The simulated and measured results indicate that a -10 dB fractional bandwidth of 169% ranging from 18 MHz to 218 MHz is achieved for the NFC matched ESMA. And the measured results are in agreement with the simulation ones.

Submitted On: May 4, 2019
Accepted On: June 6, 2019

II. ANALYSIS OF THE ELECTRICALLY SMALL MONOPOLE ANTENNA

In this paper, an ESMA that consists of a hollow aluminum conductor, a brass ground plane and a probe-fed with N-type connector is devised. The ESMA has a height of H1=300 mm and a radius of 20 mm, which is installed on a FR4 substrate with a thickness of 2 mm and a size of L×W=200×160 mm^2. A brass ground plane is printed under the FR4 substrate with the same size, which is designed to meet the requirement of the platform in our project empirically. The antenna model is implemented and analyzed in the HFSS. In addition, a hollow cylinder with the height of H2=240 mm and a radius of 10 mm is also removed from inside of the ESMA to lighten its weight and make it easy to install. The model of the ESMA is presented in Fig. 1

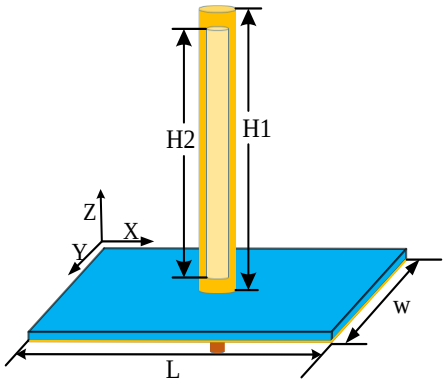

Fig. 1. The geometry of the designed ESMA.

The designed ESMA is simulated and optimized based on the HFSS. To verify the performance of the simulated ESMA, the proposed antenna is also fabricated and measured. The comparison of the simulated and measured reflection coefficients (S11s), real part, imaginary part of input impedance are demonstrated in Figs. 2, 3, and 4, where the measured results are obtained by utilizing the Keysight ENA Series Network Analyzer E5061B.

In Fig. 2, we can see that the antenna is not matched with 50 Ω, and the real is very small given in Fig. 3. From Fig. 4, the simulated imaginary part of the proposed antenna is consistent with the measured result. While there is a little discrepancy between the simulated real part, reflection coefficients and the measured results, which may be caused by the fabrication error and the soldering in the experiments. Anyhow, the simulated and measured input impedance imply that the devised ESMA like other ESAs is still characterized by large reactance and small radiation resistance as observed in Fig. 3 and Fig. 4, which will lead to the mismatch for the ESMA as shown in Fig. 2. Thus, extra effort is needed to increase the bandwidth of the ESMA.

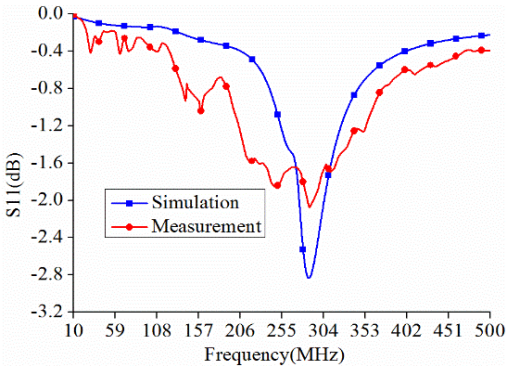

Fig. 2. The reflection coefficients of the ESMA.

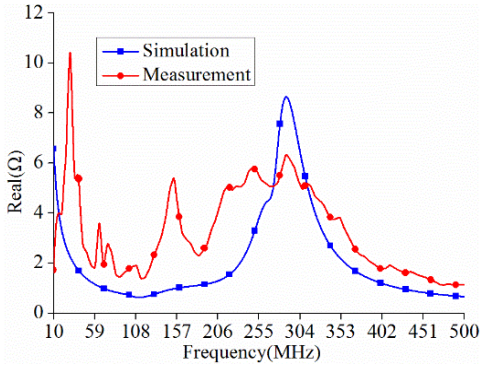

Fig. 3. The real part of the ESMA.

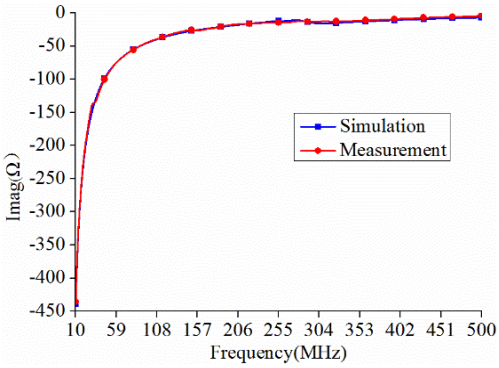

Fig. 4. The imaginary part of the ESMA.

Generally, conventional matching method to broaden the bandwidth of the ESAs is to employ a passive matching network that is composed of some inductors and capacitances in parallel. Like other ESAs, the devised ESMA matched by the passive matching network is presented in Fig. 5, where an inductor and capacitance are utilized, and the simulated S-parameter file of the ESMA is exported into the circuit. Different optimized values of C and L are set to get different operating bandwidth. The results are shown in Fig. 6 and Table 1.

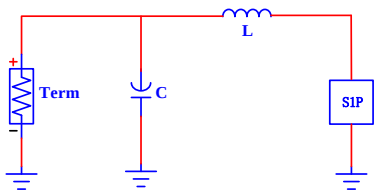

Fig. 5. The schematic of passive matching for the ESMA.

From Fig. 6 and Table 1, it can be concluded that the ESMAs matched by four different passive matching networks all have a fairly narrow fractional bandwidth. Moreover, the fractional bandwidth decreases with the operating center frequency shifting toward lower frequency, which means that the lower the frequency band is, the more difficult it is for the ESMA to be matched by using passive matching network. This circumstance can be explained by [2, 3, 22]:

$$B_v = \frac{1}{\eta}\frac{1}{Q}\frac{VSWR-1}{\sqrt{VSWR}}, \quad (1)$$

$$Q = \frac{1}{ka} + \frac{1}{(ka)^3}, \quad (2)$$

where Q is the quality factor, k is the wavenumber ($2\pi/\lambda$), a is the radius of the smallest sphere enclosing the entire antenna system, η is the radiation efficiency, VSWR is the voltage standing wave radio, B_v is the fractional bandwidth of the antenna, respectively. According to (1) and (2), B_v is inversely proportional to Q, while Q is inversely proportional to k. Thus, B_v is proportional to the frequency, which implies that the passive network matched ESMA will lead to narrow bandwidth especially at lower frequency band. To overcome the limitation of the passive matching method, a floating NFC is developed to enhance the bandwidth of the ESMA in this paper.

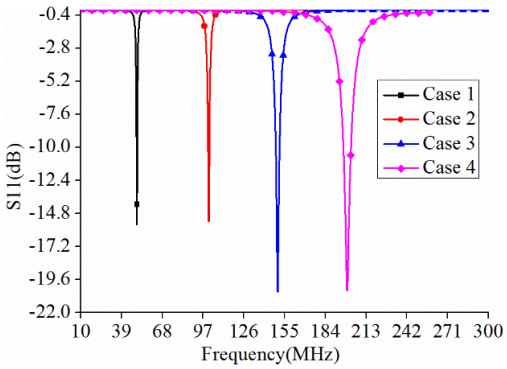

Fig. 6. The reflection coefficients of the passive network matched ESMA.

Table 1: The results of different cases

	C (pF)	L (nH)	Frequency Band (MHz)	Fractional Bandwidth
Case 1	324	313	49.7-50.1	0.8%
Case 2	222	80	99.5-100.5	1%
Case 3	138	37	148.7-151.4	1.8%
Case 4	91	22	196.9-202.1	2.6%

III. NON-FOSTER CIRCUIT MATCHING FOR THE DESIGNED MONOPOLE ANTENNA

In this section, a floating NFC is utilized to match the ESMA. The basic model of a floating NFC is shown in Fig. 7, where port 2 is terminated with the device to be matched by adjusting the load Za, and port 1 is connected with a 50-ohm transmission line. The floating NFC is functioned as a negative inductor or capacitance, which is determined by the impedance of Za.

To choose the proper value of Za, an ideal matching circuit consisting of two ideal elements is constructed to offset the reactance of the ESMA as is demonstrated in Fig. 8. The simulation result is given in Fig. 9, where the major imaginary part of the ESMA is canceled by using the ideal circuit from 10 MHz to 300 MHz. The negative capacitance and negative inductor are -36 pF and -3 nH, respectively.

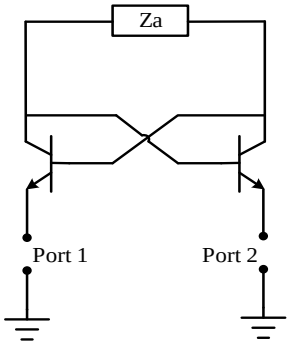

Fig. 7. The model of a floating NFC.

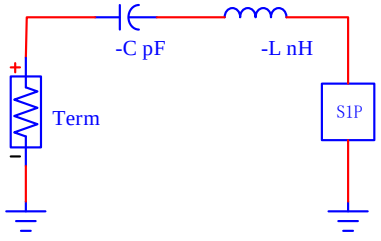

Fig. 8. Ideal matching circuit for the ESMA.

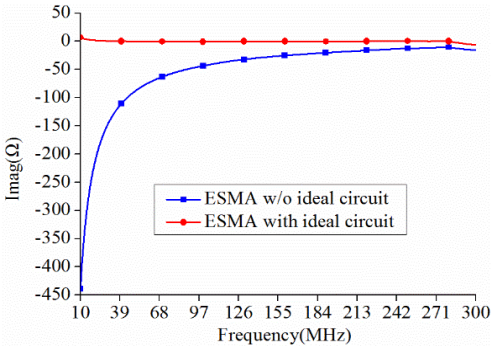

Fig. 9. The imaginary part of the ESMA with/without ideal circuit.

According to the basic model, a floating NFC is built in Fig. 10, where C_block is set to block DC signal and Lb is used to keep the AC signal from disturbing of the DC bias circuit that consists of Rb1, Re1, DC_V1 and Rb2, Re2, DC_V2. The BJT1 and the BJT2 are implemented by NE85633_19960601. The C_load and L_load are employed to cancel the imaginary part of the ESMA, whose values are based on the results of the ideal circuit presented in Fig. 8. To decrease the loss of the NFC, the R_load can be properly adjusted. The simulated results are shown in Fig. 11.

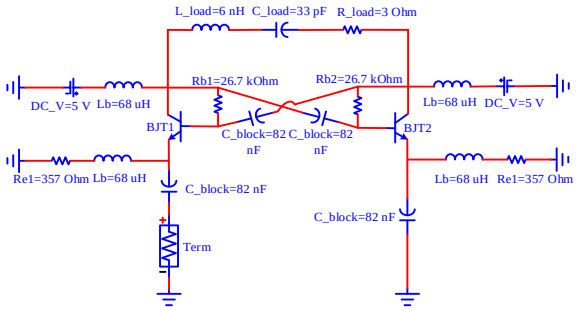

Fig. 10. The designed non-foster circuit.

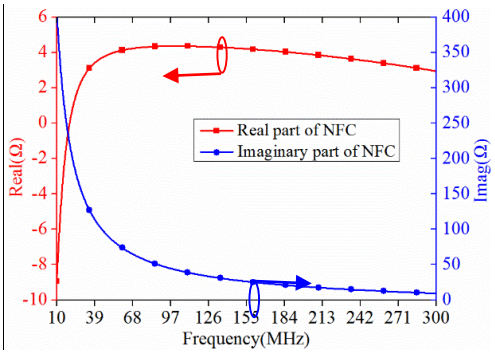

Fig. 11. The input impedance of the designed NFC.

From Fig. 11, the real part of the input impedance is greater than 0 Ω and less than 5 Ω from 20 MHz to 300 MHz, which can guarantee the stability and small loss of the designed NFC in the operating band. The imaginary part of the input impedance acts as the characteristic of a negative capacitance. According to the formula (3):

$$C = -\frac{1}{2\pi \cdot freq \cdot imag(Zin)} \times 10^{12} (pF), \qquad (3)$$

where *imag(Zin)* is the imaginary part of input impedance, the equivalent negative capacitance of the NFC and ideal circuit can be calculated, which is shown in Fig. 12. By comparing the two lines, it is found that the equivalent capacitance of the NFC is in agreement with that of the ideal circuit. In other words, the designed NFC with small loss and good stability is quite good for matching the ESMA.

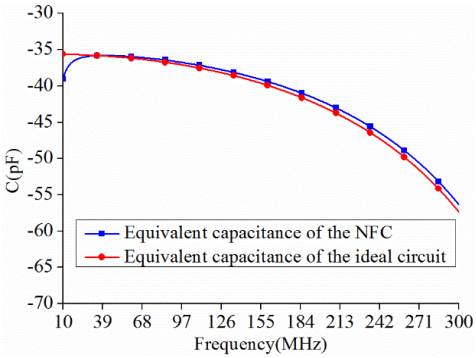

Fig. 12. Equivalent negative capacitance of the designed NFC and ideal circuit.

Based on the former simulation analyses, the entire antenna system is constructed in Fig. 13, where term 1 is connected with a 50-ohm transmission line and the input impedance of the designed ESMA is exported into the term 2 functioning as the ESMA. The NFC, as designed in Fig. 10, is utilized to cancel the large reactance of the ESMA. In addition, a Balun balance-unbalance transformer is employed, which is set to make the real part of the ESMA match to the 50 Ω connector. The simulated results are presented in Fig. 14.

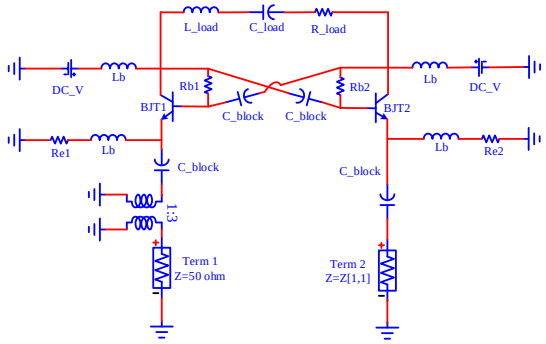

Fig. 13. The schematic of the entire antenna system.

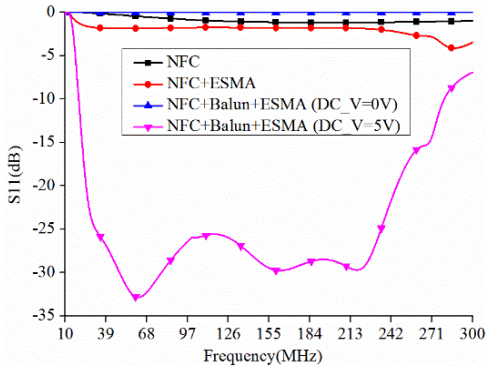

Fig. 14. S11 of the matched and unmatched ESMA.

Figure 14 compares the reflection coefficients of the NFC, the NFC matched to ESMA, and the NFC matched to ESMA with Balun when the voltage resource DC_V turns off/on. It is found that a wide bandwidth can be achieved only when the ESMA is matched by the designed NFC with Balun and DC_V turns on. The obtained wide bandwidth ranges from 20 MHz to 280 MHz, which provides a fractional bandwidth of 173%. The results also demonstrate that this matching method for the ESMA is certainly more effective than the passive matching, especially at lower operating band.

In fact, the NFC is a particularly sensitive circuit, whose performance may be greatly influenced by the parasitic of the circuit layout. To get more precise simulation results, the layout of the designed NFC is modeled and simulated in the HFSS which is shown in Fig. 15, where the lumped ports are utilized to connect the active and passive components. The simulated S-parameter model of the layout is exported into the ADS to construct the co-simulation environment. The results are given, which aims to give a better guidance for the fabrication of the NFC.

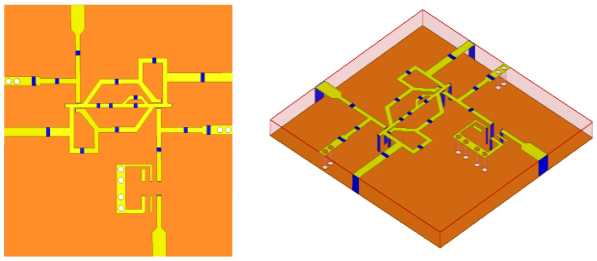

(a) Top view (b) Side view

Fig. 15. The layout of the devised NFC.

To verify the simulation results, the antenna system including the ESMA and the designed NFC is fabricated, which is presented in Fig. 16. All the results are shown in Fig. 17.

From Fig. 17, it can be found that the designed NFC matched ESMA will be mismatched when the simulated layout model is exported into the co-simulation without optimization. It is implied that the layout has great impact on the performance of the designed antenna system. At last, we optimize the values of C_load (35 pF) and L_load (22 nH) to eliminate the effect of the layout, and then, a -10 dB fractional bandwidth of 169% ranging from 18 MHz to 218 MHz is obtained and verified by the experiment. The measured return loss is almost in agreement with the simulated result. There is some difference at lower bands, which may be caused by the fabrication error, the soldering and the parasitic effects of the electronic components.

To better understand the principle of the NFC matching of the ESMA, the measured input impedance of the entire antenna system is presented in Fig. 18. From Fig. 18, the imaginary part of the input impedance is about 0 Ω from 18 MHz to 218 MHz, which indicates the reactance of the ESMA has been well canceled by the designed NFC. The real part of the input impedance is about 50 Ω from 18 MHz to 218 MHz, which means that the entire antenna system has been matched to a 50 Ω connector.

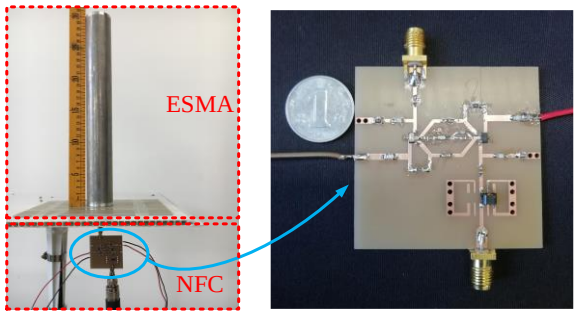

Fig. 16. The fabricated antenna system.

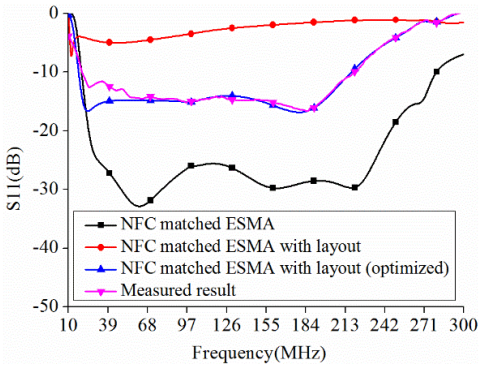

Fig. 17. Simulated and measured return loss.

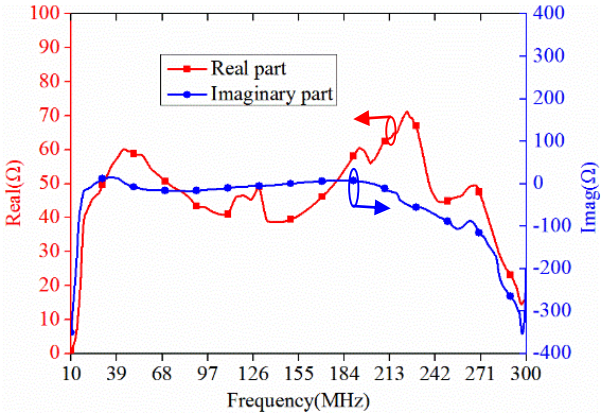

Fig. 18. The measured input impedance of the entire antenna system.

At last, the gain measurement of the fabricated NFC matched ESMA is constructed on a professional test ground, which is shown in Fig. 19. In the process of the measurement, three-antenna method is utilized, which is a popular method for the measurement of this frequency band. The measured results are presented in Fig. 20.

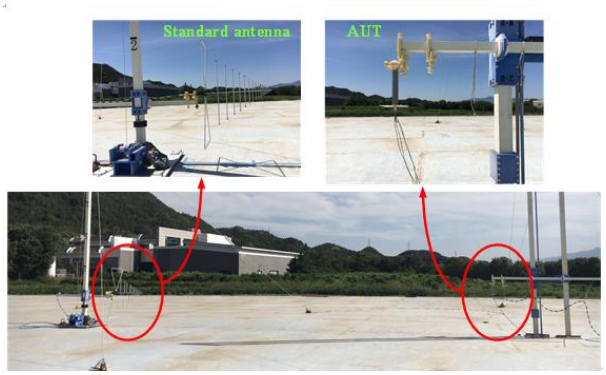

Fig. 19. The measurement setup of the NFC matched ESMA.

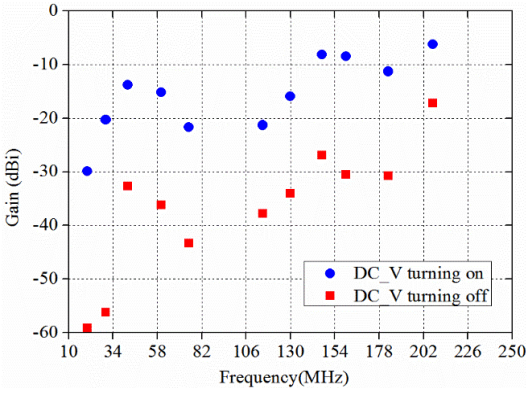

Fig. 20. The measured gain of the NFC matched ESMA.

From Fig. 20, it can be concluded that the gain is improved by about 10 dB when the DC_V turning on in comparison with that the DC_V is off. The results demonstrate that the gain of the ESMA matched by the NFC can be greatly enhanced especially at low frequency band. Moreover, the maximum gain reaches to -6.2 dBi at 207 MHz, which is a good result for the ESMA.

IV. CONCLUSION

In this paper, a 30-cm electrically small monopole antenna is designed for the HF/VHF bands. A non-foster circuit is developed to match the electrically small monopole antenna, which has been conformed to be more effective than the conventional passive matching method. Besides, the design procedure is presented in detail, and an electromagnetic and circuit co-simulation is presented to guarantee the experimental accuracy. The simulation results also verify the great effect of the layout on the performance of entire antenna system. Finally, a -10 dB fractional bandwidth of 169% is obtained, which is also proved by the measured result. In the future, the proposed technique can be used for active metamaterial developments [23] and integrated into the wideband MIMO antenna decoupling [24-31].

ACKNOWLEDGMENTS

This work was partially supported by the National Key Research and Development Program of China (2016YFE111100), Key Research and Development Program of Heilongjiang (GX17A016), the Science and Technology innovative Talents Foundation of Harbin (2016RAXXJ044), the Natural Science Foundation of Beijing (4182077), China Postdoctoral Science Foundation (2017M620918) and the Fundamental Research Funds for the Central University (HEUCFG201829, 3072019CFG0801).

REFERENCES

[1] H. A. Wheeler, "Fundamental limitations of small antennas," *Proc. IRE*, vol. 35, no. 12, pp. 1479-1484, Dec. 1947.

[2] L. J. Chu, "Physical limitations of omni-directional antennas," *J. Appl. Phys.*, vol. 19, no. 12, pp. 1163-1175, May 1948.

[3] J. S. McLean, "A re-examination of the fundamental limits radiation Q of electrically small antenna," *IEEE Trans. Antennas Propag.*, vol. 44, no. 5, pp. 672-676, May 1996.

[4] R. M. Fano, "Theoretical limitations on the broad-band matching arbitrary impedances," *J. Franklin Inst.*, vol. 249, no. 1, pp. 57-83, 1950.

[5] J. G. Linvill, "Transistor negative impedance converters," *Proc. IRE*, vol. 41, no. 6, pp. 725-729, June 1953.

[6] P. Jin and R. W. Ziolkowski, "Broadband, efficient, electrically small metamaterial-inspired antennas facilitated by active near-field resonant parasitic elements," *IEEE Trans. Antennas Propag.*, vol. 58, no. 2, pp. 318-327, Feb. 2010.

[7] Z. Ning and R. W. Ziolkowski, "Active metamaterial-inspired broadbandwidth, efficient, electrically small antennas," *IEEE Antennas Wireless Propag. Lett.*, vol. 10, pp. 1582-1585, 2011.

[8] M. Barbuto, A. Monti, F. Bilotti, and A. Toscano, "Design of non-foster actively loaded SRR and application in metamaterialinspired components," *IEEE Trans. Antennas Propag.*, vol. 61, no. 3, pp. 1219-1227, Mar. 2013.

[9] M. Tang, T. Shi, and R. W. Ziolkowski, "Electrically small, broadside radiating huygens source antenna augmented with internal non-foster elements to increase its bandwidth," *IEEE Antennas Wireless Propag. Lett.*, vol. 16, pp. 712-715, Aug. 2016.

[10] J. Church, J. C. S. Chieh, L. Xu, J. D. Rockway, and D. Arceo, "UHF electrically small box cage loop antenna with an embedded non-foster load," *IEEE Antennas Wireless Propag. Lett.*, vol. 13, pp. 1329-1332, July 2014.

[11] S. Koulouridis and J. L. Volakis, "Non-foster circuits for small broadband antennas," *2009 IEEE Antennas and Propagation Society International Symposium*, Charleston, South Carolina, USA, July 2009.

[12] Y. Xia, Y. Li, and S. Zhang, "A non-foster matching circuit for an ultra-wideband electrically small antenna," *13th European Conference on Antennas and Propagation*, Krakow, Poland, 2019.

[13] J. T. Aberle, "Two-port representation of an antenna with application to non-foster matching networks," *IEEE Trans. Antennas Propag.*, vol. 56, no. 5, pp. 1218-1222, May 2008.

[14] N. Zhu and R. W. Ziolkowski, "Design and measurements of an electrically small, broad bandwidth, non-Foster circuit-augmented protractor antenna," *Appl. Phys. Lett.*, vol. 101, no. 2, July 2012.

[15] T. Shi, M. Tang, Z. Wu, H. Xu, and R. W. Ziolkowski, "Improved signal-to-noise ratio, bandwidth-enhanced electrically small antenna augmented with internal non-Foster elements," *IEEE Trans. Antennas Propag.*, vol. 67, no. 4, pp. 2763-2768, Jan. 2019.

[16] S. E. Sussman-Fort and R. M. Rudish, "Non-foster impedance matching of electrically-small antenna," *IEEE Trans. Antennas Propag.*, vol. 57, no. 8, pp. 2230-2241, June 2009.

[17] H. Mirzaei and G. V. Eleftheriades, "A resonant printed monopole antenna with an embedded non-foster matching network," *IEEE Trans. Antennas Propag.*, vol. 61, no. 11, pp. 5363-5371, Nov. 2013.

[18] C. R. White, J. S. Colburn, and R. G. Nagele, "A non-foster VHF monopole antenna," *IEEE Antennas Wireless Propag Lett.*, vol. 11, pp. 584-587, June 2012.

[19] Z. Huang, H. Yang, and T. Liu, "Influence analysis of transmission lines on a stable non-foster-loaded electrically small dipole," *Int. J. Antennas Propag.*, vol. 2019, Article ID: 1273574, Jan. 2019.

[20] M. M. Jacob and D. F. Sievenpiper, "Non-foster matched antennas for high-power applications," *IEEE Trans. Antennas Propag.*, vol. 65, no. 9, pp. 4461-4469, Sept. 2017.

[21] A. M. Elfrgani and R. G. Rojas, "Stability of non-Foster circuits for broadband impedance matching of electrically small antennas," *2015 IEEE Radio and Wireless Symposium*, San Diego, CA, USA, June 2015.

[22] A. D. Yaghjian and S. R. Best, "Impedance, bandwidth, and Q of antennas," *IEEE Trans. Antennas Propag.*, vol. 53, no. 4, pp. 1298-1324, Aug. 2005.

[23] Y. Fan, "Research and Design of Non-foster Active Metamaterial," *Ph.D. Thesis*, Queen Mary, University of London, UK, 2013.

[24] S. Luo, Y. Li, Y. Xia, and L. Zhang, "A low mutual coupling antenna array with gain enhancement using metamaterial loading and neutralization line structure," *Applied Computational Electromagnetics Society Journal*, vol. 34, no. 3, pp. 411-418, 2019.

[25] K. Yu, Y. Li, and X. Liu, "Mutual coupling reduction of a MIMO antenna array using 3-D novel meta-material structures," *Applied Computational Electromagnetics Society Journal*, vol. 33, no. 7, pp. 758-763, 2018.

[26] T. Jiang, T. Jiao, Y. Li, and W. Yu, "A low mutual coupling MIMO antenna using periodic multi-layered electromagnetic band gap structures," *Applied Computational Electromagnetics Society Journal*, vol. 33, no. 3, pp. 305-311, 2018.

[27] T. Jiang, T. Jiao, and Y. Li, "Array mutual coupling reduction using L-loading E-shaped electromagnetic band gap structures," *International Journal of Antennas and Propagation*, vol. 2016, Article ID:6731014, pp. 1-9, 2016.

[28] L. Zhao, F. Liu, X. Shen, G. Jing, Y. Cai, and Y. Li, "A high-pass antenna interference cancellation chip for mutual coupling reduction of antennas in contiguous frequency bands," *IEEE Access*, vol. 6, pp. 38097-38105, 2018.

[29] Y. Kong, Y. Li, and W. Yu, "A minimized MIMO-UWB antenna with high isolation and triple band-notched functions," *Frequenz*, vol. 70, no. 11-12, pp. 463-471, 2016.

[30] Y. Li, W. Li, and W. Yu, "A multi-band/UWB

MIMO/diversity antenna with an enhance isolation using radial stub loaded resonator," *Applied Computational Electromagnetics Society Journal*, vol. 28, no. 1, pp. 8-20, 2013.

[31] S. Luo, Y. Li, Y. Xia, G. Yang, L. Sun, and L. Zhao, "Mutual coupling reduction of a dual-band antenna array using dual-frequency metamaterial structure," *Applied Computational Electromagnetics Society Journal*, vol. 34, no. 3, pp. 403-410, 2019.

A Novel Frequency Reconfigurable Polarization Converter Based on Active Metasurface

Guangyao Liu, Jiaqi Han, Xiaohe Gao, Haixia Liu*, and Long Li**

Key Laboratory of High Speed Circuit Design and EMC of Ministry of Education
School of Electronic Engineering, Collaborative Innovation Center of Information Sensing and Understanding
Xidian University, Xi'an 710071, China
*hxliu@xidian.edu.cn, **lilong@mail.xidian.edu.cn

Abstract ─ In this paper, a novel frequency reconfigureable polarization converter (FRPC) based on active metasurface tuned by positive-intrinsic-negative (PIN) diodes is proposed. The metasurface unit cell of the FRPC consists of truncated metal square patches and bias lines, which are all etched on a substrate backed by a metal ground. On one hand, the FRPC can convert linearly polarized waves along the *x*- and *y*-axis into left- and right-hand circularly polarized waves from 5.13 to 5.61 GHz and from 5.37 to 6.72 GHz when all PIN diodes are turned ON and OFF, respectively. On the other hand, the proposed FRPC shows good angle stabilities when the incident angle ranges from 0° to 30° over the dual frequency bands. The simulated results show that the total 3 dB axial ratio relative bandwidth is more than 26%. To validate the polarization converter, a prototype of the FRPC is fabricated and measured. Measured results agree well with the simulation ones.

Index Terms ─ Active metasurface, frequency reconfigurable, PIN diode, polarization converter.

I. INTRODUCTION

Recently, due to the appearance of metasurface, manipulations of electromagnetic waves become more flexibly. Thereby, a series of progress has been achieved in the microwave, millimeter wave, terahertz and other frequency bands [1-8]. Applications include planar lenses, reflectarray and transmitarray antennas, digitally encoded antennas, etc. As the communication frequency bands become increasingly tight and the requirement of radar cross-section (RCS) reduction, multiple polarization methods are adopted to enhance the working band reuse capability. Some metasurface polarization converters (MPCs) have outstanding conversion efficiency [9,10]. And one or more polarization conversions mode can be implemented in a wide band or multiple bands [11]. At the same time, the thickness of the MPCs can be greatly reduced [12,13]. So the MPCs as a way to obtain multi-polarization have got growing research interest. So far, there have been many MPCs devices that implement transmissive or reflective linear-to-linear polarization, linear-to-circular polarization, and circular-to-circular polarization. For example, a bi-layered chiral metamaterial as a transmission polarization converter has been achieved, through which linear polarized (LP) waves can be converted into cross-polarization waves in a wideband [14]. Akbari et al. [15] proposed a broadband polarization converter operating at Ka band is realized by using a multi-layer board structure, and its 3 dB axial ratio (AR) relative bandwidth reaches 42%, meanwhile with an insertion loss less than 0.5 dB. References [16] demonstrated a novel THz half-wave polarization converter for cross-polarization conversions of both linear and circular polarizations. Furthermore, the polarizer can also be regulated by graphene. However, functionalities of the above MPCs cannot be changed after fabrication.

Then, the reconfigurable polarization converters (RPCs) based on metasurface have been reported. In [17], a polarization-reconfigurable converter using multi-layer frequency selective surface was proposed to convert the linear polarization (LP) into LP, right-hand circular polarization (RHCP) and left-hand circular polarization (LHCP) by mechanically rotating the metasurface screen. However, it is difficult to switch the device states quickly and exactly because of the mechanical rotation. In order to solve this shortcoming, some MPCs combined with active components (e.g., varactors, PIN diodes, MEMS) are proposed. Ratni et al. [18] loaded a varactor on each metasurface unit, and by adjusting the bias voltage load on the varactors, the RPC can convert LP into circular polarization (CP) in different frequency bands. But the performance of the 3 dB AR bandwidth is relative limited 10%. Apart from this, compared to the PIN diodes, varactors and MEMS show higher loss and their bias circuits are more complicated [19,20].

In this paper, a novel frequency reconfigurable polarization converter (FRPC) based on the reflective metasurface and PIN diodes is proposed. When the PIN diodes are turned ON and OFF, the FRPC can convert LP

Submitted On: December 28, 2018
Accepted On: May 6, 2019

waves into CP waves in successive different frequency bands. This paper is organized as follows. In Section II, the structure of FRPC is presented and operational principle of tuning the polarization state of an incident LP wave is described. Section III provides the experimental results and compares them with the simulated results. Finally, the paper is concluded in Section IV.

II. DESIGN AND ANALYSES

A. Structure of the FRPC unit

The unit of the proposed FRPC is illustrated in Fig. 1. The 3-D topology expanded view is shown in Fig. 1 (a), which consists of two metal layers, PIN diode, inductor and one dielectric layer. These two metal layers are composed of a metal ground on the back of the dielectric slab and a metasurface which is the truncated square patch with internally slotted. The bias line is deliberately designed to minimize the biasing circuit loss and simplify the structure. The biasing point is positioned at the zero-electric-field point along the non-radiating edge of the patch. Furthermore, in order to suppress the influence of the high frequency signal introduced by the power supply, a 27 nH inductor is placed between the bias line and the patch.

The top view and side view of the FRPC element is depicted in Fig. 1 (b). By optimization, the geometric parameters of the unit element are as follows: the patch with edge length W = 17 mm and is truncated a corner with edge P2 = 11 mm. A gap with width Gap = 0.45 mm is etched on the patch. And the gap is placed P1 = 4.2 mm from corner and parallels to the diagonal direction of the patch. In addition, the width of a bias line is Bia_*w* = 0.8 mm. The thickness and edge length of F4B substrate are H = 3.3 mm and *L* = 20 mm, which are about $\lambda_0/15$ and $\lambda_0/3$ respectively, where λ_0 is the wavelength at the center frequency. The diameter of the via from the top to the metal ground is Via_*r* = 0.6 mm.

MACOM MADP-000907-14020, which shows low insertion and can achieve an excellent electrical performance more than 10 GHz, is employed as the PIN diode in this paper [21]. For ON or OFF state, the PIN diode is modeled as a series of lumped resistance (R) and inductance (L) or capacitance (C) and inductance (L), respectively. Table 1 lists the homologous circuit parameters in the aimed frequency band.

B. Theory of operation

When the incident electromagnetic wave is LP wave with the electric field $\vec{E}_{in}$ in the *y*-direction and travels toward -*z*-direction. The incident electrical field radiated by an antenna can be written as two orthogonal linear components:

$$\vec{E}_{in} = \vec{E}_u + \vec{E}_v, \tag{1}$$

$$\left|\vec{E}_u\right| = \left|\vec{E}_v\right|, \tag{2}$$

where $\vec{E}_u$ and $\vec{E}_v$ are the components of the $\vec{E}_{in}$ in the *u* and *v* direction, respectively. $\left|\vec{E}_u\right|$ and $\left|\vec{E}_v\right|$ indicate the magnitude of the corresponding electric field.

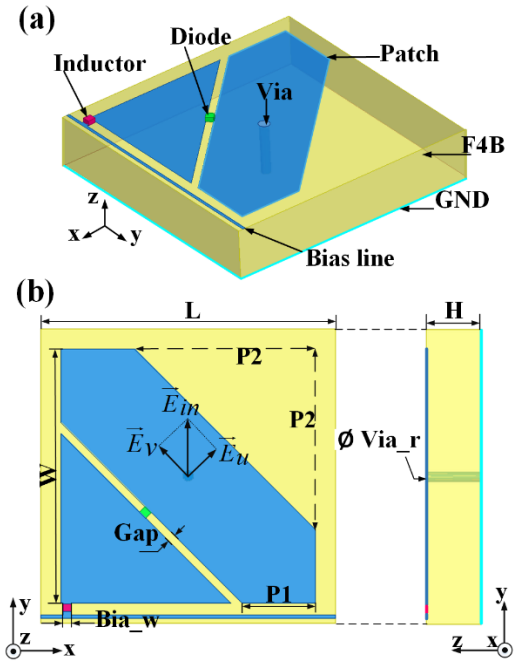

Fig. 1. Structure of the proposed FRPC unit cell: (a) 3-D topology expanded view, and (b) top view and side view.

Table 1: Equivalent circuit parameters of the PIN diode

Parameters	ON State	OFF State
R	7.8 Ω	-
L	30 pH	30 pH
C	-	0.025 pF

For the incident wave illuminates the FRPC element, the reflected electric field is also a sum of two orthogonal linearly polarized components:

$$\vec{E}_r = R(\vec{E}_u + \vec{E}_v) = R_u\vec{E}_u + R_v\vec{E}_v, \tag{3}$$

where R_u and R_v are the reflection coefficients for *u* direction and *v* direction. As R_u and R_v have the same magnitude $\left|R_u\right|$ and $\left|R_v\right|$. Meanwhile, the components of reflected electric field in two orthogonal linear directions with $\Delta\phi$ phase difference, which can be expressed as:

$$\left|R_u\right| = \left|R_v\right|, \tag{4}$$

$$\Delta\phi = \phi_u - \phi_v, \tag{5}$$

where ϕ_u and ϕ_v are the phase of $R_u\vec{E}_u$ and $R_v\vec{E}_v$, respectively. And if $\Delta\phi = \pm 90^\circ$ and $\left|R_u\right| = \left|R_v\right|$, the LP

incident wave can be converted into the CP wave for transmitting in the free space. In this paper, according to the formula (4) and (5), we can get the following conclusions. When the incident LP wave is in *x*-direction with $\Delta\phi = 90^\circ$ phase difference, the incident wave can be converted to LHCP wave. In addition, since the metasurface unit structure is symmetric about the diagonal, as the incident wave is *y*-polarized with $\Delta\phi = -90^\circ$ phase difference, the LP wave can be converted to RHCP wave. For the sake of understanding the working mechanism of the FRPC well, the relation between the polarization of incident wave and the reflected wave from the FRPC array is depicted in Fig. 2.

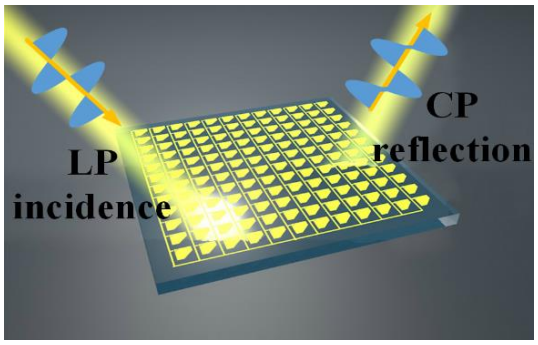

Fig. 2. Schematic model of a reflective polarization converter.

C. Simulation results

To verify the design functionality and explore the reflection characteristics, HFSS 15.0 is used to analyze and optimize the proposed element. The element is simulated by periodic boundary condition combined with Floquet port. Moreover, the PIN diode and inductor embedded on the unit cell are replaced by lumped elements in the corresponding cases under different operating states which are described above. As shown in Fig. 3 (a), the AR of the reflected wave varies with frequency when the incident wave is *x*-polarized or *y*-polarized, and the incident angle θ is to be zero in Floquet port. It is clear that the incident wave polarization direction does not affect the polarization conversion performance of the FRPC. As PIN diode under different states, the 3 dB AR bandwidth and the corresponding center frequency are different, specific parameter indicators are listed in Table 2. It is worth mentioning that the 3 dB AR bandwidth in two states is continuous, so the polarization converter can achieve the 3dB AR relative bandwidth of 26.74%.

When the incident wave is *y*-polarized, the amplitude and phase difference of the reflected wave electric field in the *u* and *v* directions are plotted, as shown in Fig. 3 (b). In different operating frequency bands, the electric field amplitudes in both directions are almost equal, and the phase difference approximate to $\Delta\phi = -90^\circ$. Since the amplitudes of the incident electric fields in both directions are equal, according to formula (3), $|R_u|$ and $|R_v|$ are approximately equal. In order to clearly display the polarization states of the reflected wave, the current distributions on the patch are plotted at the center frequency of the two operating states, as shown in Figs. 4 (a) and (b). The surface current vector distributions ranges from 0° to 270° with a 90° interval. As the incident wave is in the y-polarized, the reflected wave is the RHCP wave in both states.

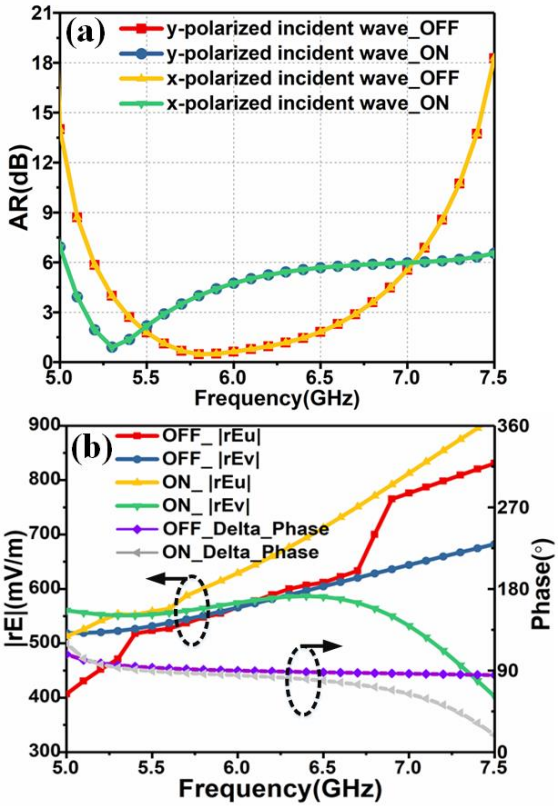

Fig. 3. Simulated reflected waves characteristics: (a) AR of the reflected wave varies with frequency when the incident wave is *x*-polarized or *y*-polarized, and (b) the amplitude and phase difference of the reflected electric field in the *u* and *v* directions.

Table 2: Index of reflected wave under different states

State	3dB AR Bandwidth (GHz)	Fractional Bandwidth	Center Frequency (GHz)
OFF	5.37 – 6.72	22.17%	6.05
ON	5.13 – 5.61	8.86%	5.37

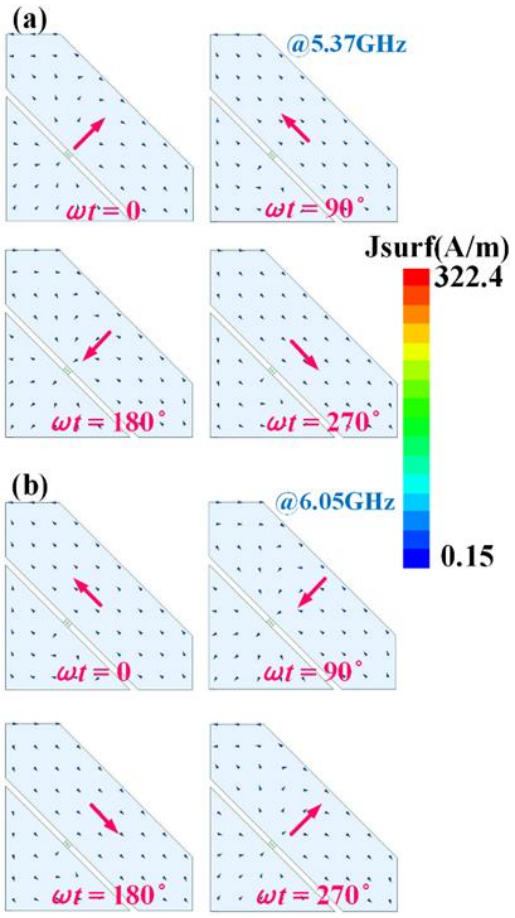

Fig. 4. Surface current distributions on the truncated square patch for four different instants: (a) RHCP at 5.37 GHz, and (b) RHCP at 6.05 GHz.

In addition, Fig. 5 (a) and 5 (b) illustrate the simulated AR characteristics for *y*-polarized electromagnetic waves with different incident angles θ under different states. It can be seen that the 3 dB AR relative bandwidth is more than 26%, when the incident angles range from 0° to 30°. In summary, although the waveforms are slightly different, the FRPC can efficiently reflect LP waves into CP waves in the conversion mode.

III. FABRICATION AND MEASUREMENT

In order to verify the simulation results, an FRPC metasurface array consisting of 18 × 18 unit cells is fabricated. The prototype with the size of 435 × 415 mm^2 is shown in Fig. 6, and all the bias lines are connected together and directed to the back of the array through a metallized via. In the measurements, two standard gain rectangular horn antennas are connected to an Agilent vector network analyzer E8364A as transmitter and receiver that are set on the front of the prototype. Besides, the bias voltage of the entire circuit is set to 5 volts. In operation, the transmitter horn antenna radiates *y*-polarized incident wave onto the prototype and the receiver horn antenna is used to receive *x*- and *y*-polarized reflected waves, respectively.

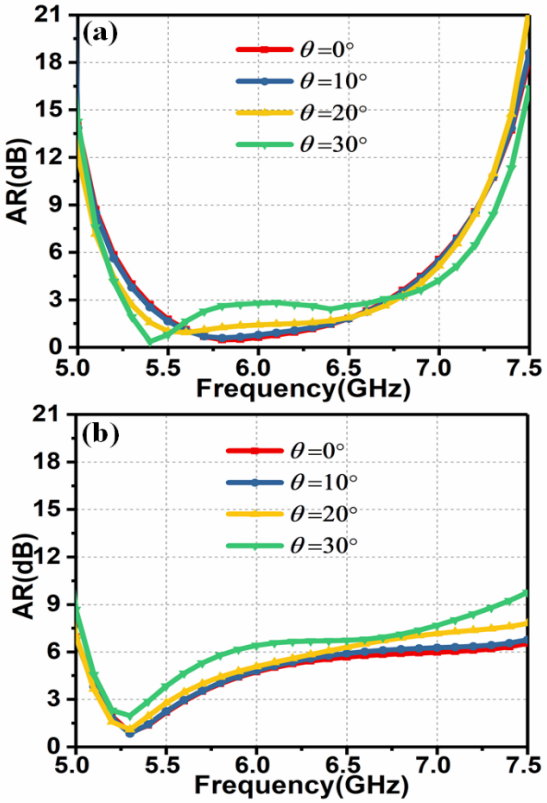

Fig. 5. Simulated AR characteristics for different incident angles at (a) OFF state and (b) ON state.

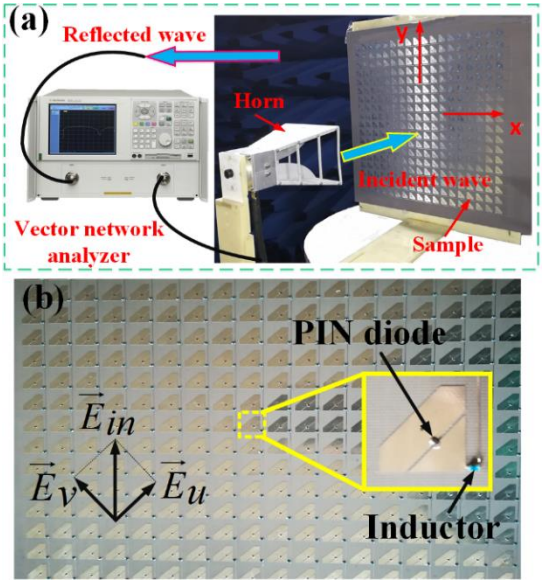

Fig. 6. 1-bit 18 × 18 FRPC prototype and measurement system: (a) system assembly and (b) sample zoom view.

The measured and simulated AR are illustrated in Fig. 7, there is a high consistency between the measured results and simulated results except a little error. In measurements, 3dB AR relative bandwidth of the FRPC is 8.23% (5.24–5.69 GHz) when the diodes are turned on, and the corresponding value is 21.12% (5.42–6.7 GHz) when the diodes are turned off. This difference with simulation results may be caused by tolerances in the fabrication and measurement processes. Thus, the measured results conform to the operating frequency band of the FRPC can be reconfigured by adjusting the state of the PIN diodes.

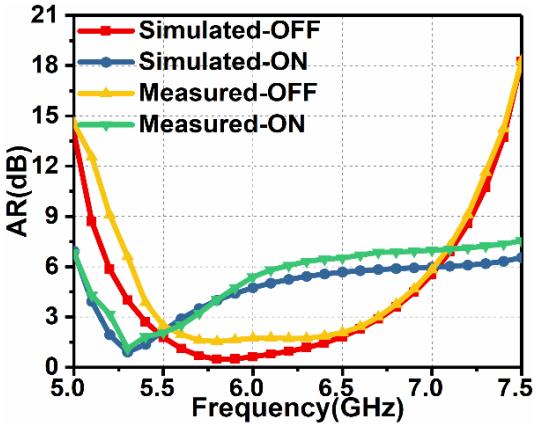

Fig. 7. Measured and simulated AR for different states of PIN diode.

IV. CONCLUSION

In this paper, a novel FRPC is realized based on active metasurface, which can reconfigure the operating frequency by switching the states of the PIN diodes. An electronically tuned FRPC with 18 × 18 unit cells is thoroughly investigated with measurements. Both simulations and experimental results reveal that the proposed FRPC can convert the LP waves into LHCP (RHCP) waves from 5.13 to 5.61 GHz when the PIN diodes are turned ON. Moreover, the FRPC can convert the LP waves into LHCP (RHCP) waves from 5.37 to 6.72 GHz as the PIN diodes are turned OFF. In addition, the experimental results demonstrate that two states the FRPC can change the LP incident waves into CP reflected waves with the 3 dB AR relative bandwidths more than 24%. The FRPC has great potentials in RCS reduction, communication, and the CP reflectarray applications, etc.

ACKNOWLEDGMENT

This work is supported by Shaanxi Outstanding Youth Science Foundation (2019JC-15) and National Key R&D Program of China.

REFERENCES

[1] V. K. Kothapudi, et al., "A 6-Port two-dimensional 3×3 series-fed planar array antenna for dual-polarized X-band airborne synthetic. Aperture radar applications," *IEEE Access*, vol. 6, pp. 12001-12007, Mar. 2018.

[2] Y. Dong, "Metamaterial-based antennas," *Proceedings of the IEEE*, vol. 100, no. 7, pp. 2271-2285, July 2012.

[3] S. Yu, H. Liu, and Long Li, "Design of near-field focused metasurface for high efficient wireless power transfer with multi-focus characteristics," *IEEE Transactions on Industrial Electronics*, vol. 66, no. 5, pp. 3993-4002, 2019.

[4] Y. Zhao, M. A. Belkin, and A. Alù, "Twisted optical metamaterials for planarized ultrathin broadband circular polarizers," *Nature Communications*, vol. 3, 10.1038/ncomms1877, May 2012.

[5] A. A. High, et al., "Visible-frequency hyperbolic metasurface," *Nature*, vol. 522, pp. 192-196, June 2015.

[6] N. Yu and F. Capasso, "Flat optics with designer metasurfaces," *Nature Materials*, vol. 13, pp. 139-150, Jan. 2014.

[7] J. N. Gollub, et al., "Large metasurface aperture for millimeter wave computational imaging at the human-scale," *Scientific Reports*, vol. 7, 10.1038/srep42650, Feb. 2017.

[8] C. L. Holloway, et al., "An overview of the theory and applications of metasurfaces: The two-dimensional equivalents of metamaterials," *IEEE Antennas and Propagation Magazine*, vol. 54, no. 2, pp. 10-35, July 2012.

[9] H. L. Zhu, et al., "Linear-to-circular polarization conversion using metasurface," *IEEE Transactions on Antennas and Propagation*, vol. 61, no. 9, pp. 4615-4623, Sept. 2013.

[10] Xi Gao, et al., "Ultrawideband and high-efficiency linear polarization converter based on double V-shaped metasurface" *IEEE Transactions on Antennas and Propagation*, vol. 63, no. 8, pp. 3522-3530, Aug. 2015.

[11] R. Li, et al., "High-efficiency cross polarization converters by plasmonic metasurface," *Plasmonics*, vol. 10, no. 5, pp. 1167-1172, Oct. 2015.

[12] X. Liu, et al., "Three-band polarization converter based on reflective metasurface," *IEEE Antennas and Wireless Propagation Letters*, vol. 16, pp. 924-927, Sep. 2016.

[13] Z. Li, et al., "Realizing broadband and invertible linear-to-circular polarization converter with ultra-thin single-layer metasurface," *Scientific Reports*, vol. 5, 10.1038/srep18106, Dec. 2015.

[14] W. Mo, et al., "Ultrathin flexible terahertz

polarization converter based on metasurfaces," *Optics Express*, vol. 24, no. 12, pp. 13621-13627, June 2016.
[15] F. Mirzamohammadia, et al., "A bi-layered chiral metamaterial with high-performance broadband asymmetric transmission of linearly polarized wave," *International Journal of Electronics and Communications*, vol. 98, pp. 58-67, Jan. 2019.
[16] M. Akbari, et al., "Ka-band linear to circular polarization converter based on multilayer slab with broadband performance," *IEEE Access*, vol. 5, pp. 17927-17937, Aug. 2017.
[17] L. Peng, et al., "A novel THz half-wave polarization converter for cross-polarization conversions of both linear and circular polarizations and polarization conversion ratio regulating by graphene," *Journal of Lightwave Technology*, vol. 36, pp. 4250-4258, May 2018.
[18] L. Li, et al., "Novel polarization reconfigurable converter based on multilayer frequency-selective surfaces," *Proceedings of the IEEE*, vol. 103, no. 7, pp. 1057-1070, July 2015.
[19] B. Ratni, et al., "Electronic control of linear-to-circular polarization conversion using a reconfigurable metasurface," *Applied Physics Letters*, vol. 111, no. 21, 101063, Nov. 2017.
[20] B. Schoenlinner, et al., "Switchable low-loss RF MEMS Ka-band frequency-selective surface," *IEEE Transactions on Microwave Theory and Techniques*, vol. 52, no. 11, pp. 2474-2481, Nov. 2004.
[21] Mouser Electronics. Skyworks Solutions, Inc. SMP1340-040LF PIN Diode Data.

Guangyao Liu received the B.S. degrees in School of Electrical Engineering and Automation from Shanxi Agricultural University, in 2017. He is currently pursuing the M.S. degree with Xidian University, Xi'an, China. His research interests include reconfigurable metasurface and its applications.

Jiaqi Han received the B.S. degrees in School of Electrical and Electronics Engineering from Henan Normal University, Xinxiang, China, in 2014. He is currently pursuing the Ph.D. degree with Xidian University, Xi'an, China. His research interests include reconfigurable metasurface and its application.

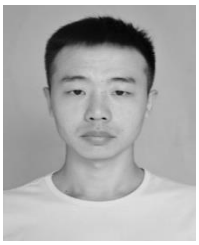

Xiaohe Gao received the B.Eng. degree in Electronic Information Engineering from North China Institute of Aerospace Engineering, Langfang China, in 2018. He is currently pursuing the Master of Engineering degree in Environmental Science and Engineering at Xidian University, Xian, China. His current research interests include the structural design of novel metamaterials and their applications in electromagnetic wave.

Haixia Liu (M'13) received the B.S. degree and the M.S. degree in Test and Measurement Technique and Instrumentation from Xidian University, Xi'an, China, in 1998 and 2001, respectively. She studied at Shizuoka University, Shizuoka, Japan, as a cooperative graduate in 2001. From 2002, she worked at Xidian University. She received the Ph.D. degrees in Electromagnetic Fields and Microwave Technology from Xidian University, Xi'an, China, in 2014. Her research interests include circuit analysis, frequency measurement and control, wireless power transfer, antennas, and electromagnetic compatibility.

Long Li (M'06-SM'11) received the B.E. and Ph.D. degrees in Electromagnetic Fields and Microwave Technology from Xidian University, Xi'an, China, in 1998 and 2005, respectively.

He was a Senior Research Associate in the Wireless Communications Research Center, City University of Hong Kong in 2006. He received the Japan Society for Promotion of Science (JSPS) Postdoctoral Fellowship and visited Tohoku University, Sendai, Japan, as a JSPS Fellow from Nov. 2006 to Nov. 2008. He was a Senior Visiting Scholar in the Pennsylvania State University, USA, from Dec. 2013 to July 2014. He is currently a Professor in the School of Electronic Engineering, Xidian University. He is also the Director of Key Lab of High Speed Circuit Design and EMC, Ministry of Education, China. His research interests include metamaterials, computational electromagnetics, electromagnetic compatibility, novel antennas, and wireless power transfer and harvesting technology.

A Novel Multi-Functional Electronically Tuned Polarization Converter Based on Reconfigurable Reflective Metasurface

Jiaqi Han, Guangyao Liu, Yajie Mu, Haixia Liu*, and Long Li**

Key Laboratory of High Speed Circuit Design and EMC of Ministry of Education
School of Electronic Engineering, Collaborative Innovation Center of Information Sensing and Understanding
Xidian University, Xi'an 710071, China
*hxliu@xidian.edu.cn, **lilong@mail.xidian.edu.cn

Abstract ― In this paper, a novel multi-functional electronically tuned polarization converter based on reconfigurable reflective metasurface is proposed. The proposed polarizer can convert linearly polarized waves to left-hand circular polarization, right-hand circular polarization and crossed linear polarization waves without changing the polarization of incident waves. By controlling the varactors that mounted on the metasurface element, the reflection phase difference of the two orthogonal components of the incident linear polarization waves covers from -110° to 210° when the polarizer operates from 4.65 GHz to 5.35 GHz. Moreover, a 14 × 14 prototype is fabricated and measured to validate the proposed polarizer. Measured axial ratios agree well with the simulation results.

Index Terms ― Axial ratio, multi-functional polarizer, reconfigurable metasurface, varactor.

I. INTRODUCTION

Polarization converter, which is also known as polarizer, is a special device that can convert polarization of electromagnetic (EM) waves from one form to another form, e.g., from linear polarization (LP) to left-hand circular polarization (LHCP) or right-hand circular polarization (RHCP), and LP to crossed linear polarization (CLP) [1, 2]. Having such characteristics, polarization converters were widely used in phased array feeding systems, wireless communication systems, and satellite communication systems [3-5].

As the definition of circular polarization (CP) implies, CP waves can be decomposed into two orthogonal LP waves with same amplitude and 90° phase difference. Therefore, to realize polarization conversion, we need to advance or delay the phase of one of the orthogonal components. Inductive and capacitive components can give rise to this effect. As a result, metallic stripes, meander-line and equivalent structures were used to achieve different inductive or capacitive features [1, 6-7]. When they are properly excited, polarization conversion will be implemented.

In recent years, metamaterials, which can readily manipulate EM waves and show abnormal and excellent EM properties, are proposed to tailor EM waves [8-11]. Metamaterials that are made of subwavelength special artificial structures and arrangements were employed to realize polarization converters [12-17]. Metasurfaces, which are the planar two dimensional form of metamaterials, can also exhibit polarization conversion characteristics [18].

Recently, researchers have shown an increased interest in reconfigurable polarizers using active metasurfaces. Reconfigurability was realized by introducing mechanical rotation, PIN diode, varactor diode, and liquid crystal to metasurfaces [19-24], etc. Comparing to conventional design of polarizer, reconfigurable polarization metasurfaces show multi-functionalities, e.g., from LP incident waves to CP (including RHCP and LHCP) or CLP waves.

However, current reconfigurable polarizer can only convert LP waves into RHCP or LHCP. To get the crossed CP, a CLP incident waves are required. In this paper, a novel polarizer based on reconfigurable reflective metasurface is proposed to convert LP waves into RHCP and LHCP without changing the polarization of incident waves. The electronically multi-functional polarization converter is implemented by mounting varactor diodes on metasurfaces. The proposed polarizer operates from 4.65 GHz to 5.35 GHz. The RHCP, LHCP and CLP waves are obtained at the working frequency band when the correct bias voltages are applied. Due to the bias voltage of varactor can be tuned continuously, phase difference of the decomposed reflected LP waves ranges from -110° to 210°, thereby, elliptical polarization waves also can be generated.

This paper is organized as follows. Manipulation principle and varactor tuned polarizer element are described in Section II. In Section III, a 14 × 14 reconfigurable polarization converter is constructed and tested. Finally, Section IV concludes this paper.

Submitted On: December 28, 2018
Accepted On: January 26, 2019

II. MANIPULATION PRINCIPLE AND RECONFIGURABLE ELEMENT

A. Manipulation principle

Previous designs of reconfigurable polarizer using metasurface mainly focused on advancing or delaying phase of the orthogonal components of incident LP waves. By introducing PIN diode or varactor along one of the orthogonal components, we can manipulate the phase of this component. To continuously regulate the phase differences, varactor is used in this paper. In our previous study [19], truncated square metallic patch showed good polarization conversion characteristics. When the size of the truncated corner varies, phase of the two decomposed LP components leads alternatively. Based on this result, we use two varactors at the truncated corner to formally adjust the corner size. Therefore, as bias voltage changes, LHCP, RHCP, CLP and elliptical polarization waves can be realized.

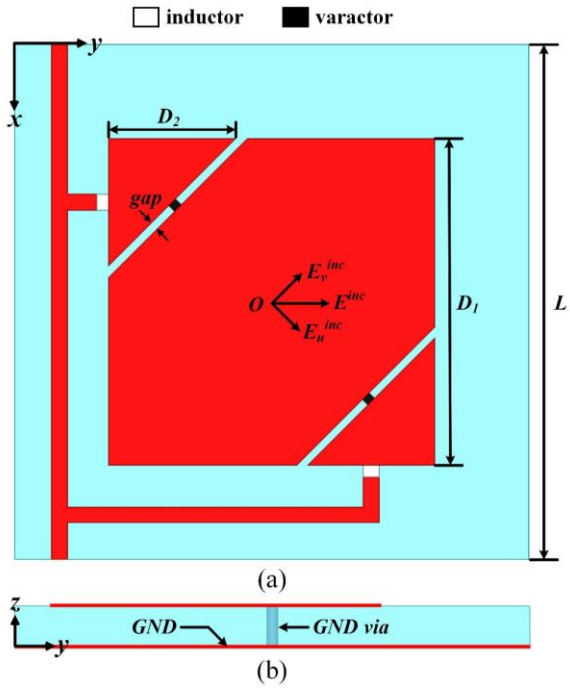

Fig. 1. The proposed reconfigurable polarizer element: (a) top view and (b) side view.

B. Reconfigurable element design

As aforementioned, a varactor tuned reconfigurable polarizer element is designed, as shown in Fig. 1. Period of the element is L = 26 mm. Side length of the truncated square patch is D_1 = 16.5 mm with corner size D_2 = 7 mm. Gap of the truncated patch and the triangle corner patch is *gap* = 0.4 mm. The element and the bias lines are etched on a F4B substrate with permittivity of 2.65 and tanδ = 0.005. And thickness of the substrate is 2 mm. Metallic ground plane is designed to reflect the incoming waves. A ground via is placed at the center of truncated patch, thereby, the ground plane serves as radio frequency (RF) and direct circuit (DC) ground. Bias lines are connected to the triangle corner patch to regulate the two varactors simultaneously. It should be noting that two 1 uH inductors are designed to choke RF circuits. Width of all bias lines is 0.8 mm. The Skyworks SMV 1405-040LF varactor is selected in this design. The junction capacitance ranges from 0.63 pF to 2.67 pF as the reverse voltage ranges from 30 V to 0 V.

The proposed element can realize polarization conversion when incident LP wave along *y*-axis is applied. Let us decompose the incident LP wave E^{inc} into E_u^{inc} and E_v^{inc}, thereby, the total reflected waves can be expressed as the sum of reflected waves along *u* and *v* directions:

$$E^{ref} = R_u e^{j\varphi_u} \bullet E_u^{inc} + R_v e^{j\varphi_v} \bullet E_v^{inc}, \quad (1)$$

where $R_u e^{j\varphi_u}$ and $R_v e^{j\varphi_v}$ are the reflection coefficients. Phase difference $\Delta\varphi = \varphi_u - \varphi_v$ changes when the bias voltage changes.

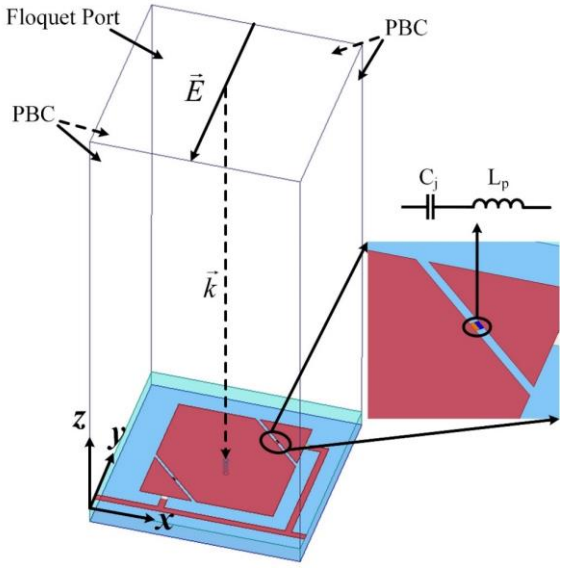

Fig. 2. Full-wave simulation configuration.

We simulated the proposed reconfigurable polarizer element by using Ansys HFSS 15.0, as shown in Fig. 2. It worth noting that the element was simulated under periodic boundary condition (PBC) combined with Floquet port. Plus, the inductors and varactors were modeled with lumped RLC boundary condition. The incident LP waves propagates in negative *z*-direction. Equivalent circuit of the selected varactor is junction capacitance in series with package inductance. The package inductance is 0.45 nH which can be founded in the datasheet of varactor. It should be pointed out that the equivalent circuit is modeled with two adjacent lumped

RLC boundary condition in HFSS 15.0, which is shown in the inset of Fig. 2. Detail simulation approach of reconfigurable element is described in [10].

First, we simulated the S-parameter with incident LP waves along *y*-axis, which is shown in Fig. 3 (a). It can be clearly seen that reflection magnitude is less than -1 dB when bias voltages varies, which indicates good reflection characteristic. Then, we assigned incident LP waves along *u*- and *v*-axis to investigate the $\Delta\varphi$ versus bias voltages, which is shown in Fig. 3 (b). From the figure, we can obtain that $\Delta\varphi$ can reach -90°, 90°, and 180° when bias voltages are 0 V, 4 V, and 20 V respectively. Therefore, LHCP, RHCP, and CLP waves can be achieved as reverse voltage assigned correctly. The operational bandwidth of the element generating LHCP waves is from 4.65 GHz to 4.95 GHz, while the RHCP waves is from 4.8 GHz to 5.1 GHz.

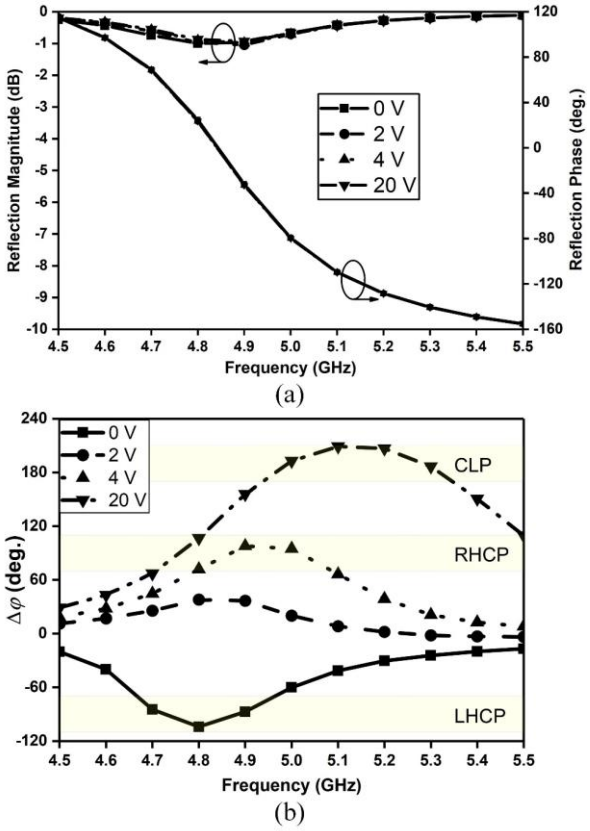

Fig. 3. (a) Simulated reflection magnitudes and phases versus different bias voltages. (b) $\Delta\varphi$ versus different bias voltages.

Moreover, the surface current distributions on the truncated square patch are investigated to figure out how the reflected circular polarizations are generated. The incident waves are *y*-axis polarized. In Fig. 4, we illustrate surface current vector distributions for four time phases which ranges from 0° to 270° with a 90° interval. As mentioned before, when the reverse voltages are 0 V and 4 V, LHCP and RHCP can be generated. Figure 4 (a) shows the surface currents rotate in the clockwise direction at 4.8 GHz when the reverse voltage is 0 V, indicating a LHCP waves. As the reverse voltage applied to varactor changes to 4 V, the surface currents rotate in the opposite direction at 5 GHz. Undoubtedly, the reflected waves are RHCP polarized.

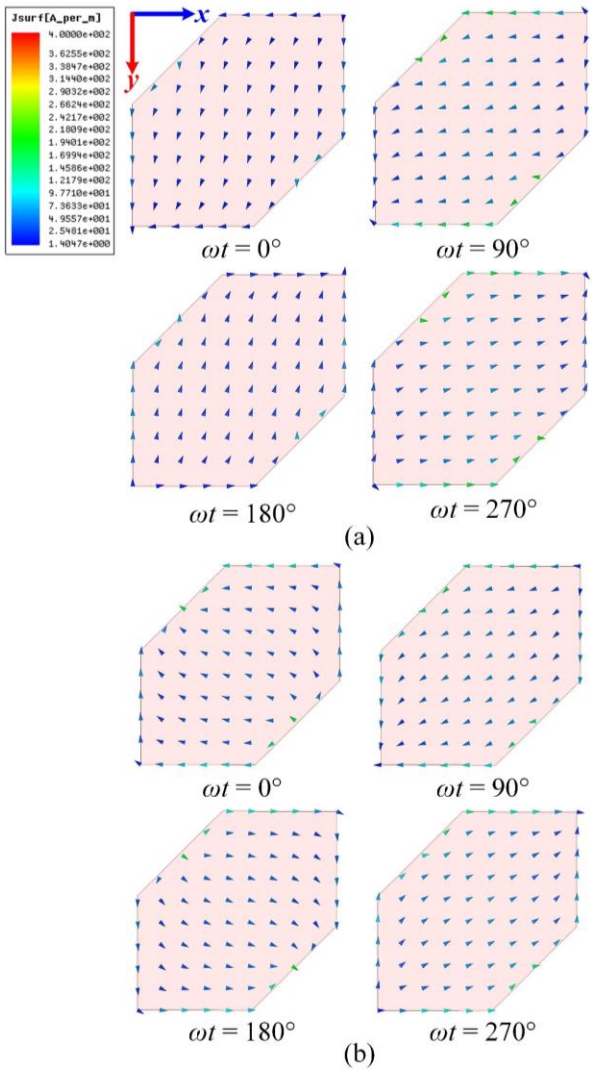

Fig. 4. Surface current distributions on the truncated square patch for four different instants and polarizations: (a) LHCP at 4.8 GHz and (b) RHCP at 5.0 GHz.

III. PROTOTYPE DESIGN AND MEASUREMENT

A. 14 × 14 prototype design

Based on the proposed reconfigurable element, a 14 × 14 polarization converter prototype is designed and

fabricated, as shown in Fig. 5 (a). Total size of the prototype is 430 × 410 mm^2. A LP horn antenna whose working frequency band is from 2 GHz to 18 GHz is placed 400 mm from the polarizer, serving as LP incident wave which is along *y*-axis. It worth noting that the polarizer is at the far-field of the feed horn.

Due to all the varactors should be regulated simultaneously, all bias lines are gathered together as positive DC power. Additionally, the gathered bias lines pass through a metallized via hole which is designed at the edge of the metasurface to the bottom plane. Moreover, a positive DC power line was soldered to the gathered bias line pad. Meanwhile, we soldered a line on the ground plane, serving as negative DC power. The bias voltage configuration is shown in Fig. 5 (b).

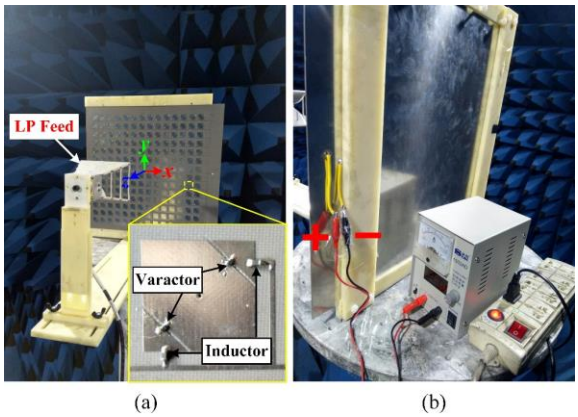

Fig. 5. (a) Fabricated 14 × 14 reconfigurable polarization converter. (b) Bias voltage configuration, red line as positive power and black line as negative power.

B. AR and pattern measurement

We measured the fabricated 14 × 14 reconfigurable polarization converter in anechoic chamber. In order to investigate the axial ratio (AR) of the prototype, we placed the polarizer on the turn table. Next, boresight AR characteristics were measured in the far-field when 0 V and 4 V bias voltages were supplied. It worth noting that *E*-field in two orthogonal directions were measured for calculating the ARs. The simulation and measurement results are plotted in Fig. 6 (a) and Fig. 6 (b). As can be seen from the figure, measured ARs at 0 V and 4 V agree well with the simulated ones. The LHCP and RHCP waves were successfully generated and measured. However, the measured AR shows slightly working frequency band offset. This is mainly due to the fabrication and measurement errors. The measured LHCP 3 dB AR absolute bandwidth is from 4.65 GHz to 4.95 GHz. And the measured RHCP 3 dB AR absolute bandwidth is from 4.88 GHz to 5.2 GHz.

Furthermore, directivity patterns of the two reflected CP waves for 0 V and 4 V are measured, which are shown in Fig. 7. The two patterns are measured at 4.8 GHz and 5.0 GHz respectively in *xoz*-plane. However, crossed polarization of the CPs are not shown due to measurement limitation. From the measured patterns, we obtained the LHCP and RHCP waves as the reverse voltage varies without changing the incident LP polarization.

Prior studies realized the reconfigurable polarizer by using PIN diodes and varactor diodes. To obtain the LHCP and RHCP waves, LP feed or the polarization converter should be rotated. This constraint limits the application of the previous reconfigurable polarizer in some conditions. In this paper, varactor tuned truncated square patch is proposed to implement polarization conversions without mechanical rotation. The reflected LHCP and RHCP waves are generated and measured successfully. From the view of Poincaré sphere, previous reconfigurable polarizer only can cover the half space of the sphere. Nevertheless, in this paper, the proposed electronically tuned polarizer can cover the hole Poincaré sphere.

In summary, a novel multi-functional electronically tuned polarizer is designed and measured. It can thus be suggested that LP to diverse elliptical polarization waves including CP waves can be achieved through advancing and delaying phases states using varactors.

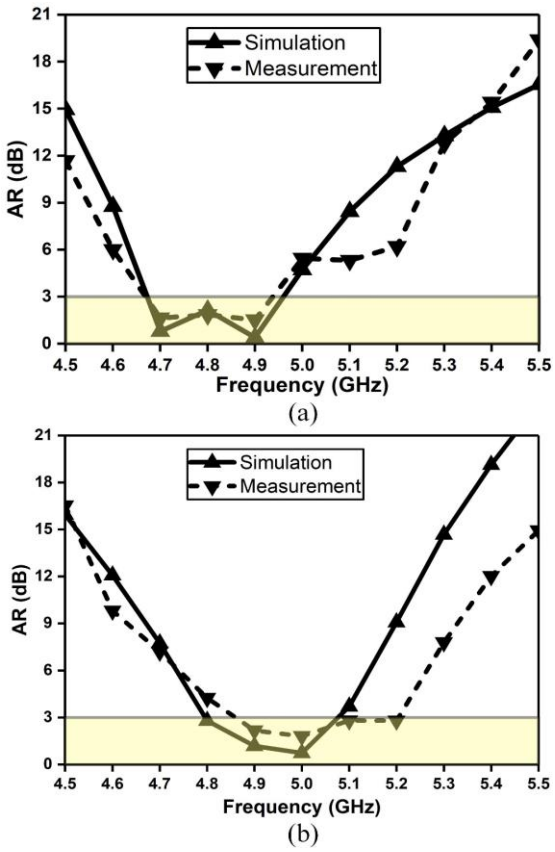

Fig. 6. Boresight AR results of simulation and measurement at bias voltage of: (a) 0 V (LHCP) and (b) 4 V (RHCP).

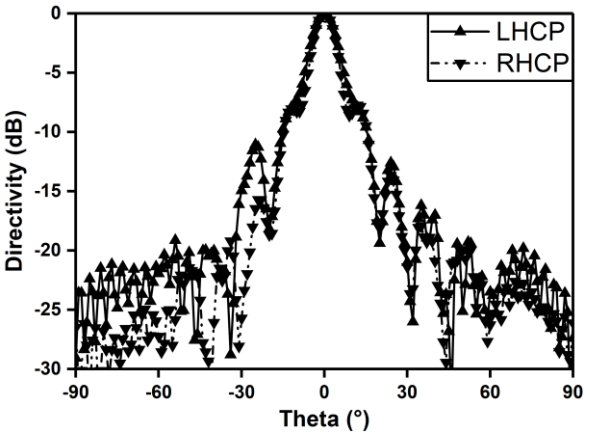

Fig. 7. Measured directivities of the two reflected circular polarization waves for 0 V (LHCP) at 4.8 GHz and 4 V (RHCP) at 5.0 GHz.

IV. CONCLUSION

This paper presents a novel multi-functional electronically tuned polarization converter which is based on reconfigurable reflective metasurface. The polarizer can convert incident LP waves into LHCP, RHCP and CLP waves without changing the polarization of incident waves. The approach, which can both advance and delay the phase of the orthogonal components of the incident LP waves, is feasible to convert LP waves to desired CP and elliptical polarization waves. By leveraging varactors, we can design multi-functional polarization converter based on reconfigurable metasurface. It is applicable for developing satellite communication systems, RCS reduction, and polarization transformers.

ACKNOWLEDGMENT

This work is supported by National Key R&D Program of China, and is supported by National Natural Science Foundation of China under Contract No. 51477126, and supported by the Science and Technology Project of State Grid Corporation of China.

REFERENCES

[1] D. S. Lerner, "A wave polarization converter for circular polarization," *IEEE Tans. Antennas Propagat.*, vol. 13, no.1, pp. 3-7, 1965.

[2] M. F. Bolster, "A new type of circular polarizer using crossed dipoles," *IRE Trans. Microwave Theory Techniques*, vol. 9, no. 5, pp. 385-388, 1961.

[3] M. H. Chen and G. N. "A wide-band square-waveguide array polarizer," *IEEE Tans. Antennas Propagat.*, vol. 21, no. 3, pp. 389-391, 1973.

[4] J. A. Ruiz-Cruz, M. M. Fahmi, M. Daneshmand, and R. R. Mansour, "Compact reconfigurable waveguide circular polarizer," *IEEE MTT-S International Microwave Symposium*, 2011.

[5] C. Dietlein, A. Luukanen, Z. Popovic, and E. Grossman, "A w-band polarization converter and isolator," *IEEE Trans. Antennas Propagat.*, vol. 55, no. 6, pp. 1804-1809, 2007.

[6] L. Young, L. A. Robinson, and C. A. Hacking, "Meander-line polarizer," *IEEE Trans. Antennas Propagat.*, vol. 21, no. 3, pp. 376-378, 1973.

[7] Q. Zheng, C. Guo, and J. Ding, "Wideband metasurface-based reflective polarization converter for linear-to-linear and linear-to-circular polarization conversion," *IEEE Antennas Wireless Propagat. Lett.*, vol. 17, no. 8, pp. 1459-1463, 2018.

[8] R. A. Shelby, D. R. Smith, and S. Schultz, "Experimental verification of a negative index of refraction," *Science*, vol. 292, no. 5514, pp. 77-79, 2001.

[9] D. Schurig, *et al.*, "Metamaterial electromagnetic cloak at microwave frequencies," *Science*, vol. 314, no. 5801, pp. 977-980, 2006.

[10] Y. Li, W. Li, and Q. Ye, "A reconfigurable triple-notch-nand antenna integrated with defected microstrip structure band-stop filter for ultra-wideband cognitive radio applications," *International Journal of Antennas and Propagation*, vol. 2013, Article ID 472645, 2013.

[11] K. Yu, Y. Li, and X. Liu, "Mutual coupling reduction of a MIMO antenna array using 3-D novel meta-material structures," *Applied Computational Electromagnetics Society Journal*, vol. 33, no. 7, pp. 758-763, 2018.

[12] Y. Tamayama, K. Yasui, T. Nakanishi, and M. Kitano, "A linear-to-cirular polarization converter with half transmission and half reflection using a single-layered metamaterial," *Appl. Phys. Lett.*, 105, 021110, 2014.

[13] Y. Chiang and T. Yen, "A composite-meta-material-based terahertz-wave polarization rotator with an ultrathin thickness, an excellent conversion ratio, and enhanced transmission," *Appl. Phys. Lett.*, 102, 011129, 2013.

[14] H. F. Ma, W. X. Tang, Q. Cheng, and T. H. Cui, "A single metamaterial plate as bandpass filter, transparent wall, and polarization converter controlled by polarizations," *Appl. Phys. Lett.*, 113, 101104, 2018.

[15] J. Zi, Q. Xu, Q. Wang, C. Tian, Y. Li, X. Zhang, J. Han, and W. Zhang, "Antireflection-assisted all-dielectric terahertz metamaterial polarization converter," *Appl. Phys. Lett.*, 105, 021110, 2014.

[16] Y. Z. Cheng, W. Withayachumnankul, A. Upadhay, D. Headland, Y. Nie, R. Z. Gong, M. Bhaskaran, S. Sriram, and D. Abbott, "Ultra-broadband reflective polarization converter for terahertz waves," *Appl. Phys. Lett.*, 105, 181111, 2014.

[17] J. Chen and A. Zhang, "A linear-to-circular polarizer

using split ring resonators," *Applied Computational Electromagnetics Society Journal*, vol. 28, no. 6, pp. 507-512, 2013.

[18] Y. Li, J. Zhang, S. Qu, J. Wang, L. Zheng, Y. Pang, Z. Xu, and A. Zhang, "Achieving wide-band linear-to-circular polarization conversion using ultra-thin bi-layered metasurfaces," *Appl. Phys. Lett.*, 117, 044501, 2015.

[19] L. Li, Y. Li, Z. Wu, F. Huo, Y. Zhang, and C. Zhao, "Novel polarization-reconfigurable converter based on multilayer frequency-selective surfaces," *Proceedings of the IEEE*, vol. 103, no. 7, pp. 1057-1070, 2015.

[20] B. Li and Q. Xue, "Polarization-reconfigurable omnidirectional antenna combining dipole and loop radiators," *IEEE Antennas Wireless Propagat. Lett.*, vol. 12, pp. 1102-1105, 2013.

[21] W. Li, S. Gao, Y. Cai, Q. Luo, M. Sobhy, G. Wei, J. Xu, J. Li, C. Wu, and Z. Cheng, "Polarization-reconfigurable circularly polarized planar antenna using switchable polarizer," *IEEE Trans. Antenna Propagat.*, vol. 65, no. 9. pp. 4470-4477, 2017.

[22] W. Li, S. Xia, B. He, J. Chen, H. Shi, A. Zhang, Z. Li, and Z. Xu, "A reconfigurable polarization converter using active metasurface and its application in horn antenna," *IEEE Trans. Antenna Propagat.*, vol. 64, no. 12, pp. 5281-5290, 2016.

[23] X. Gao, W. L. Yang, H. F. Ma, Q. Cheng, X. H. Yu, and T. J. Cui, "A reconfigurable broadband polarization converter based on an active meta-surface," *IEEE Trans. Antenna Propagat.*, vol. 66, no. 11, pp. 6086-6095, 2018.

[24] E. Doumanis, G. Goussetis, R. Dickie, R. Cahill, P. Baine, M. Bain, V. Fusco, J. A. Encinar, and G. Toso, "Electronically reconfigurable liquid crystal based mm-wave polarization converter," *IEEE Trans. Antenna Propagat.*, vol. 52, no. 4, pp. 2302-2307, 2014.

The Temperature Compensation for TE011 Mode Resonator with Bimetal Material

Q. Wu [1], J. Zhang [1], Y. Yang [2,3], and X. Shi [1]

[1] School of Electrical Engineering
Xidian University, Xi'an, 710071, China
qywu@xidian.edu.cn, jbozhang@stu.xidian.edu.cn, xwshi@mail.xidian.edu.cn

[2] The China Academy of Space Technology
Xi'an, China

[3] The Chinese University of Hong Kong
Shatin NT, Hong Kong
yeemeen.yang@gmail.com

Abstract ─ This paper proposes a temperature compensation design for TE011 mode resonator based on multiphysics analysis. The relationship between structure and electrical performance of circular waveguide resonator is specifically analyzed. Furthermore, a novel temperature compensation structure with bimetal material is proposed by using multiphysics analysis. The proposed TE011 mode resonator is fabricated and tested to verify the design method. The temperature drift coefficient of the compensated TE011 mode resonator can be dramatically reduced from 21.387 ppm/°C to 0.93ppm/°C.

Index Terms ─ Bimetal material, multiphysics analysis, temperature compensation, TE011 mode resonator.

I. INTRODUCTION

Microwave waveguide cavity devices are widely applied in communication systems, especially in satellite communication systems and 5G millimeter wave communication systems. The frequency response of the device is usually affected by temperature, due to thermal expansion and contraction of metal. It is especially serious in narrowband or high-power applications. Therefore, temperature compensation design is very important to ensure the stable electrical performance of waveguide devices [1].

Conventionally, materials with low coefficient of thermal expansion (CTE) are usually applied in cavity structures to achieve stable frequency response, such as Invar [2]. However, Invar's high density, poor thermal conductivity and high hardness limit its application. In [3], Shape Memory Alloys (SMAs) is used in temperature-compensated cavity resonators. But accurate analysis and design for temperature compensation is difficult to achieve, due to the nonlinear characteristics of SMA parameters. Dielectric resonators are also widely used to obtain temperature stability [4-5] in applications other than high power conditions. In addition, dielectric sphere for temperature compensation is proposed in [6], which introduced a perturbation in electromagnetic field to eliminate temperature drift. [7-9] introduced bimetal material to the tuning screw, which shows good compensated results by controlling the size of the tuning screw. In [9], we first proposed the method of temperature compensation based on multiphysics simulation. It introduced bimetal material to the tuning screw in the waveguide filter. Compared with other methods, the use of bimetal can realize flexible temperature compensation structures with low cost and easy processing. However, bimetal loaded tuning screws reduced structural stability and increased assembly complexity. Moreover, TE011 mode resonator plays an important role in communication systems due to its high Q value [10-13].

This paper proposes a temperature compensated TE011 mode resonator with bimetal material. The relationship between the structure and electrical performance of TE011 mode resonator is completely analyzed in detail. With the numerical solution, the whole design can be implemented by using multiphysics analysis. The designed temperature compensated TE011 mode resonator is fabricated and tested from -20°C to 80°C. The simulated and measured results suggest it has excellent temperature drift coefficient as 0.93ppm/°C.

II. ANALYSIS AND DESIGN

As well known, TE011 mode resonator has no longitudinal current. And when transmission power is constant, the cavity power loss decreases as the increasing of frequency. It has a high Q value and is

Submitted On: December 4, 2018
Accepted On: March 3, 2019

widely used in high power applications. To achieve precise temperature compensation design, deformation analysis of the TE011 mode resonator is needed.

A. The deformation analysis of TE011 mode resonator

The cavity deformation of TE011 mode resonator caused by temperature change can be equivalent to the metal cylindrical model. Figure 1 is the equivalent deformation model of aluminum at 80°C.

Figure 1 (a) represents the circumferential deformation of the equivalent deformation model and Fig. 1 (b) is the axial deformation. The green part in the Fig. 1 represents the smallest deformation, and red represents the largest deformation. When the temperature changes, the resonator will not only have a circumferential deformation [12], but also an axial deformation. Both affect the electrical performance. The relationship between frequency response and deformation is derived as follows. The frequency of TE011 mode resonator [14] can be expressed as (1):

$$f_{nml}=\frac{c}{2\pi\sqrt{\mu_r\varepsilon_r}}\sqrt{\left(\frac{p'_{nm}}{a}\right)^2+\left(\frac{l\pi}{d}\right)^2}. \tag{1}$$

Where a is the radius of the circular cavity and d is the height of circular cavity (at normal temperature: 20°C). p'_{nm} is the root of Bessel (n, m and l are the number of standing waves of extension radius, radius and axial).

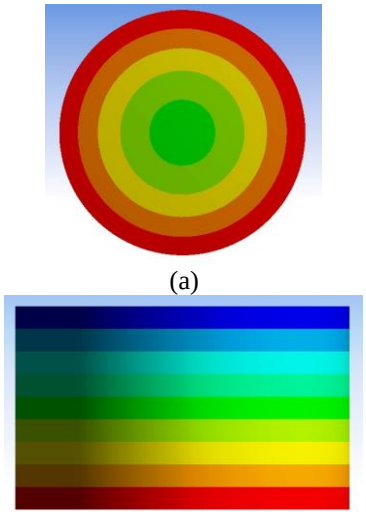

(a)

(b)

Fig. 1. The circumferential and axial deformation of the equivalent model: (a) the circumferential deformation, and (b) the axial deformation.

Due to the deformation of metal is linear, the deformation of cavity can be shown as (2). Where a' and d' are cavity radius and height at changed temperature. Δa and Δd are the difference [15]:

$$\begin{cases} a'=a+\Delta a \\ d'=d+\Delta d \end{cases}. \tag{2}$$

After deformation, the frequency response of the TE011 mode resonator can be obtained as (3):

$$f'_{nml}=\frac{c}{2\pi\sqrt{\mu_r\varepsilon_r}}\sqrt{\left(\frac{p'_{nm}}{a'}\right)^2+\left(\frac{l\pi}{d'}\right)^2}. \tag{3}$$

The change of frequency caused by temperature is:

$$\Delta f = f'_{nml}-f_{nml}. \tag{4}$$

In order to simplify analysis, $f'_{nml}+f_{nml}$ is introduced as shown in (5):

$$\begin{aligned}\Delta f\left(f'_{nml}+f_{nml}\right)&=\left(\frac{c}{2\pi\sqrt{\mu_r\varepsilon_r}}\right)^2 \\ &\cdot\left(\left(\frac{p'_{nm}}{a'}\right)^2+\left(\frac{l\pi}{d'}\right)^2-\left(\frac{p'_{nm}}{a}\right)^2-\left(\frac{l\pi}{d}\right)^2\right).\end{aligned} \tag{5}$$

Therefore, when set $\Delta f=0$, the frequency shift caused by circumferential deformation can be compensated as shown in (6):

$$\left(\frac{p'_{nm}}{a}\right)^2\frac{2a\Delta a}{(a+\Delta a)^2}+\left(\frac{l\pi}{d}\right)^2\frac{2d\Delta d}{(d+\Delta d)^2}=0. \tag{6}$$

That is,

$$|\Delta d|=\left(\frac{p'_{nm}}{l\pi}\right)^2\left(\frac{d}{a}\right)^3\Delta a. \tag{7}$$

It can be seen that circumferential deformation can be compensated, when Δa is proportional to Δd. Thus, it can be compensated by controlling the height of the cavity.

Furthermore, the axial expansion deformation Δd_1 can be calculated as:

$$\Delta d_1=d\cdot(T-20^\circ C)\cdot\alpha. \tag{8}$$

Where d is the height of cavity and T is ambient temperature. α is the coefficient of thermal expansion. Obviously, the axial deformation can be directly compensated by changing the height of the cavity. That is, the temperature drift of TE011 mode resonator can be fully compensated by controlling the height of the cavity. Therefore, it is essential to propose a structure that can control the height of the cavity. In this work, a loading structure is proposed to achieve the temperature compensation, which will be introduced in detail as follows.

B. Temperature compensation design based on bimetal material

To achieve the temperature compensation, the height change of the resonator should be controlled as ΔD:

$$\Delta D=\left(\frac{p'_{nm}}{l\pi}\right)^2\left(\frac{d}{a}\right)^3\Delta a+L\cdot(T-20^\circ C)\cdot\alpha. \tag{9}$$

The first important part of the loading structure is

a control structure. Bimetal material is introduced to realize the control structure. Bimetal material is combined of two layers of metals with different thermal expansion coefficients. The bend of bimetal is caused by the different CTE of each layer. As shown in Fig. 2, in bimetal, the layer with a relatively large coefficient of thermal expansion is called active layer (A) and the relatively small layer is called passive layer (B). Due to its linear characteristic at temperature, the deformation of bimetal can be used to control the height of the cavity.

Based on the deformation of bimetal, the loading structure is proposed as shown in Fig. 3. It includes a control structure and a ceiling part. The double-ended fixed structure of the bimetal ensures that the deformation can only produce in the axial direction. Since the deformation of the bimetal controls the height of the ceiling, ΔD is applied to calculation the size of bimetal under certain boundary conditions.

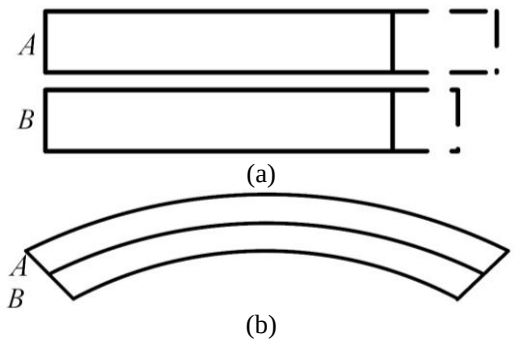

Fig. 2. The deformation of bimetal: (a) the deformation of the passive layer (A) and the active layer (B), respectively, and (b) the whole deformation of the bimetal.

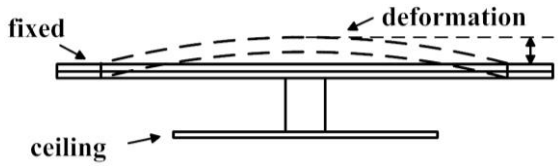

Fig. 3. The deformation of bimetal when two-ended fixed.

III. THE TEMPERATURE COMPENSATION OF TE011 MODE RESONATOR

As shown in Fig. 4, the relationship among electromagnetic, thermal and structural stress field can be obtained with multiphysics analysis [16]. ① represents the influence of electromagnetic field input power on the temperature and ② is the effect of the temperature field directly act on the electrical performance of the filter. The heat loss caused by the input power and the ambient temperature acts through ③ on the structural stress field. Structural deformation ⑤ caused by the temperature change will affect the frequency response of the filter. The environmental load and structural parameters act on the structural stress field through ④ and then affect the electromagnetic fields through the ⑤.

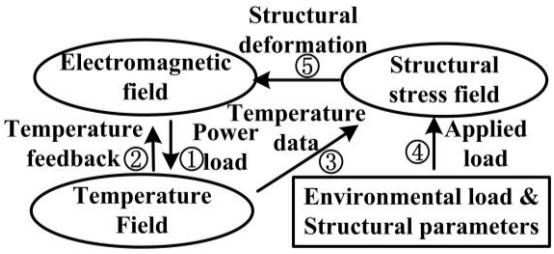

Fig. 4. The coupling relationship among multiphysics.

The final design of TE011 mode resonator is shown in Fig. 5. When the temperature changes, the center of bimetal structure will generate the biggest deformation and control the height of ceiling in the vertical direction to realize the temperature compensation. Symmetrically slots are added on both sides of bimetal to ensure the theoretical temperature compensated value.

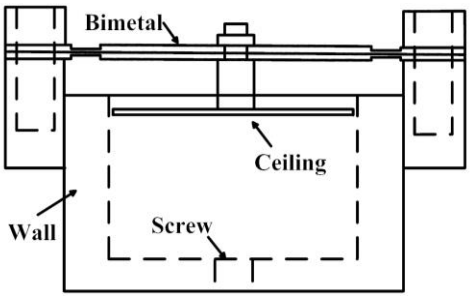

Fig. 5. The TE011 mode cavity resonator.

First, design a resonator that meets the electrical performance requirements. Then the deformation caused by temperature can be analyzed in static structural module of Ansys workbench. Finally, electrical analysis of the deformation structure is carried out with the updated grid data from structural stress field. Figure 6 shows the deformation comparison of the loading structure. As shown in Fig. 6, using slotted double-ended fixed structure can obtain a larger deformation range. When the center deformation of bimetal is equal to the ΔD, the structural size can be obtained.

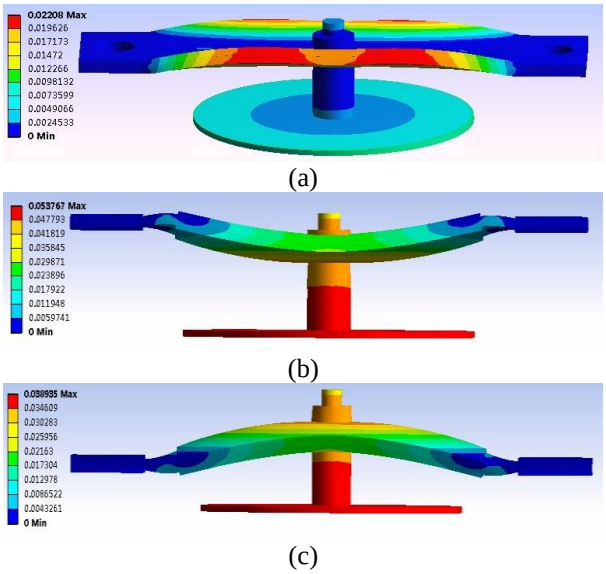

Fig. 6. The deformation of temperature compensated structure with bimetal: (a) double-ended fixed structure, (b) slotted double-ended fixed structure at 80°C, and (c) slotted double-ended fixed structure at -20°C.

The deformation of the ceiling is mainly concerned since the height directly affects the cavity frequency. In Fig. 6 (a), the maximum displacement of ceiling is 0.0074mm under 80°C. However, in Figs. 6 (b) and (c), the maximum displacement of ceiling is 0.0537mm under 80°C and 0.0389mm under -20°C. The movement (initial values) of the ceiling achieves the theoretical values. The size of bimetal can be obtained.

Figure 7 shows the final temperature compensation design for TE011 mode resonator at -20°C and 80°C. When the temperature drops, the height (final values) of the ceiling will be increased, vice versa.

Take a TE011 mode resonator operating at 21.5 GHz as an example. Figure 8 is the frequency response of the TE011 mode resonator. In Fig. 8 (a), without temperature compensation, the frequency response offsets 46 MHz from -20°C to 80°C. The temperature drift coefficient is 21.387ppm/°C. As shown in Fig. 8 (b), with the proposed design, the frequency drifts only 1 MHz. And its temperature drift coefficient is dramatically reduced to 0.465ppm/°C.

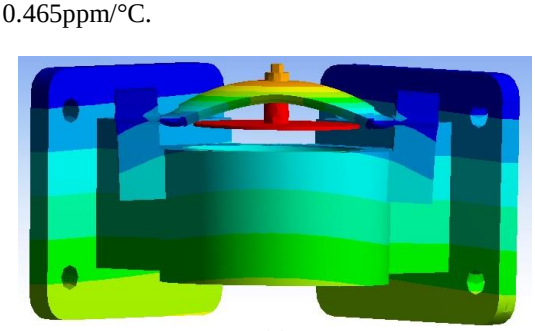

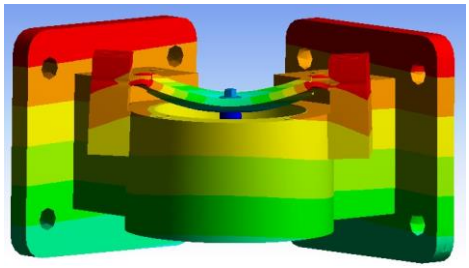

Fig. 7. The temperature compensated TE011 mode resonator: (a) the deformation at -20°C, and (b) the deformation at 80°C.

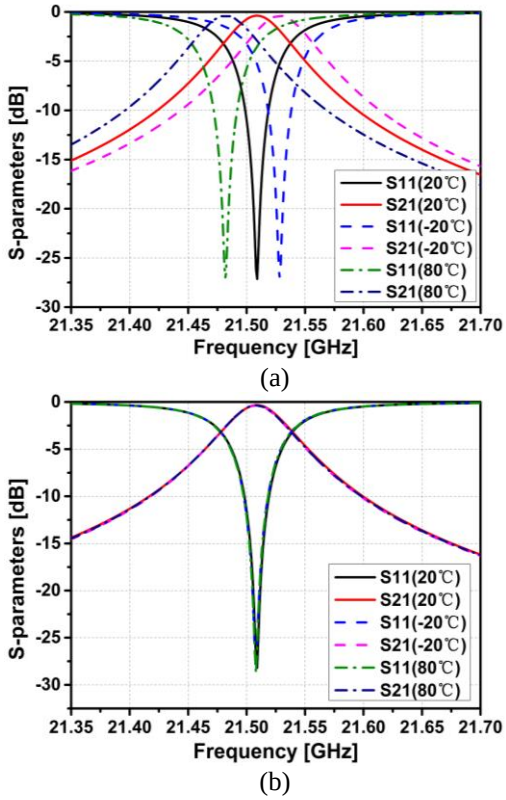

Fig. 8. The frequency response of TE011 mode resonator: (a) without temperature compensation, and (b) the proposed design.

The simulation results show the efficiency of the method and implement high thermal stability. The difference between the theoretical temperature compensated values and final values is shown in Table 1. Mainly due to some higher order component in (9) is neglected to get the theoretical values.

Table 1: Temperature compensated values (μm)

Temperature (°C)	-20	0	40	60	80
Final Values	36.7	19.2	15.7	33.2	52.3
Theoretical Values	38.8	20	16.4	35	53.4
Difference	2.1	0. 8	0. 7	1.8	1.1

IV. EXPERIMENT

The photograph of the temperature compensated TE011 mode resonator is shown in Fig. 9. Testing in a thermostat and the frequency response is given in Fig. 10. In the uncompensated structure, the frequency drift of TE011 mode resonator is 46 MHz from -20°C to 80°C. The temperature drift coefficient is 21.378ppm/°C. The frequency drift of proposed design is 2 MHz at -20°C to 80°C. The temperature drift coefficient is 0.93ppm/°C.

Fig. 9. The photograph of the temperature compensated TE011 mode resonator.

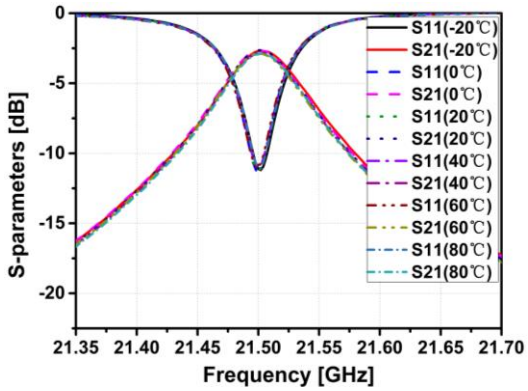

Fig. 10. The measured results of the temperature compensation TE011 mode resonator from -20 to 80°C.

The simulation results are consistent with the measured results, which verified the design. The proposed temperature compensated TE011 mode resonator can be easily extended to the filter temperature compensation easily.

A comparison with other reported works is given in Table 2. This work takes into account a wider range of application temperatures. As it is shown, with the proposed loading structure in this work, the temperature drift coefficient of the resonator can be dramatically reduced to 0.93ppm/°C. The method makes it easier for assembly and application.

Table 2: Comparison of the proposed temperature design

Refs.	Frequency (GHz)	Temperature Range (°C)	Temperature Drift Coefficient
[12]	12	20~100	1.56 ppm/°C
[13]	12.2	24~84	2.3 ppm/°C
This work	21.5	-20~80	0.93ppm/°C

V. CONCLUSION

This work proposes compensation for TE011 mode resonator using bimetal material is proposed with the multiphysics analysis. The relationship between the structure and electrical performance of TE011 mode resonator is completely analyzed. The modeling method is presented in detail with the numerical solution. The simulation and measure results confirm the effectiveness of the proposed design method.

ACKNOWLEDGMENT

This work is supported partly by the National Natural Science Foundational of China.

REFERENCES

[1] M. Yu and R. Snyder, *IEEE Workshop on Practical Aspects of Microwave Filter Design and Realization*, May 2007.

[2] D. J. Rosowsky and D. Wolk, "A 450-W output multiplexer for direct broadcasting satellites," *IEEE Trans. Microwave Theory Tech.*, vol. 30, no. 9, pp. 1317-1323, Sep. 1982.

[3] B. F. Keats, R. B. Gorbet, and R. R. Mansour, "Design and testing of SMA temperature-compensated cavity resonators," *IEEE Trans. Microwave Theory Tech.*, vol. 51, no. 12, pp. 2284-2289, Dec. 2003.

[4] S. W. Chen, K. A. Zaki, and R. G. West, "Tunable, temperature-compensated dielectric resonators and filters," *IEEE Trans. Microwave Theory Tech.*, vol. 38, no. 8, pp. 1046-1052, Aug. 1990.

[5] L. Murphy, J. Mautz, M. Yazdani, E. Arvas, and S. Tozin, "Uniaxial dielectric waveguide filter design accounting for losses using mode matching technique," *Applied Computational Electromagnetics Society (ACES) Journal*, vol. 29, no. 7, pp. 515-520, Apr. 2014.

[6] J. Ju, "A novel configuration of temperature compensation in the resonant cavities," *IEEE Trans. Microwave Theory Tech.*, vol. 52, no. 1, pp. 139-143, Jan. 2004.

[7] Y. Wang and Q. Sui, "A new temperature compensation method of rectangular waveguide resonant cavities," *Asia-Pacific Microwave Conference Proceedings*, Suzhou, China, pp. 4, Dec.

2005.

[8] B. F. Keats, R. R. Mansour, and R. B. Gorbet, "Design and testing of a thermally stable filter using bimetal compensation," *IEEE MTT-S Int. Microwave Symp. Dig.*, Honolulu, HI, pp. 1293-1296, June 2007.

[9] X. Liu, Q. Wu, and X. Shi, "Multi-physics analysis of waveguide filters for wireless communication systems," *IEEE MTT-S International Conference on Numerical Electromagnetic and Multiphysics Modeling and Optimization (NEMO)*, Beijing, China, pp. 1-2, July 2016.

[10] B. Yassini, M. Yu, and B. Keats, "A Ka-band fully tunable cavity filter," *IEEE Trans. Microwave Theory Tech.*, vol. 60, no. 12, pp. 4002-4012, Dec. 2012.

[11] B. Yassini, M. Yu, and B. Keats, "A Ka-band planar TE011 mode cavity tunable cavity filter using a mode-splitter ring," *IEEE MTT-S Int. Microwave Symp. Dig.*, Montreal, QC, pp. 1-3, June 2012.

[12] A. E. Atia and A. E. Williams, "Temperature compensation of TE-011 mode circular cavities," *IEEE Trans. Microwave Theory Tech.*, vol. 24, no. 10, pp. 668-669, Oct. 1976.

[13] R. Cameron, M. Lisi, and S. Strijk, "Resonateur à cavitès avec dispositive de com pensation thermique," *Brevetd' Invention*, no. 8607497, 16 May 1986.

[14] D. M. Pozar, *Microwave Engineering*. Wiley, New Jersey, 2015.

[15] J. E. Shigley and C. R. Michke, *Mechanical Engineering Design*. McGraw-Hill, New York, 1989.

[16] M. Celuch, M. Soltysiak, and U. Erle, "Computer simulations of microwave heating with coupled electromagnetic, thermal, and kinetic phenomena," *Applied Computational Electromagnetics Society (ACES) Journal*, vol. 26, no. 4, pp. 275-283, Apr. 2011.

Transient Electro-Thermal Analysis of a Common Source Amplifier Circuit with a Physics-based MOSFET Model

Tao Pan, Dazhi Ding*, Hanxiang Li, and Xiaolin Cheng

Department of Communication Engineering, Nanjing University of Science and Technology, Nanjing, 210094, China
dzding@njust.edu.cn

Abstract ─ An algorithm that combines a common source amplifier with the physics-based metal-oxide-semiconductor field effect transistor (MOSFET) model is proposed. By solving the coupled drift-diffusion model equations with spectral element time-domain (SETD) method, the distribution of electron quasi-Fermi potential, hole quasi-Fermi potential and the potential inside the MOSFET is obtained. The corresponding current densities and electric intensities distributed in the device can be used to couple the heat conduction equation. Furthermore, the Kirchhoff laws should be satisfied when the MOSFET device is inserted in the circuit. The Newton-Raphson method is used to solve the nonlinear circuit equations due to the existence of semiconductor devices. The transient electro-thermal characteristics of a common source amplifier circuit have been analyzed, and the numerical results demonstrate the validity of the proposed method.

Index Terms ─ Amplifier, electro-thermal characteristics, MOSFET, SETD, transient simulation.

I. INTRODUCTION

The semiconductor devices are playing an increasingly important role in many practical applications. Under the actual work environment, the heat produced in the semiconductor not only increases energy consumption, will also have an impact on the performance of the device itself. Thereby, it is significant to execute the transient electro-thermal analysis of the semiconductor devices and circuits. To get an accurate description of the complex electrical characteristics of semiconductors, the equivalent-circuit-model-based and physical-model-based simulation are the two most common methods. However, the equivalent-circuit-models highly rely on the experiment measurements to persevere its validity for different semiconductor devices [1]-[3]. The physical-model-based multi-physics simulation is a preferred alternative method for the transient electro-thermal analysis of semiconductors, which equivalent-circuit-model expounded the transient physical process [4]-[6]. The drift-diffusion model (DDM) is a common way to describe the interior carrier behavior of semiconductors, and the heat conduction equation is intended for denoting the transient variation with temperature. The DDM can provide the distribution of heat source to the heat conduction equation, and the temperature change the mobility of carriers in return. [7] Research works [8-9] have been introduced to analyze the circuits including semiconductor devices, which are only for PIN diode with quasi one-dimension structure by finite difference method (FDM). The spectral element time-domain (SETD) method has shown its higher accuracy and lower computation cost than finite element method (FEM) or FDM [10-11], and received a rapid development in nanodevice simulation and computational electromagnetics [12-14].

In this paper, the transient electro-thermal characteristics of the semiconductors with the physics-based Model are analyzed by the SETD method. The electron and hole quasi-Fermi potential and electric potential are selected as the unknown variables for DDM, which is different from the traditional way [6-8]. The basic electro-thermal characteristics of a common source amplifier circuit with the MOSFET device has been analyzed which combined the physics-based multi-physics model and the circuit simulation.

In previous studies, we used electron concentration, hole concentration, and potential as variables. When studying complex models, if the mesh is not dense enough when simulating the breakdown characteristics, it will cause non-physical oscillations in electron concentration or hole concentration, and there will be a large number of negative values, resulting in solution divergence. However, if the mesh is too dense, the unknown will increase, the memory consumption and solution time will be increased, and the efficiency will be reduced.

The difference from the previous work is that the paper takes the electronic quasi-fee potential, the hole quasi-Fei potential and the potential as variables. The numerical distribution of the electron quasi-fee potential and the hole quasi-Fermi potential is small, and non-physical oscillation does not occur like the carrier

Submitted On: December 1, 2018
Accepted On: May 28, 2019

concentration. It is easier to converge without encrypting the mesh and ensuring the proper unknown.

The frame of this paper is as follows. In Section II, the physical model for semiconductors has been introduced briefly. The basic theory of SEM based on GLL (Gauss-Lobatto-Legendre) polynomials has been described for the physical model when the electron and hole quasi-Fermi potential and the potential are selected as the unknowns. The Newton iterative method is used to solve the nonlinear system of the circuits with semiconductors. In Section III, the transient electron-thermal characteristics of a common source amplifier circuit have been analyzed to demonstrate the validity with the proposed method. Finally the conclusion is given in Section IV.

II. PHYSICS-BASED MODEL AND NUMERICAL SCHEME

The drift-diffusion model equations [15, 16] are normalized as follows:

$$\mathbf{J}_n = -\mu_n n \nabla \phi_n , \tag{1}$$

$$\mathbf{J}_p = -\mu_p p \nabla \phi_p , \tag{2}$$

$$\frac{\partial n}{\partial t} = \nabla \cdot \mathbf{J}_n + G - R , \tag{3}$$

$$\frac{\partial p}{\partial t} = -\nabla \cdot \mathbf{J}_p + G - R , \tag{4}$$

$$\nabla^2 \varphi = (n - p - \Gamma), \tag{5}$$

where φ is the electrostatic potential, q is the electric charge, Γ is the electrically active net impurity concentration, and n and p are the electron and hole carrier densities. G and R describe the generation phenomena and recombination processes respectively. The relationships between the electron and hole quasi-Fermi potential and the electron and hole carrier densities are described as the following equations:

$$n = \exp[\varphi - \phi_n], \tag{6}$$

$$p = \exp[\phi_p - \varphi], \tag{7}$$

The heat conduction equation [16] is formulated as (8):

$$\frac{\partial T}{\partial t} = \frac{k_t}{\rho_m c_m} \nabla^2 T + \frac{P_d}{\rho_m c_m} , \tag{8}$$

$$P_d = -(\mathbf{J}_n + \mathbf{J}_p - \varepsilon \frac{\partial (\nabla \varphi)}{\partial t}) \cdot \nabla \varphi , \tag{9}$$

where ρ_m is the specific mass density, c_m is the specific heat capacity, k_t is the temperature dependent thermal conductivity, ε is the permittivity, and P_d is the inside heat generation rate described as formula (9).

A. SETD for semiconductor simulation

The difference between SEM and FEM lies in the choice of the expansion basis functions. In order to achieve the high accuracy, the GLL basis functions are employed throughout this article. The Nth order GLL basis functions in a 3-D cubic element $(\xi, \eta, \zeta) \in [-1,1] \times [-1,1] \times [-1,1]$ can be written as:

$$\Phi_{rst}(\xi, \eta, \zeta) = \phi_r^{(N_\xi)}(\xi) \phi_s^{(N_\eta)}(\eta) \phi_t^{(N_\zeta)}(\zeta) , \tag{10}$$

for $r = 0,1,..., N_\xi; s = 0,1,..., N_\eta; t = 0,1,..., N_\zeta$. $\phi_r^{(N_\xi)}(\xi)$, $\phi_s^{(N_\eta)}(\eta)$ and $\phi_t^{(N_\zeta)}(\zeta)$ represent the basis functions with three directions and have the following definition:

$$\phi_j^{(\mathrm{N})} = \frac{-1}{N(\mathrm{N}+1)\mathrm{L}_N(\xi_j)} \frac{(1-\xi^2)\mathrm{L}_N^{'}(\xi)}{(\xi - \xi_j)} , \tag{11}$$

where $\mathrm{L}_N(\xi)$ and $\mathrm{L}_N^{'}(\xi)$ are the Legendre polynomial of Nth order and its derivative. The points $\{\xi_j, \mathrm{j}=0,1,...,\mathrm{N}\}$ are the zeros of $(1-\xi^2)\mathrm{L}_N^{'}(\xi_j) = 0$. Because of the basis functions definition on the reference domain at the above standard cubic element, the mapping from the physical element to the reference domain is essential for general meshes [13-14].

Here, the electron and hole quasi-Fermi potential and electric potential are selected as the unknown variables. The fully coupled Newton iterative method is employed to solve the nonlinear equations. For the time partial derivative, the backward difference operator is employed to achieve the unconditional stability with a large time step size represented by Δt. The detail of the backward difference operated on the normalized electronic current continuity equation is given as the following:

$$F_n(\phi_n^{\,m}, \phi_p^{\,m}, \varphi^m) = f_n(\phi_n^{\,m}, \phi_p^{\,m}, \varphi^m) \cdot \Delta t - \left(\phi_n^{\,m} - \phi_p^{\,m-1}\right) = 0 , \tag{12}$$

where $f_n(\phi_n, \phi_p, \varphi) = \nabla \cdot (\mu_n \nabla n - \mu_n n \nabla \varphi) - (R - G)$. Using the Taylor series, the formula (12) can be expanded as (13), which ignores the second and higher order items:

$$\begin{aligned} & F_n\left(\phi_n, \phi_p, \varphi\right) + \left.\frac{\partial F_n\left(\phi_n, \phi_p, \varphi\right)}{\partial \phi_n}\right|_{\substack{\phi_n = \phi_n^{\,m,l} \\ \phi_p = \phi_p^{\,m,l} \\ \varphi = \varphi^{m,l}}} \left(\phi_n^{\,m,l+1} - \phi_n^{\,\mathrm{m},l}\right) + \\ & \left.\frac{\partial F_n\left(\phi_n, \phi_p, \varphi\right)}{\partial \phi_p}\right|_{\substack{\phi_n = \phi_n^{\,m,l} \\ \phi_p = \phi_p^{\,m,l} \\ \varphi = \varphi^{m,l}}} \left(\phi_p^{\,m,l+1} - \phi_p^{\,m,l}\right) + \\ & \left.\frac{\partial F_n\left(\phi_n, \phi_p, \varphi\right)}{\partial \varphi}\right|_{\substack{\phi_n = \phi_n^{\,m,l} \\ \phi_p = \phi_p^{\,m,l} \\ \varphi = \varphi^{m,l}}} \left(\varphi^{m,l+1} - \varphi^{m,l}\right) = 0. \end{aligned} \tag{13}$$

The superscript m is used to indicate the variables at the time of $m\Delta t$, and l presents the variables obtained by the l_{th} iteration. Applying the Galerkin weighted-residual method, the formula (13) can be transformed to a form of equation system.

Repeat the above operations for the hole current continuity equation and Poisson equation, the final

system equation (14) can be obtained:

$$\begin{pmatrix} \mathbf{TN} & \mathbf{NP} & \mathbf{NF} \\ \mathbf{PN} & \mathbf{TP} & \mathbf{PF} \\ \mathbf{FN} & \mathbf{FP} & \mathbf{TF} \end{pmatrix} \begin{pmatrix} \phi_n^{m,l+1} - \phi_n^{m,l} \\ \phi_p^{m,l+1} - \phi_p^{m,l} \\ \varphi^{m,l+1} - \varphi^{m,l} \end{pmatrix} = \begin{pmatrix} \mathbf{BN} \\ \mathbf{BP} \\ \mathbf{BF} \end{pmatrix}. \quad (14)$$

The elemental matrices are defined as follows:

$$TN_{i,j} = \iiint_V \Delta t \mu_n \exp\left(\varphi^{m,l} - \phi_n^{m,l}\right) \nabla N_i \cdot \nabla \phi_n^{m,l} N_j dV - \iiint_V \exp\left(\varphi^{m,l} - \phi_n^{m,l}\right) N_i N_j dV$$
$$- \iiint_V \Delta t \mu_n \exp\left(\varphi^{m,l} - \phi_n^{m,l}\right) \nabla N_i \cdot \nabla N_j dV + \Delta t \int N_i \cdot N_j \frac{\partial (G-R)^{m,l}}{\partial \phi_n} dV,$$

$$NP_{ij} = \Delta t \int N_i \cdot N_j \frac{\partial (G-R)^{m,l}}{\partial \phi_p} dV,$$

$$NF_{i,j} = -\iiint_V \Delta t \mu_n \exp\left(\varphi^{m,l} - \phi_n^{m,l}\right) \nabla N_i \cdot \nabla \phi_n^{m,l} N_j dV + \iiint_V \exp\left(\varphi^{m,l} - \phi_n^{m,l}\right) N_i N_j dV$$
$$+ \Delta t \int N_i \cdot N_j \frac{\partial (G-R)^{m,l}}{\partial \varphi} dV,$$

$$PN_{ij} = \Delta t \int N_i \cdot N_j \frac{\partial (G-R)^{m,l}}{\partial \phi_n} dV,$$

$$TP_{i,j} = \iiint_V \Delta t \mu_p \exp\left(\phi_p^{m,l} - \varphi^{m,l}\right) \nabla N_i \cdot \nabla \phi_p^{m,l} N_j dV + \iiint_V \exp\left(\phi_p^{m,l} - \varphi^{m,l}\right) N_i N_j dV$$
$$+ \iiint_V \Delta t \mu_p \exp\left(\phi_p^{m,l} - \varphi^{m,l}\right) \nabla N_i \cdot \nabla N_j dV + \Delta t \int N_i \cdot N_j \frac{\partial (G-R)^{m,l}}{\partial \phi_p} dV,$$

$$PF_{i,j} = -\iiint_V \Delta t \mu_p \exp\left(\phi_p^{m,l} - \varphi^{m,l}\right) \nabla N_i \cdot \nabla \phi_p^{m,l} N_j dV - \iiint_V \exp\left(\phi_p^{m,l} - \varphi^{m,l}\right) N_i N_j dV$$
$$+ \Delta t \int N_i \cdot N_j \frac{\partial (G-R)^{m,l}}{\partial \phi_p} dV,$$

$$FN_{i,j} = \iiint_V \exp\left(\varphi^{m,l} - \phi_n^{m,l}\right) N_i N_j dV,$$

$$FP_{i,j} = \iiint_V \exp\left(\phi_p^{m,l} - \varphi^{m,l}\right) N_i N_j dV,$$

$$TF_{i,j} = -\iiint_V \varepsilon_2 \left[\exp\left(\varphi^{m,l} - \phi_n^{l}\right) + \exp\left(\phi_p^{m,l} - \varphi^{m,l}\right)\right] N_i N_j dV$$
$$- \iiint_V \varepsilon_1 \nabla N_i \cdot \nabla N_j dV,$$

$$BN_i = \iiint_V \Delta t \mu_n \exp\left(\varphi^{m,l} - \phi_n^{m,l}\right) \nabla N_i \cdot \nabla \phi_n^{m,l} dV + \iiint_V \Delta t N_i (G-R) dV$$
$$- \iiint_V N_i \left[\exp\left(\varphi^{m,l} - \phi_n^{m,l}\right) - \exp\left(\varphi^{m-1} - \phi_n^{m-1}\right)\right] dV,$$

$$BP_i = -\iiint_V \Delta t \mu_p \exp\left(\phi_p^{m,l} - \varphi^{m,l}\right) \nabla N_i \cdot \nabla \phi_p^{m,l} dV + \iiint_V \Delta t N_i (G-R) dV$$
$$- \iiint_V N_i \left(\exp\left(\phi_p{}^{m,l} - \varphi^{m,l}\right) - \exp\left(\phi_p{}^{m-1} - \varphi^{m-1}\right)\right) dV,$$

$$BF_i = \iiint_V \nabla N_i \cdot \nabla \varphi^{m,l} dV + \iiint_V N_i \left[\exp\left(\varphi^{m,l} - \phi_n^{m,l}\right) - \exp\left(\phi_p^{m,l} - \varphi^{m,l}\right) - \Gamma\right] dV.$$

When the norm of the solutions is less than the setting of tolerance, $(\phi_n^{l+1}, \phi_p^{l+1}, \varphi^{l+1})^T$ can be accounted as the approximate solution of the original nonlinear system.

For the analysis of electro-thermal interaction of semiconductor, the heat conduction equation should be solved after the system equation (14) solved by the Newton iterative method. In particular, the heat conduction equation can be solved easily by the SETD method, which is a linear equation system. For the sake of simplicity, this process is omitted over here. But it needs to be stressed that the procedure of heat conduction equation solving should be repeatedly implemented on each iterative process of the Newton iterative method.

B. Circuits with semiconductor devices

For the transient simulation of the MOSFET common source amplifier circuit, the goal is to obtain a solution satisfying both the external circuit constraint and MOSFET physical model equations. Figure 1 shows the configuration of a MOSFET common source amplifier circuit [18]. Two load resistors, R0 and RL, are connected to the transistor. VDD is the voltage imposed on the drain of the MOSFET through R0. The source of the transistor is grounded. The input voltage Vgs is composed of two signals: the DC bias voltage VGG and the AC signal Vg. The output voltage Vds is equivalent to the drain-to-source voltage of the amplifier.

Firstly, the MOSFET in the amplifier can be treated as a system with the input signals Vgs and Vds, and the output signals can be the drain current Id and the heat distribution among the transistor. This multi-physics simulation under a certain input signal can be implemented utilizing the method proposed in Section A. The input voltage Vgs is a given value at a certain moment. Therefore, the transient relationship between drain current and the drain voltage can be described as the following formula (15):

$$I_d = f_t(V_{ds}). \quad (15)$$

For this common-source amplifier circuit, the constraint equation of the output circuit is as follows:

$$V_{DD} = (I_d + \frac{V_{ds}}{R_L}) R_0 + V_{ds}. \quad (16)$$

Substituting (15) into (16), the coupled circuit equation with physics-based MOSFET model becomes:

$$F_t(V_{ds}) = (f_t(V_{ds}) + \frac{V_{ds}}{R_L}) R_0 + V_{ds} - V_{DD} = 0. \quad (17)$$

Due to the existence of nonlinear system $f_t(V_{ds})$, Newton-Raphson method is employed to solve equation (17). The derivative of this equation has the following form:

$$F_t'(V_{ds}) = \left[f_t'(V_{ds}) + \frac{1}{R_L} \right] R_0 + 1. \quad (18)$$

The derivative approximate expression can be defined as the difference between two adjacent time intervals:

$$f_t'(V_{ds}) = \frac{I_d - I_{d0}}{V_{ds} - V_{ds0}}, \quad (19)$$

where $V_{ds0} = V_{ds} - \beta$ and β is a relative tiny value to ensure the accuracy of the approximation.

Use Taylor series expansion for (17), we can get (20):

$$F_t(V_{ds}^l) + F_t'(V_{ds}^l)(V_{ds}^{l+1} - V_{ds}^l) = 0. \quad (20)$$

Take the formula (18) and (19) into (20), we can get Newton iteration:

$$V_{ds}^{l+1} = V_{ds}^{l} - \frac{(I_d^l R_L + V_{ds}^l)R_0 + (V_{ds}^l - V_{DD})R_L}{(I_d^l - I_{d0}^l)R_0 R_L + (R_0 + R_L)(V_{ds}^l - V_{ds0}^l)}(V_{ds}^l - V_{ds0}^l). \quad (21)$$

Then V_{ds}^{l+1} can be obtain, the convergence condition of Newton iteration is:

$$\left| \frac{V_{ds}^{l+1} - V_{ds}^{l}}{V_{ds}^{l+1}} \right| < \tau, \quad (22)$$

τ is the setting value of tolerance. When the criterion is satisfied, this V_{ds}^{l+1} can be accounted as the approximate solution of the circuit at the current time. Then, substituting V_{ds}^{l+1} into the physics-based MOSFET model once again, the actual electro-thermal behavior can be described finally.

For the transient characteristics simulation of the amplifying circuit, the goal is actually to require a transient solution that satisfies both external circuit constraints and the MOSFET model equation. For the voltage control current device, the input voltage and the output current can be written into a certain functional relationship, and then the circuit equation of the external circuit can be used to obtain the corresponding voltage and current by using the Newton method.

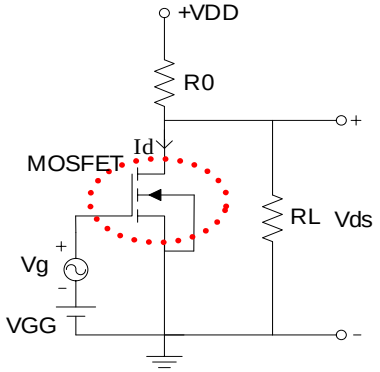

Fig. 1. Common source amplifier circuit with MOSFET.

III. NUMERICAL EXAMPLES

In order to verify the accuracy of the proposed method, the common source amplifier circuit is chosen as the numerical model. The N-channel MOSFET in the circuit is analyzed by solving the drift-diffusion model, and it is convenient to get the thermal characteristics. Here, it should be indicated that all the numerical examples are computed on an Intel(R) Core(TM)2 with 2.83GHz CPU (the results are computed by only one processor) and 8 GB RAM. The tolerance is set to be 10^{-6}.

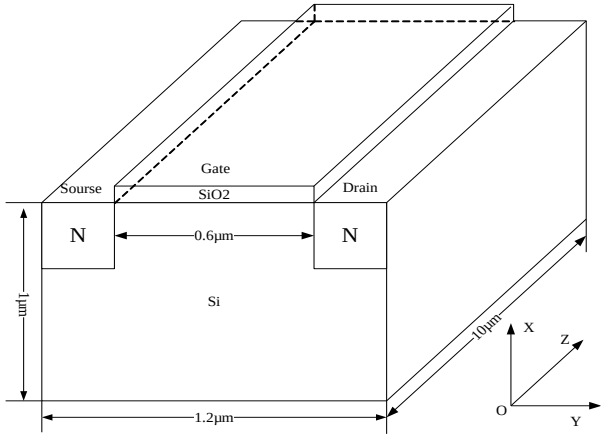

Fig. 2. A 3-D N-channel MOSFET model.

A. Simulation of MOSFET

First, the simulation of a single semiconductor device is implemented to prove the validity of the SETD method. The size of the MOSFET is as shown in Fig. 2, and the doping distribution in Fig. 3. The MOSFET has a size of 1.2*1*10 um, the drain junction depth of 0.3 um, and the oxide thickness of 50nm. The VA characteristic curve is given in Fig. 4, and the comparative results with the COMSOL software have shown the validity of the proposed method. In order to demonstrate the transient characteristic under the electromagnetic pulse with fast rise time, the response with a changing gate voltage has been shown in Fig. 5 and the voltage imposed in the drain is 0.5V. The overshoot current phenomena can be observed in MOSFET transistor from Fig. 5. It takes about additional 15 picoseconds to achieve stability for the particular state change [19]. The calculation of the program takes a little longer than COMSOL, but COMSOL takes up a lot more memory than the program.

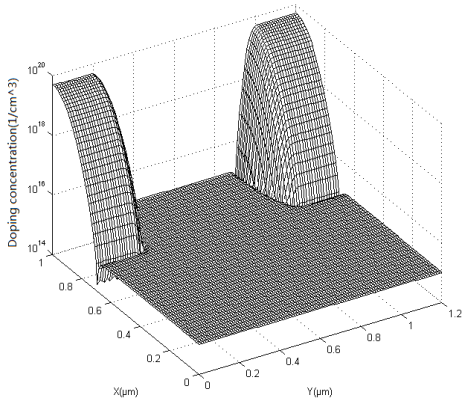

Fig. 3. The doping concentration of MOSFET.

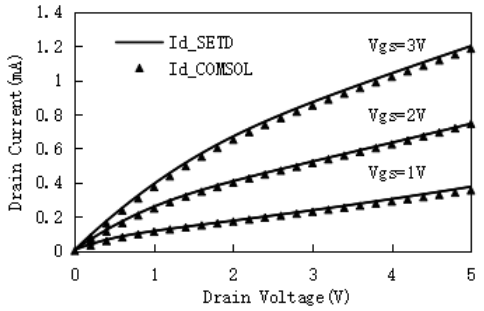

Fig. 4. The VA characteristic curve.

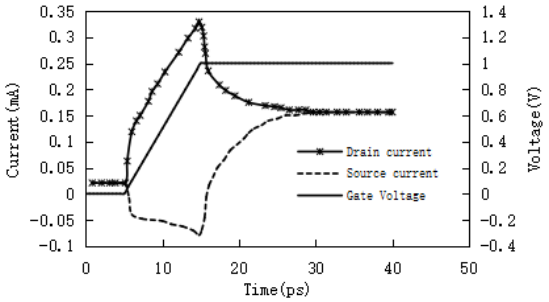

Fig. 5. The transient response with a changing gate voltage.

B. Electron-thermal analysis of circuit

A common source amplifier circuit as shown in Fig. 1 is simulated to analyze its electron-thermal characteristics. In the circuit, the model of MOSFET is the same as the above numerical example, and the simulation of the only semiconductor has been proven to be correct. The electron-thermal analysis of the circuit is following. The remaining setting of the elements in the circuit is as follows: VDD=20 V, R0=20 $K\Omega$, RL=100 $K\Omega$, VGG=1 V. The input signal of Vg and its response with Vds are shown in Fig. 6. The current Id through the MOSFET is shown in Fig. 7 and the transient Maximum temperature varying curve in the MOSFET is shown in Fig. 8. The thermal accumulation effect [6] can be found obviously.

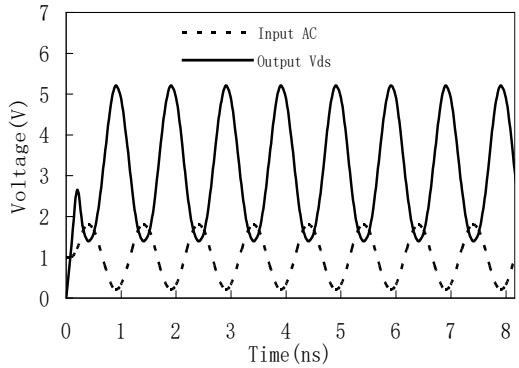

Fig. 6. The input and output voltages with Common Source Amplifier circuit.

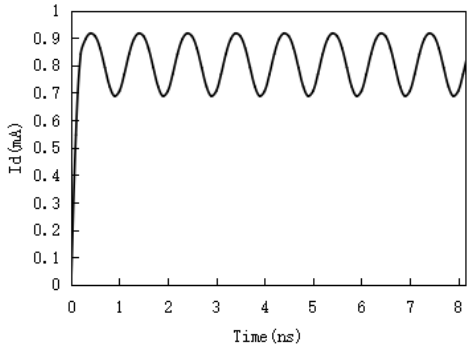

Fig. 7. The current in the MOSFET.

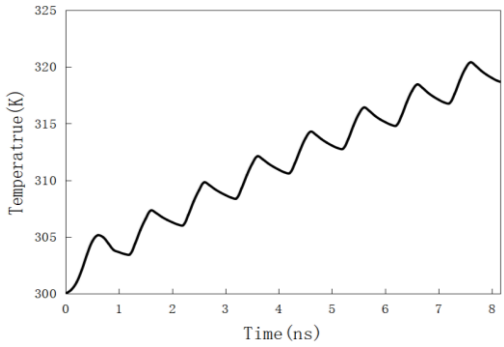

Fig. 8. The transient maximum temperature varying curve.

IV. CONCLUSION

In this paper, the simulation of semiconductor device based on the physical model by the spectral element method in time domain is presented. The VA characteristics of the N-channel MOSFET are analyzed, moreover, the transient response with the changing gate voltage is obtained. Finally, by the co-simulation of an external circuit with physics-based MOSFET model, the behavior of the common source amplifier circuit has been analyzed, the output voltage and current characteristic curves of the common source amplifier circuit has been obtained and the thermal accumulation effect can be found obviously.

ACKNOWLEDGMENT

This work was supported in part by National Key Lab. under Grant 614220503030317, by National Key Lab. of Science and Technology on Space Microwave under Grant 2018SSFNKLSMT-06, Natural Science Foundation of 61871228, the Fundamental Research Funds for the Central Universities No. 30918011202.

REFERENCES

[1] H. A. Mantooth and J. L. Duliere, "A unified diode model for circuit simulation," *IEEE Trans. Power Electron.*, vol. 12, no. 5, pp. 816-823, Sep. 1997.

[2] K. Kranti, "Microwave-frequency non-linear

universal model for PIN diode," *in Proc. IWPSD*, pp. 119-122, 2007.

[3] C. C. Enz and Y. Cheng, "MOS transistor modeling for RF IC design," *IEEE Trans. Solid-State Circuits*, vol. 35, no. 2, pp. 186-201, Feb. 2000.

[4] M. Pokorny and Z. Raida, "Multi-physics model of Gunn diode," *in Proc.17th Int. Conf. MIKON*, pp. 1-4, May 19-21, 2008.

[5] K. Shinohara and Q. Yu, "Reliability evaluation of power semiconductor devices using coupled analysis simulation," *in Proc. 12th IEEE Intersoc. Conf. Thermal Thermomech. Phenom. Electron. Syst.*, pp. 1-9, June 2-5, 2010.

[6] Z. Ren, W. Y. Yin, Y. B. Shi, and Q. H. Liu, "Thermal accumulation effects on the transient temperature responses in LDMOSFETs under the impact of a periodic electromagnetic pulse," *IEEE Trans. Electron Devices*, vol. 57, no. 1, pp. 345-352, Jan. 2010.

[7] S. Yan, A. Greenwood, J. M. Jin, "Modeling of plasma formation during high-power microwave breakdown in air using the discontinuous Galerkin time-domain method," [J]. *IEEE Journal on Multiscale & Multiphysics Computational Techniques*, 1:2-13, 2017.

[8] X. Chen, J. Chen, K. Huang, and X. B. Xu, "A circuit simulation method based on physical approach for the analysis of Mot_bal99lt1 p-i-n diode circuits," *IEEE Trans. Electron Devices*, vol. 58, no. 9, pp. 2862-2870, Sep. 2011.

[9] J. Chen, X. Chen, C. J. Liu, K. Huang, and X. B. Xu, "Analysis of temperature effect on p-i-n diode circuits by a multiphysics and circuit cosimulation algorithm," *IEEE Trans. Electron Devices*, vol. 59, no. 11, pp. 3069-3077, Nov. 2012.

[10] J.-H. Lee and Q. H. Liu, "A 3-D spectral-element time-domain method for electromagnetic simulation," *IEEE Trans. Microw. Theory Tech.*, vol. 55, no. 5, pp. 983-991, May 2007.

[11] I. Mahariq, M. Kuzuoglu, I. H. Tarman, and H. Kurt, "Photonic nanojet analysis by spectral element method," *IEEE. Photonics Journal*, vol. 6, no. 5, pp. 85-90, Oct. 2014.

[12] J.-H. Lee and Q. H. Liu, "An efficient 3-D spectral-element method for Schrödinger equation in nanodevice simulation," *IEEE Trans. Computer Aided Design of Integrated Circuits and Systems*, vol. 24, no. 12, pp. 1848-1858, Dec. 2005.

[13] Y. Sheng, K. Xu, D. Wang, and R. S. Chen, "Performance analysis of FET microwave devices by use of extended spectral-element time-domain method," *International Journal of Electronics*, vol. 100, no. 5, pp. 699-717, May 2013.

[14] K. Xu, R. S. Chen, Y. Sheng, P. Fu, C. Chen, Q. Yan, and Y. Y. Yu, "Transient analysis of microwave Gunn oscillator using extended spectral element time domain method," *Radio Science*, vol. 46, no. 5, pp. 369-380, Sep. 2011.

[15] R. E. Bank, D. J. Rose, and W. Fichtner, "Numerical methods for semiconductor device simulation," *IEEE Trans. Electron Devices*, vol. 30, no. 9, pp. 1031-1041, Sep. 1983.

[16] W. Fichtner, D. J. Rose, and R. E. Bank, "Semiconductor device simulation," *IEEE Trans. Electron Devices*, vol. 30, no. 9, pp. 1018-1030, Sep. 1983.

[17] S. Rzepka, K. Banerjee, E. Meusel, and C. Hu, "Characterization of self-heating in advanced VLSI interconnect lines based on thermal finite element simulation," *IEEE Trans. Compon. Packag. Manuf. Technol. A*, vol. 21, no. 3, pp. 406-411, Sep. 1998.

[18] R. Sayyah, M. Hunt, T. Macleod, and F. D. Ho, "Modeling a common-source amplifier using a ferroelectric transistor," *Integrated Ferroelectrics: An International Journal*, vol. 124, no. 1, pp. 147-156, 2011.

[19] S. Chen, D. Ding, and R. Chen, "A hybrid volume–surface integral spectral-element time-domain method for nonlinear analysis of microwave circuit," [J]. *IEEE Antennas and Wireless Propagation Letters*, vol. 16, pp. 3034-3037, 2017.

Analysis of the Charge Collection Mechanism of the Diamond Based on a Multi-physics Method

Yong Li [1,2*], Haiyan Xie [2], Linyue Liu [2], and Jianfu Zhang [2]

[1] School of Electronic and Information Engineering
Xi'an Jiaotong University, Xi'an 710049, China
liyong@mail.nint.ac.cn

[2] Northwest Institute of Nuclear Technology
Xi'an, 710024, China
xiehaiyan@nint.ac.cn, liulinyue@nint.ac.cn, zhangjianfu@nint.ac.cn

Abstract ─ Diamond is one of the most important wide-band-gap semiconductors for radiation detection and electronic device upgrading, however, for the lack of effective quantitative simulation method, the generation, recombination and movement of carriers in this material are still far from fully studied. In this paper, a multi-physics method for quantitative analysis of these complicated processes in diamond is established. Furthermore, charge collection process in a diamond detector with incident protons is quantitatively studied by using this method. It can be concluded that the influence of carrier lifetime on charge collection efficiency (CCE) is saturated when the value of carrier lifetime is greater than the characteristic time for carriers to cover the diamond device. The influence of electric field on CCE is saturated when the value of electric field strength is greater than 1 MV/m. By comparison of the simulated results and the theoretical results of an ideal case, good agreements have been acquired in both saturated electric field and unsaturated electric field conditions. All these results indicate that this method is useful for quantitative simulation and further optimization design of diamond detectors and other devices.

Index Terms ─ Charge collection efficiency, charge collection mechanism, diamond, drift-diffusion model, semiconductor.

I. INTRODUCTION

Because of the distinguished material characteristics [1-4], including high response speed, low leakage current, high carrier drift velocity, excellent thermal hardness, and long carrier lifetime, the diamond material has attracted special attentions in high energy physics applications such as detectors of α particles [5], X-rays [6-8], neutrons [9, 10], and other devices [11-14].

Charge collection efficiency (CCE) plays a vital role in the performance of a particle detector. Many efforts have been taken on chemical vapor deposition and other experimental methods to ameliorate the CCE of the diamond detectors [5, 15]. Though quantitative analysis of the charge collection mechanism is important for the improvement of CCE, there is still a lack of effective methods to study this problem. Most of the actual case cannot be dealt with by theoretical analysis which is based on an ideal condition [15]. By the Monte Carlo (MC) method, the energy loss of incident particles in material can be derived [17], and the total amount of the electron/hole pairs (*e-h* pairs) ionized by the incident particle can also be derived. However, not all the *e-h* pairs can be collected. The carrier movement and the carrier recombination cannot be studied by the MC method directly, and the CCE cannot be derived. Because of the complexity of this multi-physics process, developing a quantitative method to analyze the charge collection mechanism of the diamond material remains difficult. To the best of authors' knowledge, very few researches have been reported about the multi-physics method that can be used to study the complex processes in the diamond.

In this study, a multi-physics method based on the drift-diffusion model (DDM) [16] is presented. The charge collection process of the diamond is analyzed by this method. Carrier generation, carrier movement, and carrier recombination are quantitatively researched. The influences of parameters of both the electric field and the diamond material on CCE are illustrated. This work provides an useful method for further optimization of diamond detectors and other devices. This is the main motivation of this work.

This paper is organized as follows. In Section II, the carrier ionizations inside the diamond caused by the incident particle and the carrier movements are expressed by Partial Differential Equations (PDEs). In Section III, a schematic structure of the diamond detector and its parameters are given. In Section IV, The carrier

Submitted On: December 26, 2018
Accepted On: April 3, 2019

generation and carrier movement are presented. The influence of parameters of incident particles on CCE are illustrated in this section. The numerical results derived from this multi-physics method are theoretically verified. In Section V, some conclusions are given.

II. THEORETICAL MODEL

A. Mechanism of the diamond detector

Diamonds adopted in particle detectors are high-purity [1-3]. Without the incident particles, the free carriers are presented in the material due to thermal excitation. For intrinsic semiconductor material at finite temperature T, the intrinsic carrier concentration n_i can be expressed as follows [18, 19]:

$$n_i = \sqrt{N_C N_V}\exp(-\frac{E_g}{2k_b T}), \tag{1}$$

where N_c is the density of states on the bottom of the conduct band and N_v is the density of states on the top of the value band. The value of n_i can be derived by taking the material parameters in Table 1 into (1), and the intrinsic carrier concentration of the diamond at room temperature 300 K is 3.99×10^{-27} cm^{-3}. It is a very small value while the value of silicon material for Si-PIN detector is about 1.0×10^{10} cm^{-3} [18, 19]. However, because of unexpected impurities, a few carriers still exist in the diamond and can lead a leakage current without incident particles, which is usually less than 10×10^{-12} A [3, 15].

As illustrated in Fig. 1, when particles penetrate the diamond, *e-h* pairs are ionized along the tracks of particles. The electrons and holes are collected by the anode and the cathode respectively under a bias voltage and result in a current which can be measured in the back-end circuit.

In the rest parts of this section, the theoretical models of generation and movement of carries will be discussed in detail.

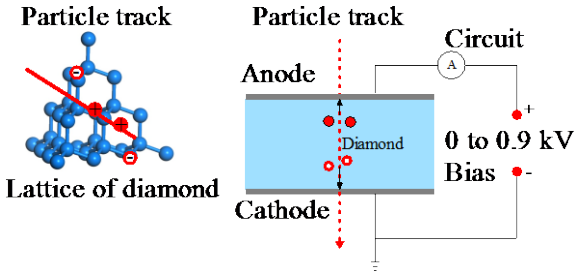

Fig. 1. The mechanism and the sketch map of the diamond detector. *e-h* pairs are ionized by incident particles in the diamond lattice. Then the *e-h* pairs are collected by electrodes under bias voltage results in a current, and the current can be detected by back-end circuit.

B. Equations of carrier ionization inside diamond

As analyzed in the previous part, without incident particles, the leakage current is very small. When particles penetrate into the diamond, the current in the diamond is much greater than the leakage current, and this current is mainly caused by the carriers ionized by incident particles. *e-h* pairs are ionized from the lattice of diamond by absorbing the energy lost by particles.

When a particle penetrates the diamond, the generation rate of *e-h* pairs induced by the particle can be expressed as a Gaussian function:

$$G_n = G_0 \exp[-\frac{(t-t_{\max})^2}{2\tau_0^{\ 2}}], \tag{2}$$

where t_{max} is the time instant when electron-hole pair generation rate reaches its maximum. τ_0 is the characteristic time. G_0 is the unitary constant which can be denoted as follows:

$$G_0 = \frac{2E}{E_0\tau_0\sqrt{\pi}}, \tag{3}$$

where E_0 is the average energy for generating a single *e-h* pairs, and the value is given in Table 1. E is the particle deposition energy, which is deposited by the carbon atoms of the diamond. The particle deposition energy in the diamond depends on the particle energy and particle species and can be numerically derived by the Monte Carlo simulation [17]. The particle deposition energy can be defined as:

$$E_{dep} = \int_0^{\lambda} \rho\delta(L)dL, \tag{4}$$

where δ is the linear energy transfer (LET) derived by the Monte Carlo simulation. ρ is the density of the diamond. λ is the incident depth of the particle.

The amount of *e-h* pairs of the unit length along the incident particle trace can be expressed as:

$$\Delta N = \frac{\rho\delta(L)}{E_0}. \tag{5}$$

The total amount of *e-h* pairs can be derived by the integral of (5) and can be expressed as:

$$N = \int_0^{\lambda} \frac{\rho\delta(L)}{E_0}dL = \frac{E_{dep}}{E_0}, \tag{6}$$

where the value of E_0 is given in Table 1.

C. Equations of carrier movement inside diamond

Behaviors of charges in electromagnetic field have attracted many attentions [20]. In this simulation, the DDM [16] has been used to describe the carrier movement inside other semiconductor material [21], and here is used to describe the diamond under a bias voltage, and can be expressed as follows:

$$\frac{\partial n_n}{\partial t} = \nabla\cdot(n_n\mu_n\mathbf{E} + \mu_n\frac{k_bT}{q}\nabla n_n) - (U-G), \tag{7}$$

$$\frac{\partial n_p}{\partial t} = -\nabla \cdot (n_p \mu_p \mathbf{E} - \mu_p \frac{k_b T}{q} \nabla n_p) - (U - G), \quad (8)$$

$$\nabla \cdot \varepsilon \nabla \psi = -q(n_p - n_p + N_D - N_A) - \rho_s, \quad (9)$$

where n_n is the n-type carrier concentration and n_p for p-type, μ_n is the n-type carrier mobility and μ_p for p-type, **E** is the electric field, t is the time, T is the temperature, k_b is the Boltzmann constant, q is the unit charge, U is the recombination rate of carriers and G is the ionization rate. ε is the dielectric constant in the semiconductor. Ψ is the potential in the semiconductor. ρ_s is the surface charge density. N_D is the donor doping concentration and N_A is the acceptor doping concentration. For a high-purity diamond, N_D, ρ_s, and N_A are all set to be zero, then (9) can be written as:

$$\nabla \cdot \varepsilon \nabla \psi = -q(n_p - n_n) = \rho . \quad (10)$$

In this study, n-type carriers are electrons ionized by incident particles, while p-type carriers are holes. T here is set to be uniform at room temperature 300 K.

Because of the high bias voltage which is attached to electrodes of the detector, the electric field inside the diamond is strong. The electron mobility and hole mobility in strong field can be expressed as:

$$\mu_i = \frac{\mu_{i0}}{1 + \mu_{i0} E / v_{si}}, (i = n, p), \quad (11)$$

where μ_{in} is the low field electron mobility. μ_{ip} is the low field hole mobility. μ_{sn} is the saturated velocity of electrons. μ_{sp} is the saturated velocity of holes. E is the electric field strength. The values are listed in Table 1.

D. Equations of carrier recombination inside diamond

When a bias voltage is applied to electrodes of the detector, carriers are moving toward electrodes, forced by electric field. However, not all of the carries can be collected by electrodes and come into current, a part of the *e-h* pairs recombine in the course moving towards electrodes. CCE η is defined as the ratio between collected charge and total generated charge and can be expressed as follows:

$$\eta = Q_c / Q_g . \quad (12)$$

As a wide band gap semiconductor material, high-purity diamond analyzed here contains very few impurities, then the Shockley-Read-Hall (SRH) recombination which occurs nearby traps in energy gap is the primary mechanism of carrier recombination [18-19]. The SRH recombination rate U_{SRH} can be expressed as follows:

$$U_{SRH} = \frac{n_p n_n - n_i^2}{\tau_p [n_n + n_i \exp(\frac{E_{trap}}{k_b T})] + \tau_n [n_p + n_i \exp(-\frac{E_{trap}}{k_b T})]}, \quad (13)$$

where τ_n is the n-type carrier lifetime and τ_p is the p-type carrier lifetime. E_{trap} is the energy difference between the trap energy level and the intrinsic Femi energy level. n_i is the intrinsic carrier concentration. n and p are respectively the n-type carrier concentration and the p-type carrier concentration.

III. NUMERICAL METHOD

Finite element method and Finite Volume Method (FVM) are used to carried out the PDEs of electromagnetic problems [22-23] and the DDM [24-25]. In this paper, FVM is adopted. In order to describe the DDM briefly, solution vector **Q**, flux vector **F**, and source term **S** are introduced into the equations, they can be expressed as follows:

$$\mathbf{Q} = \begin{pmatrix} 0 \\ n_n \\ n_p \end{pmatrix}, \quad (14)$$

$$\mathbf{F} = \begin{pmatrix} \varepsilon \nabla \psi \\ \frac{1}{q} \mathbf{J}_n \\ -\frac{1}{q} \mathbf{J}_p \end{pmatrix}, \quad (15)$$

$$\mathbf{S} = \begin{pmatrix} \rho \\ U - G \\ U - G \end{pmatrix}. \quad (16)$$

where the current density vectors **J** is defined as:

$$\mathbf{J} = \mathbf{J}_n + \mathbf{J}_p , \quad (17)$$

where electron current density vectors and hole current density vectors are defined as:

$$\mathbf{J}_n = n_n \mu_n \mathbf{E} + \mu_n \frac{k_b T}{q} \nabla n_n , \quad (18)$$

$$\mathbf{J}_p = n_p \mu_p \mathbf{E} + \mu_p \frac{k_p T}{q} \nabla n_p . \quad (19)$$

Equations of the DDM can be expressed as:

$$\frac{\partial \mathbf{Q}}{\partial t} = \nabla \cdot \mathbf{F} + \mathbf{S} . \quad (20)$$

Using the Green's equation, it can be expressed as:

$$\int_{\Omega_m} \frac{\partial \mathbf{Q}_m}{\partial t} dV = \sum_e \mathbf{F}_e l_e + \int_{\Omega_i} \mathbf{S}_m dV \mathbf{S} , \quad (21)$$

where Ω_m is the m controlled volume, $\mathbf{F}_e$ is the projection component of **F** in the boundary of controlled volume. l_e is length of the boundary.

Electron and hole concentrations in a controlled volume are both set to be uniform approximately. Then the left side of Eq. (21) can be expressed as:

$$\int_{\Omega_m} \frac{\partial \mathbf{Q}_m}{\partial t} dV = \frac{\partial \mathbf{Q}_m}{\partial t} \Delta V_{\Omega_m} , \quad (22)$$

where $\Delta V_{\Omega m}$ is the cubage of controlled volume m.

The generation of carrier is set to be as initial condition before the calculation, and the generation of carrier during a single time step is ignored. Meanwhile, the recombination rate is set to be constant. Then the source term **S** can be expressed as:

$$\int_{\Omega_m} \mathbf{S}_m dV = \mathbf{S}_m \Delta V_{\Omega_m} . \quad (23)$$

In the calculation, triangle mesh of controlled volume as shown in Fig. 2 are adopted. Then the functions of flux in points *i*, *j* and *k* can be expressed as:

$$\mathbf{F}_i = (J_j d_j - J_k d_k)\hat{n}, \quad (24)$$

$$\mathbf{F}_j = (J_k d_k - J_i d_i)\hat{n}, \quad (25)$$

$$\mathbf{F}_k = (J_i d_i - J_j d_j)\hat{n}, \quad (26)$$

where *i*, *j*, and *k* are the vertexes of the triangle mesh of controlled volume *m* respectively. $\hat{n}$ is the unit vector along the direction of the flux. Point *O* is the center of circumcircle of the triangle mesh. $\widehat{s_i}$, $\widehat{s_j}$, and $\widehat{s_k}$ are the unit vectors in boundaries of a triangle mesh respectively. J_i, J_j, and J_k are the average projections of current in the boundaries of *i*, *j* and *k* of the triangle mesh respectively. J_k can be expressed as:

$$J_k = \mathbf{J} \cdot \widehat{s_k}. \quad (27)$$

In the calculation, electric field strength and current vary slowly along the boundary of the triangle mesh, then this problem can be dealt as three one-dimension problems. Then electron current and hole current of J_k in (27) can be expressed respectively as follows:

$$J_{nk} = \frac{q\mu_n V_T}{L_k}[n_{nj}B(\frac{\psi_j - \psi_j}{V_T}) - n_{ni}B(-\frac{\psi_j - \psi_i}{V_T})], \quad (28)$$

$$J_{pk} = \frac{q\mu_p V_T}{L_k}[n_{pi}B(\frac{\psi_j - \psi_j}{V_T}) - n_{pj}B(-\frac{\psi_j - \psi_i}{V_T})], \quad (29)$$

where V_T is the threshold voltage of the diamond material, defined as:

$$V_T = \frac{k_b T}{q}. \quad (30)$$

Function B in (28) and (29) is the Bernoulle function, and can be expressed as:

$$B(x) = \frac{x}{e^x - 1}. \quad (31)$$

J_i and J_j can be derived by the same steps. The steps of the calculation are shown in the flowchart of Fig. 3.

IV. PARAMETERS OF THE DIAMOND DETECTOR

The working mechanism of the diamond detector is briefly described in part II. In this simulation, the diamond detector is set to be cylindrical symmetry as illustrated in Fig. 1. A finite volume method code as introduced in Section III is used to carry out the PDEs. The material parameters of the diamond used in the simulation are shown in Table 1. The thickness of the diamond in the detector is set to be 300 μm as reported [15].

The generation of carriers follows a Gaussian function as denoted in (2). In the following numerical simulations, t_{max} is set to be 10 ps and characteristic time τ_0 is set to be 1 ps.

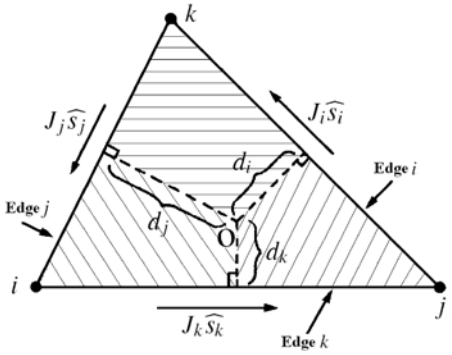

Fig. 2. The triangle mesh in the code.

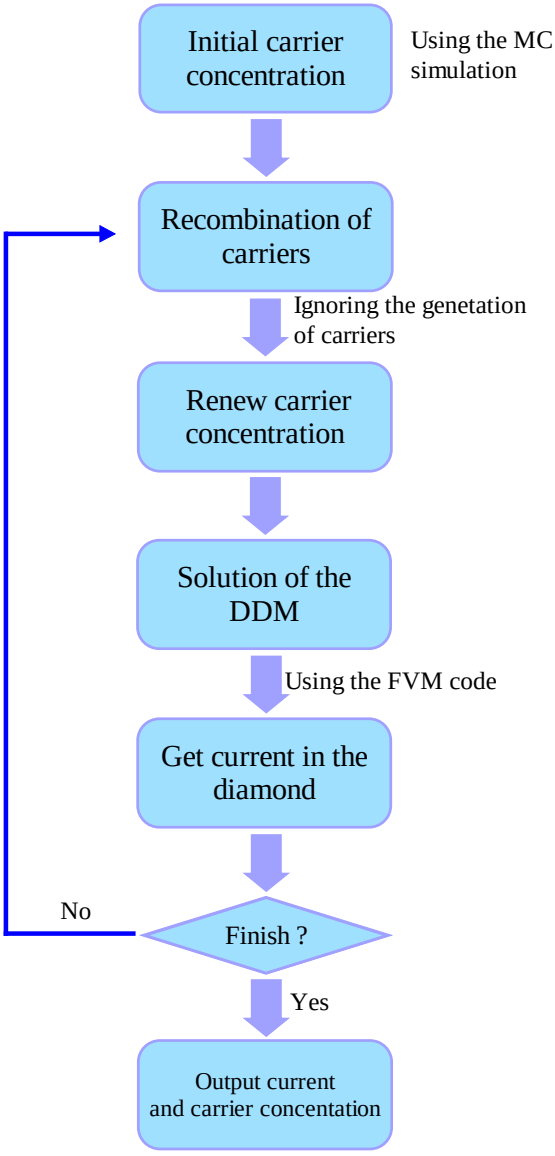

Fig. 3. Flowchart of the simulation.

Table 1: Material parameters of the diamond used in the simulation

Parameters	Parameter Name	Value
E_g	Band gap of diamond	5.5 eV
T_m	Melting point	4273 K
E_{Af}	Affinity of Si	4.15 eV
ε_{dia}	Relative permittivity of the diamond	5.7
μ_{n0}	Low field electron mobility	1714 $cm^2/V/s$
μ_{p0}	Low field hole mobility	2064 $cm^2/V/s$
v_{sn}	Electron saturated velocity	9.6×10^6 cm/s
v_{sp}	Hole saturated velocity	14.1×10^6 cm/s
N_c	Density of states on bottom of conduct band	6.57×10^{19} cm^{-3}
N_v	Density of states on top of value band	1.80×10^{19} cm^{-3}
E_0	Ionization energy of a single *e-h* pair	13 eV
E_{BR}	Breakdown field	10×10^4 V/cm
ρ (dia)	Density of diamond	3.515 g/cm^{-3}
c_p (dia)	Specific heat of diamond	0.52 J/g/K
k_b	Boltzmann constant	1.381×10^{-23} J/K
q	Unit charge	1.602×10^{-19} C

The LET depends on parameters of the incident particles. In the simulation, incident particles are all protons, so the energy of the incident proton is the dominant of the LET. Four proton energies are studied in the simulation, they are 4.5 MeV, 6.62 MeV, 7.65 MeV, and 9.71 MeV. In the following simulations, LET of different protons is set according to the MC simulation results which are illustrated in Table 2. As shown in Fig. 4, the 9.71 MeV proton penetrates through the diamond, other three are absorbed by the diamond. The density of *e-h* pairs along the trace of the incident proton can be derived by (6).

The Bias voltage is set from 50 V to 900 V. So the electric field in the diamond varies from 0.6×10^6 V/m to 3×10^6 V/m, and is less than the breakdown field as listed in Table 1.

The interfaces between the diamond and metal electrodes are set to be Ohmic contact boundaries.

By using the parameters in Table 1, the electron velocity and the hole velocity can be derived from (11) as illustrated in Fig. 5. When the electric field is greater than 1×10^6 V/m, both the electron velocity and the hole velocity increase very slowly versus the electric field strength and reach saturation points gradually.

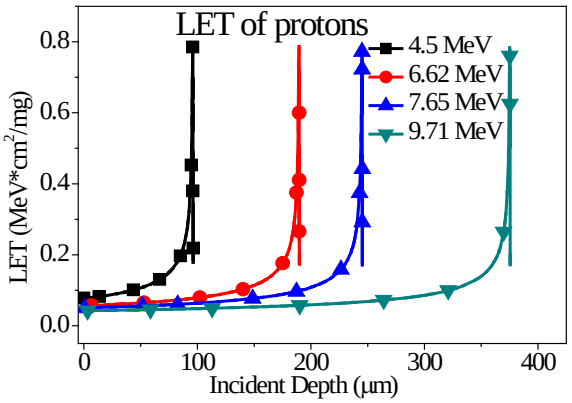

Fig. 4. The values of LET derived by the MC simulation. The proton energies are 4.5 MeV, 6.62 MeV, 7.65 MeV and 9.71 MeV. The 9.71 MeV proton penetrates through the diamond.

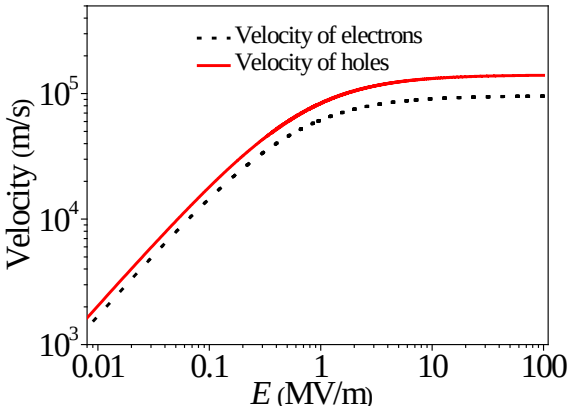

Fig. 5. Velocity of electrons and holes vs. electric field based on (11).

Table 2: Mc simulation results of the protons

Energy of Proton	Incidence Depth	Ionized Charge
4.5 MeV	96.19 μm	5.496×10^{-14} C
6.62 MeV	189.87 μm	8.073×10^{-14} C
7.65 MeV	245.32 μm	9.934×10^{-14} C
9.71 MeV	300 μm	7.096×10^{-14} C

V. CALCULATION RESULTS AND DISCUSSION

The initial distributions of space charges which are generated by the 4.5 MeV proton and the 9.71 MeV proton are illustrated in Fig. 6. The values of LET in the end of the incident traces are much higher, so the amount of charges in these positions are much higher. On the contrary, the 9.71 MeV proton penetrates through the

diamond, and the charge concentration is uniform because of the uniform LET. Electric fields of both two cases are affected by the distribution of space charges, as illustrated in Fig. 6.

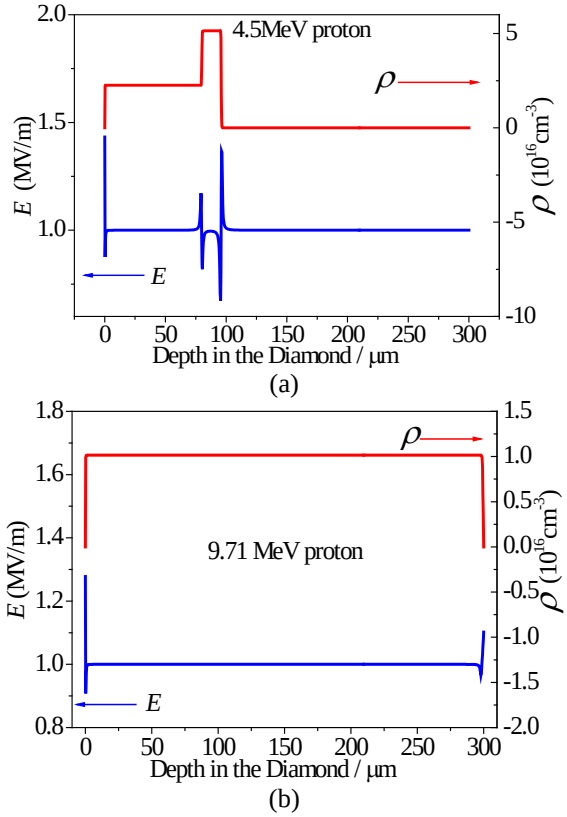

Fig. 6. The initial concentration of the space charges ionized by the proton. Energies of incident protons are 4.5 MeV and 9.71 MeV respectively. The lifetime of carriers is 1 ns. The electric field in the diamond is 1 MV/m. (a) 4.5 MeV and (b) 9.71 MeV.

The currents in the electrodes, which are induced by different incident protons are illustrated in Fig. 7. Every current in Fig. 7 consists of two parts: the displace current part and the conduction current part. The displace current part arises at almost the same time when space charges are generated by the incident protons. The conduction current part arises later, limited by the velocities of electrons and holes.

The peak value of the displace current part is determined by the total amount of the space charges, and the peak value is not affected by the carrier lifetime, as illustrated in Fig. 8. However, the conduction current part is determined by the amount of charges which are collected by the electrodes. Shorter carrier's lifetime means higher probability of charge recombination, which results in a greater loss of the charges which can arrive in electrodes. The currents of different carrier lifetimes are illustrated in Fig. 8.

More details of the charge collection mechanism and the movements of charges will be discussed in the following parts.

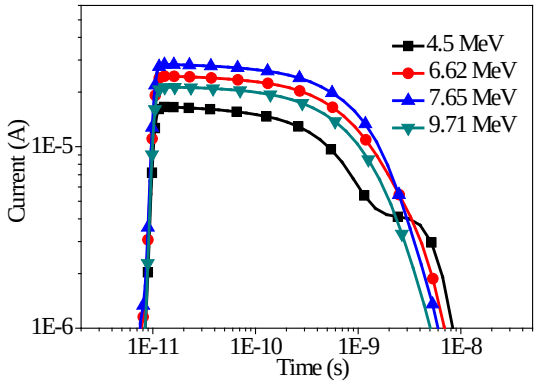

Fig. 7. Currents in the diamond. Energies of incident protons are 4.5 MeV, 6.62 MeV, 7.65 MeV and 9.71 MeV respectively. The lifetimes of the carriers are all 1 ns. The electric field in the diamond is 1 MV/m.

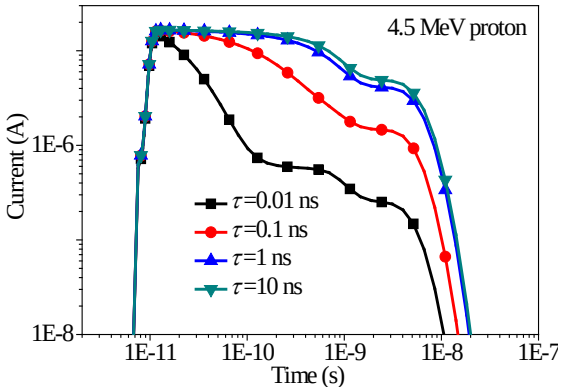

Fig. 8. Currents in the diamond. Energy of the incident proton is 4.5 MeV. The carrier lifetimes are 0.01ns, 0.1 ns, 1 ns and 10 ns, respectively. The electric field in the diamond is 1 MV/m.

A. Movements of charges

The charge concentrations at different time are illustrated in Fig. 9. Because of the carrier recombination, the peak value of charge concentrations falls down at the later time. Simultaneously, the space charges move towards the electrodes forced by the electric field.

B. Influence of the carrier lifetime

As mentioned in Fig. 8, shorter carriers lifetime results in a greater loss of the charges which can arrive in electrodes. The distributions of electrons and holes with various carrier lifetimes are illustrated in Fig. 10. During the same time, carriers of shorter lifetime recombines at a higher probability, result in a smaller peak value of

concentration.

The flight time for carriers to cover the diamond can be derived as:

$$\Delta t = L / (v_n + v_p), \quad (32)$$

where L is the distance between the cathode and the anode. v_n is the electron velocity and v_p is the hole velocity. When the electric field in the diamond is 1 MV/m, v_n = 6.1573×10^4 m/s, v_n =8.3772×10^4 m/s. Then Δt = 2.07 ns. If the values are greater than Δt, the influence of carrier lifetime on increasing CCE becomes exiguous. The results are illustrated in Fig. 11.

C. Influence of electric field

The drift velocity of electrons and holes versus electric field is expressed in (11) and illustrated in Fig. 5. The drift velocity becomes saturated when the electric field is greater than 1 MV/m. As illustrated in Fig. 12, the influence of electric field on the movements of carriers becomes exiguous when the electric field is greater than 1 MV/m. The influence of the electric field on CCE is illustrated in Fig. 13. For all the four incident protons, the saturated values of CCE are derived when the electric field is greater than 1 MV/m.

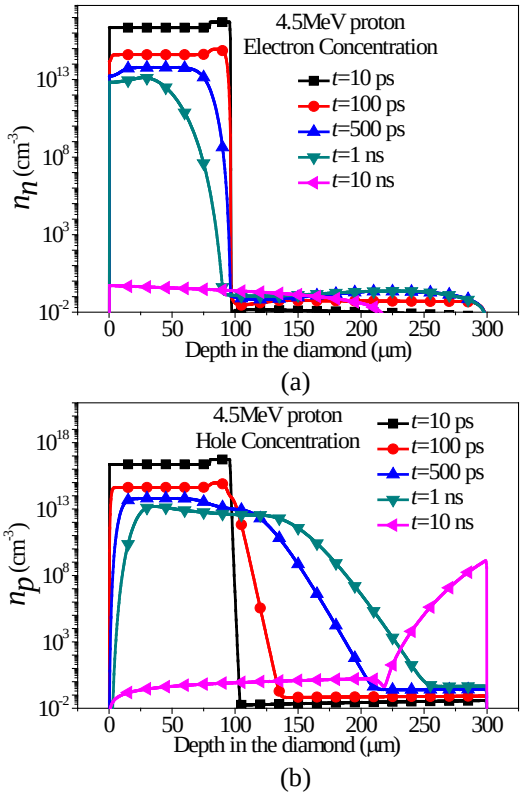

Fig. 9. The charge concentrations at different time. The energy of the incident particle is 4.5 MeV. The lifetimes of carriers are 1 ns. The electric field in the diamond is 1 MV/m: (a) the electron concentrations and (b) the hole concentrations.

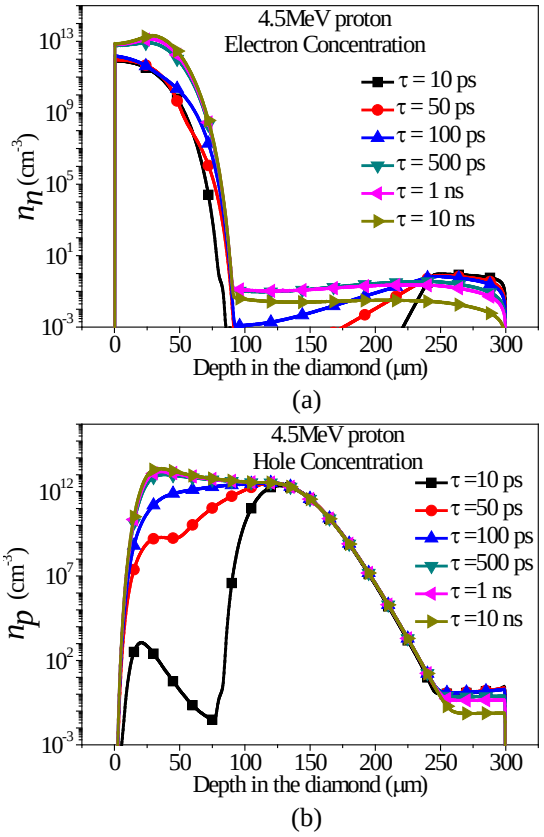

Fig. 10. The charge concentrations with various carrier lifetimes. The energy of the incident particle is 4.5 MeV. The electric field in the diamond is 1 MV/m. The time is 1 ns after the proton penetrated into the diamond: (a) the electron concentrations and (b) the hole concentrations.

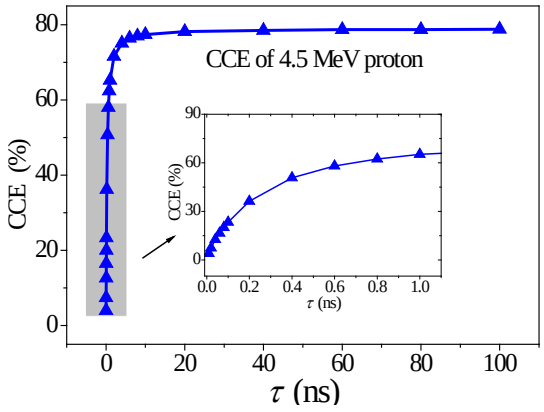

Fig. 11. CCE of the diamond with various lifetimes of carriers. The energy of the incident particle is 4.5 MeV. The electric field in the diamond is 1 MV/m.

D. Verification of the method

In the case of a perfect and uniform distribution of space charges, the CCE can be theoretically derived [15, 26], and can be written as a function of charge collection

distance (CCD) as:

$$\eta = \frac{\sigma}{L}[1-\frac{\sigma}{4\lambda}(1-e^{-2\lambda/\sigma})(1+e^{2(\lambda-L)/\sigma})]. \quad (33)$$

where L is the distance between cathode and anode. λ is the incident depth of radiation particles. In the penetrating-through case, λ is set to be equal to L. The CCD is defined as:

$$\sigma = (\frac{\mu_n}{1+\mu_n E/v_{sn}} + \frac{\mu_p}{1+\mu_p E/v_{sp}})\tau E = (v_n + v_p)\tau. \quad (34)$$

where v_n is the electron velocity and v_p is the hole velocity, as mentioned in (11). τ is the average carrier lifetime. The values of τ are reported to be in a range of 10^2~10^3 ps [15] to 30 ns [27].

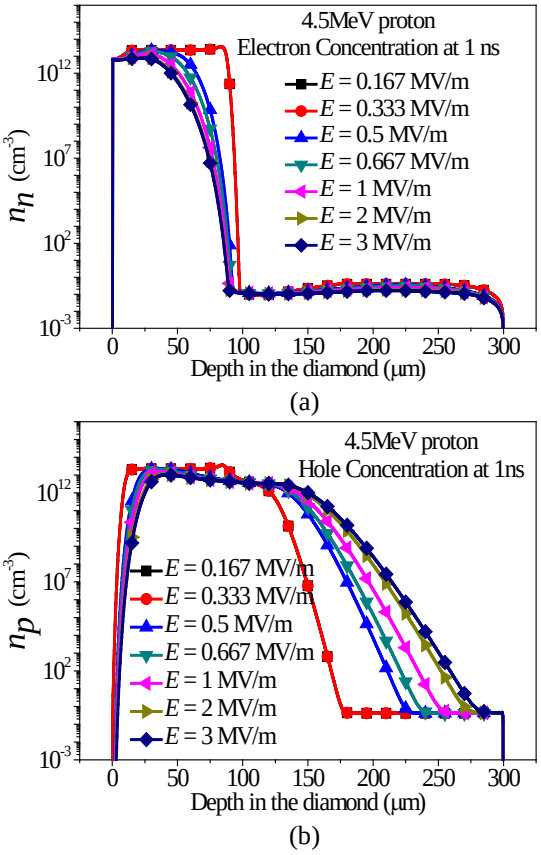

Fig. 12. The charge concentrations with various electric fields. The energy of the incident particle is 4.5 MeV. The lifetime of carriers is 1 ns: (a) the electron concentrations and (b) the hole concentrations.

The theoretical results derived from (34) is based on the physical hypothesis: carriers, both electrons and holes, distribute uniformly in the whole the diamond. However, as shown in Fig. 6, this ideal hypothesis is hard to achieve in a real case. Carrier concentrations in the case of 9.71 MeV proton can be treated as uniform approximately as shown in Fig. 6. Comparisons of simulated results based on this multi-physics method and theoretical results from (33) are illustrated in Fig. 14. In the case of small CCE, which means the length of the trace for a single carrier is short, the heterogeneity during the trace is also small and can be ignored. In that case, the difference between the simulated results and the results from (33) is small. In the case of large CCE, which means the length of the trace for a single carrier is great, the heterogeneity during the trace becomes great. As a result, the difference between simulated results and the results from (33) becomes great.

As shown in Fig. 14, curves in small CCE case and large CCE case both follow the analysis mentioned above. This result indicates that this multi-physics method is physically reliable. Meanwhile, this method is effective for the complicated case which does not match the ideal hypothesis.

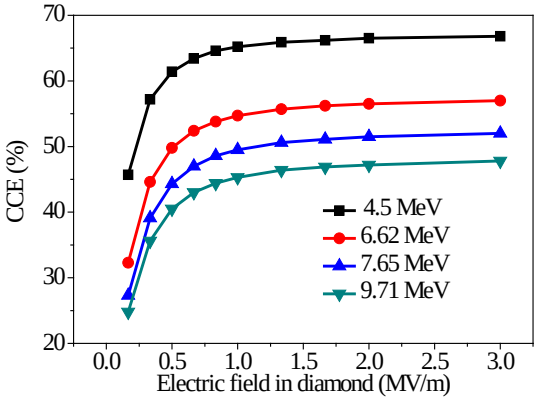

Fig. 13. CCE of the diamond versus electric field. Energies of the incident protons are 4.5 MeV, 6.62 MeV, 7.65 MeV and 9.71 MeV respectively. The lifetimes of the carriers are all 1 ns.

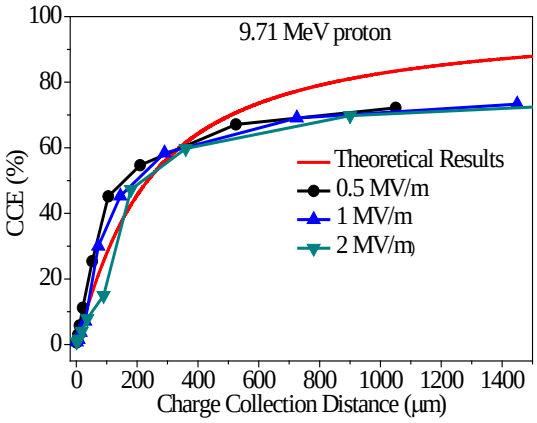

Fig. 14. CCE comparisons between the simulated results and the theoretical results based on (33).

VI. SUMMARY AND CONCLUSION

In this paper, a multi-physics method which synthesizes the complicated processes of the diamond is presented. The carrier generation, carrier recombination and carrier movement are analyzed quantitatively by this method. Based on the previous analyses, conclusions are made as follows:

1) The current in the diamond induced by an incident proton consists of two parts: the displace current part and the conduction current part. The peak value of the displace current part is determined by the total amount of space charges which are generated by the incident protons.

2) The carrier lifetime and the electric field are important factors of CCE. The influence of carrier lifetime is saturated when the value of carrier lifetime is greater than the flight time for carriers to cover the diamond. The influence of electric field is saturated when the value of electric field strength is greater than 1 MV/m.

3) This multi-physics method is verified by the comparison between the simulated results using this method and the theoretical results. Good agreements are presented in both saturated electric field and unsaturated electric field.

This work brings an effective method for quantitative analysis of diamond detectors and is useful for further optimization of diamond detectors and other diamond devices.

ACKNOWLEDGMENT

This work was supported by the National Natural Science Foundation of China (under Grant 61231003 and Grant 11605140).

The authors would like to thank Prof. Xiaoping Ouyang of the Northwest Institute of Nuclear Technology for the discussion on the interaction between particles and the diamond.

Also thank Dr. Chen Shen and Ding Gong of the Cogenda Company for their helps on the MC simulation.

REFERENCES

[1] J. Isberg, J. Hammersberg, E. Johansson, et al., "High carrier mobility in single-crystal plasma-deposited diamond," *Science*, vol. 297, pp. 1670-1672, 2002.

[2] H. Kagan, "Recent advances in diamond detector development," *Nucl. Instr. and Meth. A*, vol. 541, pp. 221-227, 2005.

[3] X. Ouyang, L. Wang, R. Fan, et al., "Preparation of diamond film based radiation detector," *Acta. Phys. Sin.*, vol. 55, no. 5, pp. 2170-2174, 2006.

[4] S. Almaviva, M. Marinelli, E. Milani, et al., "Chemical vapor deposition diamond based multi-layered radiation detector: Physical analysis of detection properties," *Journal of Applied Physics*, vol. 107, no. 1, p. 014511, 2010.

[5] M. Marinelli, E. Milani, A. Paoletti, et al., "High-quality diamond grown by chemical-vapor deposition: Improved collection efficiency in α-particle detection," *Applied Physics Letters*, vol. 75, no. 20, pp. 3216-3218, 1999.

[6] L. Hou, F. Li, Y. Yuan, et al., "Chemical vapor deposited diamond detectors for soft X-ray power measurement," *Acta. Phys. Sin.*, vol. 59, no. 02, pp. 1137-1141, 2010.

[7] B. Yu, B. Chen, L. Hou, et al., "Hard X-ray measurement for indirect-driven imploding by chemical vapor deposited diamond detectors," *Acta. Phys. Sin.*, vol. 62, no. 5, p. 058102, 2013.

[8] L. Liu, X. Ouyang, J. Zhang, et al., "Properties comparison between nanosecond X-ray detectors of Polycrystalline and single-crystal diamond," *Diamond & Related Materials*, vol. 73, pp. 248-252, 2017.

[9] M. Marinelli, E. Milani, G. Prestopino, et al., "High performance ^{6}LiF-diamond thermal neutron detectors," *Applied Physics Letters*, vol. 297, no. 14, p. 143509, 2002.

[10] L. Liu, X. Ouyang, Z. Zhang, et al., "Polycrystalline chemical-vapor-deposited diamond for fast and ultra-fast neutron detector," *Science China: Technological Sciences*, vol. 22, no. 9, pp. 2640-2645, 2012.

[11] X. Chang, Q. Wu, I. Ben-Zvi, et al., "Electron beam emission from a diamond-amplifier cathode," *Physics Review Letters*, vol. 105, no. 16, p. 164801, 2010.

[12] L. Liu, X. Ouyang, J. Zhang, et al., "Polycrystalline diamond based detector for Z-pinich plasma diagnosis," *Review of Scientific Instruments*, vol. 81, no. 8, p. 083502, 2010.

[13] L. Liu, X. Ouyang, J. Zhang, et al., "Polycrystalline CVD diamond detector: Fast response and high sensitivity with large area," *AIP Advanced*, vol. 4, no. 1, pp. 017114, 2014.

[14] X. Wang, J. Wang, and L. Wang, "Single-layer nano-carbon film, diamond film, and diamond/ nano-carbon composite film field emission performance comparison," *Applied Physics Letters*, vol. 108, no. 19, p. 191602, 2016.

[15] L. Wang, "Studies on CVD Diamond Detectors for Pulsed Radiation Detection," *Ph.D. Thesis*, Tsinghua University, Beijing, China, 2008.

[16] H. K. Gummel, "A self-consistent iterative scheme for one-dimensional steady state transistor calculations," *IEEE Trans. Electron Devices*, vol. 9, no. 11, pp. 455-465, 1964.

[17] S. Agostinelli, J. Alison, K. Amoko, and et al., "GEANT4: A simulation toolkit," *Nucl. Instr. and Meth. A*, vol. 506, pp. 250-303, 2003.

[18] S. M. Sze and K. K. Ng, *Physics of Semiconductor*

Devices. 3rd edition, New York: John Wiley & Sons, 2006.
[19] L. Ye, *Physics of Semiconductor*. Beijing, China: Beijing, Higher Education Press, 2007.
[20] J. Wang, D. Zhang, C. Liu, et al., "UNIPIC code for simulation of high power microwave devices," *Physics of Plasma.*, vol. 16, no. 3, pp. 03310801-03310810, 2009.
[21] H. Bao, D. Ding, J. Bi, W. Gu, and R. Chen, "An efficient spectral element method for semiconductor transient simulation," *Applied Computational Electromagnetics Society Journal*, vol. 31, no. 11, pp. 1337-1342, 2016.
[22] Y. Zhou, L. Shi, N. Liu, C. Zhu, H. Liu, and Q. H. Liu, "Spectral element method and domain decomposition for low frequency subsurface," *IEEE Geosci. Remote Sens. Lett.*, vol. 13, no. 4, pp. 550-554, 2016.
[23] Y. Zhou, L. Shi, N. Liu, C. Zhu, Y. Sun, and Q. H. Liu, "Mixed spectral-element method for overcoming the low-frequency breakdown problem in subsurface EM exploration," *IEEE Geosci. Remote Sens.*, vol. 55, no. 6, pp. 3488-3500, 2017.
[24] A. Jameson, "A solution of the Euler equations for two dimensional transonic flow by a multi-grid method," *Applied Mathematics and Computation.*, vol. 13, pp. 327-355, 1983.
[25] J. V. Soulis, "Finite volume method for three-dimensional transonic potential flow through turbo-machinery blade rows," *International Journal of Heat and Fluid Flow.*, vol. 4, no. 2, pp. 85-96, 1983.
[26] K. Hecht, "Zum mechanismus des lichtelektrischen primarstromes in isolierenden kristallen," *Z. Physik*, vol. 77, pp. 235-245, 1932.
[27] H. Pernegger, S. Roe, P. Weilhammer, et al., "Charge-carrier properties in synthetic single-crystal diamond measured with the transient-current technique," *Journal of Applied Physics*, vol. 97, no. 07, p. 073704, 2005.

Yong Li was born in Anhui Province, P.R. China, on January 28, 1984. He obtained the B.S. and M.S. degrees in Physics from University of Science and Technology of China (USTC), Hefei Anhui, P.R. China, in 2006 and 2009 respectively. Since 2016, he is currently working toward the Ph.D. degree in the School of Electronic and Information Engineering, Xi'an Jiaotong University, Xi'an, P.R. China.

He is currently with the Northwest Institute of Nuclear Technology (NINT) as an Assistant Scientist. His research interests mainly include electromagnetic compatibility, electromagnetic effect of semiconductor devices and circuits.

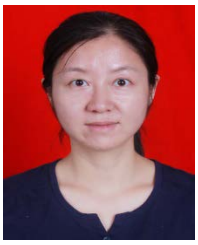

Haiyan Xie was born in Anhui Province, P.R. China, on February 27, 1984. She received the B.S. and Ph.D degrees in Engineering Physics from Tsinghua University, Beijing, P.R. China, in 2005 and 2010, respectively. She received best doctoral thesis of Tsinghua University in 2010.

During 2011 to 2012, she conducted her post-doctoral research at Northwest Institute of Nuclear Technology (NINT). Now, she serves NINT as an associate scientist.

Her research interests mainly include electromagnetic compatibility, electromagnetic interference, and trans-mission line analysis.

Linyue Liu was born in Shannxi Province, P.R. China, 1983. She obtained the B.S. degree in Material Physics from University of Science and Technology of China (USTC), Hefei Anhui, P.R. China, in 2005. She obtained the Ph.D. degree in Nuclear Science and Technology from Xi'an Jiaotong University, Xi'an, P.R. China in 2018.

Her research interests mainly include neutron detection, wide-gap semiconductor detectors, and particle physics.

Jianfu Zhang was born in Jiangxi Province, P.R. China, 1977. Now, he serves NINT as an Associate Scientist. His research interests mainly include detectors and particle physics.

Geometrical Dependence in Fixtures for 2D Multipole Micromagnets Magnetization Pattering

Miriam Martinez-Muñoz [1], Efren Diez-Jimenez [1], Gabriel Villalba Alumbreros [1], Marcin Michalowski [2], and Alberto Lastra-Sedano [3]

[1] Mechanical Engineering Area, Universidad de Alcalá, Spain
gabriel.villalba@edu.uah.es , efren.diez@uah.es, miriam.martinezm@uah.es

[2] Warsaw University of Technology, Inst. Micromechanics & Photonics, Faculty of Mechatronics, Poland
m.michaloswki@mchtr.pw.edu.pl

[3] Physics and Mathematics Department, Universidad de Alcalá, Spain
alberto.lastra@uah.es

Abstract ─ Different approaches have been used for micro-magnets multipole magnetization like fixed micro-fixtures, thermomagnetic patterning or laser machining. With previous techniques, inversion of magnetic polarizations is only partially achieved. In this work, a preliminary design of the fixtures for micro-magnets with 10, 100 and 1000 μm thickness is done. The magnetizing field dependence in respect to the geometrical parameter of the fixture is analyzed. Maps of the required current permit to pre-select an adequate pulse power source. An experimental test has been done in order to validate designs. Design recommendations to optimize the magnetizing field and to minimize the current, thus the heat, are given.

Index Terms ─ Magnetic polarization patterning, magnetizing fixtures, micro-magnets.

I. INTRODUCTION

Electromechanical systems miniaturization of has become one of the pillars for microelectronics development. Motors [1]–[4], clutches/brakes [5]–[8], micro-magnetic gears [9], [10], vibrational energy harvesters/dampers [11] and other micro-electromagnetic devices [12] have inspired growing interest in recent years.

Up to now, if micro-magnetic assemblies are required, the most common approach is to machine small magnets out of larger bulks and then axially magnetize the individual micro-magnets and subsequently assembly them into the micro-system. This is a cost-intensive manufacturing process because magnets are mostly magnetized before assembly and handling and positioning such micro-magnets is not straightforward. Post-assembly magnetizations are also possible [13],[14]. Alternatively, multipole magnetization of assembled micro-magnets may provide a solution to previous technical problems.

In general, multi-pole magnetic structures can be created by pulse magnetization [15]. A magnetizing fixture with copper wire is used. If a high pulse current passes through the fixture, it produces a magnetizing field strong enough to permanently magnetize the micro-magnet. Special considerations have to be taken when operating at low temperatures because materials magnetic properties may vary significantly [16], [17]. Pulsed magnetization is a macroscale standard process [18]. However, for micro-magnets, this cannot be easily done because fixture has to be smaller than micro-magnets themselves, complicating the whole process [19].

Different approaches have been used for micro-magnets multipole magnetization. Previous developments have demonstrated the creation of multipole in hard magnetic films [20] using a combination of fixed electrical conductors and soft magnetizing heads to imprint smm period of magnetic north/south poles.

Moreover, thermomagnetic patterning has been also used to make patterns with lateral dimensions down to ~70 μm but only in the relative surface of the layer (1-μm deep) [21]. Additionally, a technique based on the use of a single laser-machined soft magnetic head to selectively reverse the magnetization direction in a hard magnetic layer was developed [22]. The main limitation of previous described techniques is that the inversion of the magnetic polarizations is only superficially achieved, thus the magnetic product remaining in the polarized volumes is smaller than the potential achievable one.

A radical different technique has been proposed for magnetization patterning in macroscale magnets [23]. This new technique generates magnetization patterns by magnetizing locally the magnet bulk with north or south polarization. The circular fixture is small but strong enough to magnetize a small portion of the magnet, then

Submitted On: December 5, 2018 Accepted On: May 6, 2019

the fixture is moved X-Y to a next location over the magnet and it magnetizes the next volume as desired. In this way, pixelated magnetization patterns can be created. This technique has been successfully used for macroscale magnets providing a magnetic pixel size as small as 4 mm [24] and a thicknesses larger than 3 mm.

The novelty of the present work is to use 2D multipole magnetization printing applied to micro-magnets. Such small moving magnetizing fixtures need to be carefully designed and optimized to reduce the necessary current, because the generated heat may damage the fixture. The first approach presented in this article is a trade-off analysis oriented to minimize the needed current for a certain magnetizing field level while keeping a good pixel size.

In this work, a preliminary design of the fixtures applied to micro-magnets of 10, 100 and 1000 µm thick is done. The magnetizing field dependence in respect to the geometrical parameter of the fixture is analyzed. Maps of the required current for normalized magnetizing fields are also given. These maps permit to pre-select an adequate pulse power source. An experimental test has been done in order to validate designs. Design recommendations to optimize the magnetizing field and to minimize the current, thus the heat, are given.

II. DESIGN OF FIXTURE FOR 2D MAGNETIC PATTERNING

As already stated, 2D magnetic patterning consists of one pair of movable magnetizing coils, with or without inner core, located above and below the permanent magnet bulk that locally magnetize it creating the sou97 hght pattern. This allows magnetization of shapes such as hollowed cylinders or plates with alternative polarization, Fig. 1.

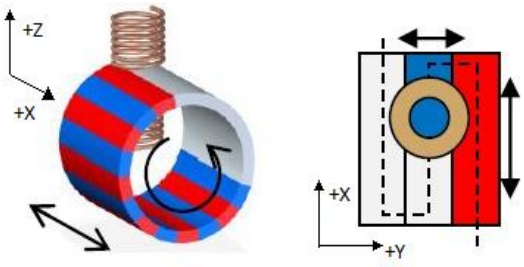

Fig. 1. 2D magnetic pattern: hollow cylinder and plate.

Figure 2 shows the diagram used for denomination of the different geometric parameters. The diagrams depicts the sample to be magnetized (1), top and a bottom cylindrical coils (2) and coil inner core (3). Both coils are connected in series generating the magnetizing field in the same direction. Five geometrical parameters have been defined: e – thickness of the permanent magnet bulk, R_{INT} – inner radius of the coil, R_{EXT} – outer radius of the coil and H_C – height of the coil.

No magnetic material is considered in the inner core either, just vacuum. Although a ferromagnetic material in the inner core could increase the final magnetizing field, there are several drawbacks that prevent from its inclusion. The main pitfall is the magnetic interaction that would appear between a ferromagnetic inner core and those volumes previously magnetized. In addition, from the electrical point of view the coils inductance would be orders of magnitude larger, thus the speed of the 2D patterning would be much lower.

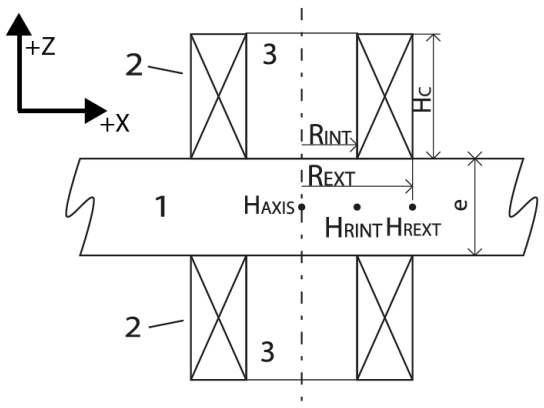

Fig. 2. Parameters of the axil-symmetrical model.

Current density perpendicular to the cross-section circulates through each coil. This current is considered uniformly distributed throughout the cross-section in all calculations. The space between coils, corresponding with the sample, will be considered as vacuum.

Magnetic field intensity generated by the designed fixtures has two symmetries: axial and middle section plane, Fig. 3 (a). It can be noticed that the lowest values are achieved in the middle section of the sample. Figure 3 (b) shows the magnetic field intensity along a radius of the middle section. This magnetic field has a maximum located at the axis and then it decreases as long as it approaches radially to the end of the coil. Just around the end of the coil, the magnetic field intensity vector is inverted to negative values. These negative values have typically an order of magnitude lower than the maximum so the effect on the adjacent magnetizations is small outside the outer radius of the coil. The variation in respect to the radius depends on the coil geometry so it is necessary to relate the shape of the applied magnetizing field for each coil geometry.

Analyzing geometrical parameters with magnetizing field cannot be practically done for any point radial points. In consequence, the magnetic field intensity (H) will be only calculated at three key points: point H_{AXIS}, located at the middle section of the sample in the symmetry axis; point $H_{RINT,}$ located at the middle section of the sample and radially at the start of the coil and

H_{REXT}, located at the middle section of the sample and radially at the end of the coil. Magnetizing field at first point H_{AXIS} will represent the minimum magnetizing field that will be available in the axis. In a simplified manner, it is considered that if this H_{AXIS} is larger than the magnetic coercivity of the material, the sample would be 100% magnetized in the axis.

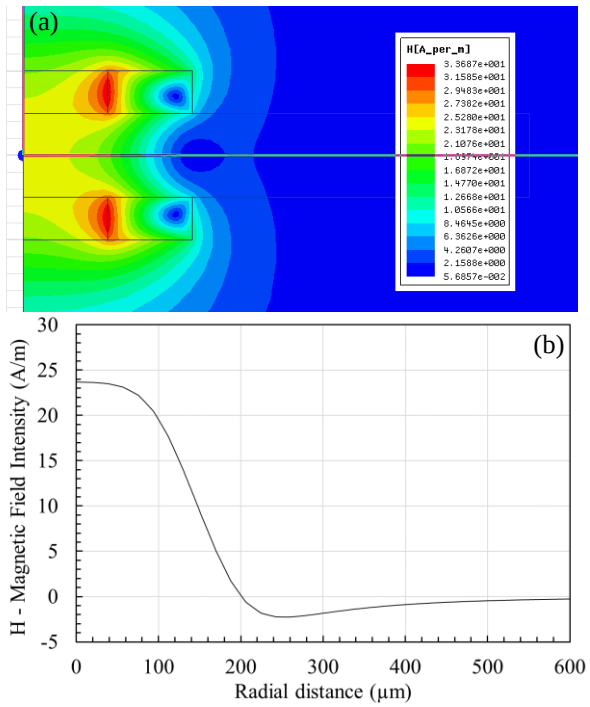

Fig. 3. (a) H - magnetic field intensity distribution (e = 100 µm, R_{INT} = 100 µm, R_{EXT} = 200 µm); (b) H - magnetic field intensity along a middle section radius.

III. FINITE ELEMENT MODEL

All calculations have been done using a finite element model (FEM) software for electromagnetic fields. The solver chosen is the magnetostatic solver. The magnetostatic field solution verifies the following two Maxwell's equations:

$$\nabla \times \vec{H} = \vec{J} \text{ and } \nabla \cdot \vec{B} = 0. \quad (1)$$

With the following relationship applicable at each material:

$$\vec{B} = \mu_0(\vec{H} + \vec{M}) = \mu_0 \cdot \mu_r \cdot \vec{H} + \mu_0 \cdot \vec{M}_p. \quad (2)$$

Where *H* is the magnetic field intensity, B is the magnetic field density, J is the conduction current density, M_p is the permanent magnetization, μ_0 is the vacuum permeability and µr is the relative permeability.

For nonlinear materials, the dependence between H and B fields is nonlinear and can be isotropic or orthotropic (in the case of anisotropic behavior, is a tensor). If nonlinearity occurs in soft materials, the software requires that BH curves for the principal directions in the respective material(s) are provided. From these curves, energy dependence on H is extracted for each of the respective principal directions and it is used in the process of obtaining the nonlinear permeability tensor used in the Newton-Raphson iterative solution process.

There are major advantages of this formulation over other ones, including using considerably fewer computational resources (due to the scalar nature of the DOFs), not requiring gauge due to numerical stability, that significantly reduces cancellation errors and capably of automatically multiply connected iron regions [25].

The design model for the FEM is shown in Fig. 4. It is an axil-symmetrical 2D model. Z-axis is the axial symmetry axis. In this model, all the geometrical parameters from Fig. 2 can be modified automatically by software. Mesh model size is proportional to the main geometrical parameters e and R_{INT}, being finer in the surroundings interfaces.

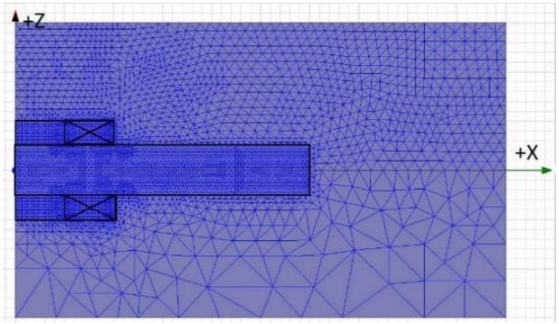

Fig. 4. Detail of the model with the initial mesh (e = 100 µm, R_{INT} = 100 µm, R_{EXT} = 200 µm, H_C = 50 µm).

Materials considered in the simulation are two: vacuum and copper. The values chosen for the properties are: magnetic permeability of vacuum $\mu_0 = 4\pi\ 10^{-7}$ H/m, relative permeability of copper μ_{rCu} = 0.99991 and conductivity of copper at 20ºC $\sigma_{Cu} = 5.8 \cdot 10^7$ S/m.

As boundary conditions a "Balloon" type condition has been applied in the external edges. Balloon condition models the region out-side the model space as being nearly "infinitely" large. Moreover, axisymmetric condition around Z axis has been imposed.

The external excitation of the model is a constant current density uniformly distributed in the copper coil cross section, pointing perpendicular outside of the XZ plane. Value for this current density is j=1 A/mm^2, allowing a result normalization since the magnetizing field depends directly on current density.

IV. SIMULATION DESCRIPTIONS AND POST-PROCESSING

Each simulation corresponds to a single combination of the four geometrical parameters described in Fig. 2.

The solver uses an adaptive meshing solver process. Typically, three to four iterations from the initial mesh have been enough for a correct convergence of the simulation. The total number of triangular elements is around 20000 elements. The mesh has been designed for achieving less than 0.03% of energy error within a simulation time of less than 5 seconds per simulation.

Table 1: List of simulations

Nº sim.	e (μm)	H_C (μm)	R_{INT} (μm)	R_{EXT} (μm)
1	10	5	1.25 to 20 (1.25 step)	R_{INT} + (1.25 to 20)
2	10	1.25 to 40 (1.25 step)	2.5	3.75, 12.5 and 22.5
3	100	50	12.5 to 200 (12.5 step)	R_{INT} + (12.5 to 200)
4	100	12.5 to 400 (12.5 step)	25	37.5, 125 and 225
5	1000	500	125 to 2000 (125 step)	R_{INT}+ (125 to 2000)

The simulations have been done in a workstation with an Intel Core i5-4690 with 8Gb of RAM memory.

Three different sample thicknesses have been analyzed: 10 μm, 100 μm and 1000 μm. For each, a combination of the rest of parameters has been done. Combinations are listed in Table 1.

The simulation plan has been proposed in order to assess how the coil width affects to the magnetizing field and to determine the point where increasing the coil height is not efficient anymore. Each simulation returns the magnetic field intensity in the points described in Section 2, H_{AXIS}, H_{REXT} and H_{RINT}. Some analysis can be done from the magnetic field in those three key points. For example, magnetic field at second point H_{RINT} divided by magnetic field at H_{AXIS} indicates the amount of magnetizing field at the beginning of the coil, representing the magnetized pixel width (*% Pixel*). Magnetic field at third point H_{REXT} in respect to the magnetic field at H_{AXIS} (*% Out*) indicates the type of transition between magnetized pixels. Expressions for those calculations are:

$$\%\, Pixel = \frac{H_{RINT}}{H_{AXIS}} \cdot 100, \quad (3)$$

$$\%\, Out = \frac{H_{REXT}}{H_{AXIS}} \cdot 100. \quad (4)$$

Furthermore, voltages can be calculated as:

$$V = I \cdot R = j \cdot S \cdot \rho \cdot \frac{l}{S} = j \cdot \rho \cdot \pi \cdot (R_{INT} + R_{EXT}). \quad (5)$$

Where I is the total current circulating across the fixture cross-section, R is the total resistance of the cylindrical coil considered as a complete cylinder; j is the current density, as default 1 A/mm^2; $S = H_C \cdot (R_{EXT} - R_{INT})$ is the cross-section surface; l is the length, in this case considered as $l = 2\pi \cdot (R_{INT} + \frac{R_{EXT} - R_{INT}}{2})$; and ρ is the copper resistivity. Copper resistivity value is critical for the right determination of voltage. However, as the cylinder will heat up by joule effect, the resistivity property varies with time. Indeed, the maximum admissible current, thus the maximum magnetizing field, will depend on this temperature rise. As a first approximation, the chosen value is the one considering operation at intermediate temperature between 20ºC and copper fusion temperature which is 1085 °C. Therefore,

$$\rho = \rho_{20} \cdot (1 + \alpha \cdot \Delta T) = 1.71 \cdot 10^{-8}(1 + 3.9 \cdot 10^{-3} \cdot (545 - 20)) = 5.13 \cdot 10^{-8}\ \Omega m.$$

In this calculation, skin effect has been considered negligible. This assumption is fairly valid provided that pulse duration is longer than 10 ms for copper conductors [26].

In terms of thermal behavior, the power density generated by the coil can be expressed as:

$$P_{Vol} = \frac{I^2 \cdot R}{H_C \cdot \pi \cdot (R_{EXT}{}^2 - R_{INT}{}^2)} = \frac{(j \cdot S)^2 \cdot \rho \cdot \frac{l}{S}}{H_C \cdot \pi \cdot (R_{EXT}{}^2 - R_{INT}{}^2)} = \frac{j^2 \cdot S \cdot \rho \cdot l}{H_C \cdot \pi \cdot (R_{EXT}{}^2 - R_{INT}{}^2)} = \frac{j^2 \cdot \rho \cdot H_C \cdot (R_{EXT} - R_{INT}) \cdot 2\pi \cdot \left(R_{INT} + \frac{R_{EXT} - R_{INT}}{2}\right)}{H_C \cdot \pi \cdot (R_{EXT}{}^2 - R_{INT}{}^2)} = j^2 \cdot \rho. \quad (6)$$

It implies that power density, and thus volumetric temperature raise, is independent of coil geometry. But, as current density needs to be large for achieving a magnetizing field, geometries with lower magnetizing field capacity would suffer a higher temperature.

V. RESULTS AND DISCUSSION

A. Thickness e = 10 μm - Simulation number 1 and 2

Next Figs. 5-7 present the results from simulation number 1. In this simulation, the magnetizing field has been analyzed by varying R_{INT} and R_{EXT} for a single height of the coil value H_C = 5 μm.

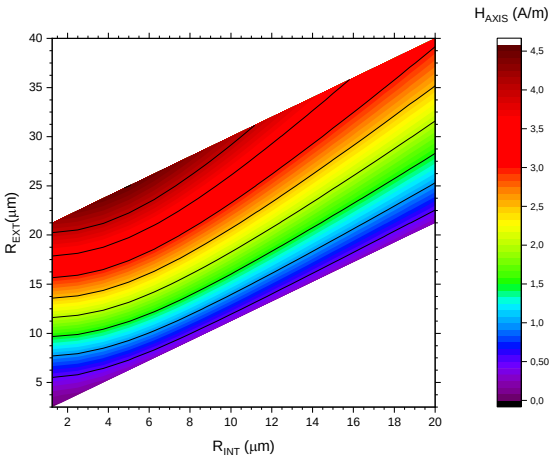

Fig. 5. H_{AXIS} in respect to R_{INT} and R_{EXT} for e = 10 μm and Hc = 5 μm.

Figure 5 shows magnetizing field contour map H_{AXIS} for different combinations of R_{INT} and R_{EXT}, with a thickness *e* and a fixed coil height H_C. The values vary from 0.12 to 4.52 A/m for a current density of 1 A/mm^2. The maximum values are achieved at R_{INT} = 5 µm and R_{EXT} = 25 µm. The minimum values are achieved at R_{INT} = 1.25 µm and R_{EXT} = 2.5 µm. For any R_{INT} value, magnetizing field increases when increasing R_{EXT}, i.e., the thicker is the coil, the larger the magnetizing field is. H_{AXIS} behavior is almost linear with respect to R_{INT} and R_{EXT}. This means that it can be worth in terms of magnetizing field to use thick coils. However, by using thicker coils the pixel will also be larger, decreasing the pattern resolution.

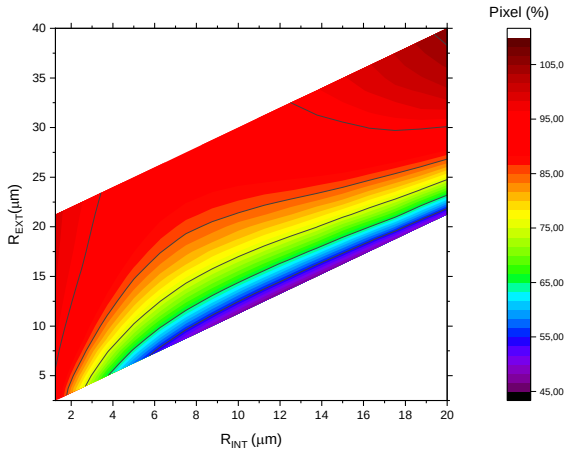

Fig. 6. % Pixel in respect to R_{INT} and R_{EXT} for e = 10 µm and Hc = 5 µm.

Figure 6 presents a contour map of *% Pixel* for different combinations of R_{INT} and R_{EXT}, with a thickness *e* and a fixed coil height H_C. The values vary from 46.8% to 106.2%. The maximum values are achieved at R_{INT} = 20 µm and R_{EXT} = 40 µm. In this case, the magnetizing field in the coils proximities is even larger than in the axis because the pixel diameter, given by R_{INT}, is very large. The minimum values are achieved at R_{INT} = 10 µm and R_{EXT} = 13.75 µm. This case has a sharp decrease from axis to coil beginning. There is a wide number of combinations where *% Pixel* remains between 85-95%.

Combining Fig. 5 and Fig. 6, we can determine that a combination around R_{INT} = 12.5 µm and R_{EXT} = 25 µm is a good trade-off between high magnetizing field, high *% Pixel* and pixel diameter without excessive coil thickness.

Figure 7 displays a contour map of the *% Out* for different combinations of R_{INT} and R_{EXT}, with a thickness *e* and a fixed coil height H_C. The values vary from 0% to 53%. The maximum values are achieved at R_{INT} = 1.25 µm and R_{EXT} = 2.5 µm. In this case, the magnetizing field outside the coil is very large for an adequate pixel resolution, significantly affecting to adjacent volumes. Minimum values are achieved at R_{INT} = 1.5 µm and R_{EXT} = 20 µm. This combination has a negligible effect on the adjacent volumes. Again, there is a vast number of combinations where *% Out* remains between 0-10%.

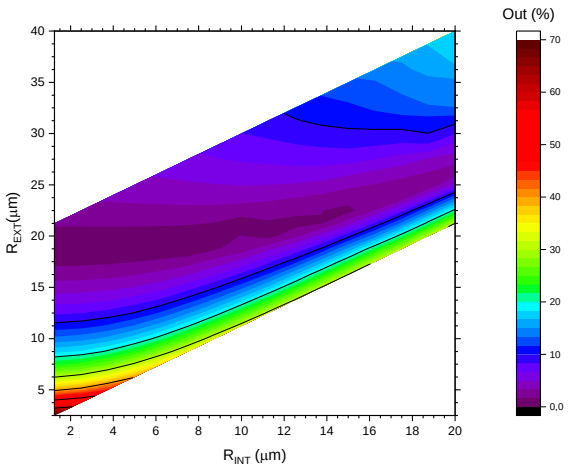

Fig. 7. % Out in respect to R_{INT} and R_{EXT} for e = 10 µm and Hc = 5 µm.

For the pre-selected combination of R_{INT} = 12.5 µm and R_{EXT} = 25 µm, the *% Out* is 5% which reinforces the benefits of this combination selection.

Next Figs. 8-9 show the results from simulation number 2. In this simulation, the magnetizing field has been analyzed by varying the height of the coil H_C, for three specific combinations of R_{INT} and R_{EXT} (R_{INT} = 2.5 µm combined with R_{EXT} = 3.75, 12.5 and 22.5 µm).

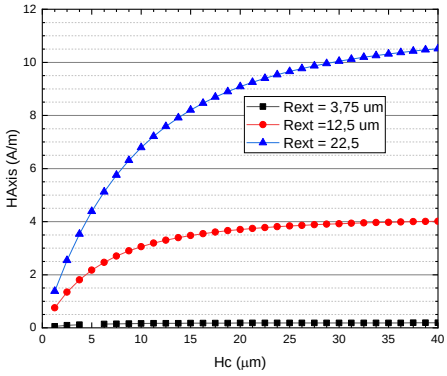

Fig. 8. H_{AXIS} in respect to H_C for e = 10 µm, R_{INT} = 2.5 µm combined with R_{EXT} = 3.75, 12.5 and 22.5 µm.

Figure 8 displays three plots of the magnetizing field H_{AXIS} as a function of coil height H_C with R_{INT} and e fixed, and for different coils width given by $R_{EXT} - R_{INT}$. It can be observed that all the plots have an asymptotic behavior. This means that for a certain coil value of coil height it will not be worth to continue increasing H_C.

Increasing H_C will also raise the total resistance and therefore the voltage needed for a certain current

It has been selected ¾ of maximum magnetizing field as the optimal point for coil height. For the cases of R_{EXT} = 12.5 and 22.5 µm the coil height corresponding with ¾ of maximum magnetizing is $H_C \approx (R_{EXT} - R_{INT})$. In the case of R_{EXT} = 3.75 µm, the ratio $H_C/(R_{EXT} - R_{INT})$ = 0.85, slightly lower than for larger coil width. Therefore, a design guideline for coil height is to choose a similar height than coil thickness.

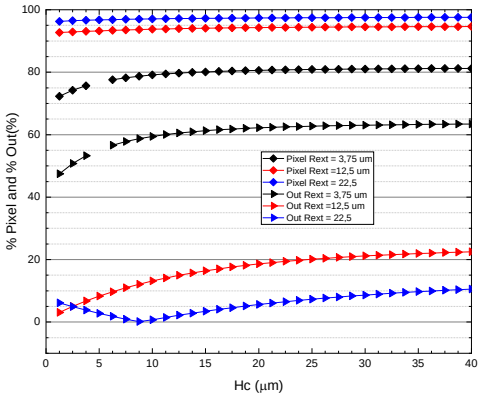

Fig. 9. % Pixel and % Out in respect to H_C for e = 10 µm, R_{INT} = 2.5 µm with R_{EXT} = 3.75, 12.5 and 22.5 µm.

Figure 9 shows three plots of *% Pixel* and *% Out* as a coil height H_C function with R_{INT} and e fixed, and for different coils width given by $R_{EXT} - R_{INT}$. Regarding *% Pixel*, asymptotic value is quickly achieved. No significant variation from the initial value and the asymptotic one is found. Therefore, coil height does not affect to *% Pixel*. On the contrary, *% Out* varies from initial values to asymptotic ones. This variation can be more than 10% of the absolute value of *% Out*. Thus, values of *% Out* from Fig. 8, where H_C was just 5 µm, should be corrected for the case of larger height coils.

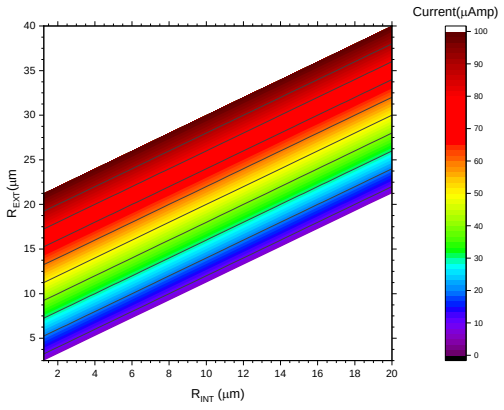

Fig. 10. Currents in respect to R_{INT} and R_{EXT} for e = 10 µm and Hc = 5 µm.

Current depends directly on current density and on the cross section. Hence, total current flowing through a cross section is directly proportional to $(R_{EXT} - R_{INT})$, i.e., coil width. This behavior is described in Fig. 10. Minimum values for total current are found in those combinations with thinner section while maximums are for the thicker ones. The order of magnitude in Fig. 10 is micro-ampere. This figure can be used to determine the current to be provided by the pulse power source.

B. Thickness e = 100 µm - Simulation nº 3 and 4

Next Fig. 11 shows the results from simulation number 3. In this simulation, the magnetizing field has been analyzed by combining R_{INT} and R_{EXT} for a single height of the coil value H_C = 50 µm.

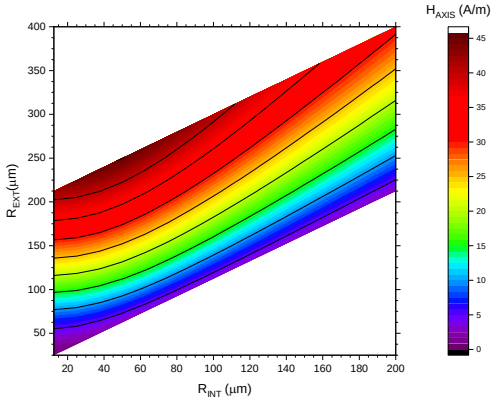

Fig. 11. H_{AXIS} in respect to R_{INT} and R_{EXT} for e = 100 µm and Hc = 50 µm.

Figure 11 presents a magnetizing field H_{AXIS} contour map for different combinations of R_{INT} and R_{EXT}, with a thickness e and a fixed coil height H_C. Values vary from 1.2 to 45.2 A/m for a current density of 1 A/mm^2, ten times larger than for e = 10 µm. Maximum values are achieved at R_{INT} = 50 µm and R_{EXT} = 250 µm. Minimum values are achieved at R_{INT} = 12.5 µm and R_{EXT} = 25 µm. This result is almost the same presented in Fig. 5 but one order of magnitude larger in the magnetizing field and in geometrical values. It makes sense since all the geometrical parameters have been scaled one order of magnitude so volume does. % Pixel and % Out for simulation 3 results are also similar to those presented in Figs. 6-7 and so do conclusions.

Next Figs. 12-13 show the results from simulation number 4. In this simulation, magnetizing field has been analyzed by varying the coil height H_C, with three specific combinations of R_{INT} and R_{EXT} (R_{INT} = 25 µm combined with R_{EXT} = 375, 125 and 225 µm).

Figure 12 presents three plots of the magnetizing field H_{AXIS} as a function of coil height H_C with R_{INT} and fixed e, and for different coils width given by $R_{EXT} - R_{INT}$. It can be observed that all the plots have

an asymptotic behavior. It means that for a certain coil height value, it will not be worth to continue increasing H_C. Increasing H_C will also raise the total resistance and therefore the voltage needed for a certain current.

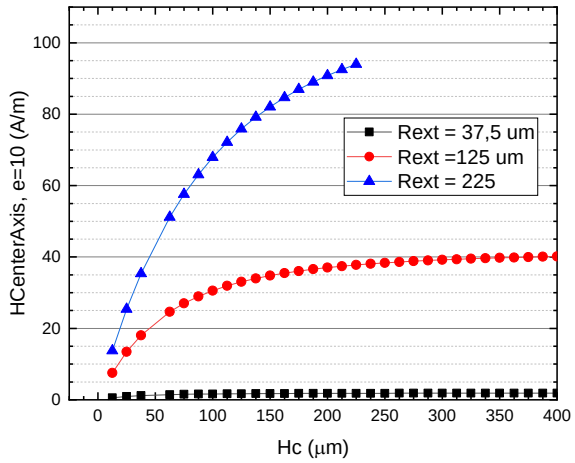

Fig. 12. H_{AXIS} in respect to H_C for e = 100 µm, R_{INT} = 25 µm combined with R_{EXT} = 375, 125 and 225 µm.

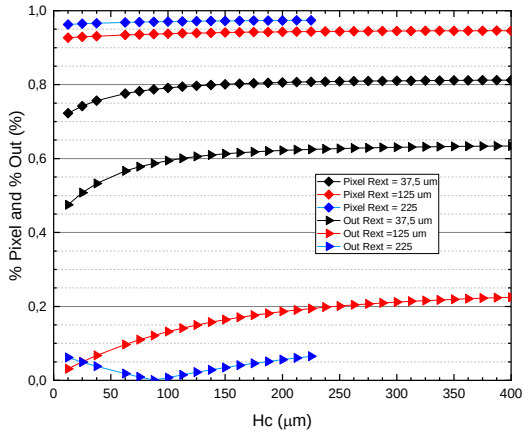

Fig. 13. % Pixel and % Out in respect to H_C for e = 100 µm, R_{INT} = 25 µm with R_{EXT} = 375, 125 and 225 µm.

Figure 13 gathers three plots of *% Pixel* and *% Out* as a function of coil height H_C with R_{INT} and fixed e, and for different coils width given by $R_{EXT} - R_{INT}$. Regarding *% Pixel* the asymptotic value is quickly achieved. No significant variation from the initial value and the asymptotic one is found. Therefore, coil height does not affect to *% Pixel*. On the contrary, *% Out* varies from initial values to asymptotic ones. This variation can be more than the 10% of the absolute value of *% Out*. Thus, *% Out* values from figure 13, where H_C was just 50 µm, should be corrected in larger height coils cases.

The behavior described in Fig. 10 is the same than described in Fig. 14 but currents are two order of magnitude larger according to its dependence on cross-section size.

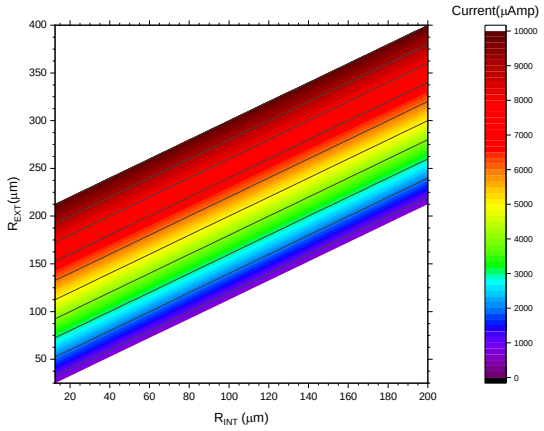

Fig. 14. Currents in respect to R_{INT} and REXT for e = 100 µm and Hc = 50 µm.

C. Thickness e = 1000 µm - Simulation number 5

Next Fig. 15 displays the results from simulation number 5. In this simulation, the magnetizing field has been analyzed by combining R_{INT} and R_{EXT} for a single height of the coil value H_C = 500 µm.

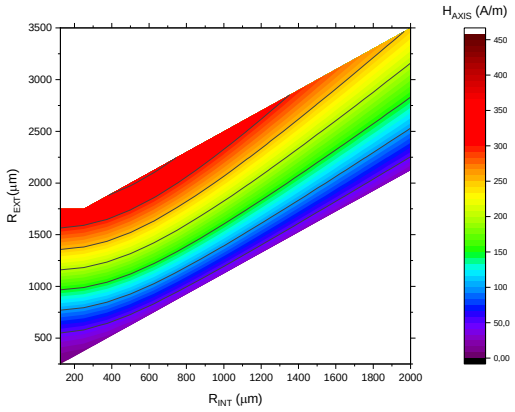

Fig. 15. H_{AXIS} in respect to R_{INT} and R_{EXT} for e = 1000 µm and Hc = 500 µm.

Figure 15 presents a magnetizing field H_{AXIS} contour map for different combinations of R_{INT} and R_{EXT}, with a thickness e and a fixed coil height H_C. Values vary from 12 to 452 A/m with a current density of 1 A/mm^2. The maximum values are achieved at R_{INT} = 500 µm and R_{EXT} = 200 µm. The minimum values are achieved at R_{INT} = 125 µm and R_{EXT} = 250 µm. For any R_{INT} value, magnetizing field increases when increasing R_{EXT}, i.e., the thicker is the coil, the larger the magnetizing field is. This result is almost the same presented in Fig. 5 but two orders of magnitude larger in the magnetizing fields

and in the geometrical values. The rest of the results for simulation 5 corresponding to previous Figs. 6-7 are also similar and so conclusions. In any case, the results are presented in next Figs. 16-17.

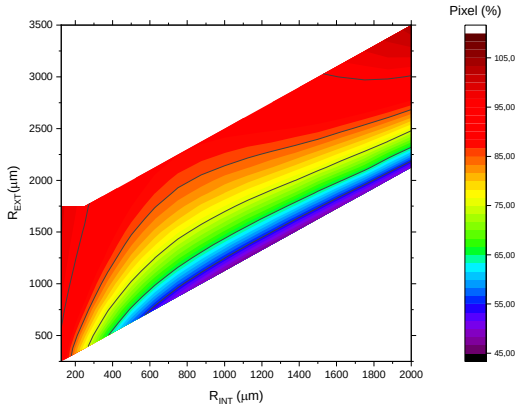

Fig. 16. % Pixel in respect to R_{INT} and R_{EXT} for e = 1000 µm and Hc = 500 µm.

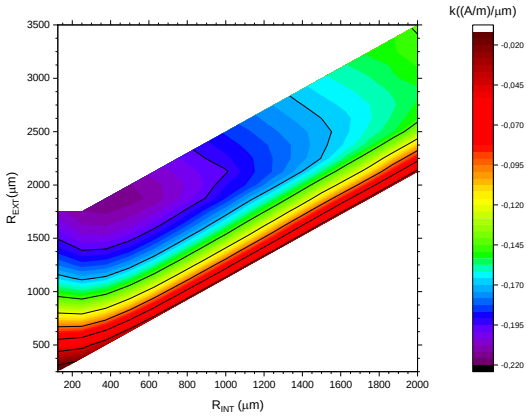

Fig. 17. % Out in respect to R_{INT} and R_{EXT} for e = 1000 µm and Hc = 500 µm.

Combining Fig. 16 and Fig. 17, we can determine that a combination around R_{INT} = 1250 µm and R_{EXT} = 2000 µm is a good trade-off between high magnetizing field, high *% Pixel* and pixel diameter without excessive coil thickness. For the pre-selected combination of R_{INT} = 1250 µm and R_{EXT} = 2500 µm, the *% Out* is 5% which reinforces the trade-off benefits of this combination.

Figure 18 presents currents calculations from simulation number 5.The behavior described in Fig. 18 is the same than described in Fig. 20 but currents are two orders of larger according to its dependence on cross-section size.

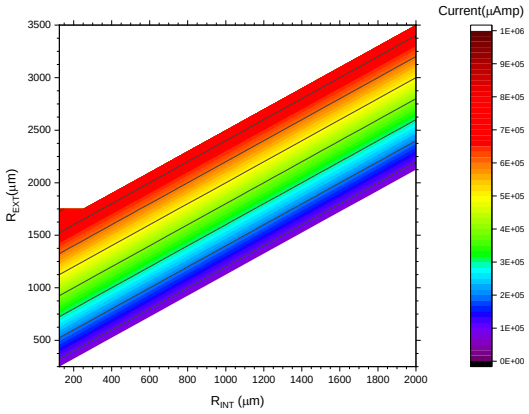

Fig. 18. Currents in respect to R_{INT} and R_{EXT} for e = 1000 µm and Hc = 500 µm.

D. Coil design model – Experimental validation

An experimental validation of the models has been done by using two real milimetric size coils. As coils two air core fixed micro-inductors from electronics components provider have been mounted on a 3D printed frame as shown in Fig. 19. More specifically, coils are two units of model AL12A18N5GTR from AVX RF Inductors corp. with dimensions are: R_{INT} = 1000 µm, R_{EXT} = 1500 µm and Hc = 5800 µm. Coils are made by a 0.5 mm diameter wire wrapped around with 5 wire turns. Separation distance of coils was set for e = 1000 µm.

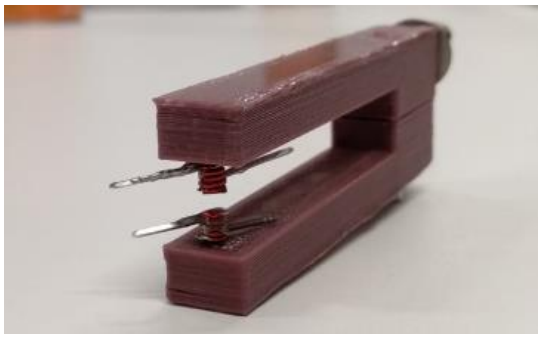

Fig. 19. Prototype for model validation: two units of model AL12A18N5GTR separated e = 1000 µm.

Coils have been connected in serial to an external power source and mounted on a XY displacement table as shown in Fig. 20. The magnetic field generated by the coils has been measured in the middle of the coils separation empty space, located in the axis. In order to measure the magnetic field, a GM08 model magnetometer from Hirst Magnetic Instruments Ltd with transvers hall

probe has been used.

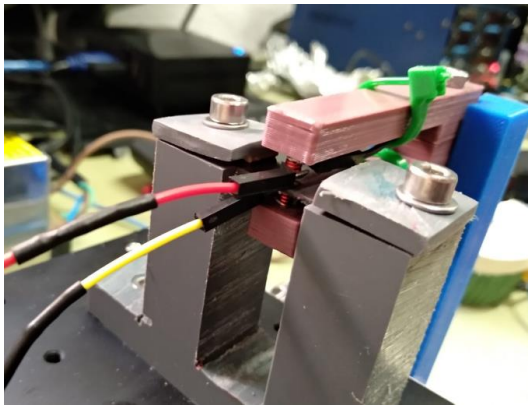

Fig. 20. Prototype coils connected in series and mounted on the XY displacement table.

The current applied has been 1.01 across a total section of 0.98 mm^2, i.e., an approximate current density of 1 A/mm^2. With this current density applied, the magnetic field obtained has been 325 A/m.

From Fig. 15 and with the combination of R_{INT} = 1000 µm, R_{EXT} = 1500 µm, the value of the expected magnetic field at H_{AXIS} is 175 A/m. It is important to notice that this value is expected if the coil height was 500 µm. However, for the experimental case, coil height was ten times larger which means that values should be in the asymptotic point. Analyzing Figs. 8 and 12, (R_{INT} = 12.5 µm and 125 µm respectively) values at the asymptotic point are almost twice the value for H_C = 5 and 50 µm respectively. Therefore, the expected H_{AXIS} value has to be corrected by a factor of two, reaching 350 A/m, which is in good agreement with the measured value.

VI. CONCLUSION

This work presents the potential of 2D multipole magnetization printing applied to micro-magnets is as a technique for microsystems magnets. The research shown in this article is a trade-off analysis to minimize the needed current, and thus voltage, for a certain magnetizing field level while keeping a good pixel size.

In this work, the technique is oriented to micro-magnets with 10, 100 and 1000 µm thickness. The magnetizing field dependence in respect to the fixtures geometrical parameter is analyzed. Some design recommendations are:

- The thicker is the coil, the larger the magnetizing field is. However, by using thicker coils the pixel will also be larger, decreasing the pattern resolution.
- There is a vast number of geometrical combinations where % Pixel remains between 85-95%.
- There is a vast number of combinations where % Out remains between 0-10%.
- An optimal coil height selection is to choose a height similar to the coil thickness.
- The geometrical dependence is the same for the three orders of magnitude analyzed.
- Current flowing through a cross section is directly proportional to coil width.
- Volumetric Joule effect heat is independent of the geometry of the coil.

Maps of the required current for normalized magnetizing fields are also given. These maps permit to pre-select an adequate pulse power source.

An experimental test has been done in order to validate simulation models with a good agreement.

Therefore, the results and conclusions presented in this work will allow to accelerate significantly trade-off procedures when designing 2D multipole magnetization patterning fixtures for specific industry applications.

ACKNOWLEDGMENT

This work has been funded by Universidad de Alcalá, under Grant No. CCGP2017-EXP/011. Authors want to recognize the work of Alba Martínez Pérez in figures preparation and English corrections.

REFERENCES

[1] E. Diez-Jimenez, J. L. Perez-Diaz, and J. C. Garcia-Prada, "Local model for magnet–superconductor mechanical interaction: Experimental verification," *J. Appl. Phys.*, vol. 109, no. 6, pp. 063901-063901-5, 2011.

[2] E. Diez-Jimenez, "Design and analysis of a non-hysteretic passive magnetic linear bearing for cryogenic environments," *Proc. Inst. Mech. Eng. Part J J. Eng. Tribol.*, 2014.

[3] S. Wu, S. Zuo, X. Wu, F. Lin, and J. Shen, "Magnet modification to reduce pulsating torque for axial flux permanent magnet synchronous machines," *Appl. Comput. Electromagn. Soc. J.*, vol. 31, no. 3, pp. 294-303, 2016.

[4] B. Rezaeealam and F. Rezaee-Alam, "Optimization of permanent magnet synchronous motors using conformal mappings," *Appl. Comput. Electromagn. Soc. J.*, vol. 32, no. 10, pp. 915-923, 2017.

[5] R. Rizzo, A. Musolino, F. Bucchi, P. Forte, and F. Frendo, "A multi-gap magnetorheological clutch with permanent magnet," *Smart Mater. Struct.*, vol. 24, no. 7, 2015.

[6] R. Rizzo, "An innovative multi-gap clutch based on magneto-rheological fluids and electrodynamic effects: Magnetic design and experimental characterization," *Smart Mater. Struct.*, vol. 26, no. 1, 2017.

[7] R. Rizzo, A. Musolino, and H. C. Lai, "An electrodynamic/magnetorheological clutch powered by permanent magnets," *IEEE Trans. Magn.*, vol.

53, no. 2, pp. 1-7, Feb. 2017.

[8] E. Diez-Jimenez, A. Musolino, M. Raugi, R. Rizzo, and L. Sani, "A magneto-rheological brake excited by permanent magnets," *Appl. Comput. Electromagn. Soc. J.*, vol. 34, no. 1, pp. 186-191, 2019.

[9] M. Muñoz-Martínez, E. Diez-Jimenez, M. J. Gómez-García, R. Rizzo, and A. Musolino, "Torque and bearing reaction forces simulation of micro-magnetic gears," *Appl. Comput. Electromagn. Soc. J.*, vol. 3, 2019.

[10] E. Diez-Jimenez, R. Sanchez-Montero, and M. Martinez-Muñoz, "Towards miniaturization of magnetic gears: Torque performance assessment," *Micromachines*, vol. 9, no. 1, p. 16, Dec. 2017.

[11] J. L. Perez-Diaz, *et al.*, "A novel high temperature eddy current damper with enhanced performance by means of impedance matching," *Smart Mater. Struct.*, vol. 28, no. 2, p. 025034, 2019.

[12] S. Barmada, A. Musolino, and R. Rizzo, "Equivalent network approach for the simulation of MEMS devices," *Appl. Comput. Electromagn. Soc. J.*, vol. 21, no. 1, pp. 16-25, 2006.

[13] M.-F. Hsieh, Y.-M. Lien, and D. G. Dorrell, "Post-assembly magnetization of rare-earth fractional-slot surface permanent-magnet machines using a two-shot method," *IEEE Trans. Ind. Appl.*, vol. 47, no. 6, pp. 2478-2486, Nov. 2011.

[14] E. Diez-Jimenez, A. Musolino, R. Rizzo, and E. Tripodi, "Analysis of the static and dynamic behavior of a non hysteretic superconductive passive magnetic linear bearing by using an electromagnetic integral formulation," *Prog. Electromagn. Res. M*, vol. 50, pp. 183-193, 2016.

[15] Y. N. Zhilichev, "Precise multipole magnetization of disc magnet for sensor application," *IEEE Trans. Magn.*, vol. 39, no. 5, pp. 3301-3303, Sep. 2003.

[16] E. Diez-Jimenez, *et al.*, "Magnetic and morphological characterization of Nd2Fe14B magnets with different quality grades at low temperature 5–300 K," *J. Magn. Magn. Mater.*, vol. 451, pp. 549-553, Apr. 2018.

[17] E. Diez-Jimenez, J. L. Perez-Diaz, F. Canepa, and C. Ferdeghini, "Invariance of the magnetization axis under spin reorientation transitions in polycrystalline magnets of Nd2Fe14B," *J. Appl. Phys.*, vol. 112, no. 6, p. 063918, 2012.

[18] J. Töpfer, B. Pawlowski, H. Beer, K. Plötner, P. Hofmann, and J. Herrfurth, "Multi-pole magnetization of NdFeB magnets for magnetic micro-actuators and its characterization with a magnetic field mapping device," *J. Magn. Magn. Mater.*, vol. 270, no. 1-2, pp. 124-129, 2004.

[19] J. Töpfer and V. Christopher, "Multi-pole magnetization of NdFeB sintered magnets and thick films for magnetic micro-actuators," *Sensors Actuators, A Phys.*, vol. 113, no. 2, pp. 257-263, 2004.

[20] A. Garraud, *et al.*, "Microscale magnetic patterning of hard magnetic films using microfabricated magnetizing masks," *Proc. IEEE Int. Conf. Micro Electro Mech. Syst.*, pp. 520-523, 2014.

[21] F. Dumas-Bouchiat, *et al.*, "Thermomagnetically patterned micromagnets," *Appl. Phys. Lett.*, vol. 96, no. 10, 2010.

[22] A. Garraud, N. M. Dempsey, and D. P. Arnold, "Microscale magnetic patterning of hard magnetic films using microfabricated magnetizing masks," in *Proceedings of the IEEE International Conference on MEMS*, pp. 520-523, 2014.

[23] L. Fullerton, "System and Method for producing Magnetic Structures," 2015.

[24] "Catalog of Polymagnets (R)," 2018. [Online]. Available: http://www.polymagnet.com/

[25] "Ansoft Ansys Maxwell v15 - Help assistant," 2018.

[26] W. H. Hayt, *Engineering Electromagnetics*. 1989.

The Influence of Thermal Deformation on the AMB-rotor System of HTR-PM Helium Circulator

Jinpeng Yu, Guowei Du, Hong Wang, Zhe Sun, and Lei Zhao

Institute of Nuclear and New Energy Technology
Collaborative Innovation Center of Advanced Nuclear Energy Technology
The Key Laboratory of Advanced Reactor Engineering and Safety
Tsinghua University, Beijing, 100084, China
yu-jp15@mails.tsinghua.edu.cn, sun_zhe@mail.tsinghua.edu.cn*

Abstract ─ Helium circulator is the core component of High Temperature Reactor-Pebblebed Modules (HTR-PM), and its rotor is supported by active magnetic bearings (AMBs). The windings of the motor and AMBs will generate a great deal of heat due to Ohmic loss, which increases the temperature of the circulator. The high temperature will cause the thermal deformation of AMB-rotor system, leading to the clearance change between rotor and AMBs. The AMB stiffness and inductive transducer sensitivity will be affected by the changed clearance, which decrease the stability of the AMB-rotor system. In this paper, through theoretical analysis and finite element analysis (FEA), the influence of thermal deformation on the AMB stiffness and transducer measurement is studied. The simulation and experiment for the AMB-rotor system in the circulator is carried out to explore the performance of AMB controllers and the influences of thermal deformation on the unbalanced response of the AMB-rotor system is analyzed. The theoretical calculations in this paper has general applications in the controller improvement of AMBs under clearance change and provides a reference for mechanical structure design and controller design of AMBs.

Index Terms ─ AMBs, HTR-PM, thermal deformation, unbalanced response.

I. INTRODUCTION

High Temperature Reactor-Pebblebed Modules (HTR-PM) is the fourth generation nuclear reactor developed by the Institute of Nuclear Energy and New Energy Technology, Tsinghua University [1, 2]. In HTR-PM, the helium circulates in the first loop driven by the circulator, which is shown in Fig. 1. The circulator is mainly composed of the rotor, active magnetic bearings (AMBs), auxiliary bearings and the cooling system. The rotor in the circulator is supported by the AMBs [3, 4]. AMBs are a type of bearing that support a load using magnetic levitation without physical contact, and are widely applied in high-speed rotating machineries and flexible rotor-dynamic systems [5, 6]. Because AMBs have no friction and need no lubrication, its application in HTR-PM can effectively avoid the oil pollution to the helium environment in the circulator.

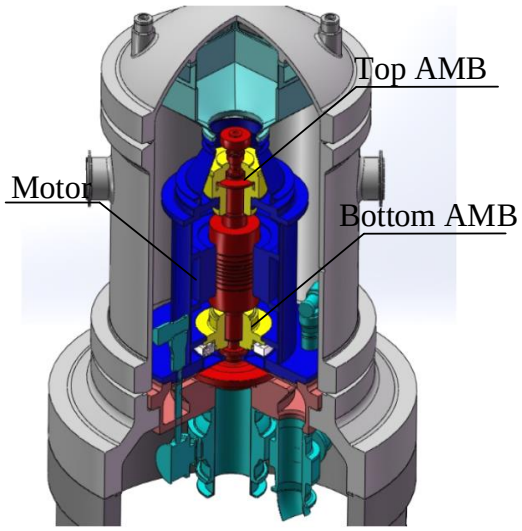

Fig. 1. 3D model of the circulator in HTR-PM.

When the circulator is running, the windings of the motor and AMBs will generate a great deal of heat due to Ohmic loss, which increases the temperature of the circulator. The components in the circulator, especially for bearings and the rotor, will deform due to the high temperature. For sliding and rolling bearings, in addition to the influence of ambient temperature, the friction between bearings and the rotor will also generate a great deal of heat, which aggravates the deformation of bearings and the rotor.

The main influence of thermal deformation is causing the clearance change between bearings and the rotor, which has influence on the dynamic performance of the bearing-rotor system. As for sliding and rolling

Submitted On: November 30, 2018
Accepted On: March 18, 2019

bearings, clearance change will affect the contact force between bearings and the rotor and change the system mode. However, clearance change affects the AMB-rotor system in different ways. AMBs are open-loop unstable systems, so the rotor position must be accurately measured by displacement transducers in real time to achieve closed-loop feedback control. Therefore, in the AMB-rotor system, the thermal deformation will not only change the AMB-rotor clearance but also the displacement transducer-rotor clearance. Since the electromagnetic force of AMBs and the voltage signals of displacement transducers are all related to the clearance, the clearance change will directly affect the performance of the AMB controller and the stability of the AMB-rotor system [7, 8].

In this paper, the influence of thermal deformation on the unbalanced response of the AMB-rotor system is studied, which provides a reference for the mechanical design of AMBs. Section II introduces and calculates the electromagnetic force of AMBs, and explores the influence of the clearance change on the AMB stiffness. The principle of inductive transducers and the influence of clearance change on the transducer measurement are analyzed. In Section III, the finite element analysis (FEA) of the circulator and transducer is carried out, and based on which the AMB-rotor system is simulated in MATLAB Simulink. Combined with theoretical analysis and FEA results, the influences of thermal deformation on the unbalanced response of the AMB-rotor system is analyzed in the experiment.

II. ANALYSIS OF THE INFLUENCE OF THE CLREANCE CHANGE

A. Influence on the AMB stiffness

In this section, the influence of the clearance change caused by thermal deformation on the electromagnetic force and AMB controller is calculated and discussed.

The AMB-rotor system is nonlinear, so it is necessary to linearize the electromagnetic force at an equilibrium point of the AMB-rotor system to simplify the AMB model and controllers design. Therefore, both the electromagnetic force and the AMB stiffness has the relationship with the clearance in the AMB-rotor system.

In a radial AMB of the circulator, as is shown in Fig. 2, there are four electromagnets (an electromagnet is composed of four magnetic poles) arranging in a ring and a pair of electromagnets in opposite directions control one degree of freedom of the rotor. Therefore, the electromagnetic force in one degree of freedom is [9, 10]:

$$F = \frac{1}{4}\mu_0 N^2 A_0 \left(\frac{(i_0+i_x)^2}{(s_0-x)^2} - \frac{(i_0-i_x)^2}{(s_0+x)^2}\right), \quad (1)$$

whose parameters are shown in Table 1.

Equation (1) can be linearized at $i_x = 0$ and $x = 0$ by Taylor expansion. Ignoring higher-order items, Equation (1) can be rewritten as:

$$F = k_x x + k_i i, \quad (2)$$

where $k_x = \mu_0 N^2 A_0 i_0^2 / s_0^3$ is the force-displacement stiffness and $k_i = \mu_0 N^2 A_0 i_0 / s_0^2$ is the force-current stiffness, all of which are directly related to the clearance s_0.

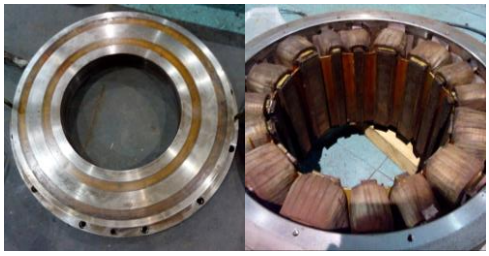

Fig. 2. A radial AMB in the circulator.

Table 1: Parameters of the electromagnetic force

Parameter	Meaning
μ_0	Magnetic permeability
A_0	Magnetic pole area
N	Coil number
s_0	Clearance
i_0	Bias current
x	Rotor displacement
i_x	Control current

When the circulator is running, AMBs and the rotor will deform due to the high temperature. The thermal deformation will cause the clearance change between AMBs and the rotor, so the notation s_0 can be rewritten as:

$$s = s_0(1 + \Delta s), \quad (3)$$

where Δs is the change of clearance and s is the clearance after thermal deformation. Therefore, the relationship between the variation ratio of the k_x, k_i and Δs is:

$$\begin{cases} \Delta k_x = [k_x(s) - k_x(s_0)]/k_x(s_0) \\ \qquad = 1/(1+\Delta s)^3 - 1 \\ \Delta k_i = [k_i(s) - k_i(s_0)]/k_i(s_0) \\ \qquad = 1/(1+\Delta s)^2 - 1 \end{cases}. \quad (4)$$

Figure 3 shows the change of Δk_x and Δk_i when Δs varies from -0.1 mm and 0.1 mm. As the clearance decreases, Δk_x and Δk_i become larger and vice versa. And Δk_x is more sensitive to the clearance than Δk_i. In the AMB-rotor system, the stiffness k_x and k_i are constant parameters in the AMB controller. Therefore, the clearance change caused by thermal deformation eventually change the AMB stiffness, which will affect the performance of the AMB controller and the stability of the AMB-rotor system.

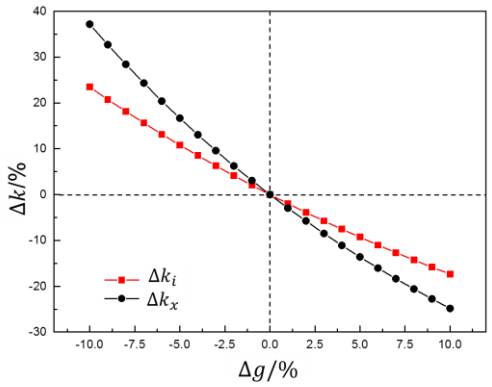

Fig. 3. The relationship between Δk_x, Δk_i and Δs.

B. Influence on the transducer sensitivity

AMBs are open-loop unstable systems, so the rotor position must be accurately measured by displacement transducer in real time to achieve closed-loop feedback control. Inductive transducers and eddy current displacement sensors are widely applied to the AMB system with their characteristics of high precision and non-contact measurement [11, 12]. In the AMB-rotor system of the circulator, differential inductive transducer is used to monitor the axis orbit of the rotor and provide feedback signal for the AMB controller.

The magnetic field generated by transducer coils will pass through transducer cores (stator), the rotor and the air-gap between the rotor and stator to form a closed magnetic circuit. The coil inductance will be affected by the air-gap length. Therefore, by measuring electrical parameters of the transducer circuit, the coil inductance can be measured, and then the rotor displacement can be obtained.

Ignoring the magnetic flux leakage and magnetic hysteresis, the magnetic circuit can be calculated:

$$\Phi = \frac{NI}{R}, \tag{5}$$

with Φ the magnetic flux, N the total coil number, I the coil current and R the reluctance. The relationship between Φ and the coil inductance L is:

$$N\Phi = LI, \tag{6}$$

and the reluctance is:

$$R = \frac{2\delta}{\mu_0 B_0}. \tag{7}$$

μ_0 is the permeability of vacuum, δ is the air-gap length and B_0 is magnetic pole area of the transducer. So according to Equations (5), (6) and (7), the coil inductance is:

$$L = \frac{N^2 \mu_0 B_0}{2\delta}. \tag{8}$$

Similar to AMBs, two transducers in opposite directions measure $\boldsymbol{\delta_1}$ and $\boldsymbol{\delta_2}$ in one direction to obtain the rotor displacement, which is the differential measurement, as is shown in Fig. 4. Therefore, the clearance is $\boldsymbol{s_0 = (\delta_1 + \delta_2)/2}$ and the rotor displacement is $\boldsymbol{x = (\delta_1 - \delta_2)/2}$. In the measurement, a resistance-balanced bridge circuit is applied to convert the inductance into a voltage output, which is transmitted to the AMB controller.

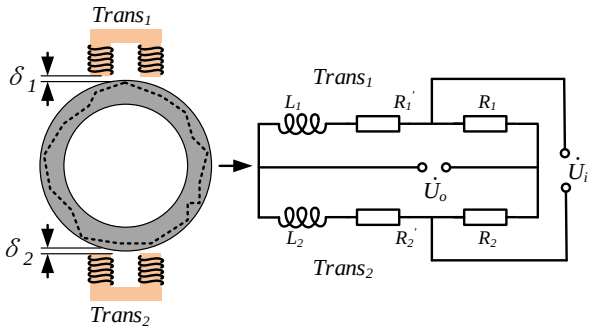

Fig. 4. Differential measurement and the resistance-balanced bridge circuit for transducer measurement.

The output voltage of the circuit is:

$$\begin{aligned} \dot{U}_o &= \frac{Z_1}{Z_1+Z_2}\dot{U}_\iota - \frac{R_1}{R_1+R_2}\dot{U}_\iota \\ &= \frac{Z_1-Z_2}{2(Z_1+Z_2)}\dot{U}_\iota, \end{aligned} \tag{9}$$

where $Z_i = j\omega L_i + R_i'$ $(i = 1, 2)$ is the impedance of the transducer coils under alternating currents, R_i' $(i = 1, 2)$ is the coil resistance, R_i $(i = 1, 2)$ is the balancing resistance, $\dot{U}_\iota$ and $\dot{U}_0$ are the input and output voltage respectively. Ignoring the coil resistance, the relationship between the output voltage and rotor displacement can be obtained according to Equations (8) and (9):

$$\dot{U}_o = \frac{x}{2s_0}\dot{U}_\iota. \tag{10}$$

It can be seen that the output voltage of the transducer is proportional to the rotor displacement. During designing the AMB controller, transducers need to be calibrated to obtain the transducer sensitivity, which is the relationship between the sensor output voltage and the actual rotor displacement:

$$\xi_0 = \frac{\dot{U}_o}{x} = \frac{\dot{U}_\iota}{2s_0}. \tag{11}$$

As shown in Equation (11), the transducer sensitivity ξ_0 is directly related to the clearance s_0. Therefore, according to Equations (3) and (11), if the clearance changes, the error caused by the sensor sensitivity is:

$$\eta = \frac{\xi}{\xi_0} - 1 = \frac{1}{(1+\Delta s)} - 1. \tag{12}$$

In the AMB controller, the transducer sensitivity is a constant parameter. Therefore, Equation (12) shows that once the thermal deformation changes the transducer-rotor clearance, the transducer sensitivity and the measurement accuracy of rotor displacement will be affected, which will reduce the performance of the AMB controller AMB-rotor stability.

III. FEA OF THE CIRCULATOR SYSTEM

A. Temperature-deformation coupled FEA for the circulator

To obtain the temperature field and thermal deformation of the circulator, the circulator model is built and analyzed in ANSYS using temperature-deformation coupled FEA. The model material is the mild steel whose parameters are shown in Table 2. The coefficients of thermal deformation, thermal conductivity and specific heat capacity can be obtained from Figs. 5-7.

Table 2: The material parameters of the mild steel

Material Parameter	Unit	Value
Density	t/mm3	7.85e-9
Young's modulus	MPa	210000
Poisson's ratio	-	0.26
Thermal deformation	1/℃	Fig. 5
Thermal conductivity	J/mm℃s	Fig. 6
Specific heat capacity	J/t℃	Fig. 7

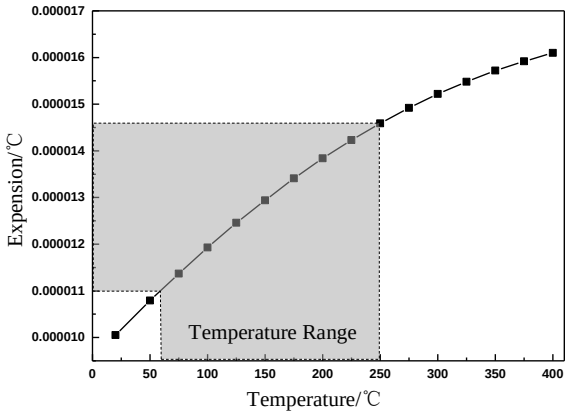

Fig. 5. Relationship between the thermal deformation and the temperature.

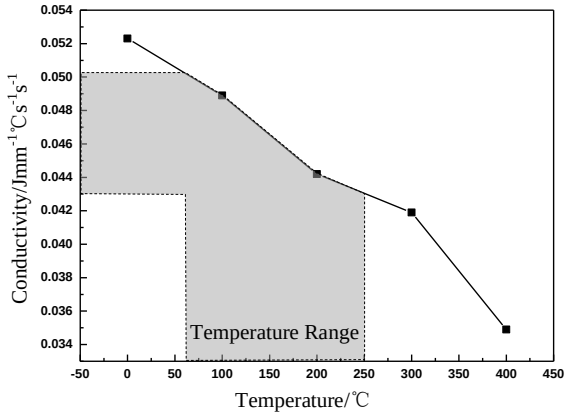

Fig. 6. Relationship between the thermal conductivity and the temperature.

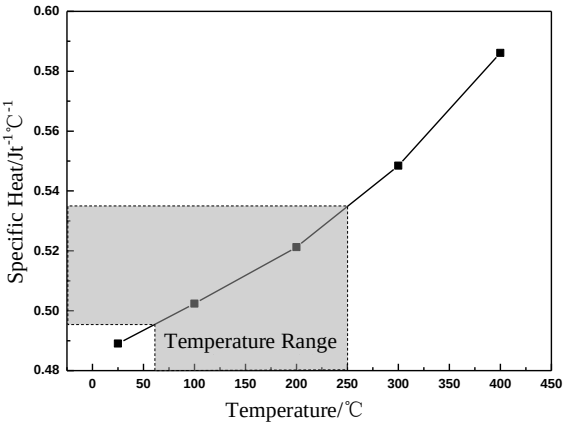

Fig. 7. Relationship between the specific heat capacity and the temperature.

The circulator model is built as shown in Figs. 1 and 8. In the FEA, the bottom of the rotor and housing constrained the freedoms of X, Y and Z directions, and the top of the rotor constrained the freedoms of X and Z directions. The original clearance $\boldsymbol{s_0}$ is **1 mm**.

The actual size model is used for simulation. Since the structure of the circulator is simple and there are no complicated components, the adaptive algorithm is used for automatic meshing. In the FEA of temperature field, stable heat sources are applied to the circulator to simulate the heat source caused by the windings of the motor, AMBs and the heat transferred by the high-temperature helium gas through the circulator components. Parameters of heat sources are obtained based on the data measured by the temperature sensor in the experiment.

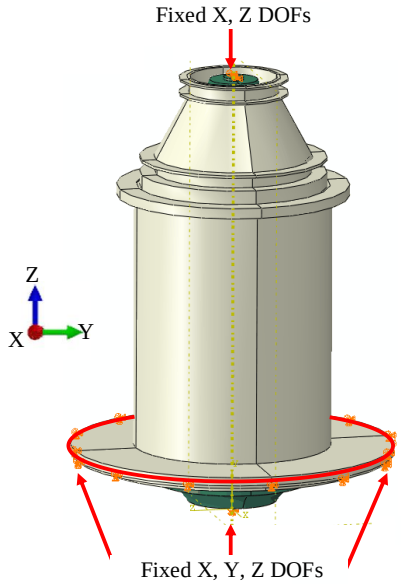

Fig. 8. The circulator model for FEA.

A forty-minute stable operation is simulated, at the beginning of which the rotor speed increase from 0 rpm to 3200 rpm. The temperature of the different components in the circulator gradually rises from 25 degrees Celsius to a steady value. The steady temperatures at different positions are listed in Table 3 and the temperature field is shown in Fig. 9.

Table 3: The steady temperatures at different positions

Position (From Top to Bottom)	Temperature/℃
Top part of auxiliary impeller	62.4
Bottom part of auxiliary impeller	69.0
Axial bearings	67.1
Top radial bearing	64.7
Top part of motor chamber	78.3
Motor winding	73.5
Bottom part of motor chamber	69.7
Bottom radial bearing	73.0
Outer surface of motor housing	65.0
Impeller chamber	250.0

It can be seen from the FEA results, that the heat from the motor and AMBs lead to the thermal deformation of the rotor and stator. Due to different geometrical dimensions, material properties and different stable temperature, the rotor and stator have different deformation ratios, which leads to clearance change of AMBs and transducers (both in the top and bottom radial AMBs). The thermal deformation of the structure can be obtained as shown in Fig. 10.

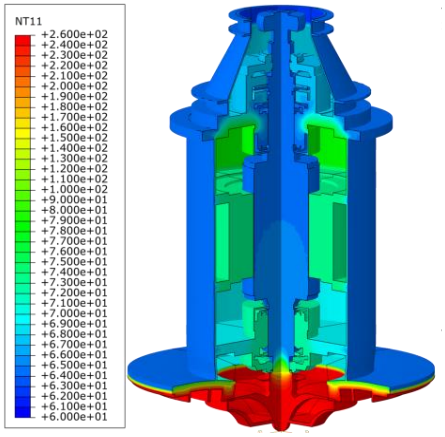

Fig. 9. The stable temperature field of the circulator.

The expansion of the stator is greater than the rotor, so the clearance is increased. It shows that the clearance increases 4.3% in the top radial AMB and 5.12% in the bottom radial AMB. The inconsistency of the clearance change in the top and bottom AMBs is because the high-temperature helium gas. When the circulator is running, the bottom AMB is close to the high-temperature helium gas, so it has a larger clearance change under higher temperature.

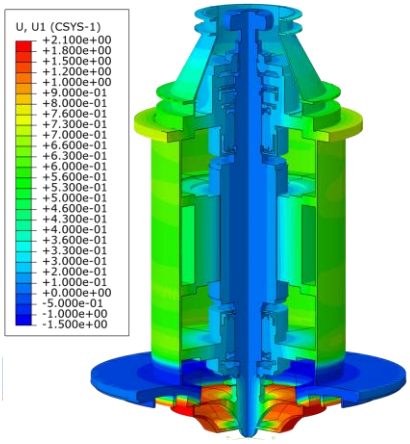

Fig. 10. The thermal deformation of the circulator

According to the calculation and analysis of Section II, the increasing clearance reduces the AMB stiffness and transducer sensitivity, which are listed in Table 4.

Table 4. The parameter variation

Top		Bottom	
Δs_t	4.3%	Δs_b	5.1%
Δk_{x_t}	-11.9%	Δk_{x_b}	-13.9%
Δk_{i_t}	-8.1%	Δk_{i_b}	-9.5%
η_t	-4.1%	η_b	-4.9%

B. Electromagnetic field FEA for the inductive transducer

Based on the clearance change calculated in the Section III (A), the electromagnetic field FEA is carried out to explore the influence of clearance change on inductive transducers.

The 3D model of the inductive transducer is built as shown in Fig. 11. Since the transducer use differential measurement in the circulator, the inductance of upper and lower transducers is calculated in FEA. The FEA is carried out with the rotor displacement of $+0.1$ mm in vertical direction. The clearance is obtained in Section III (A). The original clearance is $s_0 = 1$ mm, and the clearance change is $\Delta s_t = 4.3\%$ in the top radial AMB and $\Delta s_b = 5.1\%$ in the bottom radial AMB.

In the model, the rotor and stator are assembled with silicon steel sheets to reduce the effects of eddy current. Because the mechanical design of the model is simple and there are no complicated structural components, the adaptive algorithm is used to automatic meshing. The inductive transducer uses an alternating current (AC) excitation source, so the current in the coils is 20 KHz in the simulation. The simulation runs for one cycle of the excitation source in every project.

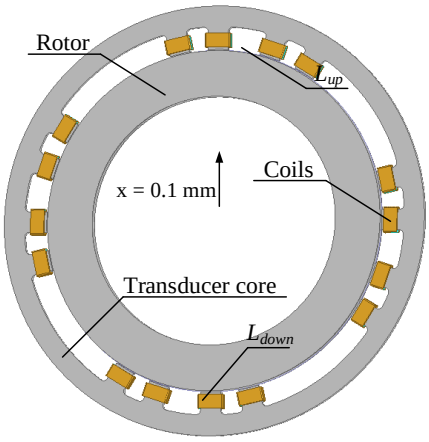

Fig. 11. 3D model of the inductive transducer.

The results of magnetic flux density in FEA are shown in Fig. 12. The picture shows the electromagnetic field distribution in the silicon steel sheets (transducer and rotor) when the current is maximum. With the same rotor displacement, the magnetic field changes significantly due to the clearance change, which directly affects the calculation of the transducer inductance.

It can be seen from the results that the increase of the clearance increases the magnetic resistance of the inductive transducer, which reduce the magnetic induction intensity inside the rotor and the stator and reduce the inductance value. The results are consistent with the analysis in Section II.

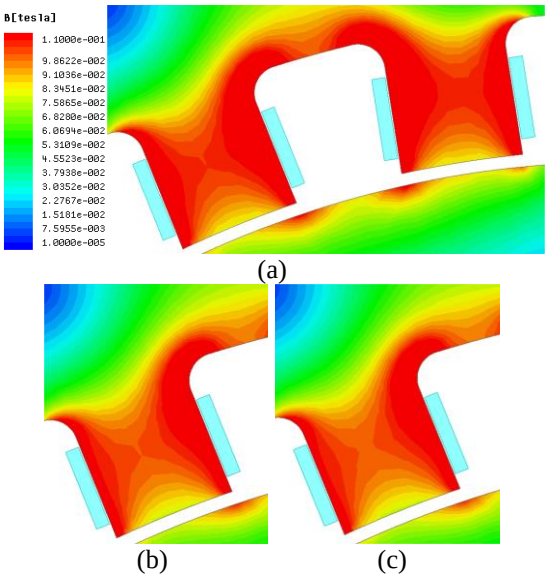

Fig. 12. The magnetic flux density in the transducer: (a) the original clearance $\boldsymbol{s_0 = 1\ mm}$, (b) $\boldsymbol{\Delta s_t = 4.3\%}$ in the top AMB, and (c) $\boldsymbol{\Delta s_b = 5.1\%}$ in the bottom AMB.

Because the transducer inductance can be obtained easily, the measurement error caused by the sensor sensitivity can be substituted by:

$$\boldsymbol{\sigma = \frac{x}{s_0}}, \tag{13}$$

which has the same changing trend with $\boldsymbol{\eta}$. According to FEA results and Equations (8), (12) and (13), the transducer inductance and measurement error are shown in Table 5. Due to the clearance change, the transducer sensitivity changes significantly, leading to measurement error of the rotor displacement. The measurement error in the top AMB is $\boldsymbol{-4.31\%}$ and the bottom is $\boldsymbol{-4.87\%}$, which are consistent with the theoretical calculation in Table 4.

Table 5: The transducer inductance and measurement error

s (mm)		L_{up} (mL)	L_{down} (mL)	σ (%)	η (%)
s_0	1.0	0.0658	0.0565	7.604	0.00
$s_0 + \Delta s_t$	1.043	0.0634	0.0548	7.276	−4.31
$s_0 + \Delta s_b$	1.051	0.0630	0.0545	7.234	−4.87

According to the simulation results, the AC excitation source of the inductive transducer leads to the changing magnetic induction intensity, which generates the eddy current in the rotor, as shown in Fig. 13. According to reference [13], the eddy current also affects the measurement accuracy of the inductive transducer. As shown in the Table 6, due to the change of the clearance, the maximum Eddy current density on rotor surface is significantly increased, which will further affect the measurement accuracy of the transducer. However, due to the complex relationship between the distribution of the eddy-current magnetic field and the rotor speed, the calculation is difficult and further theoretical analysis is needed.

Table 6. The Eddy current on the rotor surface.

s (mm)		Jz (A/m^2)
s_0	1	-8.317e+5
$s_0 + \Delta s_b$	1.051	-8.680e+5
$s_0 + \Delta s_t$	1.043	-8.684e+5

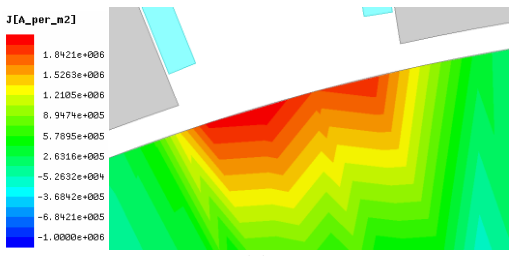

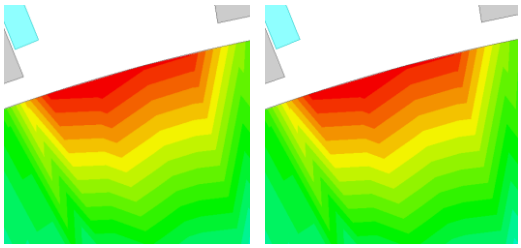

(b) (c)

Fig. 13. The eddy current density in the transducer: (a) the original clearance $\boldsymbol{s_0 = 1\ mm}$, (b) $\boldsymbol{\Delta s_t = 4.3\%}$ in the top AMB, and (c) $\boldsymbol{\Delta s_b = 5.1\%}$ in the bottom AMB.

IV. UNBALANCED RESPONSE OF THE AMB-ROTOR SYSTEM UNDER THERMAL DEFORMATION

A. Simulation of the AMB-rotor system

Due to the material inhomogeneity and machining error, the rotor possesses unbalanced mass inevitably, which will cause unbalance force for the rotor. When the circulator is running, the rotor unbalanced vibration caused by the unbalanced force will increase with the increasing rotor speed, but the AMB controller will suppress the rotor unbalanced vibration via active electromagnetic force [14-16]. However, the AMB controller is designed based on the original AMB-rotor system, which means the clearance change will change the controller parameters and affect the unbalanced response of the AMB-rotor system. In this section, the simulation of AMB-rotor system is carried out to study the influence of thermal deformation on the unbalanced response of the AMB-rotor system.

Based on the FEA of the thermal deformation and transducer measurement, the AMB-rotor system in circulator is built and simulated in MATLAB Simulink, as is shown in Fig. 14. The system includes the rotor module that considers the gyroscopic effect and unbalanced mass, the cross-feedback module, and the AMB controller module. The system is under cross-feedback PID control and the rotor speed is 60 Hz. Based on the data in Table 4, change the parameters of the system and runs the simulation.

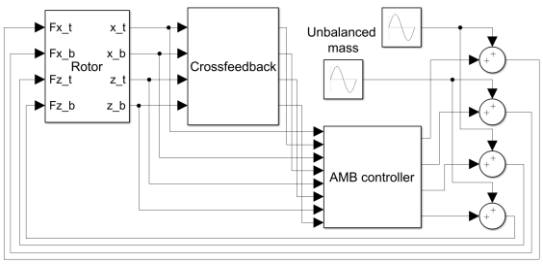

Fig. 14. The AMB-rotor system in circulator.

In the simulation, the rotor speed increase from 0 to 60 Hz and runs stably. The unbalanced vibration of the rotor is simulated by applying a periodic external force at Fx_t and Fx_b. The output of x-t and y-t compose the axis orbit of the top AMB, and x-b and y-b compose the bottom. The clearance change is simulated by changing the force-displacement coefficient and force-current coefficient of the AMB and the transfer coefficient of the transducer.

The axis orbits of the rotor at the top and bottom AMBs are shown in Fig. 15, where the horizontal axis represents the rotor displacement in the X direction and the vertical axis represents Z direction. The solid blue line and red dotted line are the axis orbits of the rotor in original clearance and changed clearance, respectively.

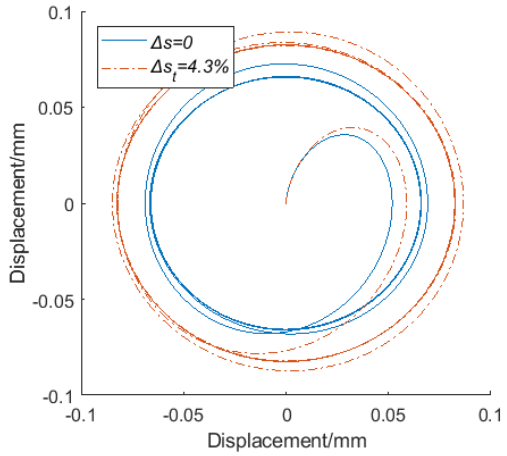

(a)

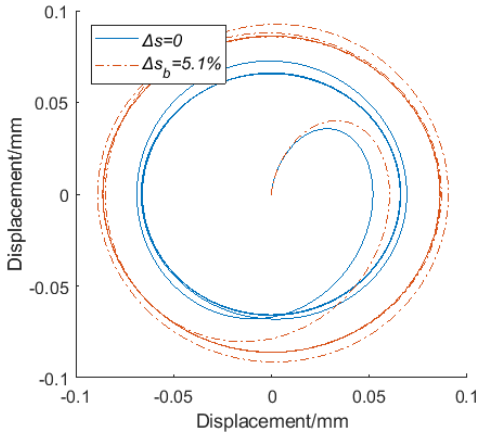

(b)

Fig. 15. Axis orbit of the rotor under different clearance change: (a) top AMB and (b) bottom AMB.

Under the influence of the unbalanced mass, the rotor vibrates when the rotor speed is fixed. However, after the thermal deformation, the clearance change leads

to the axis orbit expand both in the top and bottom AMB. The results show that the clearance change will reduce the performance of the AMB controller and aggravate the rotor vibration.

B. Operation experiment of the circulator

The experiment for circulator is carried out to explore the performance of AMB controller and stability of AMB-rotor system under high temperature environment. In the experiment, the rotor speeds up to 3200 rpm in 7 min and the axis orbit of the rotor is obtained at time A. After the circulator temperature is stable, the axis orbit of the rotor at time B is recorded. The temperatures at different position of the circulator are measured by the temperature sensor, which are the reference of the heat sources in the FEA.

Figure 16 shows the experimental result. The vertical axis on the left shows the ratio of the radial vibration amplitude to clearance and the right one shows the rotor speed. It can be seen that the rotor speed can be well controlled. Before 7 min, the vibration amplitude of the rotor increases as the rotor speeds up. This is due to the unbalanced force resulting from the unbalanced mass of the rotor. The unbalanced vibration is proportional to the rotor speed, but when the rotor speed is fixed at 3200 rpm after 7 min, the vibration amplitude of the rotor continues to increase. At this point, the factor that affect the vibration amplitude is not the rotor speed, but the clearance change caused by the thermal deformation.

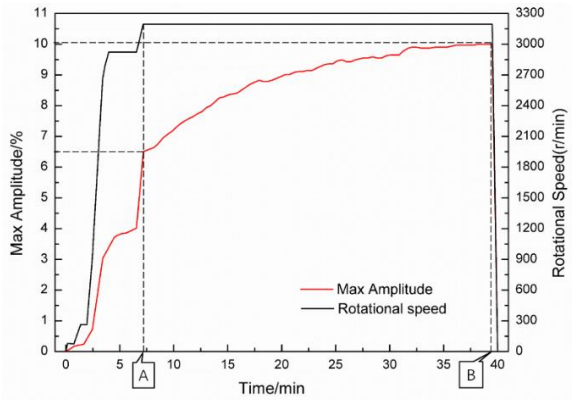

Fig. 16. Rotor speed and vibration amplitude.

In Figs. 17 and 18, the horizontal and vertical axis represents the rotor displacement. It can be seen that at time A, the axis orbit and the vibration amplitude of the rotor is small, while at time B, the vibration amplitude significantly increases.

The experimental results show that with a fixed rotor speed, the vibration amplitude of the rotor gradually increases with the increasing temperature of the circulator. And when the temperature is stable, the vibration amplitude of the rotor tends to be stable. The experiment shows that the unbalanced vibration of the rotor increases with the increasing temperature of the circulator after long-term operation. The thermal deformations affect the clearance, and then reduce the performance of the AMB controller and affect the unbalanced response of the AMB-rotor system. This is consistent with theoretical analysis and simulation.

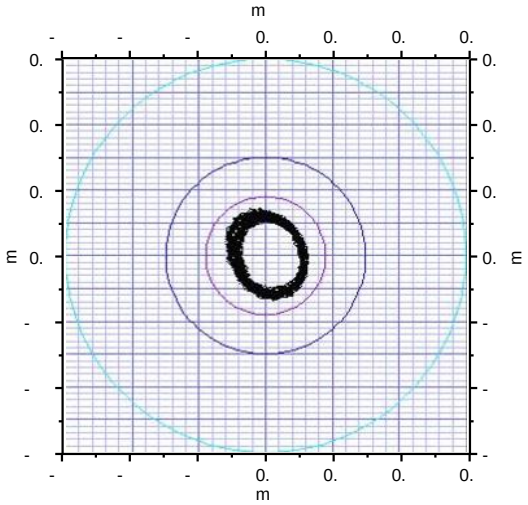

Fig. 17. Axis orbit of the top AMB at time A.

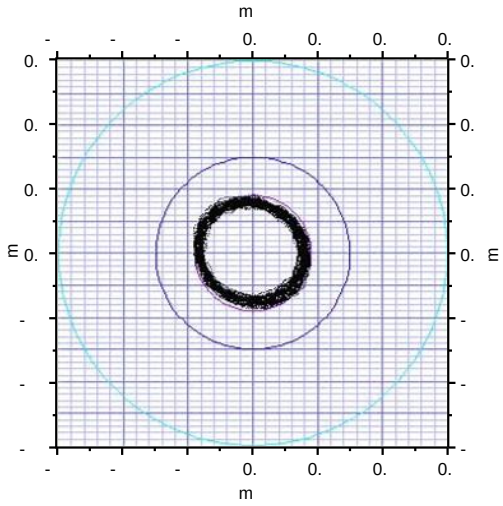

Fig. 18. Axis orbit of the top AMB at time B.

V. CONCLUSION

In this paper, the influence of thermal deformation on the unbalanced response of the AMB-rotor system is studied, which provides a reference for the mechanical design of AMBs.

According to the theoretical analysis, clearance change caused by thermal deformation eventually change the AMB stiffness. As the clearance decreases, Δk_x and Δk_i become larger and vice versa. And Δk_x is

more sensitive to the clearance than Δk_i. The thermal deformation will also change the transducer-rotor clearance, and the transducer sensitivity and the measurement accuracy of rotor displacement will be affected, which lead to the measurement error of the rotor displacement.

From the FEA results, the heat from the motor and AMBs contribute to the deformation of the circulator. The clearance increases 4.3% in the top radial AMB and 5.12% in the bottom radial AMB. Due to the clearance change, the transducer sensitivity changes significantly, leading to measurement error of the rotor displacement. The measurement error in the top AMB is -4.31% and the bottom is -4.87%, which are consistent with the theoretical calculation.

The simulation and experiment shows that with the influence of the unbalanced mass, the rotor vibrates when the rotor speed is fixed. However, after the thermal deformation, the clearance change leads to the axis orbit expand both in the top and bottom AMB. The thermal deformation will reduce the performance of the AMB controller and affect the unbalanced response of the AMB-rotor system. The experiment shows that the thermal deformations affect the clearance, and then reduce the performance of the AMB controller and affect the unbalanced response of the AMB-rotor system. This is consistent with theoretical analysis and simulation.

The influence of the clearance changing on the electromagnetic force, AMB stiffness and transducer measurement is discussed with the theoretical electromagnetic calculations, including the AMB force, transducer and eddy current. The theoretical calculations in this paper has general applications in the controller improvement of the AMBs under clearance change and provides a reference for mechanical structure design and controller design of AMBs.

ACKNOWLEDGMENT

This paper is financially supported by the National Science and Technology Major Project of China (2011ZX069) and Project 61305065 supported by NSFC.

REFERENCES

[1] Z. Zhang, Z. Wu, Y. Sun, and F. Li, "Design aspects of the Chinese modular high-temperature gas-cooled reactor HTR-PM," *Nuclear Engineering and Design*, vol. 236, no. 5-6, pp. 485-490, Mar. 2006.

[2] Z. Zhang and Y. Sun, "Economic potential of modular reactor nuclear power plants based on the Chinese HTR-PM project," *Nuclear Engineering & Design*, vol. 237, no. 23, pp. 2265-2274, Dec. 2007.

[3] G. Yang, Z. Shi, N. Mo, and L. Zhao, "Research on active magnetic bearing applied in Chinese modular high-temperature gas-cooled reactor," *Progress in Nuclear Energy*, vol. 77, pp. 352-360, Nov. 2014.

[4] G. Yang, Z. Shi, and N. Mo, "Technical design and engineering prototype experiment of active magnetic bearing for helium blower of HTR-PM," *Annals of Nuclear Energy*, vol. 71, pp. 103-110, Sep. 2014.

[5] Z. Sun, Y. He, J. Zhao, Z. Shi, L. Zhao, and S. Yu, "Identification of active magnetic bearing system with a flexible rotor," *Mechanical Systems & Signal Processing*, vol. 49, no. 1-2, pp. 302-316, Dec. 2014.

[6] Z. Sun, X. Yan, J. Zhao, X. Kang, G. Yang, and Z. Shi, "Dynamic behavior analysis of touchdown process in active magnetic bearing system based on a machine learning method," *Science & Technology of Nuclear Installations*, vol. 2017, no. 5, pp. 1-11, Oct. 2017.

[7] C. Zhang, Z. Yi, and Z. Zhang, "THD Analysis of high speed heavily loaded journal bearings including thermal deformation, mass conserving cavitation, and turbulent effects," *Journal of Tribology*, vol. 122, no. 3, pp. 597-602, July 2000.

[8] H. Suzuki, K. Urano, H. Kumehara, and K. Kusumoto, "Minimizing thermal deformation of ultraprecision machine tool induced by lubricating oil of hydrostatic bearings," *Journal of the Japan Society of Precision Engineering*, vol. 75, no. 9, pp. 1106-1111, Sep. 2009.

[9] K. Jiang, C. Zhu, L.Chen, and X. Qiao, "Multi-DOF rotor model based measurement of stiffness and damping for active magnetic bearing using multi-frequency excitation," *Mechanical Systems & Signal Processing*, vol. 60-61, pp. 358-374, Aug. 2015.

[10] J. I. Inayat-Hussain, "Nonlinear dynamics of a statically misaligned flexible rotor in active magnetic bearings," *Communications in Nonlinear Science & Numerical Simulation*, vol. 15, no. 3, pp. 764-777, Mar. 2010.

[11] M. FeLix, A. LizaRraga, A. Islas, and A. Gonzalez, "Analysis of a ferrofluid core LVDT displacement sensor," *IECON 2010-36th Annual Conference on IEEE Industrial Electronics Society*, Glendale, AZ, 2010.

[12] A. Hossain and M. J. Dwyer, "A new type of liquid density transducer based on the principle of linear variable differential transformer," *Sensors for Industry, 2001. Proceedings of the First ISA/IEEE Conference*, pp. 270-275, 2001.

[13] J. Yu and L. Zhao, "Internal vibration source analysis of AMB-rotor system in HTR-PM primary helium circulator," *ASME. International Conference on Nuclear Engineering*, London, 2018.

[14] J. Tang, B. Xiang, and Y. Zhang, "Dynamic characteristics of the rotor in a magnetically suspended control moment gyroscope with active

magnetic bearing and passive magnetic bearing," *ISA Trans*, vol. 53, no. 4, pp. 1357-1365, Nov. 2014.

[15] Y. He, Z. Shi, L. Shi, and Z. Sun, "Unbalance compensation of a full scale test rig designed for htr-10gt: a frequency-domain approach based on iterative learning control," *Science and Technology and Nuclear Installations*, vol. 2017, no. 1-15, Jan. 2017.

[16] T. Fan, Z. Sun, X. Zhang, X. Yan, J. Zhao, and Z. Shi, "Residual unbalanced mass determination of an AMBs controlled rotor based on control current analysis of the feedback loop," *ASME. International Conference on Nuclear Engineering*, London, vol. 1.

Jinpeng Yu received his B.Sc. degree in 2015 from Dalian University of Technology. Now he is studying for a Ph.D. in the Institute of Nuclear and New Energy Technology, Tsinghua University. He is mainly engaged in active magnetic bearing and its application in flywheel system.

Zhe Sun is currently an Sssociate Professor and Ph.D. Supervisor of Tsinghua University. His research interests are control and monitoring of active magnetic levitation system, rotor dynamics, statistical learning theory and its engineering application, etc. He has published more than 20 SCI/EI index papers and 10 national patents. He presides over and participates in a series of National Science and Technology Major Project of China, National Natural Science Foundation of China and National High-tech Research and Development Program of China.